Constraining neutrino interaction uncertainties for oscillation measurements in the NOvA experiment using Near Detector data

by

Maria Martinez Casales

A dissertation submitted to the graduate faculty

in partial fulfillment of the requirements for the degree of

DOCTOR OF PHILOSOPHY

Major: High Energy Physics

Program of Study Committee:
Mayly Sanchez, Co-major Professor
Matthew Wetstein, Co-major Professor
Rebecca Flint
Soeren A. Prell
Kirill Tuchin
Amanda Weinstein

The student author, whose presentation of the scholarship herein was approved by the program of study committee, is solely responsible for the content of this dissertation. The Graduate College will ensure this dissertation is globally accessible and will not permit alterations after a degree is conferred.

Iowa State University

Ames, Iowa

2023

DEDICATION

Para Mamá y Papá.

TABLE OF CONTENTS

Page

LIST OF TABLES

Page

LIST OF FIGURES

Page

ACKNOWLEDGMENTS

This dissertation is on the topic of neutrino physics, but I have learned about many more things through this journey, thanks to all of the wonderful people I have encountered.

I'd like to thank first and foremost, my advisor Mayly Sanchez. Our conversations went beyond research guidance and I deeply appreciate your mentorship and trust in my abilities to finish this analysis. I am also grateful to Alfredo Aranda and Jon Paley, without your encouragement and support I wouldn't have seriously considered pursuing a PhD in experimental particle physics. I have to mention that my scientific formation was greatly influenced by the excellent people in the NOvA collaboration. I have to especially thank Hugh Gallagher, whose encouragment and input were very impactful for my analysis. I also wish to thank Alex Himmel for the very insightful physics conversations. I also had amazing input and support, for both my analysis and life as a physicist, from Jeremy Wolcott, Zoya Vallari, Anne Norrick and Erika Catano-Mur. And I would like to add special thanks to Michael Dolce, for all the help as we both tried to understand and carry to the end our Near and Far Detector fits.

I am very grateful to the friends I met at Iowa State University: Sebastian, Carlos, Elizabeth, Tomás, Anita and Michelle, for all the good times in Ames. We had many interesting evenings talking about both science and nonsense. And thank you Sebastian, Elizabeth, and Miranda, for all the weekends and evenings spent in the windowless TA office, doing homework and studying. The first two years of grad school were tough, and it would have been much harder without our little study group. I greatly appreaciate all the conversations about physics and life with Miranda. I learned a lot from her.

Thank you to my NOvA best buddies, Pinaki and Bea. I truly treasure the fun times we had and the support we gave each other during the hardest times in grad school. There are so many friends I met at Fermilab, who have made this journey more fun than I expected: Amy, Anna,

other Anna, Barbara, Carlos, Diana, Iker, Ivan, Mehereen and Robert, thank you all. I need to especially thank my friends Rob and Xuan, by chance we became housemates and unexpectedly we chose to endure the toughest year together. I learned so many things from them that will always be a part of me. I have to also thank Marvin and Faiza. More than housemates, we became good friends and had a lot of fun times. Special thanks to Marvin, for the useful suggestions to improve this thesis.

And of course I want to thank my friends in Mexico. Nini, we saw each other only a handful of times in the past few years, but every interaction we had lit up my day. Thanks as well to Arturo, who reminds me of who I am outside of physics. And of course, thanks to Adri: our frequent conversations kept me grounded and sane in the last few years.

I don't have enough words to thank Everardo. His genuine understanding and words of encouragement were especially important in the last few months. This thesis wouldn't be written in time without his support.

And last but not least, I want to thank my family: Mamá, Papá, Martin y Ruy. I wouldn't have made it this far wihtout them. Their unconditional support has been my fuel in this journey.

ABSTRACT

NOvA is a long-baseline neutrino experiment at Fermilab that studies neutrino oscillations via electron neutrino appearance and muon neutrino disappearance from the NuMI beam at Fermilab. The beam configurations allow for a muon neutrino or antineutrino enriched flux. The combined analysis of the four samples allows for the measurement of $\sin^2\theta_{23}$, Δm^2_{32} and constrain of δ_{CP} , as well as the mass hierarchy and the octant of θ_{23}. The measurement of oscillations relies on the prediction at the Far Detector(FD), which is constrained by the study of the large datasets of ν_μ and $\bar{\nu}_\mu$ at the Near Detector(ND).

The ND data is not accurately represented by the GENIE simulation, therefore the interaction model requires adjustments. I present these adjustments to the central value, the *NOvA tune*, with emphasis on the meson exchange current (MEC) model, my work, which has been included in the latest published oscillation measurement result [10].

This work is expanded by exploiting the high statistics sample of the ND via the introduction of final state-based topology samples. I present a study of the ν_μ and $\bar{\nu}_\mu$ datasets, which reveals remaining deficiencies NOvA tune. These samples are then used to constrain more parameters of the interaction model, as well as detector response and neutrino beam uncertainties. Various fake data fits are presented, which studied the parameters to which the NOvA data is not sensitive, the correlations among MEC parameters in the NOvA tune and the ability of the current model to fit fake data with a different MEC model. The result of data fits with and without the MEC tuning parameters are compared.

A novel method for the NOvA oscillation fit is presented. The resulting constrain from the ND fit to data is implemented in the fit via a covariance term. I demonstrate the fitting method with Asimov data with NOvA measurement from [10]. Two robustness studies are presented: 1) to test the use of variations in the ND constrain and 2) to test the implication of using a

constraint that does not perfectly reproduce the ND data via the use of *residual fake data*. The *residual fake data* study is also presented in two additional Asimov points that are within the observable phase space for NOvA in different mass ordering or δ_{CP} . In addition the fake data studies with a different MEC model are also evaluated.

CHAPTER 1. INTRODUCTION

The study of neutrino oscillations is one of the most promising paths for new physics. Since Pauli's proposal of the neutrino in 1930 to the big neutrino experiments today, neutrino physics has led to multiple discoveries that expand our understanding of nature. Before diving into details of the analysis of neutrino oscillations with the NOvA experiment, this chapter will introduce an overview of neutrinos in the framework of the Standard Model, the implications of neutrino oscillations and neutrino interactions in matter.

1.1 A brief history of the discovery of neutrinos

The story of neutrinos begins with the study of the $\beta-$ decay. Initially, the β decay was understood to be a two body process ($N \rightarrow N' + e$), where the nucleus spontaneously ejects an electron, leaving behind a lighter nucleus. Knowing the initial and final mass of the nucleus that underwent the decay, conservation of energy dictates the energy of the electron should be exactly equal to the mass difference. However, in 1914 James Chadwick observed a continuous energy spectrum of the electrons emitted from this process [11]. The alarming implication of this observation is that energy conservation was violated. Until 1927, the decisive experiment of Charles Drummond Ellis and W. A. Wooster confirmed the continuous spectrum of electrons from radium E (^{210}Bi) decays (see Figure 1.1) [3]. Given this situation, in 1930, with the famous letter "Dear radioactive ladies and gentlemen", Wolfgang Pauli describes his proposal of an extremely light neutral particle which he called the neutron, a "desperate remedy" to explain this energy spectrum [12]. After Chadwick's discovery of the neutron, a different particle from what Pauli proposed, the understanding of the $\beta-$ decay changed. This led to Enrico Fermi's theory of beta decay to include the newly re-named particle, the neutrino, *little neutral one* in Italian, due to is hypothesized small mass [13]. His theory proposed antineutrinos and electrons are created in

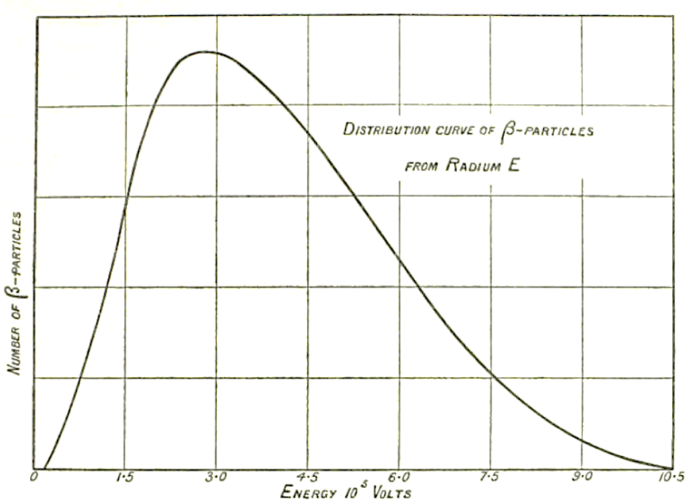

Figure 1.1: β spectrum of ^{210}Bi [3].

the $\beta-$decay process, rather than contained in the nucleus. Moreover, he derived quantitative expressions for the lifetime of β decay and the shape of the β emission spectrum. This model has inspired the modern description of all weak-interaction processes. Although Fermi's theory was successful in describing the β spectrum, the neutrino wouldn't be observed until decades later. Shortly after Fermi's theory, Hans Bethe and Rudolf Peierls showed that the probability of a neutrino interacting with a proton, via the inverse β process, consisting of the capture of a neutrino by a nucleus together with the emission of an electron (or positron), is extremely small. They calculated a cross section $\sigma < 10^{-44}\text{cm}^2$, for an average neutrino energy of 2 MeV, giving it a penetrating power of 10^{16} km in solid matter. Thus at the time it was "absolutely impossible to observe processes of this kind with the neutrinos created in nuclear transformations" [14].

After various attempts, Cowan and Reines finally detect neutrinos. Their 1953 experiment in Hanford, Washington, yielded promising evidence of neutrino detection, however the cosmic background obscured the neutrino signals [15]. In 1956, they successfully measured the cross section of antineutrinos from a nuclear reactor in Savannah River [16]. The experiment (see Figure 1.2) consisted in of two large plastic tanks (A and B) filled with water and cadmium

chloride, where the inverse β decay will occur:

$$\bar{\nu} + p \rightarrow n + \beta^{+} \tag{1.1}$$

These tanks were sandwiched between three large scintillation detectors (1,2 and 3) with a capacity of 4200 liters, with 110 photomultiplier tubes to collect scintillation light and produce electronic signals. The signal was identified using the method of Delayed-Coincidence Signals. For instance if an inverse β decay occurs in tank A, it would create two pairs of photon prompt-coincident pulses from detectors 1 and 2. The first pair of pulses would be from positron annihilation and the second from neutron capture in cadmium from the scintillator. These pairs of signals would be separated by about 3 to 10 μs. This experiment allowed to successfully measure a cross section in agreement with the theoretical value. And so after 25 years of Pauli's proposal, the neutrino was finally detected.

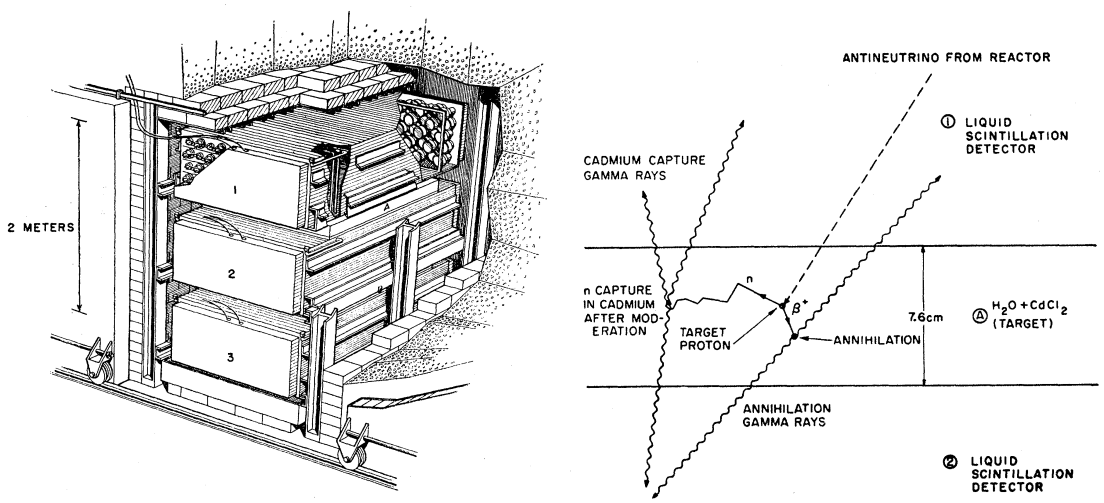

(a) (b)

Figure 1.2: (a) Schematic diagram of the The Savannah River neutrino detector , showing the initial inverse β decay, and the two pairs of photons from the positron (β^{+}) annihilation and from the cadmium capture. (b) Sketch of the detectors. Tanks 1, 2 and 3 contained liquid scintillator and a configuration of 110 photomultoplier tubes. The two water tanks labeled A and B contain water and dissolved $CdCL_2$.Figure taken from [17].

The neutrinos and antineutrinos from β decays are electron neutrinos and antineutrinos. Currently it is known that there are three families of leptons: electrons (e), muons (μ) and taus

(τ), with their corresponding neutrino (ν_e, ν_μ, ν_τ). Muons were discovered from the study of cosmic rays in 1937 [1]. It was eventually confirmed that they decay through the process $\mu^- \to e^- + \nu + \nu$. Assuming the two neutral leptons were identical, the process $\mu^- \to e^- + \gamma$ should have been observed, but it wasn't. This was an indication that the two neutral leptons were not identical, one had to be associated with the muon. Based on this observations, Pontecorvo [18] and Schwartz [19] suggested using high energy neutrino beams to test whether neutrinos from pion decays produce muons or electrons.

Eventually, in in 1962 Lederman, Schwartz and Steinberger detected the muon neutrino in Brookhaven National Lab [4]. They used a beam of protons 15 GeV from the Alternating Gradient Synchrotron, which struck a beryllium target, resulting in a shower particles, including pions, which then decayed into neutrinos via $\pi^\pm \to \mu^\pm + (\nu/\bar{\nu})$. A thick shield stopped most of the other particles, then the neutrinos were detected in an aluminum spark chamber. The basic design used for this neutrino beam (Figure 1.3), the first of its kind, is still used today.

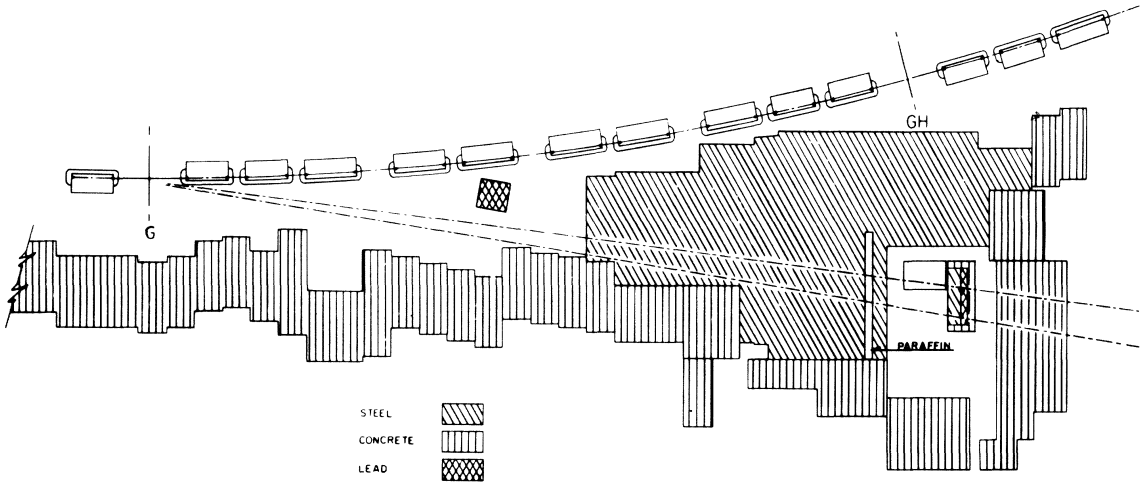

Figure 1.3: Diagram of the LSS neutrino beam. [4].

The third neutrino, ν_τ, was not detected until much later. In 1975, the tau lepton was detected in at Stanford Linear Accelerator Laboratory [20]. Along with this third lepton, the tau neutrino should exist, but it was not until 2001 that the ν_τ was observed in the DONUT

experiment at Fermilab [21]. Years earlier, in 1989, the Large Electron-Positron collider at CERN showed there were only three lepton families (three charged leptons and three neutrinos), via the measurement of the lifetime of the Z-boson, thus establishing the Standard Model of physics [22] [23] [24].

By this time Pontecorovo [25] had suggested the idea of neutrino oscillations between neutrinos and antineutrinos, analogous to the $K^0/\bar{K}^0$ oscillation (at the time when only the ν_e was known). Maki, Z. Maki, M. Nakagawa and S. Sakata [26] assumed the representation of neutrinos ν_1 and ν_2 through linear combinations of ν_e and ν_μ . V. Gribov and B. Pontecorvo proposed the phenomenological theory of two-neutrino mixing in 1969 [27].

In 1968 the first experiment to detect solar neutrinos, produced from nuclear fusion in the Sun, was conducted at the Homestake mine in South Dakota. Raymond Davis Jr. and John N. Bahcall observed a smaller flux of neutrinos than expected, which was explained by the Standard Solar Model (SSM). Just as Pontecorvo postulated, neutrino oscillations would reduce the flux from solar neutrinos to two times smaller the flux if there were no oscillations [28] [29]. But this deficit, initially believed to be an experimental flaw, known as the *solar neutrino problem*, was confirmed by later experiments with different technologies, such as the Kamiokande water Cherenkov detector in 1989 [30], and the gallium based experiments SAGE in 1991 [31] and GALLEX in 1992 [32].

The *solar neutrino problem* would not be solved until 1998, when the Super Kamiokande experiment showed evidence of an angular dependence on the flux of ν_μ produced by cosmic ray interactions in the atmosphere [33] [34]. This demonstrated that neutrinos travelling a different distances after production, and traversing the Earth at different angles on their way to the detector, were 'disappearing', thus providing evidence of neutrino oscillations. The final resolution to the *solar neutrino problem*[1] was provided by the SNO experiment, which measured the ^{8}B solar spectrum. They searched for the reaction on deuterium $\nu_x + d \rightarrow \nu_x + p + n$ (where ν_x represents any neutrino flavor), a Neutral Current interaction (NC), which would yield the total

[1] although the full explanation includes the MSW effect (see section 1.3)

rate of neutrinos from the sun, regardless of their flavor. Their astonishing finding was that indeed, the total flux of NC interactions was consistent with the SSM, and their rate of ν_e events was consistent with that measured by Super Kamiokande [35]. These two experiments' observations provided conclusive evidence that neutrinos oscillate, and therefore have mass.

Although many discoveries have been made regarding neutrinos, they are still a mysterious particle. The conclusion that they have mass poses them as the first experimental evidence of physics outside the Standard Model and questions remain such as the origin of their mass, the existence or not of sterile neutrinos, whether neutrinos are Dirac or Majorana, among others.

1.2 Neutrinos in the Standard Model

The Standard Model (SM) is successful in describing the strong, electromagnetic and weak interactions of elementary particles, in the framework of quantum field theory. It is a gauge theory based on the local symmetry group $\mathrm{SU(3)_C} \times \mathrm{SU(2)_L} \times \mathrm{U(1)_Y}$, where the subscripts C, L and Y represent color, left-handed chilarity and weak hypercharge. The gauge group determines the interactions and number of gauge bosons which correspond to the generators of such group. There are eight massless gluons that mediate the strong interactions, corresponding to the generators of $\mathrm{SU(3)_C}$; three massive ($W^{\pm}, Z$) and one massles (γ) gauge bosons, corresponding to the three generators of $\mathrm{SU(2)_L}$ and one generator $\mathrm{U(1)_Y}$, which mediate electroweak interactions. In addition, the scalar Higgs field, or Higgs boson, generates mass for the gauge bosons, with the mechanism of spontaneous symmetry breaking. The electroweak part of the SM determines the interactions of neutrinos and other fermions. We can study electroweak and strong interactions separately, given that there is no mixing between $\mathrm{SU(3)_C}$ and $\mathrm{SU(2)_L} \times \mathrm{U(1)_Y}$ sectors. The SM also contains 12 fermions (spin 1/2), which can be divided in two categories: quarks and leptons. The quarks participate in all the interactions (strong, weak, electromagnetic and gravitational). Meanwhile the leptons participate in all but the strong interactions. The corresponding antiparticles have the same mass but opposite electric charge. One of the unexplained features of

the SM is the existence of three generations of fermions with identical properties, but different masses. All of the particles of the SM with their properties are depicted in Figure 1.4.

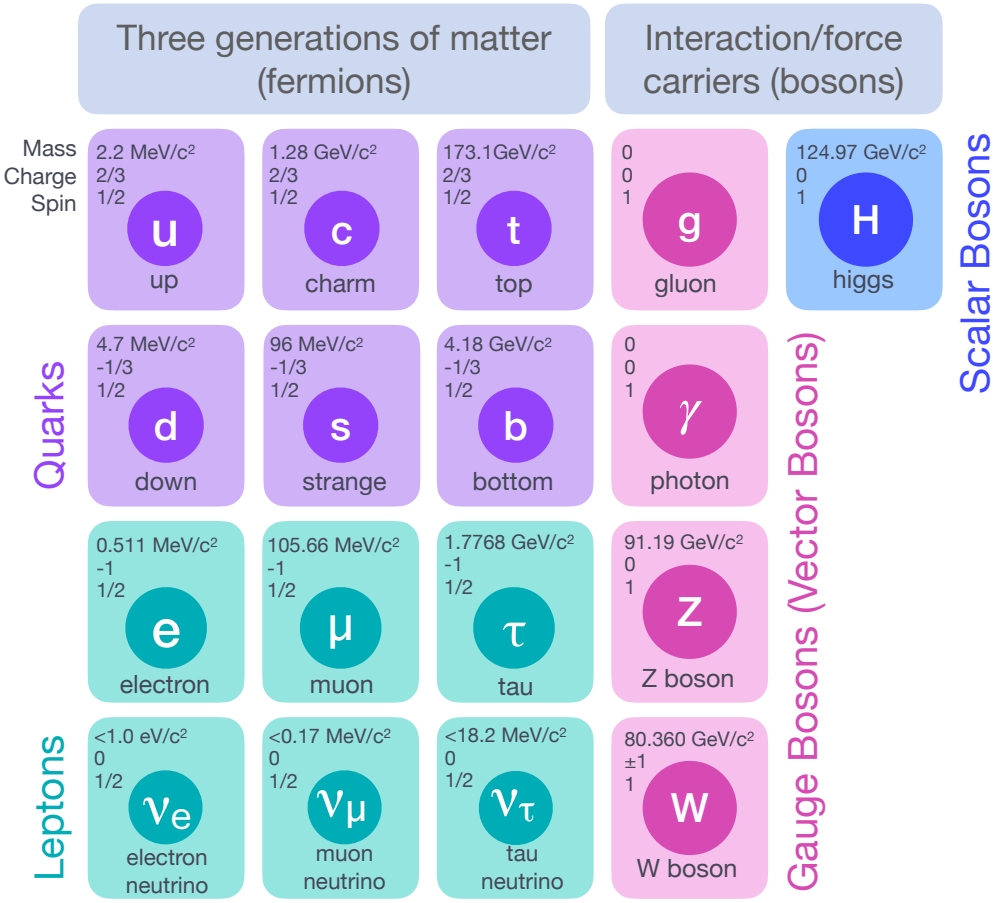

Figure 1.4: Standard Model diagram form showing the 12 fundamental fermions and the 5 bosons.

The unified theory of weak and electromagnetic interactions for leptons was formulated by Weinberg and Salam independently. Later it was extended to the quark sector by Glashow, Iliopoulos, and Maiani. In 1979, Glashow, Salam and Weinberg were awarded the Nobel Prize in Physics for the formulation of this theory. The main features of electroweak interactions can be summarized as follows:

- Electromagnetic and weak interactions involve all the elementary particles (leptons and quarks).
- Electromagnetic and weak interactions are mediated by vector fields. For electromagnetic interactions, the massless photon is the mediator. For weak interactions the mediator is a intermediate vector boson (IBV).
- Weak interactions involve a pair of leptons, such as (ν_e, e^-). Only the left handed components of leptons (e_L, ν_L) participate. Both components of the electrons e_L and e_R participate in electromagnetic interaction. ν_R does not interact with matter.
- Electromagnetic and weak interactions are universal: they have the same coupling strength for all fermions (leptons and quarks).
- The Higgs mechanism is used to generate masses for the gauge fields corresponding to the IVB mediating the weak interactions while keeping the photon field mediating electromagnetic interaction massless.

In the Weinberg-Salam model, the interaction Lagrangian can be written as:

$$\begin{aligned} \mathcal{L}^{WS} &= \mathcal{L}^{em} + \mathcal{L}^{weak} \\ \text{with } \mathcal{L}^{weak} &= \mathcal{L}^{CC} + \mathcal{L}^{NC} \end{aligned} \tag{1.2}$$

The SM is phenomenologically very successful; among others, interactions of neutrinos have been experimentally verified with high accuracy [36] (more details about this will be explained in section 1.4). Nevertheless, the SM is has 18 free parameters which are not predicted by this theory. In addition, this framework predicts massless neutrinos. The current experimental observations indicate neutrinos are not massless, and their properties, which will be described in the following sections, are not predicted by the SM. The fact that experimental evidence shows neutrinos have mass points to the existence of physics beyond the Standard Model. [37]

1.3 Neutrino mixing and oscillations

Neutrino oscillation is a quantum mechanical phenomenon, in which a neutrino fo one flavor v_α develops a component of a neutrino of another flavor ν_β, with $\alpha, \beta = e, \mu, \tau$ and $\alpha \neq \beta$. This implies the neutrino mass eigenstates (or propagation states) are different from their weak interaction, or flavor, eigenstates. The flavor state ν_α can be written as an orthonormal linear combination of the mass eigenstates ν_k, with $k = 1, 2, 3$ which are related by the unitary 3×3 matrix $U_{\alpha,k}$:

$$|\nu_\alpha\rangle = \sum_k U^*_{\alpha k} |\nu_k\rangle \qquad (\alpha = e, \mu, \tau) \tag{1.3}$$

To obtain the transition probability of $\nu_\alpha \to \nu_\beta$ in vacuum, let us start with the Schrödinger equation

$$i\frac{d}{dt}|\nu_k(t)\rangle = \mathcal{H}|\nu_k(t)\rangle \tag{1.4}$$

where the neutrino states $|\nu_k\rangle$ are eigenstates of the Hamiltoian

$$\mathcal{H}|\nu_k\rangle = E_k|\nu_k\rangle \tag{1.5}$$

with energy eigenvalues $E_k = \sqrt{p^2 + m^2}$. The solution of 1.4 would be:

$$|\nu_k(t)\rangle = e^{-iE_k t}|\nu_k\rangle \tag{1.6}$$

Considering a flavor state $|\nu_\alpha(t)\rangle$, which corresponds to a neutrino created with a definite flavor α at time $t = 0$, the time evolution of this state, from 1.3 and 1.6 is

$$|\nu_\alpha(t)\rangle = \sum_k U^*_{\alpha k} e^{-iE_k t}|\nu_k\rangle \tag{1.7}$$

Then inverting 1.3, we can write the mass states in terms of the flavor eigenstates as

$$|\nu_k\rangle = \sum_\alpha U_{\alpha k}|\nu_\alpha\rangle \tag{1.8}$$

which can be introduced into 1.6 to obtain

$$|\nu_\alpha(t)\rangle = \sum_{\beta=,e,\mu,\tau} \Big(\sum_k U^*_{\alpha k} e^{-iE_k t} U_{\beta k} \Big) |\nu_\beta\rangle \tag{1.9}$$

As it propagates, the initial state $|\nu_\alpha\rangle$ becomes a superposition of different flavor states, in the case where the mixing matrix U is not diagonal. Then the amplitude of the transition $\nu_\alpha \to \nu_\beta$ can be obtained from the coefficient of $|\nu_\beta\rangle$:

$$A_{\nu_\alpha \to \nu_\beta}(t) \equiv \langle \nu_\beta | \nu_\alpha(t) \rangle = \sum_k U^*_{\alpha k} U_{\beta k} e^{-iE_k t} \tag{1.10}$$

which yields the transition probability

$$P_{\nu_\alpha \to \nu_\beta} = \left| A_{\nu_\alpha \to \nu_\beta}(t) \right|^2 = \sum_{k,j} U^*_{\alpha k} U_{\beta k} U_{\alpha j} U^*_{\beta j} e^{-i(E_k - E_j)t}. \tag{1.11}$$

In the case of ultrarelativistic neutrinos, one can approximate

$$E_k \simeq E + \frac{m_k^2}{2E}. \tag{1.12}$$

With the squared mass difference $\Delta m^2_{kj} \equiv m^2_k - m^2_j$ and neglecting the mass contribution to the neutrino energy $E = |\vec{p}|$, 1.11 can be expressed as :

$$P_{\nu_\alpha \to \nu_\beta}(t) = \left| A_{\nu_\alpha \to \nu_\beta}(t) \right|^2 = \sum_{k,j} U^*_{\alpha k} U_{\beta k} U_{\alpha j} U^*_{\beta j} \exp\left(-i \frac{\Delta m^2_{kj} t}{2E} \right) \tag{1.13}$$

As ultrarelativistic neutrinos propagate close to the speed of light, the approximation $t = L$ is valid. Finally the probability can be written in terms of measurable quantities for experiments as:

$$P_{\nu_\alpha \to \nu_\beta}(L, E) = \left| A_{\nu_\alpha \to \nu_\beta}(t) \right|^2 = \sum_{k,j} U^*_{\alpha k} U_{\beta k} U_{\alpha j} U^*_{\beta j} \exp\left(-i \frac{\Delta m^2_{kj} L}{2E} \right) \tag{1.14}$$

The phases of neutrino oscillations $\phi_{kj} = -\frac{\Delta m^2_{kj} L}{2E}$ are determined by the experiment with neutrino energy E and distance L from the source to the detector, and the squared mass differences $\Delta m^2_{kj} \equiv m^2_k - m^2_j$. The amplitude of the oscillation is determined by the elements of the mixing matrix U.

The lepton mixing matrix U can be written as the Pontecovoro-Maki-Nakagawa-Sakata (PMNS) matrix as:

$$U = \begin{pmatrix} 1 & 0 & 0 \\ 0 & c_{23} & s_{23} \\ 0 & -s_{23} & c_{23} \end{pmatrix} \begin{pmatrix} c_{13} & 0 & s_{13}e^{-i\delta_{CP}} \\ 0 & 1 & 0 \\ -s_{13}e^{i\delta_{CP}} & 0 & c_{13} \end{pmatrix} \begin{pmatrix} c_{12} & s_{12} & 0 \\ -s_{12} & c_{12} & 0 \\ 0 & 0 & 1 \end{pmatrix}$$

$$= \begin{pmatrix} c_{12}c_{13} & s_{12}s_{13} & s_{13}e^{-i\delta} \\ -s_{12}c_{23} - c_{12}s_{13}s_{23}e^{i\delta} & c_{12}c_{23} - s_{12}s_{13}s_{23}e^{i\delta} & c_{13}s_{23} \\ s_{12}s_{23} - c_{12}s_{13}c_{23}e^{i\delta} & -c_{12}s_{23} - s_{12}s_{13}c_{23}e^{i\delta} & c_{13}c_{23} \end{pmatrix} \tag{1.15}$$

(1.16)

where $s_{ij} = \sin\theta_{ij}$, $c_{ij} = \cos\theta_{ij}$ and $(i, j = 1, 2, 3)$. θ_{ij} are called the mixing angles. The unitarity of the PMNS matrix allows to rewrite expression 1.13 as:

$$P(\nu_\alpha \to \nu_\beta) = \delta_{\alpha\beta} - 4\sum_{i>j} \mathrm{Re}\Big(U^*_{\alpha i}U_{\beta i}U_{\alpha j}U^*_{\beta j}\Big) \times \sin^2\left(\frac{\Delta_{ij}}{2}\right)$$
$$+2\sum_{i>j} \mathrm{Im}\Big(U^*_{\alpha i}U_{\beta i}U_{\alpha j}U^*_{\beta j}\Big) \times \sin(\Delta_{ij}) \tag{1.17}$$

where $\Delta_{ij} \equiv \frac{\Delta m^2_{ij}}{2E}L$. For antineutrinos, the oscillation probability is similar, except for a negative sign in the last term, as $U_{\alpha i}$ is replaced for its complex conjugate:

$$P(\bar{\nu}_\alpha \to \bar{\nu}_\beta) = \delta_{\alpha\beta} - 4\sum_{i>j} \mathrm{Re}\Big(U^*_{\alpha i}U_{\beta i}U_{\alpha j}U^*_{\beta j}\Big) \times \sin^2\left(\frac{\Delta_{ij}}{2}\right)$$
$$-2\sum_{i>j} \mathrm{Im}\Big(U^*_{\alpha i}U_{\beta i}U_{\alpha j}U^*_{\beta j}\Big) \times \sin(\Delta_{ij}). \tag{1.18}$$

For the case of survival probability ($\alpha = \beta$), the imaginary part of this equation vanishes, so the general expression for survival probability is:

$$P_{\nu_\alpha \to \nu_\alpha}(L, E) = 1 - 4\sum_{i>j} \Big(|U_{\alpha i}|^2|U_{\alpha j}|^2\Big) \sin^2\left(\frac{\Delta m^2_{ij}}{4E}L\right) \tag{1.19}$$

for $i, j = 1, 2, 3$. Note that only two of the three Δm^2_{ij} are independent:

$$\Delta m^2_{32} = m^2_3 - m^2_2 = (m^2_3 - m^2_1) + (m^2_1 - m^2_2) = \Delta m^2_{31} - \Delta m^2_{21} \tag{1.20}$$

There are two nonequivalent orderings of the neutrino masses, referred as normal ordering (NO) or inverted ordering (IO), as depicted in Figure 1.5. For NO, $m_1 < m_2 < m_3$, and for IO $m_3 < m_1 < m_2$. The smaller mass splitting is designated to be Δm^2_{21}. In other words $\Delta m^2_{32} > 0$

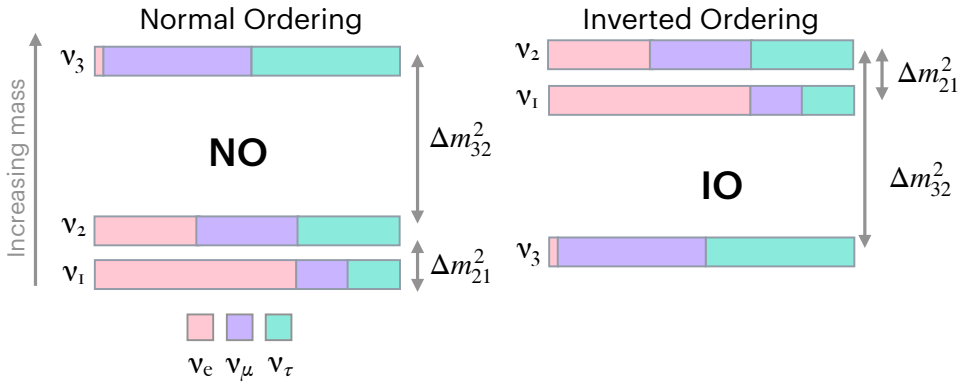

Figure 1.5: Neutrino mass orderings

for NO and $\Delta m^2_{31} < 0$ for IO.

Neutrino oscillations in matter

So far the derivation of neutrino oscillation probabilities was considered for neutrinos propagating in vacuum. However, neutrino experiments are not performed in vacuum. As neutrinos propagate in matter, such as traversing the Sun and the Earth, their evolution equation is affected by the potentials due to coherent interactions. The three flavors of neutrinos undergo NC processes with the nuclei, but ν_e and $\bar{\nu}_e$ also undergo CC interactions with electrons found in matter. The Feynman diagrams of such processes are shown in Figure 1.6

The CC interactions generate a potential V_{CC} through the W exchange:

$$V_{CC} = \sqrt{2} G_F N_e \tag{1.21}$$

where G_F is the Fermi constant, which denotes the strength of the weak interactions, and N_e is the electron density of the medium. This can be calculated for an electron neutrino propagating

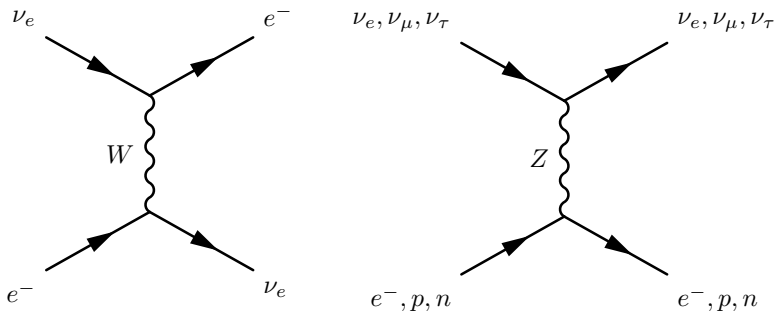

Figure 1.6: Feynman diagrams of coherent forward elastic scattering that generate matter potential. For (a) ν_e CC interactions with the electrons of matter contribute in addition to (b) the NC processes which occur for all neutrino flavors.

in a homogeneous isotropic gas of unpolarized electrons [36]. The neutral current potential

$$V_{NC} = -\frac{1}{2}\sqrt{2}G_F N_n. \tag{1.22}$$

Where N_n is the neutron density. Only the neutrons contribute to this potential, even if the NC interactions occur with protons, neutrons and electrons, because of electrical neutrality implies an equal number density of protons and electrons, terms which cancel. The two contributions yield the potential energy of ultrarelativistic left-handed neutrinos of flavor α propagating through the medium:

$$V_\alpha = V_{CC}\delta_{\alpha e} + V_{NC} = \sqrt{2}G_F\big(N_e\delta_{\alpha e} - \frac{1}{2}N_n\big), \tag{1.23}$$

where $\delta_{\alpha e}$ indicates only for electron neutrinos the CC term contributes. This potential modifies the vacuum Hamiltonian $\mathcal{H}$ from equation 1.4 (which we rename $\mathcal{H}_0$) to

$$\mathcal{H} = \mathcal{H}_0 + \mathcal{H}_I \quad \text{with} \quad \mathcal{H}_I|\nu_\alpha\rangle = V_\alpha|\nu_\alpha\rangle \tag{1.24}$$

We can now rewrite the amplitude of a transition $\nu_\alpha \to \nu_\beta$ after a time t as

$$\psi_{\alpha\beta}(t) = \langle\nu_\beta|\nu_\alpha(t)\rangle \quad \text{with} \quad \psi_{\alpha\beta}(0) = \delta_{\alpha\beta} \tag{1.25}$$

[1]Recall the Kronecker delta indicates $\delta_{ij} = 1$ for $i = j$, and $\delta_{ij} = 0$ for $i \neq j$

and using the ultrarelativistic approximation in equation 1.12 the evolution equation in space becomes

$$i\frac{d}{dx}\psi_{\alpha\beta}(x) = \left(p + \frac{m_1^2}{2E} + V_{NC}\right)\psi_{\alpha\beta}(x) + \sum_{\eta}\left(\sum_{k} U_{\beta k}\frac{\Delta m_{k1}^2}{2E}U_{\eta k}^{*} + \delta_{\beta e}\delta_{\eta e}V_{CC}\right)\psi_{\alpha\eta}(x). \quad (1.26)$$

The first term can be neglected as it is irrelevant to flavor transitions (it translates to a phase common to all flavors), yielding:

$$i\frac{d}{dx}\psi_{\alpha\beta}(x) = \sum_{\eta}\left(\sum_{k} U_{\beta k}\frac{\Delta m_{k1}^2}{2E}U_{\eta k}^{*} + \delta_{\beta e}\delta_{\eta e}V_{CC}\right)\psi_{\alpha\eta}(x). \quad (1.27)$$

This shows that the neutrino oscillations in matter (and in vacuum) only depend on the difference squared of the neutrino masses, not their absolute values.

1.3.0.1 Two flavor case

Considering the case of two flavor oscillations, with an initial state of an electron neutrino ($\alpha = e$), we can rewrite 1.27 as

$$i\frac{d}{dx}\begin{pmatrix}\psi_{ee}\\ \psi_{e\mu}\end{pmatrix} = \mathcal{H}\begin{pmatrix}\psi_{ee}\\ \psi_{e\mu}\end{pmatrix} \quad (1.28)$$

the effective Hamiltonian in the flavor basis:

$$\mathcal{H} = \frac{1}{4E}\begin{pmatrix}-\Delta m^2\cos 2\theta + A_{CC} & \Delta m^2\sin 2\theta\\ \Delta m^2\sin 2\theta & \Delta m^2\cos 2\theta - A_{CC}\end{pmatrix}, \quad (1.29)$$

where $A_{CC} = 2\sqrt{2}G_F N_e E$, has the eigenvalues

$$m_{M_\pm}^2 = \frac{1}{2}\left(m_1^2 + m_2^2 + A_{CC} \pm \sqrt{(\Delta m^2\cos 2\theta - A_{CC})^2 + (\Delta m^2\sin 2\theta)^2}\right). \quad (1.30)$$

From these masses the effective squared-mass differences become:

$$\Delta m_M^2 = \sqrt{(\Delta m^2\cos 2\theta - A_{CC})^2 + (\Delta m^2\sin 2\theta)^2} \quad (1.31)$$

and the effective mixing angle is given by

$$\tan 2\theta_M = \frac{\sin 2\theta}{\cos 2\theta - A_{CC}/\Delta m^2}\,. \quad (1.32)$$

For the case of two neutrinos, the vacuum appearance probability in eq. 1.17 reduces to

$$P(\nu_\alpha \to \nu_\beta) = \sin^2\theta \sin^2\left(\frac{\Delta m^2 L}{4E}\right). \tag{1.33}$$

And for oscillations in matter, the same result is true, substituting $\theta \to \theta_M$, and $\Delta m^2 \to \Delta m^2_M$. Notice that when the value of $A_{CC} = \Delta m^2 \cos 2\theta$, (which corresponds to the electron number density $N_e = \Delta m^2 \cos 2\theta/(2\sqrt{2}EG_F)$ there is a resonance, which translates to maximal mixing. This mechanism is named the MSW effect, named after Mikheev, Smirnov and Wolfenstein [38] [39]. In the limit of short baselines, or low matter density, the vacuum probability remains a good approximation, but near the resonance, the probability of neutrino oscillation can be enhanced with respect to the vacuum. In the case of antineutrinos, the probability would be suppressed, as the sign of the potential is reversed.

1.3.0.2 Three flavor case

The exact eigenvalues of the effective Hamiltonian $\mathcal{H}_M$, for the 3 flavor case are:

$$m^2_{M,i} = \frac{2}{3}(\alpha^2 - 3\beta)^{1/2} \cos\left[\frac{1}{3}\arccos\left(\frac{2\alpha^3 - 9\alpha\beta + 27\gamma}{2(\alpha^2 - 3\beta)^{3/2}}\right)\right] + m_1^2 - \alpha/3 \tag{1.34}$$

, with

$$\begin{aligned}
\alpha &= 2\sqrt{2}EG_F N_e + \Delta m^2 21 + \Delta m^2_{31}, \\
\beta &= \Delta m^2_{12}\Delta m^2_{13} + 2\sqrt{2}EG_F N_e\big(\Delta m^2_{21}(1 - |U_{e2}|^2) + \Delta m^2_{31}(1 - |U^2_{e3}|)\big), \\
\gamma &= 2\sqrt{2}EG_F N_e \Delta m^2_{21}\Delta m^2_{31}|U_{e1}|^2,
\end{aligned} \tag{1.35}$$

with each i index corresponding to one of the three roots of the $\cos(\frac{1}{3}\arccos)$ function [40]. This is difficult to interpret . In practice, for oscillation experiments, like NOvA, an approximation can be made To second order of $\alpha \equiv \Delta m^2_{21}/\Delta m^2_{31}$, the appearance probability for $\nu_\mu \to \nu_e$ can be

expressed as:

$$\begin{aligned} P(\nu_\mu \to \nu_e) \approx & \alpha^2 \sin^2 2\theta_{12} \cos^2 \theta_{23} \frac{\sin^2 A\Delta}{A^2} \\ & + 4 \sin^2 \theta_{13} \sin^2 \theta_{23} \frac{\sin^2 (A-1)\Delta}{(A-1)^2} \\ & + 2\alpha \sin^2 \theta_{13} \sin 2\theta_{12} \sin 2\theta_{23} \cos(\Delta + \delta_{CP}) \frac{\sin A\Delta}{A} \frac{\sin(A-1)\Delta}{A-1}, \end{aligned} \tag{1.36}$$

with $\Delta \equiv \Delta m^2_{31} L/(4E)$ and $A \equiv A_{CC}/\Delta m^2_{31}$ [41] For antineutrinos, substituting $\delta_{CP} \to -\delta_{CP}$, yields the equivalent expression. The observation of both neutrino and antineutrino channels in appearance experiments yields information about δ_{CP}.

1.3.1 Neutrino Oscillation Experiments

The basic strategy to measure neutrino oscillations in experiments with two detectors, such as NOvA, consists in measuring the flux of neutrinos in each detector to compare the flavor composition of each. The specifics of the NOvA experiment are described in detail in the next chapter. Figure 1.7 shows the setup of the experiment. The Near Detector (ND) is close to the source of neutrinos of a single flavor; in this case, using a beam of neutrinos from an accelerator. The Far Detector (FD) is placed at a strategic distance such that the neutrinos from the source have the chance to propagate and oscillate to a different flavor. Then the rate of neutrinos measured in the ND and the FD is compared in order to extract oscillations.

For the case of a source of ν_μ's the FD usually performs two measurements. The ν_μ disappearance measurement captures the fraction of neutrinos from the beam that did not oscillate, and the ν_e appearance the fraction that oscillated into e flavor.

The value of Δm^2_{ij} are sensitive to different baselines. This is summarized in table 1.1. Table 1.2 lists different neutrino sources and their sensitivity to the different oscillation parameters θ_{ij} and Δm^2_{ij}

Current world data is summarized in table 1.3

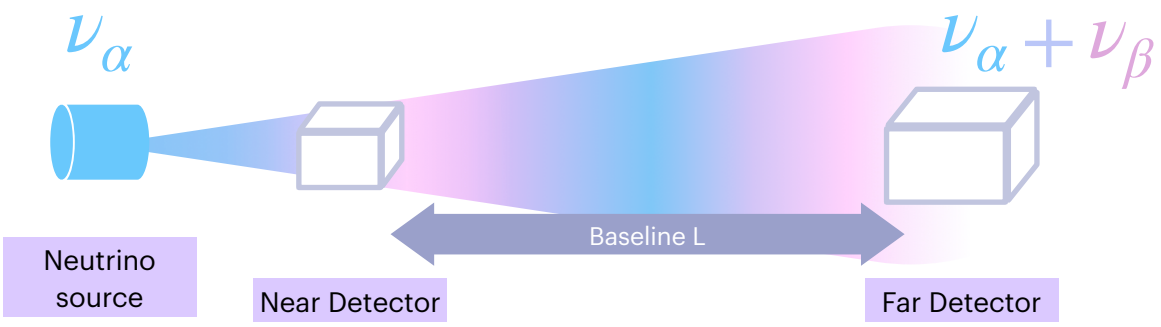

Figure 1.7: Generic setting of a long-baseline neutrino experiment.

Table 1.1: Δm^2 reach of experiment with different neutrino sources and L/E range. Adapted from [1]

ν **source**	Baseline	L(km)	E(GeV)	L/E (km/GeV)	Δm^2_{ij}(eV) reach
Accelerator	short	1	1	1	1
Reactor	medium	1	10^{-3}	10^3	10^{-3}
Accelerator	long	10^3	10	10^2	10^{-2}
Atmospheric		10^4	1	10^4	10^{-4}
Solar		10^8	10^{-3}	10^{11}	10^{-11}

1.4 Interactions with matter

As described earlier, neutrino oscillation experiments essentially count the number of neutrino interactions at their detectors, and measure their energy. The neutrino spectrum measured is a convolution of the neutrino flux and cross section. Both of these quantities are energy-dependent. The current knowledge of basic neutrino-nucleon cross section is still not better than $20-30\%$ [1], leaving neutrino interaction models as one of the most important sources of uncertainties in predicting and measuring the rate of neutrino interactions. Moreover, in order to calculate a realistic prediction of the expected rate of ν interactions, two ingredients are key: the theory of neutrino-nucleon scattering and the model of the nuclear environment. This section is a brief

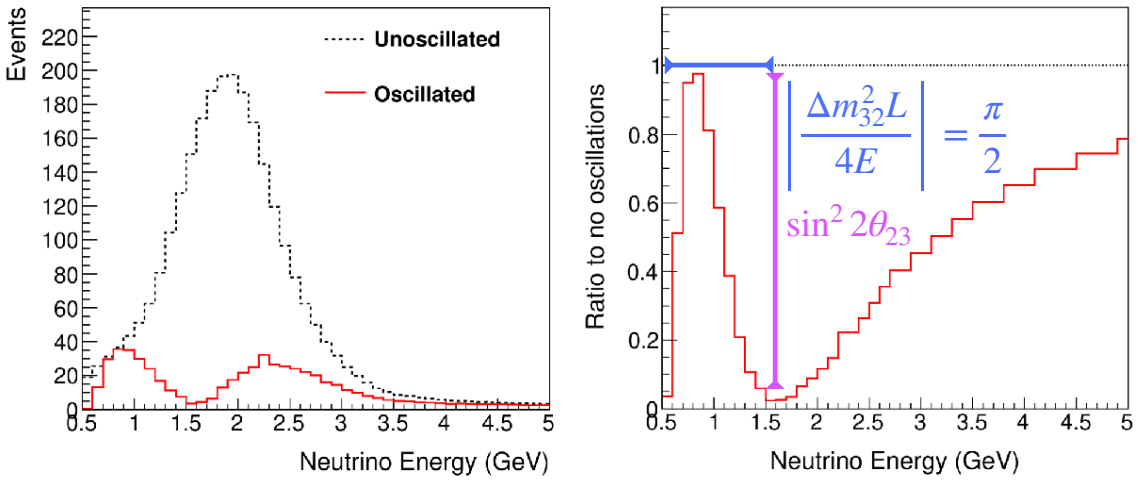

Figure 1.8: Comparison of oscillated vs unoscillated flux expected at the FD (left) and the ratio of these two fluxes (right).

Table 1.2: Neutrino oscillation experiments sensitivity to different θ_{ij} and Δm^2_{ij} taken from [1]

Experiment	**Dominant**	**Important**
Solar experiments	θ_{12}	$\Delta m^2_{21}, \theta_{13}$
Reactor LBL (KamLAND)	Δm^2_{21}	θ_{12}, θ_{13}
Reactor MBL (Daya Bay, Reno, Double Chooz)	θ_{13}	$\lvert\Delta m^2_{3\ell}\rvert$
Atmospheric experiments	θ_{23}	$\lvert\Delta m^2_{3\ell}\rvert, \theta_{13}, \delta_{CP}$
Accelerator LBL ν_μ disapp (MINOS, NOvA, T2K)	$\lvert\Delta m^2_{3\ell}\rvert, \theta_{23}$	
Accelerator LBL ν_e app (MINOS, NOvA, T2K)	δ_{CP}	$\theta_{13}, \theta_{23}, \text{sign}(\Delta m^2_{3\ell})$

overview of the current knowledge of neutrino-nucleus scattering that is relevant to the NOvA experiment.

The terms of WS interaction Lagrangian, $\mathcal{L}^{weak}$, from 1.2, relevant for neutrino and antineutrino reactions, can be written as:

$$\mathcal{L}^{\text{weak}}_{\text{int}} = -\frac{g}{2\sqrt{2}}\left(j^{\text{CC}}_{\mu} W^{\mu+} + \text{h.c.}\right) - \frac{g}{2\cos\theta_W} j^{\text{NC}}_{\mu} Z^{\mu} \tag{1.37}$$

where $W^{\pm}_{\mu}$ and Z_{μ} are the charged and neutral gauge fields; θ_W is the weak mixing angle or Weinberg angle, related to the Fermi constant G_F, the weak coupling constant g, the electron

Table 1.3: Latest best fit values of the three neutrino oscillation parameters from current neutrino data. The $*$ indicates the δ_{CP} error value includes a 1.3 scale factor [2].

Parameter	**Best Fit** $\pm 1\sigma$
$\Delta m^2_{21} 10^{-5} eV^2$	7.53 ± 0.18
$\Delta m^2_{32} 10^{-3} eV^2$ NO	2.437 ± 0.033
$\Delta m^2_{32} 10^{-3} eV^2$ IO	-2.519 ± 0.033
$\sin^2 \theta_{12}$	0.307 ± 0.013
$\sin^2 \theta_{23}$ NO	$0.534^{+0.021}_{-0.024}$
$\sin^2 \theta_{23}$ IO	$0.547^{+0.018}_{-0.024}$
$\sin^2 \theta_{13}$	2.20 ± 0.07
δ_{CP}/π	$1.23 \pm 0.21*$

charge e, and the masses of the W and Z bosons by:

$$\sin \theta_W = \frac{e}{g} \tag{1.38}$$

$$\frac{g}{2\sqrt{2}} = \left(\frac{G_F M_W^2}{\sqrt{2}} \right)^{1/2} \tag{1.39}$$

$$\frac{g}{4 \cos \theta_W} = \frac{1}{\sqrt{2}} \left(\frac{G_F M_Z^2}{\sqrt{2}} \right)^{1/2} \tag{1.40}$$

Each of these terms can be identified as the CC and NC terms from equation1.2 respectively.

Figure 1.9 shows the vertices that correspond to the weak Charged Current (CC) and (NC) vertices.

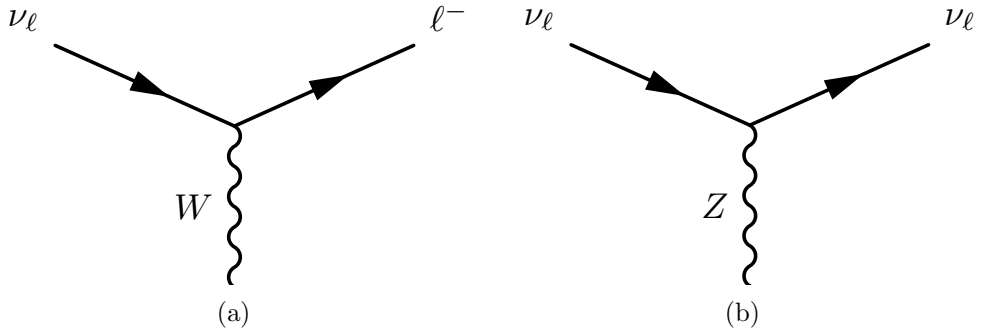

Figure 1.9: Feynman diagrams for neutrinos interacting via the weak (a) charged current and (b) neutral current.

For the interactions concerning the NOvA experiment oscillation measurements, the focus is on CC interactions. The outgoing lepton in CC interaction is a charged lepton, which can also interact electromagnetically with the detector, and therefore the flavor of the incoming neutrino can be determined. NC interactions are a background for the studies presented here.

1.4.1 Free nucleon interactions

The primary interactions that occur in the range of neutrino/antineutrino energy in NOvA (0 to a few GeV) are summarized in Figure 1.10. These refer to the three types of free nucleon interactions: Quasielastic(QE), Resonance(RES) and Deep Inelastic Scattering(DIS). The neutrino interacts with a single neutron or proton within a nucleus in the detector. In the experimental scenario, such as the measurements depicted in Figure 1.10 additional effects can alter the final state and expected kinematics of the outgoing particle. However we review the free nucleon interactions in the QE,RES and DIS sections next.

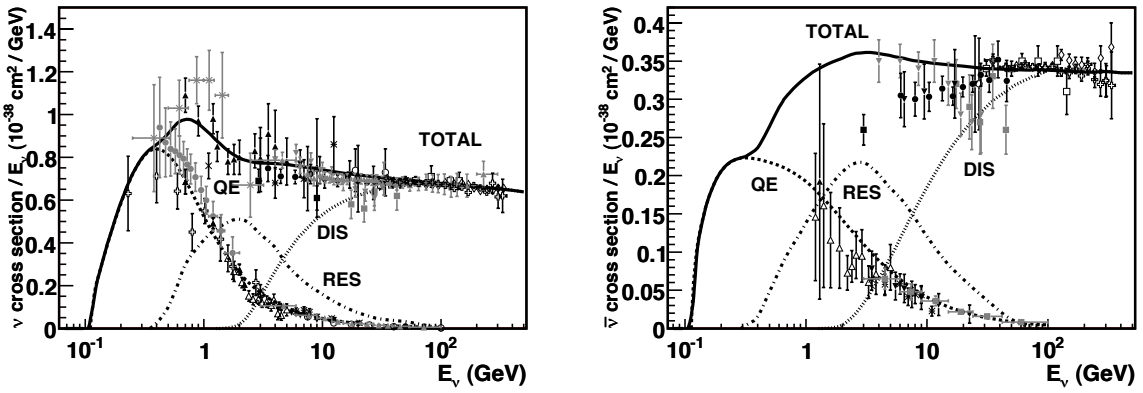

(a) (b)

Figure 1.10: Cross sections of (a) neutrino and (b) antineutrino interactions with nucleons as a function of neutrino energy. The solid line shows the total prediction, while the dashed lines show predictions from models for QE, RES, and DIS interactions with data points from various experiments [5].

1.4.1.1 Charged Current Quasielastic Scattering

The quasielastic charged-current interactions of neutrinos and antineutrinos with nucleons, is called as such because the interaction occurs with the nucleus as a whole, via the exchange of a

$W^{\pm}$ boson. Assuming no additional nuclear effects, the final state contains only two outgoing particles: the lepton and the nucleon. Therefore the energy of the incoming neutrino or antineutrino (E_ν) and the negative of the four momentum transfer square(Q^2), can be estimated using conservation of energy and momentum. These reactions are depicted in Figure 1.11, are given by

$$\nu_\ell + n \to p + \ell^-, \tag{1.41}$$

$$\bar{\nu}_\ell + p \to n + \ell^+, \tag{1.42}$$

with $\ell = e, \mu, \tau$. Where k, k', p, and p' are the momentum of each particle, and $q = k - k'$ is the four momentum transfer.

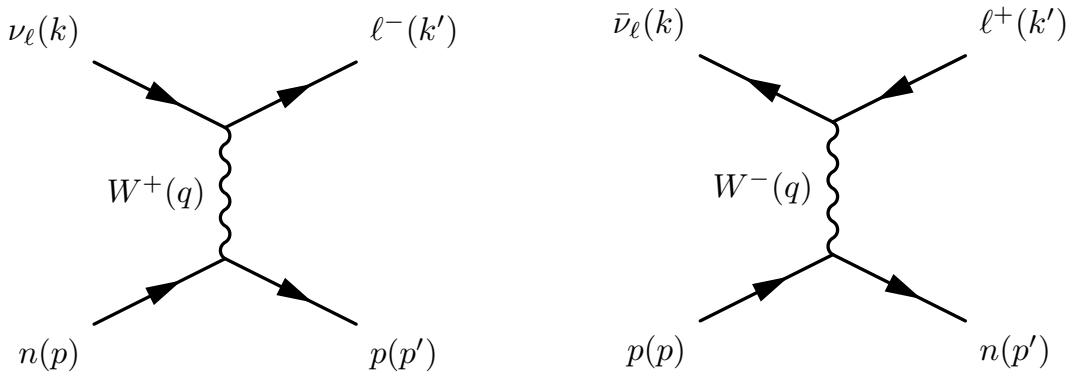

Figure 1.11: Feynman diagrams of neutrino and antineutrino CCQE interactions with a nucleon

The invariant matrix element of a charged current quasielastic reaction of a neutrino or antineutrino with a nucleon is written as

$$\mathcal{M} = \frac{G_F}{\sqrt{2}} \cos\theta_C l_\mu J^\mu, \tag{1.43}$$

where G_F is the Fermi constant, θ_C is the Cabibbo angle, the leptonic current

$$l_\mu = \bar{u}(\vec{k'})\gamma_\mu(1 \mp \gamma_5)u(\vec{k}), \tag{1.44}$$

with $+(-)$ for the antineutrino (neutrino) case, and J_μ is the hadronic current.

The differential scattering cross section can be obtained:

$$\frac{d\sigma}{dq^2} = \frac{|\mathcal{M}|^2}{4\pi M^2 E_\nu^2} = \frac{G_F^2 M^2 \cos^2\theta_C}{8\pi E_\nu^2}\left[A(q^2) \mp B(q^2)\frac{(s-u)}{M^2} + C(q^2)\frac{(s-u)^2}{M^4}\right] \tag{1.45}$$

in terms of the Mandelstam variables s, t, u:

$$s = (k+p)^2, \tag{1.46}$$

$$t = (k-k')^2, \tag{1.47}$$

$$u = (k'-p)^2, \tag{1.48}$$

M being the mass of the initial nucleon and E_ν the energy of the incoming neutrino or antineutrino. The factors $A(q^2)$, $B(q^2)$ and $C(q^2)$ [2] also depend on the mass of the outgoing lepton, as well as $f_i(q^2)$, the vector form factors, and $g_i(q^2)$ the axial vector and pseudoscalar form factors[3]. The vector form factors depend on the electromagnetic form factors. The pseudoscalar form factor $g_2(q^2)$ is proportional to the mass of the lepton. The axial form factor is parametrized as

$$g_1(q^2) = g_A(0) = \frac{g_A}{(1 + q^2/m_A)}, \tag{1.49}$$

where $a_A(0)$ can be obtained experimentally from β decay. m_A is the axial dipole mass (sometimes called *axial mass*). Many experiments that measure quasielastic neutrino interactions use the dipole parametrization in their models, however recently, the Z-expansion parametrization has been proposed, which is based on the analytic properties of strong interaction [42]. The numeric value to be used for calculations of neutrino nucleon cross section has been a subject of debate. Currently, the world average value after a re-analysis if various neutrino and antineutrino scattering experiments data, yields

$$m_A = 1.026 \pm 0.021 \text{ GeV} \tag{1.50}$$

from deuterium target and electroproduction data [43].

[2] The full expressions can be found on [37].

[3] In this particular expression it is assumed that the initial and final nucleon have the same mass and that $s - u = 4ME_\nu + q^2$.

1.4.1.2 Charged Current Resonant interactions

At higher energies, in the region starting from the threshold production of a single pion ($E_\nu \geq 150.5MeV$ for ν_e and $E_\nu \geq 277.4$ MeV for ν_μ), the neutrino interaction can excite the nucleon into a resonance state. As the energy of the neutrino increases, multiple pions can be produced, as well as strange mesons (K) and hyperons (Y), both processes relevant in the region of a few GeV.

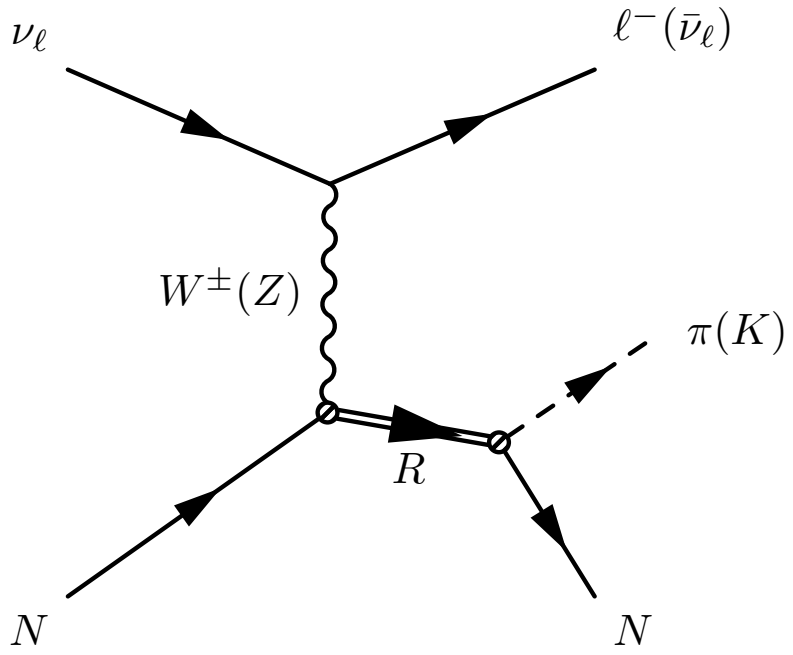

Figure 1.12: Feynman diagram for RES interaction for free nucleon.

Nucleon resonances are characterized by their mass, parity, spin and isospin. The first resonance is called the Δ resonance, and has a positive parity, mass of 1232 MeV, isospin 3/2 and spin 3/2. This is the most studied in both theory and experiment, and is also the most relevant for the interactions seen in NOvA. The intermediate Δ can decay through various possible

channels that produce pions:

$$\begin{aligned}
&\nu_\ell + p \to \ell^- + \Delta^{++} \\
&\qquad\qquad \searrow p + \pi^+ \qquad (1.51)\\
&\nu_\ell + n \to \ell^- + \Delta^{+} \\
&\qquad\qquad \searrow p + \pi^0 \\
&\qquad\qquad \searrow n + \pi^+ \qquad (1.52)\\
&\bar{\nu}_\ell + n \to \ell^- + \Delta^{-} \\
&\qquad\qquad \searrow n + \pi^- \qquad (1.53)\\
&\bar{\nu}_\ell + p \to \ell^+ + \Delta^{0} \\
&\qquad\qquad \searrow p + \pi^- \\
&\qquad\qquad \searrow n + \pi^0 \qquad (1.54)
\end{aligned}$$

The scattering cross section depends on various form factors (similar to QE), which can be expressed in terms of Q^2 the negative the four-momentum transfer: three vector form factors, $C_i^V(Q^2)$ with $i = 3, 4, 5$. vector dipole mass $M_V = 0.84$ GeV, and axial vector form factors $C_i^A(Q^2)$ $(i = 3, 4, 5)$, depends on $M_{A\Delta}$ is the axial dipole mass, generally 1.026 GeV which is obtained from the average of experimental measurements of quasielastic scattering events. In both cases the axial and vector form factors for $i = 1, 2, 3$ vanish because of CVC (conservation of vector current) theorem.

1.4.1.3 Charged Current Deep Inelastic Scattering

At energies $E_\nu >> m_N$ in the laboratory frame, the charged-current neutrino nucleon interactions are dominated by the deep inelastic scattering processes, such as

$$\nu_\ell + N \to \ell^- + X, \qquad \bar{\nu}_\ell + N \to \ell^+ + X, \tag{1.55}$$

where $N = p, n$ and X is the set of final hadrons.

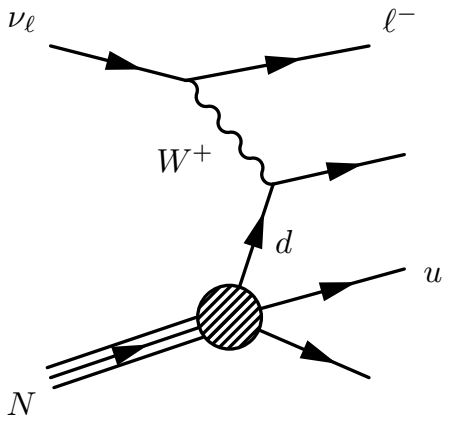

Figure 1.13: Ferynman diagrams of neutrino DIS interaction in the quark-parton model, with the elementary transition $W^+ + d \to u$, adapted from [36].

The DIS kinematic region is defined by

$$Q^2 \gg m_N^2, \quad p_N \cdot q \gg m_N^2. \tag{1.56}$$

In this energy regime, instead of interacting with the nucleon as a whole, the neutrino interacts with its quark constituents. The current understanding of DIS interactions is based on Feynman's *quark parton model* of hadrons. Its basic assumptions are [36]:

- The nucleon is a composite system made of elementary quarks.
- Interactions among constituent quarks can be neglected in the DIS kinematic region.
- The constituent quarks have three-momenta in the same direction as the nucleon, therefore negligible transverse momenta.
- Quark masses can be neglected in comparison with their energy.

Usually the DIS differential cross section is presented in the Lorentz invariants, also known as Bjorken scaling variables:

$$x \equiv \frac{Q^2}{2p_N \cdot q}, \quad y \equiv \frac{p_N \cdot q}{p_N \cdot p_\nu}, \tag{1.57}$$

, where p_N and p_ν are the initial four-momenta of the nucleon and neutrino respectively, q is the four-momentum transfer, and $Q^2 = -q^2$. The CC differential cross section is given by:

$$\frac{d^2\sigma^{\mathrm{CC}}}{dxdy} = s\frac{G_F^2}{2\pi}\left(1+\frac{Q^2}{m_W^2}\right)^{-2}\left[xy^2F_1 + (1-y)F_2 \pm xy\left(1-\frac{y}{2}\right)F_3\right] \tag{1.58}$$

with the center of mass energy $s = (p_\nu + p_N)^2$, and the nuclear structure functions F_i, which can be determined experimentally. The sign $+(-)$ indicates the expression for neutrinos(antineutrinos).

1.4.2 Nuclear Medium Effects

The free-nucleon interaction theory just reviewed, particularly in the QE and RES regime, predicts particular outgoing particles: the lepton plus a single nucleon, in QE, or a nucleon and a pion in the case of Δ reaction. However detectors are made of materials where the nuclei have multiple nucleons, which are not at rest nor not-interacting. This has effects in the kinematics and in the number and/or type of particles that are actually observed in the detector. The nuclear effects include nucleon binding, Fermi motion, Pauli blocking, short and long range nucleon-nucleon correlations, meson exchange currents and final state interactions. For this thesis, the last two of these are of particular interest. See ref. [1] for a broader overview.

Meson Exchange Currents and 2p2h A neutrino can interact with a pair of bound nuclei, thus knocking out two nucleons instead of one, as pictured in Figure 1.14. This is also referred as 2p2h, as the interaction leaves two holes in the struck nucleus. Most frequently, this occurs via the meson exchange current (MEC), where the two nucleons are interacting with each other via a meson. This process was initially proposed in electron-nucleus scattering, as the models at the time did not predict the distribution in the region between the QE and resonant peaks as a function of transferred energy, as shown in Figure 1.14a. This "dip region" is better represented when the 2p2h-MEC contribution is included in the model, as can be seen in Figure 1.14b.

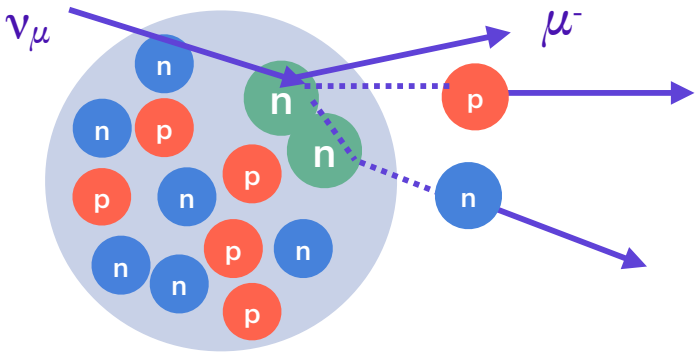

Figure 1.14: Diagram of neutrino - nucleon pair interaction

The 2p2h channels when a neutrino or antineutrino interacts with a nucelon pair are:

$$\nu_\ell + np \to \ell^- + p + p, \tag{1.59}$$

$$\nu_\ell + nn \to \ell^- + p + n, \tag{1.60}$$

$$\bar{\nu}_\ell + np \to \ell^+ + n + n, \tag{1.61}$$

$$\bar{\nu}_\ell + pp \to \ell^+ + n + p. \tag{1.62}$$

These yield a quasielastic like final state, for most cases, as the neutrons are more difficult to detect and reconstruct.

1.4.2.1 Final State Interactions

As mentioned before, the particles created after the interaction vertex of a CC reaction, are not necessarily the ones that are visible in the detector. The pions and protons from a QE or RES interactions, can also be affected by the strong interactions, so while traveling inside the nucleus they can re-interact. In the particular case of pions, there are a number of processes that can happen: absorption, (quasi)elastic scattering, charge exchange (for example $\pi^+ + n \to \pi^0 + p$). Figure 1.16 displays a representation of these processes, which can also happen multiple times,

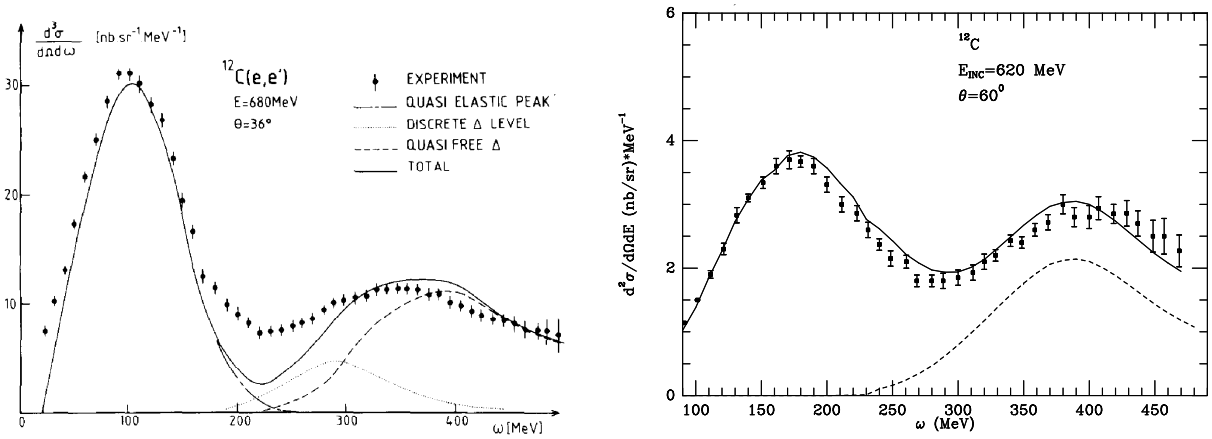

(a) (b)

Figure 1.15: (a) Electron scattering with carbon data, the two peaks represent QE and Δ resonance. Figure taken from [6]. (b) Electron - nucleon scattering model including 2p2h MEC compared to data. Figure taken from [7].

and therefore significantly affect the prediction of the final state. For instance, an interaction with resonant pion production where the pion was absorbed will mimic a quasielastic interaction in the detector.

Some of the models used in neutrino generators such as GENIE [44] are called effective intranuclear transport model (hA) and full intranuclear cascade (hN) [45].

As mentioned earlier, the predicted neutrino spectrum is highly dependent on the knowledge of neutrino interactions. Future and current neutrino oscillation experiments such as NOvA require precise neutrino energy measurements, therefore it is crucial to take into consideration the current knowledge and unknowns of the details of neutrino-nucleus scattering. Chapter 3 describes in detail the neutrino interaction model and uncertainties implemented in the NOvA experiment. Chapter 5 describes how measurements at the Near Detector can be utilized in order to constrain cross section uncertainties as well as other parameters, for the oscillation measurement.

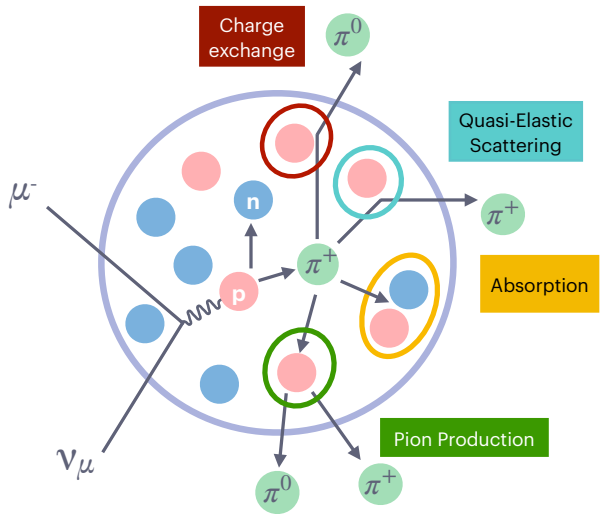

Figure 1.16: Final State interactions diagram. Adapted from T.Golan.

CHAPTER 2. THE NOvA EXPERIMENT

NOvA (Numi Off-axis ν_e Appearance) is a long-baseline neutrino oscillation experiment, based at Fermi National Accelerator Laboratory (Fermilab). The experiment consists in two detectors: the Near Detector (ND), situated in Fermilab, 1 km from the neutrino source, and the Far Detector (FD), situated at 809 km way from the ND. It observes neutrinos from the NuMI (Neutrinos from the Main Injector) beam. The two oscillation channels studied are the muon neutrino (antineutrino) ($\overset{(-)}{\nu}_\mu \rightarrow \overset{(-)}{\nu}_\mu$) appearance and electron neutrino (antineutrino) ($\overset{(-)}{\nu}_\mu \rightarrow \overset{(-)}{\nu}_e$) appearance. By observing these four oscillation channels, NOvA can measure the oscillation parameters θ_{32}, Δm^2_{32} and probe δ_{CP} in the 3-flavor oscillation paradigm.

2.1 The NuMI beam

A neutrino beam starts with a source of protons which are accelerated and directed to a target. The hadrons produced by this collision, mainly pions and kaons, can then be selected according to their charge, such that their decays produces the desired beam of neutrinos or antineutrinos. The source of neutrinos for the NOvA experiment is the NuMI beam, which starts with protons accelerated from the Main Injector.

2.1.1 Accelerating protons

Schematics of the Fermilab accelerator complex are shown in Figure 2.1. The protons originate from the H^- ions in the LINAC (Linear Accelerator) which accelerates them from 175 keV to 400 MeV [46]. When they enter the Booster, they are converted into protons accelerated to 8 GeV as 1.6 μS batches. The protons then can enter the Main Injector, which has a 7x larger circumference (slightly over 2 miles [46]), which allows it to store and accelerate 6 Booster

batches. Afterwards, the Main Injector delivers 120 GeV protons to the NuMI beamline, and other beamlines for neutrino and muon experiments.

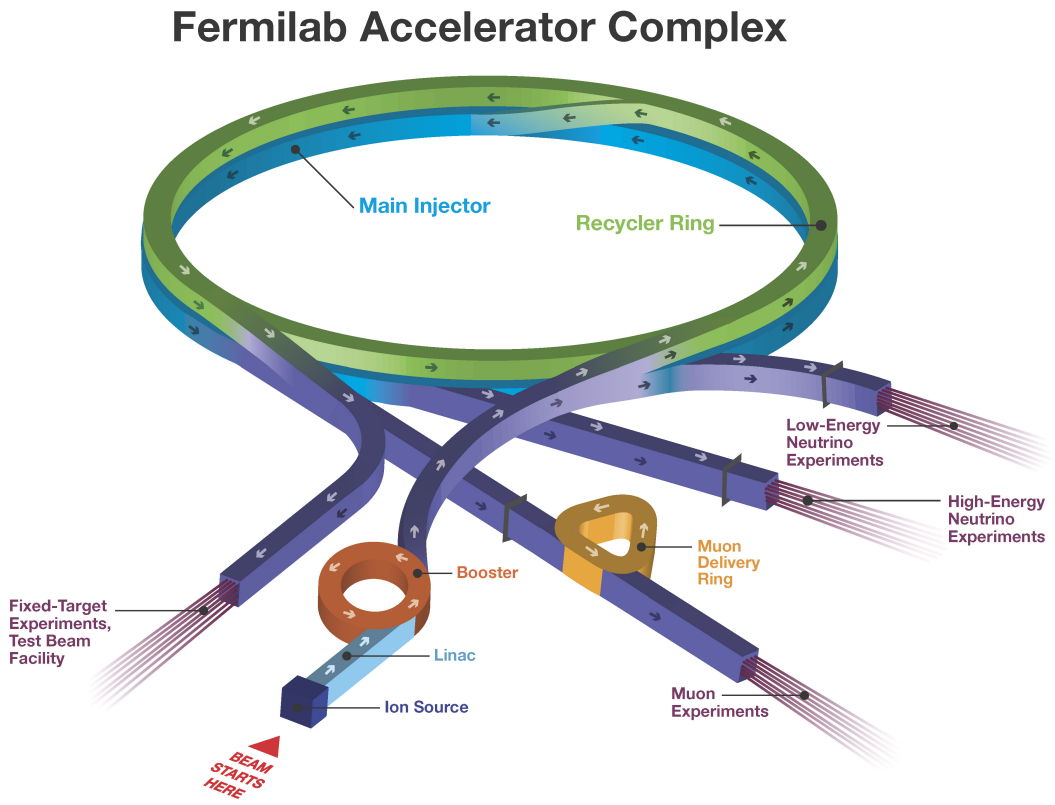

Figure 2.1: Schematic of the Fermilab accelerator complex, taken from [8].

2.1.2 Beam

Figure 2.2 displays an overview of the elements of the NuMI beamline. Neutrinos are produced from the 120 GeV protons from the Main Injector, which are steered towards a graphite target. The interaction of the protons with the target produces a shower of hadrons. These are

focused by two magnetic horns, which act as hadron lenses. Depending on the direction of the current in the horns, they select positively or negatively charged hadrons. These hadrons, primarily kaons and pions, are directed towards the decay pipe, a vacuum or low density environment, where most of the mesons decay into mostly neutrinos. At the end of the decay pipe, sits a hadron monitor followed by a 5 meter absorber, a massive aluminum, steel and concrete structure that attenuates the residual hadrons that did not decay into neutrinos. This is followed by 240 meters of unexcavated dolomite rock to absorb the remaining muons in the beam.

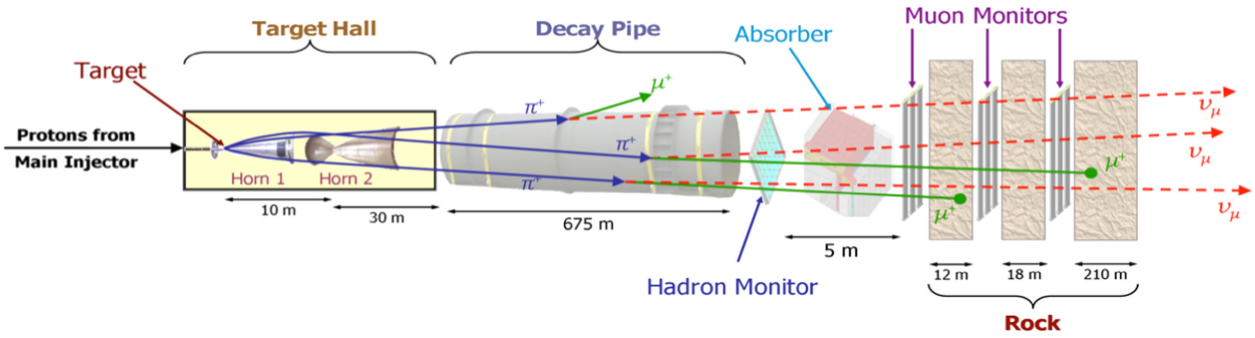

Figure 2.2: Schematic of the NuMI Beam showing its main components. Taken from [9].

The mesons from the target collision decay via the dominant modes

$$\pi^+ \to \mu^+ + \nu_\mu$$

$$K^+ \to \mu^+ + \nu_\mu$$

The beam primarily contains ν_μ, however subsequent decays of muons introduce ν_e contamination to the beam, such as

$$\mu^+ \to e^+ + \nu_e + \bar{\nu}_\mu$$
$$K^+ \to \pi^0 + e^+ + \nu_e. \tag{2.1}$$

Another possible source of contamination are the hadrons produced along the beam axis, which remain unaffected by the magnetic field of the horns. The two directions of the currents in the magnetic horns are called Forward Horn Current (FHC) or Reverse Horn Current (RHC). The

first selects the positive mesons to yield a primarily ν_μ beam, while RHC yields the $\bar{\nu}_\mu$ enhanced beam. Figure 2.3 shows a diagram of the configuration of the two magnetic horns.

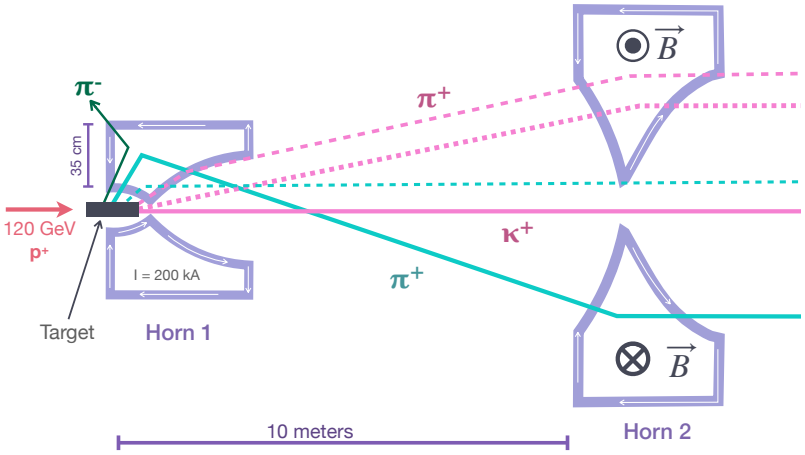

(a) Hadron trajectories through the two horns. Under or over focused hadrons by the first horn are further focused by the second horn. Adapted from [9].

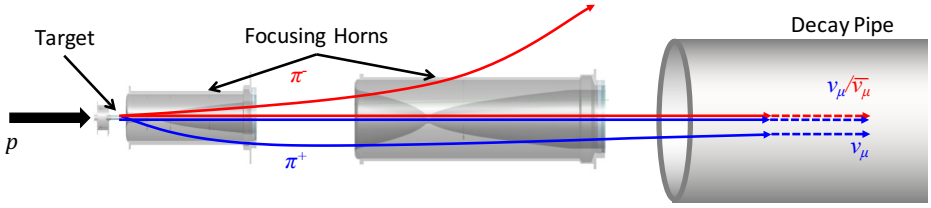

(b) Forward Horn Current (FHC) setup, producing ν_μ beam

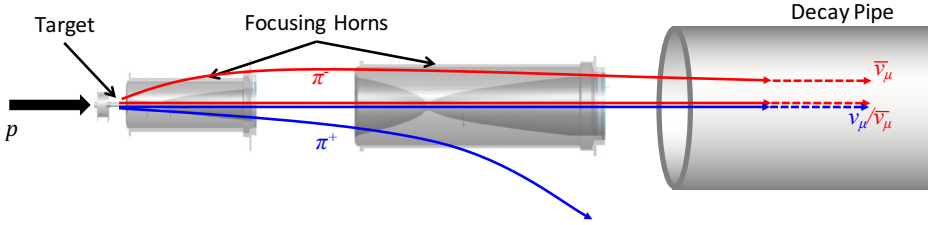

(c) Reverse Horn Current (RHC) setup, producing ν_μ beam

Figure 2.3: Magnetic horn configurations: changing the direction of the current reverses the magnetic field and therefore the sign of the focused hadrons and type of neutrinos produced.

2.1.3 Off-axis design

The NOvA detectors are placed at 14.6 mrad off the axis of the NuMI beam. This design exploits the kinematics of two body decays, in order to observe a neutrino spectrum that peaks at

about 2 GeV. This choice optimizes the flux of neutrinos close to the first oscillation maximum of the transition $\nu_\mu \to \nu_e$.

Considering a beam composed primarily of neutrinos from pion decays, the flux incident on a detector of area A located at a distance z from the source, in the lab frame is:

$$\Phi = \left(\frac{2\gamma}{1+\gamma^2\theta^2} \right)^2 \frac{A}{4\pi z^2} \tag{2.2}$$

where θ is the angle between the pion direction and the neutrino direction. E_π is the energy of the parent pion, m_π is the pion mass, and $\gamma = E_\pi/m_\pi$.

$$E_\nu \approx \frac{(1-m_\mu^2/m_\pi^2)E_\pi}{1+\gamma^2\theta^2} = \frac{0.43E_\pi}{1+\gamma^2\theta^2} \tag{2.3}$$

The same applies for decays from Kaons, substituting the factor 0.43 to 0.96 [47]. At 14 mrad the energy of the neutrino does not have a strong dependence on the energy of the parent pion. Considering the incident flux, and neutrino interaction cross section, this also yields a peak at ~ 2 GeV, near the oscillation maximum of 1.6 GeV for a 810 km baseline, assuming $\Delta m^2_{32} = 2.41$ meV^2, as can be observed in Figure 2.4. Increasing the angle would shift the beam peak closer to the oscillation maximum, though with a larger angle, the flux of incident neutrinos decreases, as can be inferred from equation 2.2. This would negatively impact the event rate to observe at the Far Detector.

2.2 NOvA detectors

The Near and Far detectors are functionally identical segmented tracking calorimeter detectors designed to optimize the observation of ν_eCC and ν_μCC interactions. This means that both detectors use similar materials and electronics. This design allows to utilize the high flux of neutrinos close to the beam to perform systematic studies with the ND, and correct the observations of the FD. The main differences between the detectors is their size, and location underground and with respect to the beam. The ND is 100 m underground, and has a mass of 290 ton, whereas the FD sits on the surface, with a mass of 14 kton. Figure 2.4a shows the

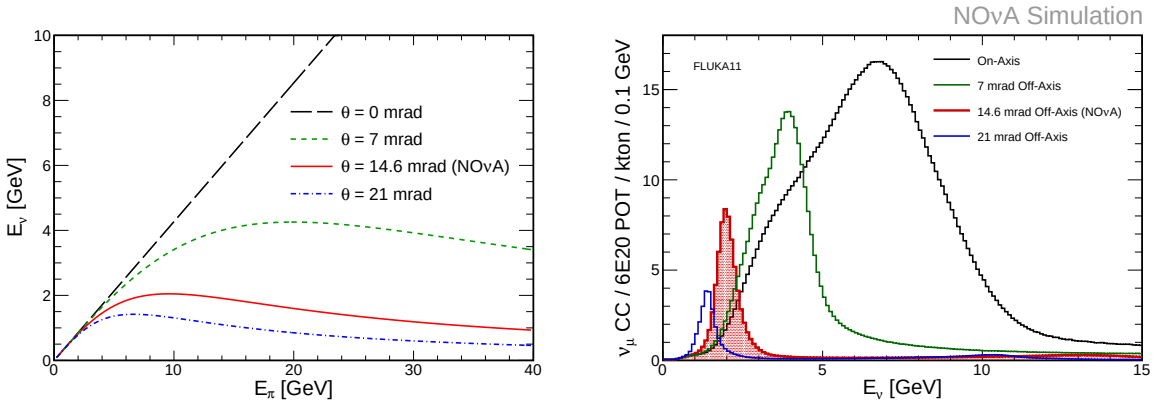

Figure 2.4: Neutrino energy as a function of the parent pion energy for different decay angles θ (left). The neutrino true energy spectra (flux times cross-section) at the Far Detector for NOvA placed on-axis and at 7, 14 and 21 mrad (right). At 14 mrad essentially all pion decays yield neutrinos in the 1-2 GeV energy range of interest for oscillations, compensating for the decrease in flux. Figure taken from [48].

geographical placement of the NOvA detectors, 14.6 mrad off-axis from the NuMI beam, and with the FD 810 km away from the ND.

The segmentation of the detectors is done via the stacking of of Polyvinyl Chloride (PVC) rectangular cells to form planes. The planes are constructed with the cell lengths parallel to the x and y directions, perpendicular to beam direction. Each plane is composed of 32 cells sealed together; multiple planes are stacked along the z direction, as shown in Figure 2.5b. Each cell corresponds to a pixel of a 3D images of a reconstructed interaction. The PVC cells are filled with liquid scintillator (mineral oil mixed with 5% pseudocumene) and a wavelength-shifting fiber that loops along the length of the cell (see Figure 2.5a). The ends of the fiber are connected to a single pixel of an avalanche photo diode (APD). As charged particles traverse a cell, the light emitted by the scintillator bounces around the cell and is eventually captured by the fiber, which shifts its wavelength from blue 400–450 nm to green 490–550 nm, and then transports it to both ends of the fiber to an APD. The green light is then digitized and amplified for further processing.

The NOvA detectors are built with low Z materials (mostly Carbon). Specifically which results in a radiation length of $\sim$36 cm, or$\sim$ 0.15 radiation lengths per layer.

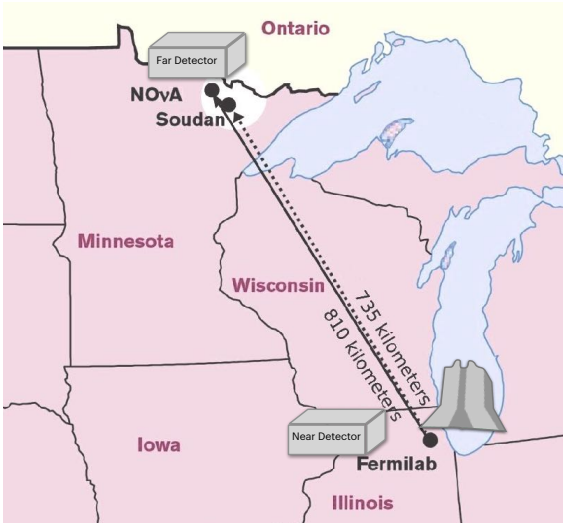

(a) Geographical location of the detectors.

(b) Relative sizes of the NOvA detectors

Figure 2.5: Left: The far detector is 810 km away from the source, in Minnesota, and the near detector is on-site, only 1 km away from the target, and underground. Right: Relative sizes of the Near and Far detectors.

2.2.1 Near Detector

The ND (see Figure 2.7 is composed of 192 planes, with dimensions of 4.1 m×4.1 m×16m, with a mas of 290 ton. It is situated 1 km from the target of the NuMI beam, and 105 m underground. This location reduces the rate of cosmic rays. The high flux of neutrinos in this location relative to the beam translates to the ND observing 5 to 10 neutrino events per spill. For the same reason, the ND does not require the same volume as the FD. Its purpose is to characterize neutrinos from the beam before oscillations.

The ND is relatively small, so to ensure the muons resulting from ν_μCC interactions produce tracks that are fully contained inside the detector volume, the last 22 planes of the detector consist of a "muon catcher". This is composed of 11 pairs of horizontal/vertical scintillator planes separated by ten steel planes, 10 cm thick. The height of the muon catcher is shorter than the rest of the detector, 2.6 m long.

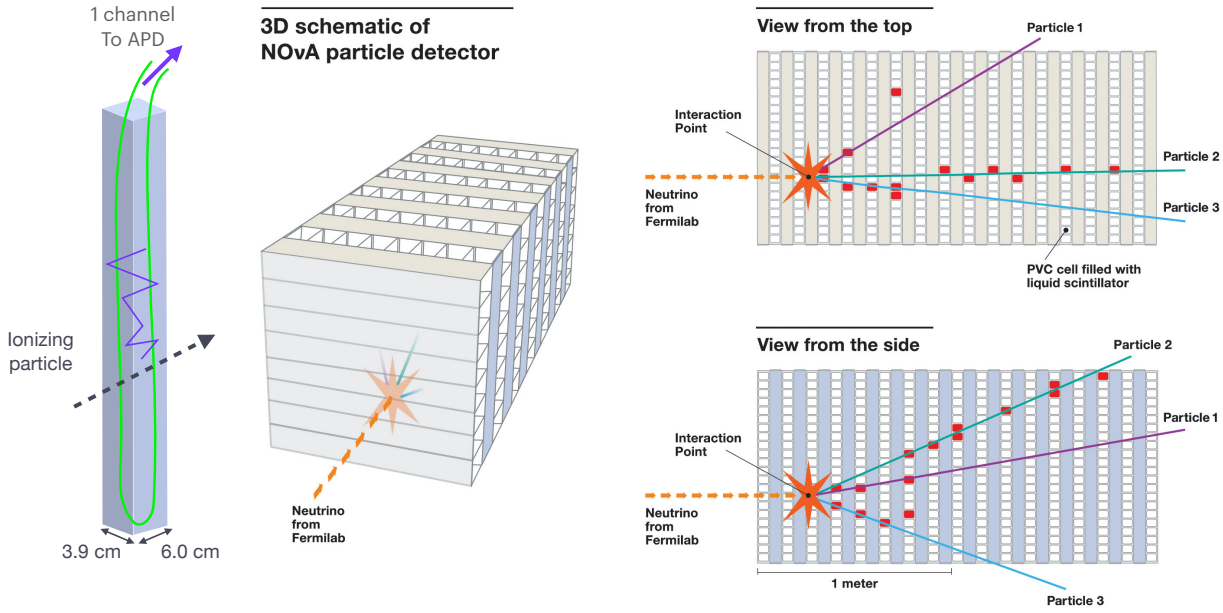

(a) (b)

Figure 2.6: Detail of a single PVC cell (left) and detector 3D view (right).

2.2.2 Far Detector

The FD, located 810 km from the NuMI production target, comprises 896 planes with 344,064 channels and a total mass of 14 kton. Its dimensions are 60 m×15.6 m×15.6 m. The primary goal of the detector is to observe the energy spectrum of ν_e interactions, from the $\nu_\mu \rightarrow \nu_e$ oscillation.

This detector is considered to be on the surface because of the small rock overburden of 1.2 m of concrete and 15 cm of barite. This implies a high cosmic ray flux. However, the data acquisition and triggering system relies on the timing of the events to discriminate between signal neutrino events and background. The cosmic events are useful to calibrate.

2.3 The Data Acquisition System

The data acquisition (DAQ) system has the function of concentrating the data from the large number of APD channels into a single stream that can be stored and analyzed. Its components are the APDs, front end boards, data concentrator modules, and timing distribution units

(a) (b)

Figure 2.7: Photos of the NOvA Near Detector: (a) side facing the beam and (b) back, displaying the muon catcher. From [49].

(TDUs). In addition there is a host of servers that manage the components and process the data. This DAQ can be described as a continuous readout, which means that the data is constantly collected and placed in a intermediate buffering location before the decision to save or discard events is made [50]. An overview of the data flow and timing system is shown in Figure 2.9. The next sections will explain with more detail each of these components of the DAQ.

2.3.1 Readout

The first step to process the data from the detector is the digitization of the light captured in the wavelength-shifting fiber. The two ends of each fiber direct the light to an avalanche photo-diode (APD). Each APD absorbs the light from 32 fibers. Light is converted to an electric

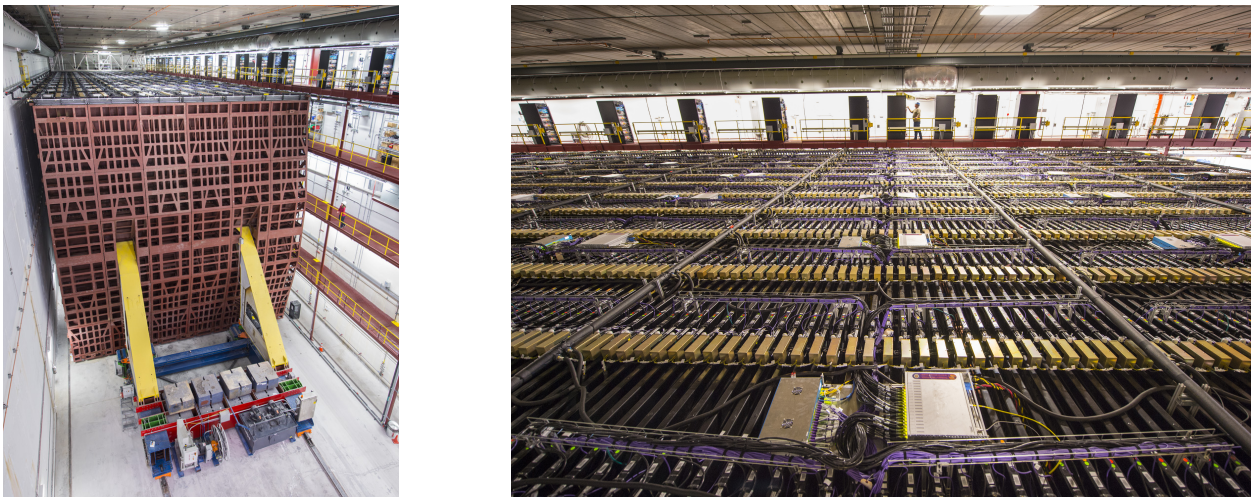

Figure 2.8: Photos of the NOvA Far Detector: (a) front side, facing the beam and (b) top view, displaying FEB (golden) boxes. From [49].

signal through the photoelectric effect. The APD has an 85% quantum efficiency for the 520-550 nm light exiting the fiber. Thermal noise produced in the APD is reduced by using a thermo-electric cooler (TEC) to keep the APD at a temperature of $-15°$C. A water cooling system is used to remove the heat from the TEC. Figure 2.10 shows the 32 channels that then connect to the 32 APD pixels, and a schematic showing the functioning of the APD.

The Front End Boards (FEB) main function is to process the signals coming from the APD pixels and extract relevant data to transmit it to the data acquisition system. A Field Programmable Gate Array (FPGA) inside the FEB formats the extracted data and sends the resulting data packet to a Data Concentrator Module (DCM), custom built single board computer. Each DCM receives input data streams from up to 64 front end boards (or 2048 channels) from a localized geographic region of the detector and time orders them into windows corresponding to 50 μs intervals, or "microslices". The data is further organized by event building software to construct larger 5 ms "millislices". To be able to correlate the signals in time, the DCMs are synchronized through the use of a sophisticated timing system.

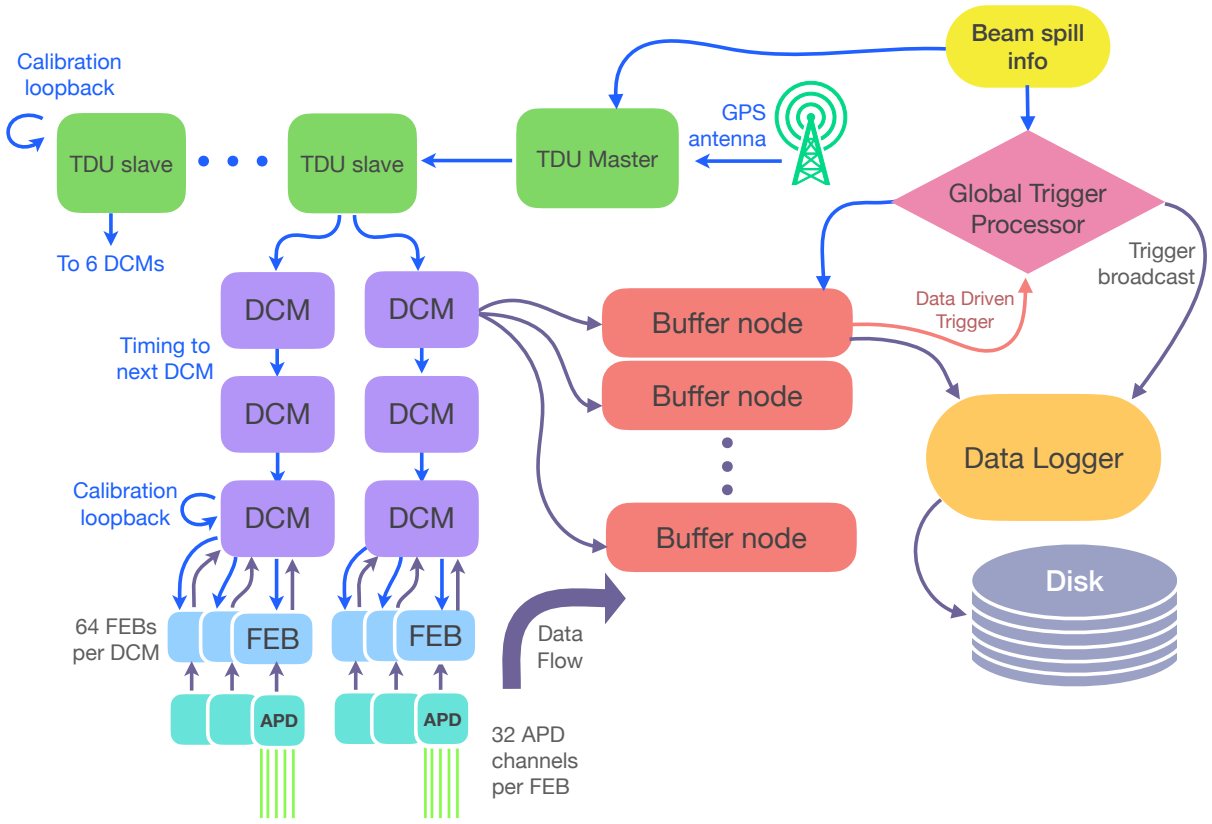

Figure 2.9: Diagram summarizing the timing synchronization system and data flow in the NOvA DAQ. The blue arrows represent the timing information from the master TDU down to the slave TDUs DCMs and FEBs. The grey arrows represent the flow of data from readout: starting from the bottom, each APD reads 32 channels (detector cells), and delivers it to the FEBs; the DCMs aggregate data from 2048 channels which is transmitted to the computing farm (buffer nodes) until the trigger system decides whether to record or discard the data.

2.3.2 Timing System

NOvA uses a continuous readout system in conjunction with an absolute time synchronization of all the readout electronics. Each channel is timestamped and synchronized to every other channel. In addition, all channels are synchronized to an external "wall clock". This stable master clock line permits the FEBs, DCMs and the timing system to be loaded and synchronized with a universal "wall time" based off of a link to the global positioning system (GPS). Specifically, the timing chain is established starting from the GPS antenna, which connects to a master timing distribution unit (MTDU). The MTDU locks onto the signal of the GPS constellation, and is

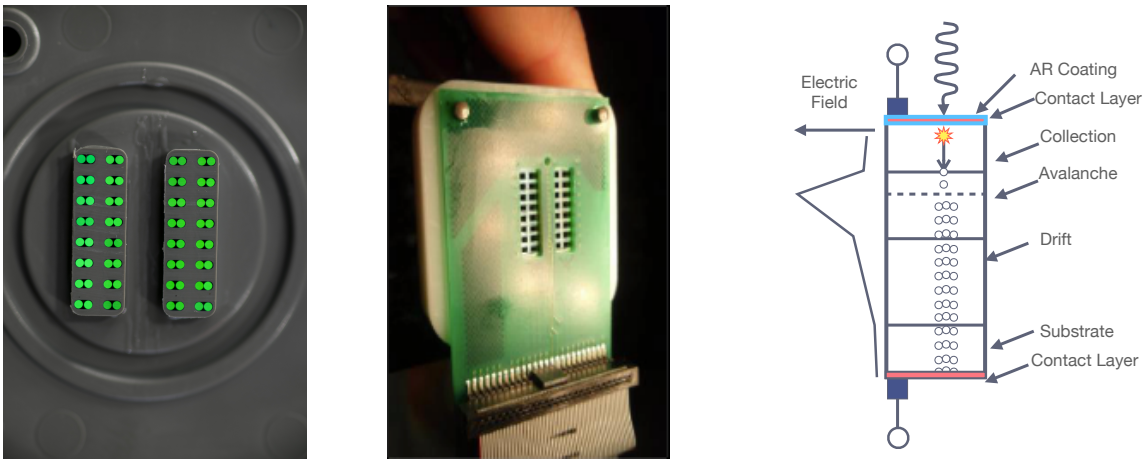

(a) (b) (c)

Figure 2.10: Avalanche Photo Diode. (a) 64 ends of wavelength-shifting fibers, corresponding to 32 cells, from [49]. (b) Custom NOvA APD, from [51]. (c) Schematic of a single wire end port of the APD: photons enter from the top, through the contact layer; through photoelectric effect they make photo-electrons, which get drifted by the electric field in the APD that causes the avalanche through the material as they travel to the bottom contact layer. Adapted from [51].

connected to a set of accelerator input lines (for the ND at Fermilab), or a reference pulser (for the FD site). The MTDU is then connected to a chain of slave TDUs; each supports two branches of 6 DCMs [52]. The TDUs and DCMs at the end of their chain have a loop-back to transmit the signal back up the chain. The loopback system is utilized to perform calibration along each leg of the timing chain and determine the delays of signal propagation device to device. Furthermore, each DCM fans out to 64 FEBs. The FD "backbone" consists of one MTDU and 14 slave TDUs. The ND is smaller, so only two slave TDUs are used to synchronize the detector.

Figure 2.9 displays the arrangement of the TDUs, DCMs and FEBs in the timing chains.

2.3.3 Triggering

The triggering system has the function of determining the data millislices to send to storage. Before this decision is made, the data is transferred to a farm of servers (buffer nodes). This servers store the data from the DCMs in a sequential fashion, meaning each consecutive millislice is stored into the next server. If all the nodes are filled, the oldest millislice is deleted, keeping what corresponds to 16-20 minutes of data. The data stays in the buffer node, awaiting for

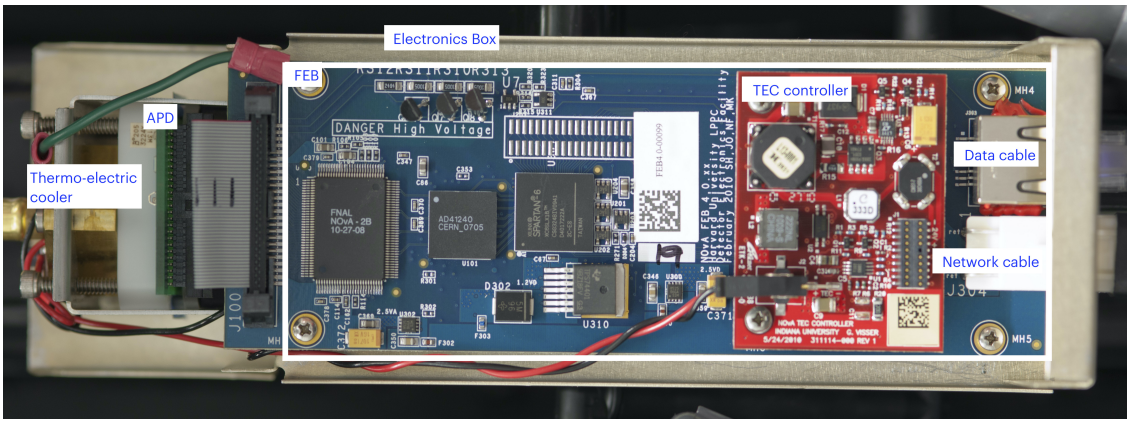

Figure 2.11: Electronics box containing an FEB and cooling system.

triggering. When a trigger is received, the buffer nodes are inspected to grab the millislices that have a timestamp corresponding to that of the trigger. All triggers on NOvA cause data for given time intervals in multiples of 50 μs to be stored. The buffer nodes then all send the triggered millislices to the data logger which saves the data to disk.

There are different triggering systems within the NOvA DAQ. The NuMI trigger requires that the timestamp in the millislice is coincident with the timestamp of when there was a spill at Fermilab. It selects the 10μs that corresponds to the beam spill plus sidebands before and after, to total a 500μs slice. The data read from this trigger is what concerns this thesis.

In addition, there are Data Driven Triggers (DDT), which are examine the data and search for interesting events not associated with the beam pulses. The DDT system executes reconstruction and analysis of unfiltered data. [53] The result of these analysis modules issue a the trigger decision to the data logger in order to send to storage the data within the time window that satisfies the trigger condition. In the ND, DDT are used to capture cosmic data for calibration. In the FD, DDT are used to record interesting slices related to supernovae, magnetic monopoles and dark matter searches, among others.

CHAPTER 3. NOvA SIMULATION

The oscillation parameters in the NOvA experiment are obtained from a fit of the predicted rate of ν_μs and ν_es to the observed data. In order to obtain the most accurate prediction possible, a detailed simulation is crucial. The simulation concentrates our understanding of the various physical processes that occur in the experiment, starting from the beam production to the response of the electronics. The NOvA simulation or Monte Carlo (MC) uses a series of simulated processes from various MC packages. Essentially it consists of four steps, where the output of each is the input of the next:

- Beam simulation: the G4Numi package is used to simulate the hadron production at the NuMI target, transport, and decay that produce the neutrino beam. This neutrino flux is corrected using constraints from hadron production experiments, using a suite of tools created for the NuMI beam called PPFX [54].
- Neutrino interactions: GENIE simulates neutrino interactions with the nucleons from the NOvA detectors. The simulation implements different models of the free nucleon interactions and the nuclear models described in chapter 1.4.
- Particle propagation: The final state particles information from the GENIE simulation is the input to the GEANT4 package, which propagates this particles through the detector composition and the results in energy depositions.
- Photon production and transport: The GEANT4 energy depositions are converted to photons from scintillation and Cherenkov light. This step transports the photons from the cells to the fibers and to the APDs.

This is summarized in Figure 3.1. The final product of the simulation are files with raw hits that mimic the actual detector data. This allows to apply the same algorithms to data and simulation

in order to develop the analysis. The next sections describe with more detail each step of the simulation chain, with emphasis on the GENIE model for neutrino interactions and its modifications.

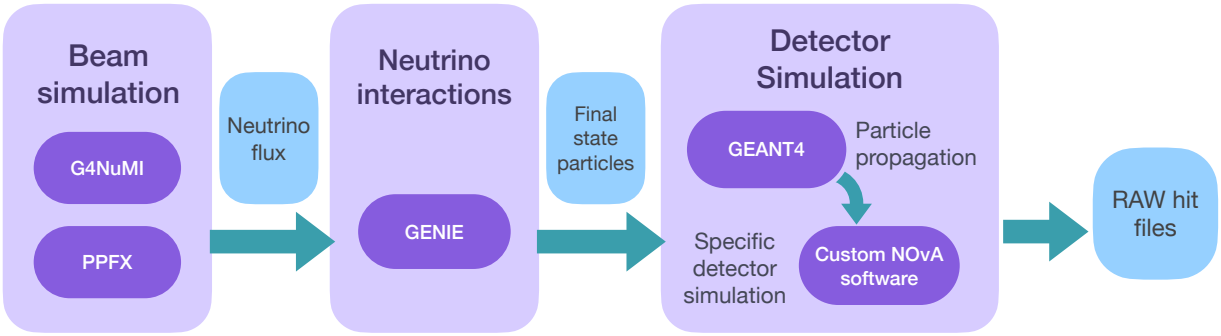

Figure 3.1: NOvA simulation chain.

3.1 Beam simulation

The expected flux of neutrinos from the NuMI beam is modeled for the near and far detectors. This is simulated using the G4NuMI package [55], which is a GEANT4 [56] based Monte Carlo simulation. It includes specifications for the NuMI beamline, including the proton beam, the magnetic horns and the geometry and composition of the target. The simulation starts generating the hadrons produced at the collision with the target, the transport, and decays that produce the neutrino beam. This neutrino flux is corrected using constraints from hadron production experiments, using a suite of tools created for the NuMI beam called Package to Predict the FluX, or PPFX [54]. This package also estimates uncertainties related to the hadron production using a multi-universe technique.

Figure 3.2 shows the predicted spectra below 20 GeV in the ND and FD for both the FHC and RHC modes.

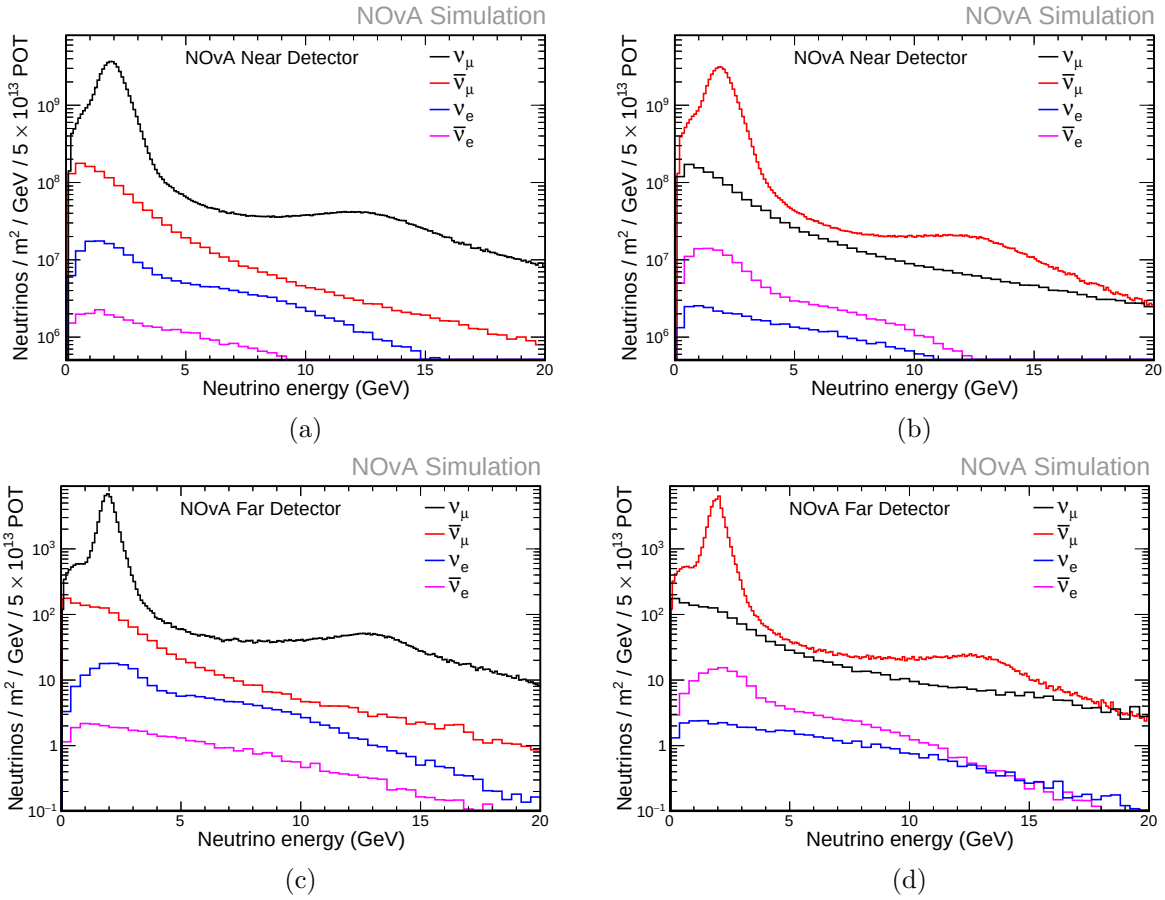

Figure 3.2: Simulated NuMI beam flux in NOvA Near (Far) detector for (a,c) FHC and (b,d) RHC beam modes. From [57].

3.2 GENIE model for Neutrino Interactions

From the output of the beam simulation, the flux of neutrinos and their kinematics are taken as inputs to simulate the neutrino interactions with nucleons of the detector. This involves taking into account the cross section models as explained in chapter 1.4, as well as the nuclear models to propagate the outputs of the neutrino interactions in the nuclear medium, and final state interactions to finally obtain the particles that will eventually deposit energy in the detector

NOvA uses a simulation based on the GENIE neutrino simulation software package, in the version 3.0.6. This contains multiple possible comprehensive model configurations (CMCs), which translates to the user having the choice among particular groupings of models for the nuclear,

neutrino-nucleus interaction and the final state interaction (FSI) pieces of the simulation. In addition to the central value for the particular CMC, GENIE also provide, to an extent, a range of values for various parameters of the model to serve as uncertainties.

This section describes the particular CMC for NOvA, named `N1810j0000`, as well as the adjustments implemented to the central value of the model including additional uncertainties required to obtain an adequate description of the NOvA ND data. The rest of the systematic uncertainties relevant for the analysis presented in this thesis will be revisited with more detail in section 5.2.

The GENIE Monte Carlo generator integrates a variety of physics models that describe different mechanisms for neutrino interactions. In the range of energies from a few MeV to hundreds of GeV, different physical processes are important, and each process can be simulated based on different models. The models can be classified into nuclear physics models, cross section models, and hadronization models [58]. The specific models incorporated in the `N1810j0000` CMC for NOvA are the following:

No simulation perfectly describes the experimental data. To mitigate the simulation shortcomings in NOvA, two adjustments are implemented: interactions with MEC are re-shaped into the NOvA 2p2h and the FSI model is adjusted with information from other experiments. These adjustments and their associated systematic uncertainties are described in the following sections.

3.2.1 Interaction model adjustments

The model from GENIE presented does not accurately represent the NOvA ND data. Figure 3.3 shows the chosen CMC from GENIE out of the box (without any modifications). A large underprediction of the ND data is observed. In order to obtain a more robust model that better describes this data, the MEC and FSI components of the simulation have customized adjustments implemented, based on NOvA ND data and external data respectively.

Table 3.1: Summary of GENIE CMC `N1810j0000` models

	Model	**Notes**
Nuclear model	Local Fermi Gas for CCQE interactions, global Fermi gas model for the rest	
Cross section models		
Quasi-Elastic interactions	Valencia model [59] [60].	Z-expansion formalism for systematic uncertainties and tune [61].
Resonance interactions	Berger-Sehgal model [62] [63].	
Deep Inelastic Scattering	Bodek Yang Model with data-driven parametrization for hadronization [64] [65].	
Meson Exchange Current	Valencia model [60]	Adjusted to NOvA ND data
Final State Interactions	Full intranuclear cascade (INC) model in INTRANUKE, (hN semi-classical cascade model) [66].	Tuned to external $\pi^+ -^{12} C$ scattering data
Hadronization	Andreopoulos-Gallagher-Kehayias-Yang (AGKY) hadronization model [67].	Determines the final state particles and 4-momenta given the nature of a neutrino-nucleon interaction and the event kinematics.

3.2.2 Final State Interactions model adjustments and systematic uncertainties

The semi-classical cascade model (hN) for Final State Interactions, as implemented in GENIE 3.0.6, did not provide the systematic uncertainties to vary the parameters that control the various channels of FSI. NOvA implemented a Boosted Decision Tree technique to construct the knobs for this systematic variations. In the process of building this uncertainties, it was found that a central value adjustment was also necessary, given that the GENIE implementation predicts cross sections that significantly disagree with external data [66]. Figure 3.4 shows said disagreement for the various channels.

In order to adjust the simulation, four free parameters that scale the cross section by modifying a physical parameter, are considered to tune the pion scattering within the hN model. Simulation with variations of the four parameters were compared to data to pick the most adequate value, starting with the mean free path (MFP), as it scales inversely proportional the

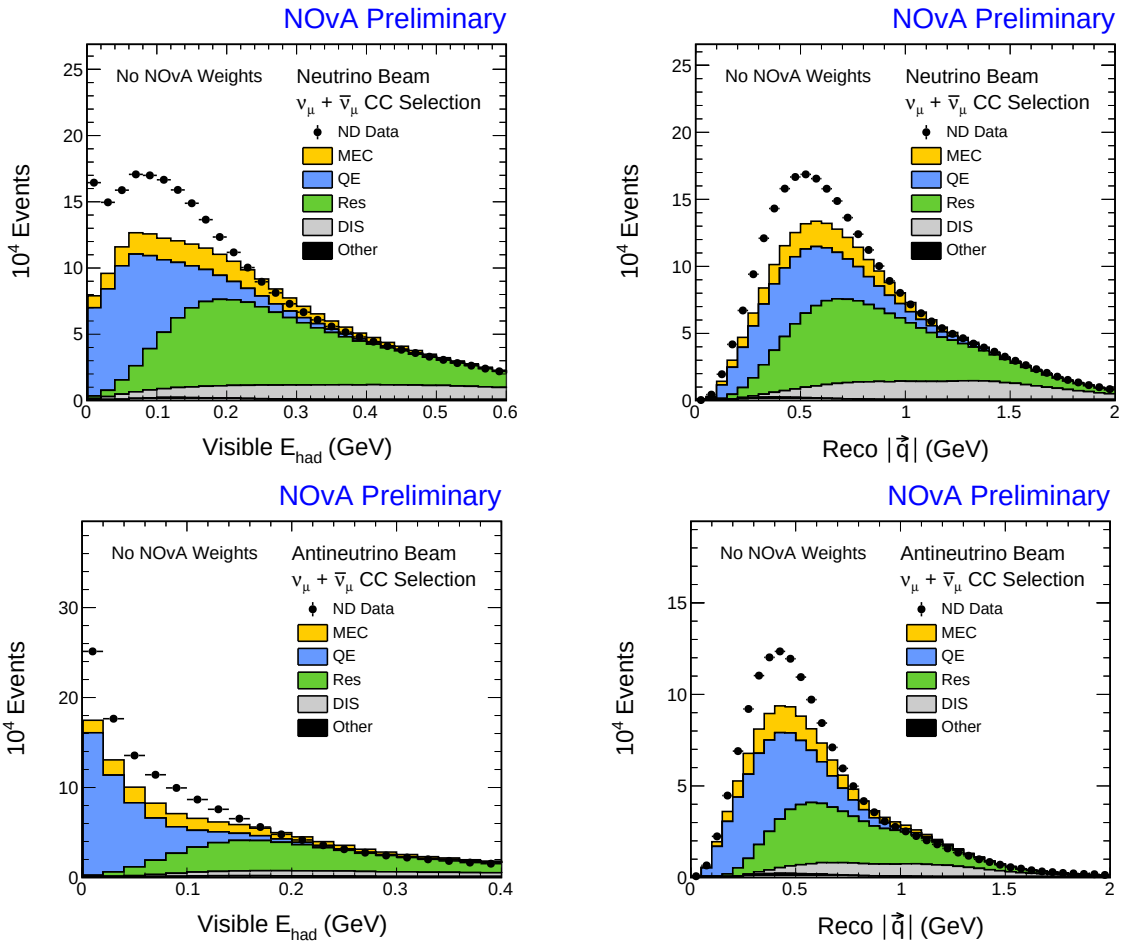

Figure 3.3: Nominal simulation and ND data in bins of reconstructed visible hadronic energy (left) and reconstructed three-momentum transfer (right) for neutrino (top) and antineutrino (bottom) beam.

REAC channel, and then the rest of the parameters. The particular values chosen and more details are described in table 3.2 and the comparison with data is shown in Figure 3.5

FSI systematic uncertainties

The 1σ uncertainties were constructed such that the ranges of the parameters adjusted contain 68.2% of the data points considered. [66] For the MFP parameter, the two values that bracket the external data in the REAC channel are chosen as the allowed systematic variation. This corresponds to the values $f_{MFP} = 0.4$ and $f_{MFP} = 0.8$. This is considered uncorrelated to the *fate fraction* parameters. The f_{QE}, f_{ABS}, and f_{CX} parameters are not independent. To obtain

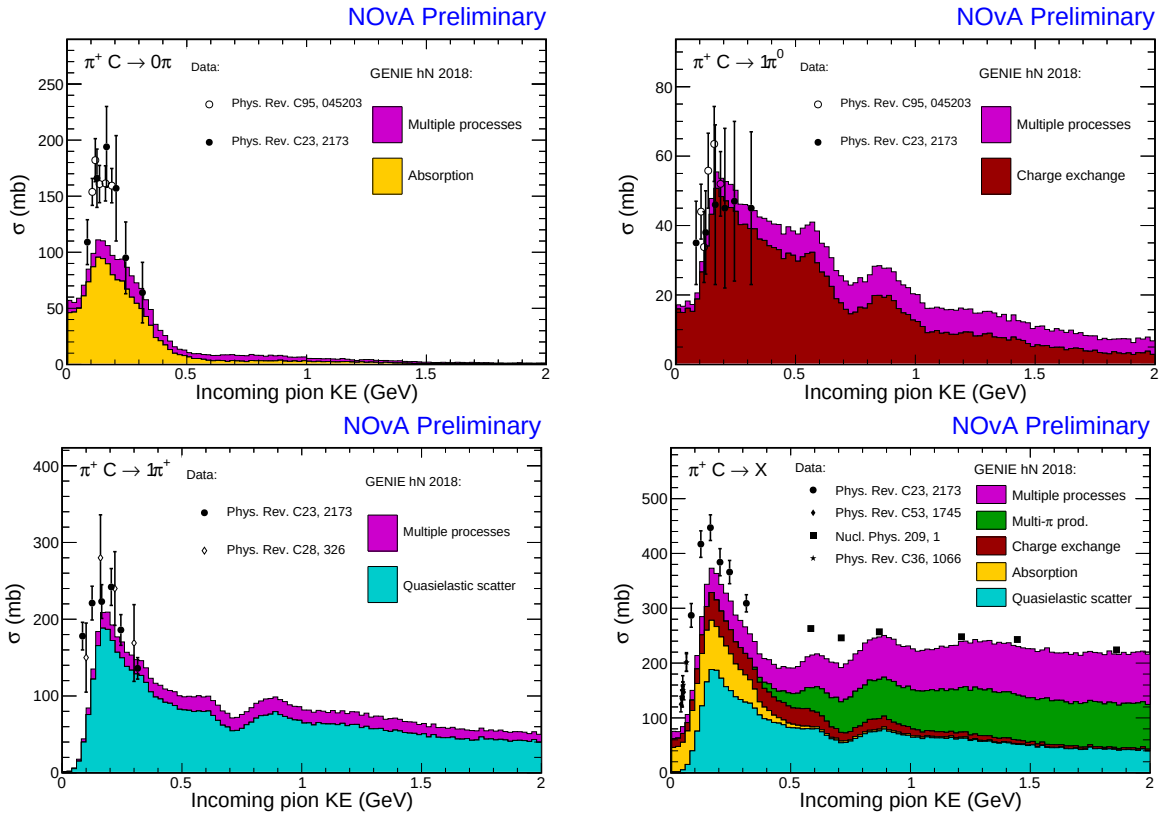

Figure 3.4: GENIE 3.0.6 hN predictions for various $\pi^+ -^{12} C$ cross sections compared to measurements. The measurement (topological) channel is indicated on the top-left of each plot. The colors indicate the true process in the simulation, that the most important pion scatter corresponds to.

their uncertainties, the procedure starts by obtaining a covariance matrix from the correlation matrix obtained with a NEUT fit, via the GNU-OCtave method, by the T2K experiment[68]. The diagonalization of this matrix results in 3 eigenvalues λ_i and eigenvectors $\vec{v}_i$. Each $\sqrt{\lambda_i}\vec{v}_i$ corresponds to an uncorrelated set of 1σ error variation for the fate fraction scales, which is added to the central value (in table 3.2) to obtain the shifted parameters. To obtain the -1σ shift, the values from $\sqrt{\lambda_i}\vec{v}_i$ are subtracted instead of added. The result is summarized in table 3.3.

3.2.3 Meson Exchange Current model adjustments and systematic uncertainties

The Valencia MEC model is reweighted to better represent the ND data. The weights are parametrized with 13 parameters that are fit, which represents an improvement from the previous

Table 3.2: Parameters tuned in hN model.

Parameter	Scale factor	Physics origin	Details
Mean free path (MFP)	$f_{MFP} = 0.6$	$\rho(\vec{r}), \sigma_{REAC}$	The mean distance traveled by pions before they undergo an interaction.
Fraction of ABS	$f_{ABS} = 1.4$	$\frac{\sigma_{ABS}}{\sigma_{REAC}}$	The fraction of pion interactions experiencing an absorption.
Fraction of CX	$f_{CX} = 0.7$	$\frac{\sigma_{CX}}{\sigma_{REAC}}$	The fraction of pion interactions experiencing charge exchange.
Fraction of QE	$f_{QE} = 0.9$	$\frac{\sigma_{QE}}{\sigma_{REAC}}$	The fraction of pion interactions experiencing quasi-elastic scatters.

Table 3.3: Within each group of rows, the upper row corresponds to the set of $+1\sigma$ shifted values; the lower row is the -1σ set.

Systematic	**Shift**(σ)	f_{MFP}	f_{ABS}	f_{CX}	f_{QE}
Fate fraction 1	$+1$	0.6	0.9	0.8	1.0
	-1	0.6	1.8	0.6	0.8
Fate fraction 2	$+1$	0.6	1.4	0.9	0.7
	-1	0.6	1.4	0.5	1.2
Fate fraction 3	$+1$	0.6	1.3	0.5	0.8
	-1	0.6	1.4	0.9	1.0
Mean Free Path	$+1$	0.8	1.4	0.7	0.9
	-1	0.4	1.4	0.7	0.9

analyses, where 200 bins fit parameters were used [69]. This was used in the latest 3-flavor oscillation analysis [10] in 2020.

Similar to the MINERvA tune [70], we used a gaussian parameterization, however using two 2D gaussians in the $(|\vec{q}|, q_0)$ space. There is an additional *baseline* parameter, which scales the normalization of all MEC events. This parameter was added to adjust the higher visible hadronic energy tail, which presented an excess using the nominal genie model. In summary, the parametrization follows the equation

$$\text{weight}_{MEC} = \text{baseline} + \text{gauss}_1(|\vec{q}|, q_0) + \text{gauss}_2(|\vec{q}|, q_0). \tag{3.1}$$

The *baseline* parameter is allowed to float freely, even towards negative values. Any resulting negative weight is reset to zero. The 13 parameters are fit by minimizing the χ^2 between data and

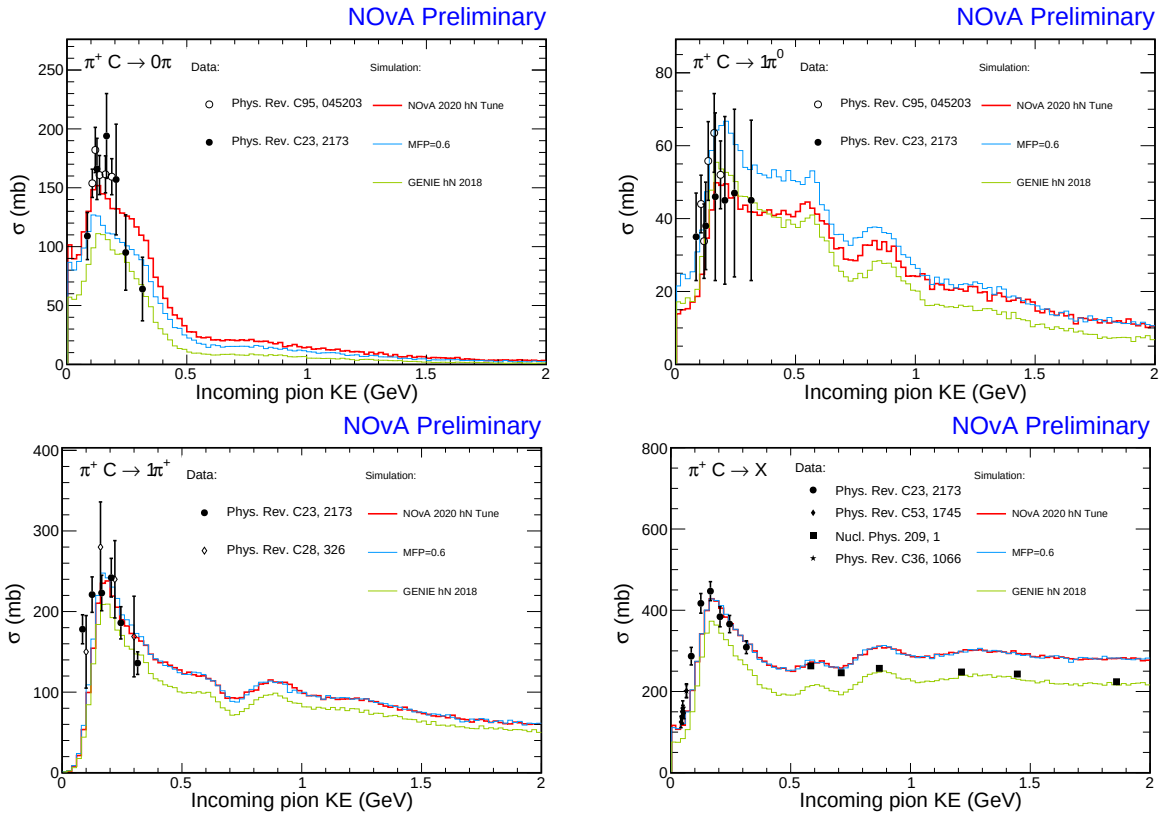

Figure 3.5: Predictions for the topological channels in $\pi^+ - {}^1 2C$ scattering compared to measurements (points with errors). NOvA's fully tuned central value prediction in red, GENIE 3.0.6's nominal hN FSI model in green, and the result of only adjusting the mean free path in blue.

simulation in bins of the reconstructed variables $(\vec{q}|, E_{had,vis})$ by allowing the simulation to vary in the true $(|\vec{q}|, q_0)$ space. The resulting values are in table 3.4 and the shape of the weights can be seen in Figure 3.6. The result indicates a need of enhancing the 2p2h interaction rate at very low q_0 values, and to lesser extent at medium $(|\vec{q}|, q_0)$ values. Such reshaping is more evident when looking at the distributions of $(|\vec{q}|, q_0)$ before and after the tune, as in Figure 3.7.

Table 3.4: Central value 2p2h tune values

Component	Parameter	Fitted value
Gaussian 1	Normalization	14.85
	Mean q_0	0.36
	Mean $\|\vec{q}\|$	0.86
	Sigma q_0	0.13
	Sigma $\|\vec{q}\|$	0.35
	Correlation	0.89
Gaussian 2	Normalization	42.0
	Mean q_0	0.034
	Mean $\|\vec{q}\|$	0.45
	Sigma q_0	0.044
	Sigma $\|\vec{q}\|$	0.31
	Correlation	0.75
Base model	Normalization	-0.08

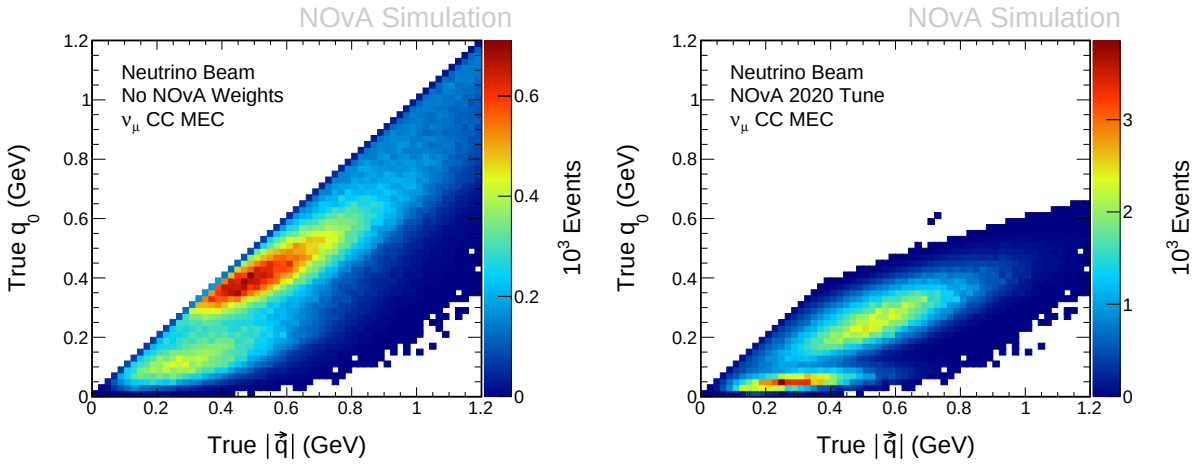

(a) (b)

Figure 3.7: Nominal GENIE simulation of MEC interactions with Valencia MEC model (a) and after the 2p2h tune (b) in bins of true $(|\vec{q}|, q_0)$.

MEC adjustment systematic uncertainty

By adjusting the kinematics of the 2p2h interactions, the simulation describes the data much better than before. This tuning technique is built with the assumption that the rest of the

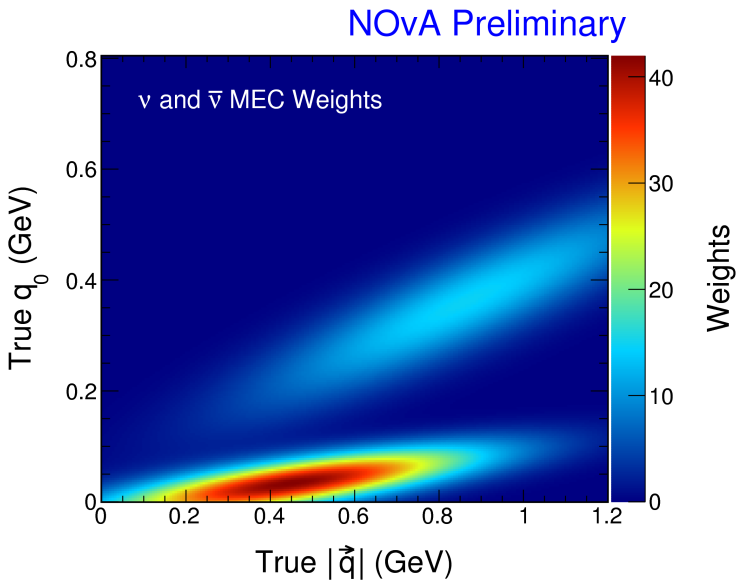

Figure 3.6: 2p2h weights parametrized as two 2D gaussians in $(|\vec{q}|, q_0)$.

simulation is *perfect*, and that the discrepancies with the data are only associated to MEC interactions. To account for the discrepancies coming from other pieces of the simulation, instead of MEC, a pair of alternative MEC weights were fit. These alternate fits start off with the simulation systematically shifted in order to enhance or suppress the Quasi-Elastic and Resonance interactions, accordingly named $QE-like$ or $RES-like$ scenarios. The list of systematic uncertainties shifted is listed in table 3.5. More details about each of these uncertainties will be discussed in chapter 5.2. Table 3.6 shows the values for the parameters in each scenario and Figure 3.9 shows the distributions of the non-2p2h components of the simulation in these alternative scenarios. The full picture can be observed in Figure 3.10, where the central value of the MEC tune is overlaid with the uncertainties obtained with the QE-like and RES-like tunes.

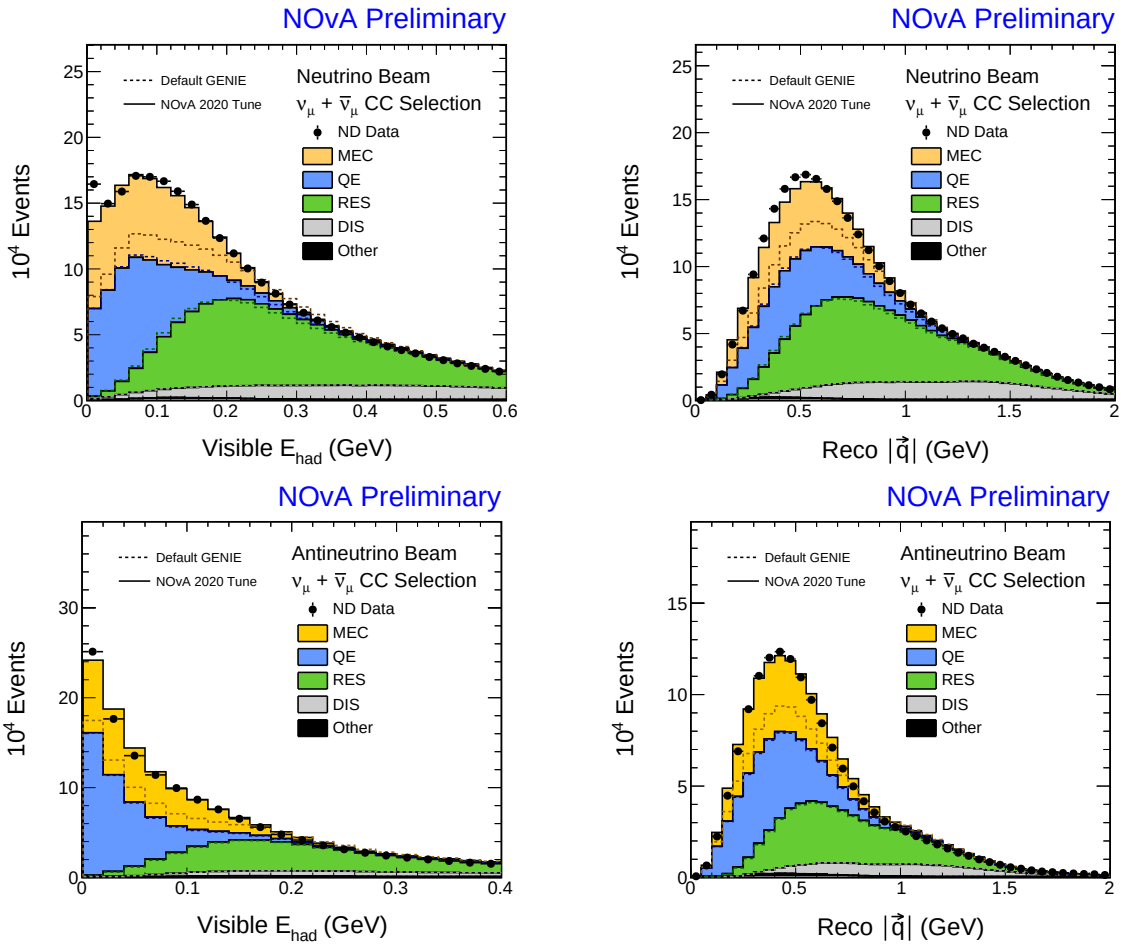

Figure 3.8: Tuned simulation and ND data in bins of reconstructed visible hadronic energy.

Table 3.5: Alternate 2p2h tuning systematically shifted parameters

Systematic uncertainty	**QE-like tune shift**	**RES-like tune shift**
Z-expansion CCQE normalization	$+1\sigma$	-1σ
Z-expansion coefficients 1,2,3, and 4	$+1\sigma$	-1σ
CCQE RPA suppression	$+1\sigma$	-1σ
CCQE RPA enhancement	$+1\sigma$	-1σ
RES M_A	-1σ	$+1\sigma$
RES M_V	-1σ	$+1\sigma$
RES low Q^2 suppression	$+1\sigma$	-1σ

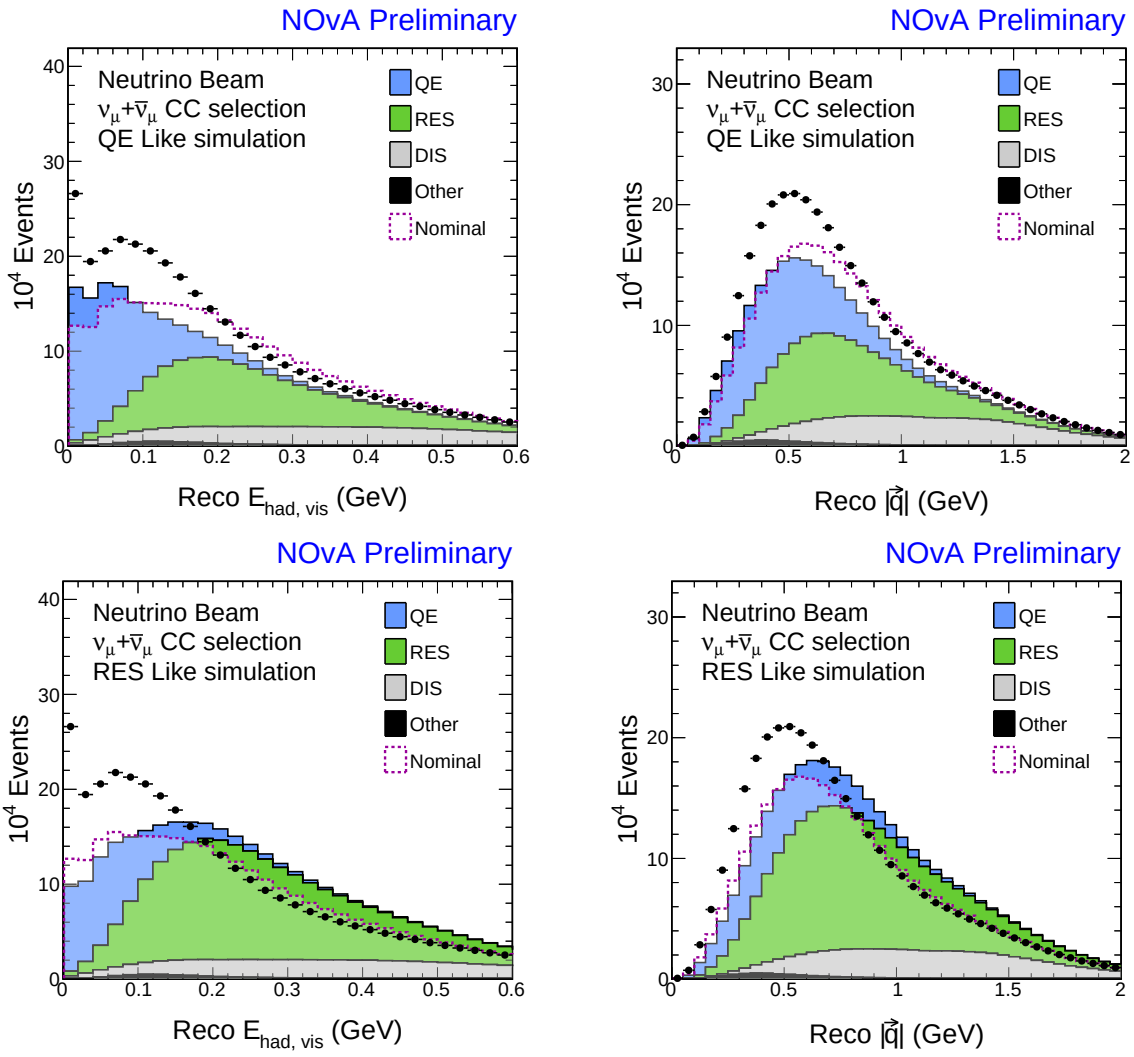

Figure 3.9: Distribution of the non-2p2h components of the simulation shifted to the QE-like (top) and RES-like (bottom) scenarios for FHC, in $|\vec{q}|$ (left) and E_{had}(right)

Additional MEC systematic uncertainties

In addition to the enhancement of the MEC event rates, there are two additional aspects of the model that are important to consider.

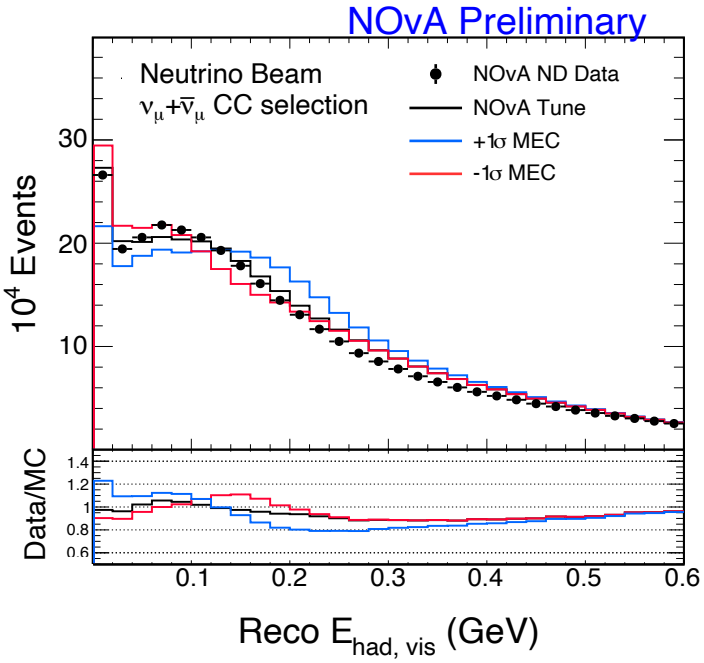

Figure 3.10: The solid black line includes the adjustments to Valencia MEC and FSI weights. The red and blue curves correspond the the 2p2h tune $\pm 1\sigma$ uncertainties.

Neutrino energy dependence In addition to considering the variation of the shape of 2p2h in the variables tuned, another source of uncertainty is the dependence with respect to the energy cross section. Figure 3.11 shows the SuSA (Megias) and Martini MEC models overlaid with Valencia MEC. These different models have very different rates at different energy ranges. These have very different normalization at different energy values. As the tune constrains the 2p2h normalization with respect to data, it is important to consider all uncertainties that produce variations in the shape.

In order to consider the energy-dependent shape variation, we compare the shapes of different models in a re-normalized basis, by re-scaling them in order to match the Valencia prediction at 10 GeV:

- The Martini prediction is scaled to have its maximum σ (at $\approx$ 1GeV) to match Valencia at 10 GeV.

Table 3.6: Alternate 2p2h tuning fit values

Component		**QE-Like**	**RES-like**
Gaussian 1	Normalization	20.0	16.86
	Mean q_0	0.52	0.29
	Mean$\|\vec{q}\|$	1.03	0.78
	sigma$\|\vec{q}\|$	0.37	0.45
	sigma q_0	0.14	0.085
	Correlation	0.97	0.91
Gaussian 2	Normalization	104.	88.0
	Mean q_0	0.026	0.036
	Mean$\|\vec{q}\|$	0.44	0.46
	sigma$\|\vec{q}\|$	0.20	0.30
	sigma q_0	0.044	0.056
	Correlation	0.82	0.82
Base model	Normalization	0.74	-0.41

- The SuSA prediction is scaled to match the Valencia prediction at 10 GeV.

Then a function with a shape that encapsulates the ratios of the different predictions with respect to the Valencia model is taken as the 1σ uncertainty. Given the significant difference of the maximum cross section of the Martini prediction with respect to the others, it was chosen to use an asymmetrical uncertainty, where the upper envelope is parametrized with a Landau distribution with $mpv = 0.4$ and $\sigma = 1$. The lower bound is defined by the function:

$$f(E_\nu) = \frac{0.5}{1 + 2(E_\nu - 0.25)} \tag{3.2}$$

.

Nucleon pair fraction Based on the fraction of nn(pp) and np pairs for neutrinos (antineutrinos) in the tuned numu selection, we use the following for neutrinos:

$$\frac{np}{np + nn} = 0.69 \begin{cases} +0.15\sigma \\ \\ -0.05\sigma \end{cases}, \tag{3.3}$$

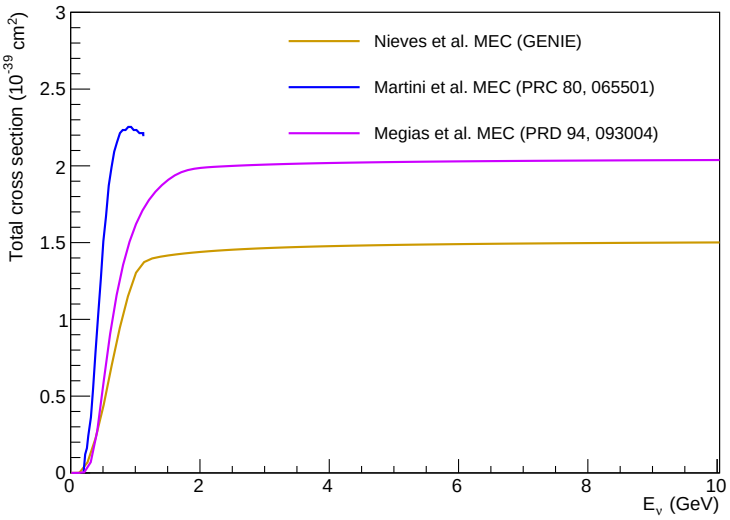

Figure 3.11: Alternative MEC models absolute cross section.

and

$$\frac{np}{np+pp} = 0.66 \begin{cases} +0.15\sigma \\ -0.05\sigma \end{cases} \tag{3.4}$$

for antineutrinos. The uncertainty is asymmetric as the intrinsic ratios in the Valencia model (0.69 and 0.66) are much smaller than the assumed ratio in empirical MEC (0.8), which was used in the previous analysis, and is at the lower end of the range of model assumptions.

3.2.4 Final agreement

After both the FSI and MEC adjustments, the overall agreement of the $\nu_\mu + \bar{\nu}_\mu$ selections for both FHC and RHC is good. Figure 3.13 shows the visible E_{had} distributions before and after the cross section adjustments described above. The 1σ uncertainty band including the MEC, FSI and other cross section parameters is included. The rest of these systematic uncertainties are described in section 5.2. Although the agreement is within this systematic uncertainties, and in the $(E_{had}, |\vec{q}|)$ range with the most events (below 0.1-0.2 GeV of hadronic energy and below 1 GeV of $|\vec{q}|$), more information can be extracted about the performance of these adjustments. One way of

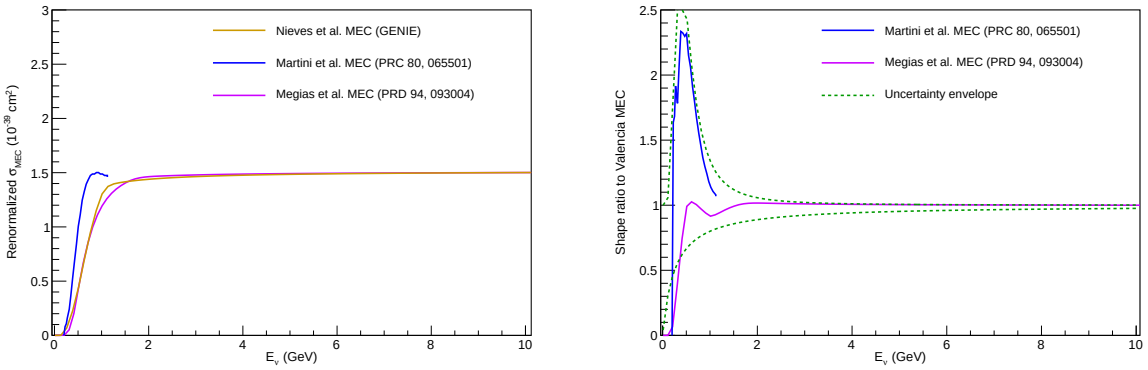

Figure 3.12: Alternative MEC models normalized to Valencia MEC (left) and their ratio with respect to Valencia MEC (right), overlaid are the two curves that wrap the relative differences between models that compose the uncertainty.

further evaluating the implementation of this tune is by looking at subsets that target the impact of different systematic uncertainties. Such study was made by looking at different subsets of this data set, subdividing by different identifiable final states, and is explained in detail in chapter 4.

3.3 Detector simulation

The detector simulation models the production and transport of photons, mainly from scintillation light, the energy depositions and the subsequent conversion to electrical signals. In terms of the simulation chain, this can be broken down in two steps: photon transport and electronic readout.

The output of the GENIE simulation is the set of final state particles and kinematics after a neutrino interaction. GEANT4 is used to simulate the propagation of these particles and their energy depositions. At this stage, additional secondary particles can be created and are also simulated.

After the GEANT4 simulation, custom NOvA software modules are used to simulate the response of the detectors to the energy depositions. This includes simulating the energy deposition converted to photons that arrive to the optical fiber and subsequently to the APD. The signal

into the APD is simulated as a combination of these photons and a model of the noise response of the APD. A different software package simulates the response of the FEBs to the APD output.

The end result of the simulation chain is a collection of hits, in the same format as the raw detector data. The simulation is then ready be processed with the same algorithms as the data in order to develop the analysis.

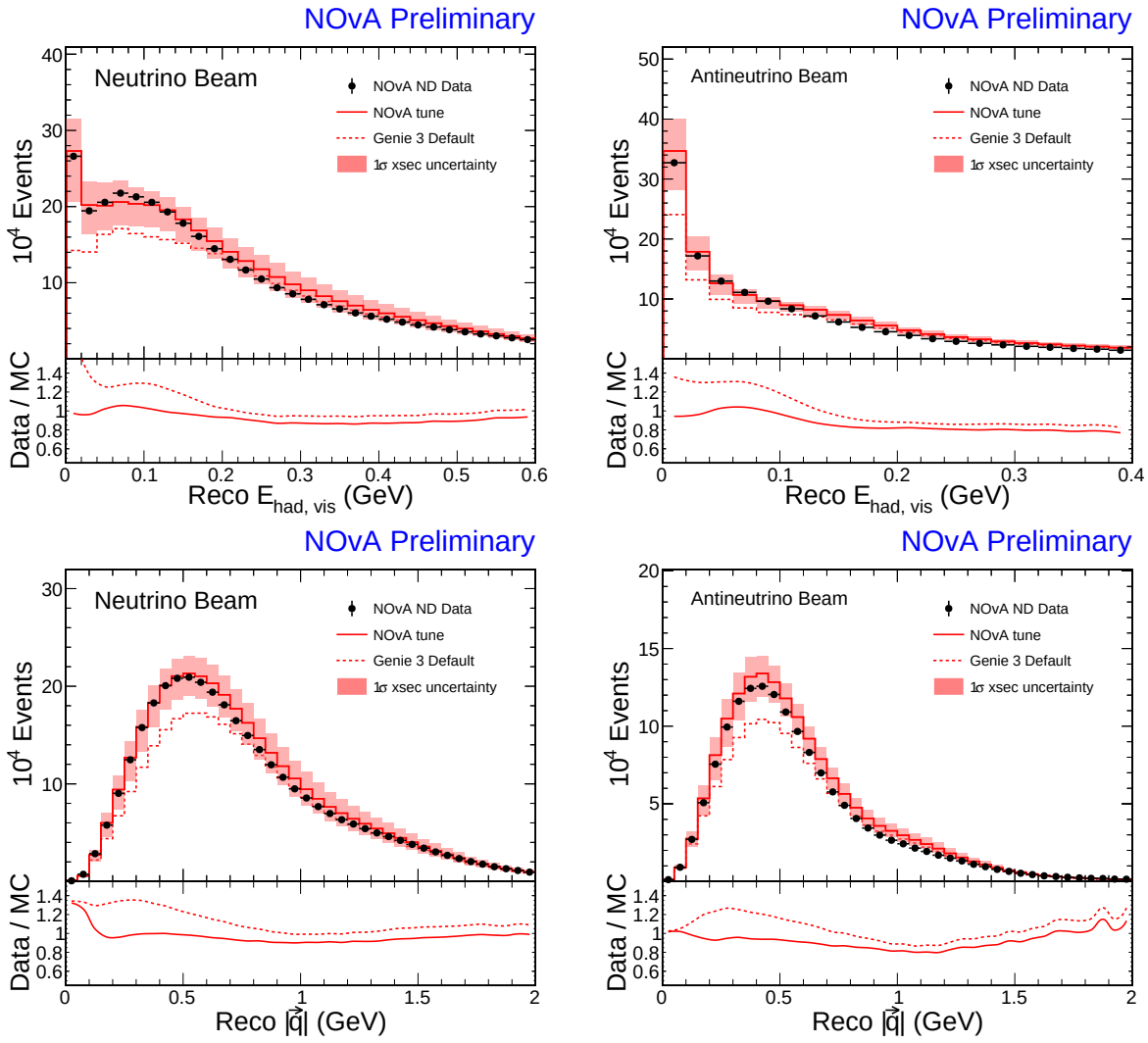

Figure 3.13: Tuned simulation and ND data in bins of reconstructed visible hadronic energy (top) and reconstructed $|\vec{q}|$ (bottom), for FHC(left) and RHC(right), including the 1σ error band for all cross section uncertainties.

CHAPTER 4. SELECTION TO EVALUATE THE NOvA NEUTRINO INTERACTION MODEL

In order to analyze the NOvA data, it is necessary to accurately identify and classify the neutrino interactions recorded in the detectors, and to extract physical quantities that can be used to infer the oscillation parameters. In order to achieve this, a series or techniques are used to identify individual neutrino interactions using spatial and timing information, classify individual particles within the the event, and estimate the energy of the incoming neutrino, along with other kinematical variables. This methods constitute the full event reconstruction. The same algorithms are applied to data and simulation, which allows to compare them, in order to validate the NOvA simulation, and identify aspects which need further constraining. This chapter describes the reconstruction and energy estimation techniques, in order to develop the ν_μ and ν_e selections in both detectors. The ND data set resulting from these techniques is used to evaluate the interaction model.

4.1 Event Reconstruction

In order to extract physics information from the hits recorded in the NOvA detectors, first it is necessary to group such hits into single interaction events. This is achieved using different algorithms. Figure 4.1 summarizes the reconstruction chain. Each step will be explained in the following sections.

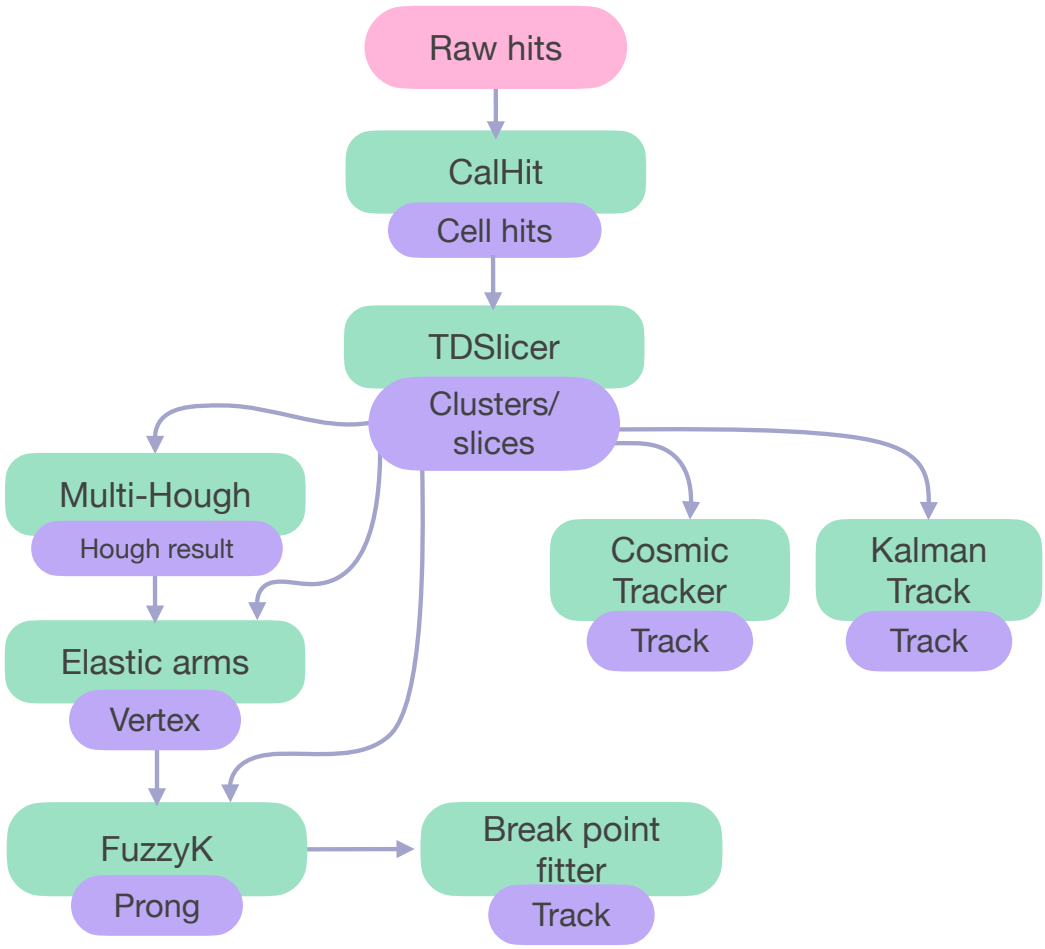

Figure 4.1: Flowchart of the reconstruction algorithms. The green boxes represent the algorithms, while the purple boxes denote the input and output of each algorithm.

4.1.1 Event slicing

An algorithm called *TDSlicer*, which stands for Time Density Slicer, is used to cluster hits based on timing and spatial information within the readout window of 550μs. Each cal hit contains a xzt or yzt (cell,plane,time) information. First, centroids are found by finding local maxima in the density of the hits s using a centroid-finding algorithm by Rogriguez and Liao

[71]. Afterwards, 3D clusters in the two viwes are created using Prim's algorithm [72]. Finally a view-merging step constructs 4D slices by merging the xzt and yzt views. An example of the input and output of the slicer is shown in Figure 4.2.

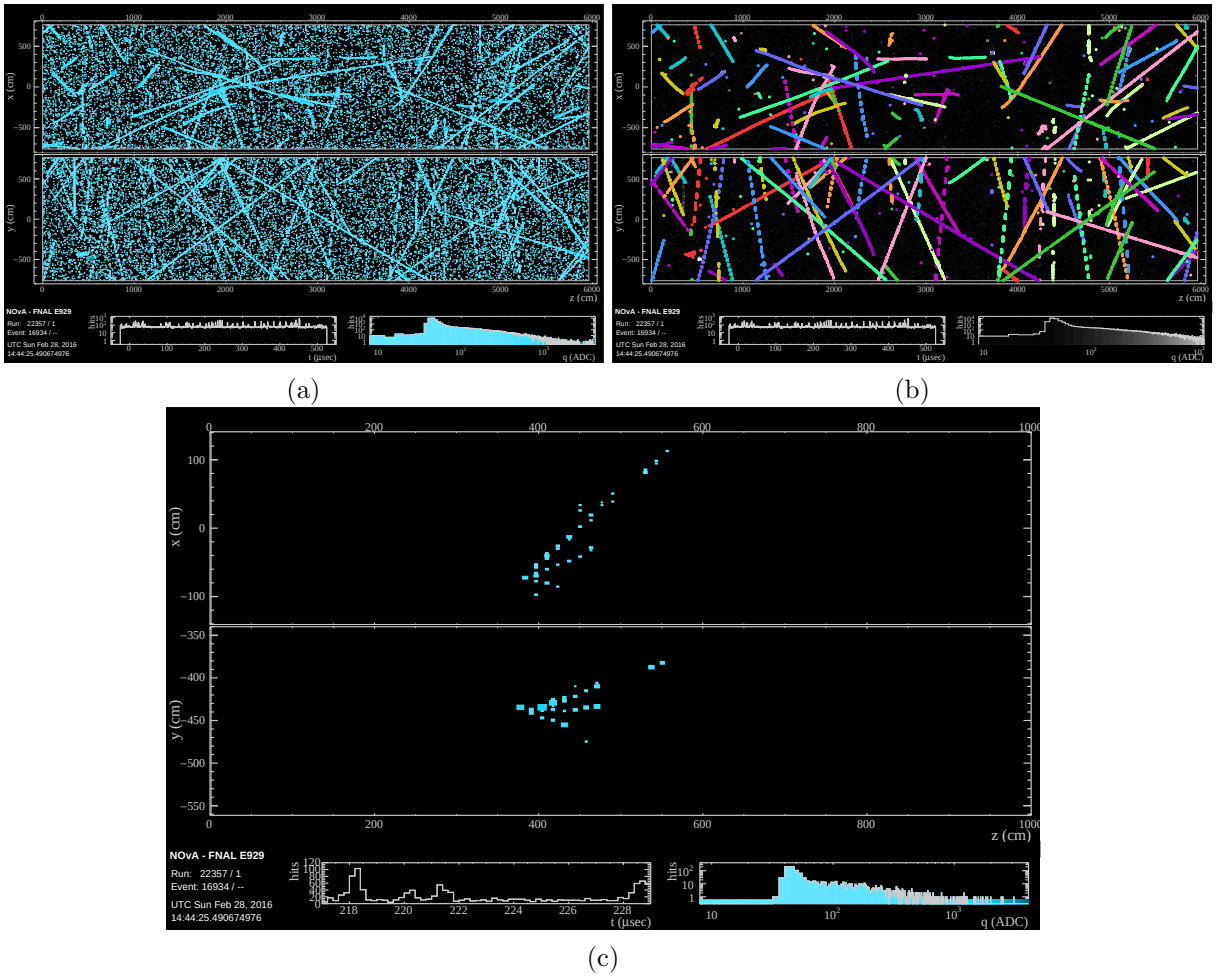

(a) (b)

(c)

Figure 4.2: FD readout window showing (a) 550 μs of deposited charge, followed by (b) slicing algorithm with each group of a single slice denoted in a single color. A single slice containing a neutrino interaction is zoomed in (c).

4.1.2 Vertex identification

The next step is to identify a location for the interaction, or "vertex". This is done after identifying major features in the event through a modified Hough transform algorithm, known as

Multi-Hough transform. This pattern recognition algorithm takes pairs of pixels in each detector view as an input, and constructs a two-dimensional array, known as the Hough space map, using polar coordinates and a Gaussian-smeared voting scheme [73]. Peaks above threshold in the Hough map are line candidates. To control the number and quality of the line candidates, pixels that have been associated with a dominant candidate are removed, and the process is iterated. The result of this algorithm is further used as a seed to find the primary neutrino interaction point using an *Elastic Arms* algorithm [74]. The intersections of the Hough lines, are identified as vertices: from these, each particle track is approximated by an "arm" (a vector pointing away from the vertex) whose direction can be adjusted to fit the event. The optimum vertex is chosen by minimizing an energy cost function [75] which accounts for goodness of fit between the hits and the arms, penalizing hits not associated with any arms, and a penalty for arms whose first hit is far from the vertex. Figure 4.3 displays the vertex found with these two algorithms.

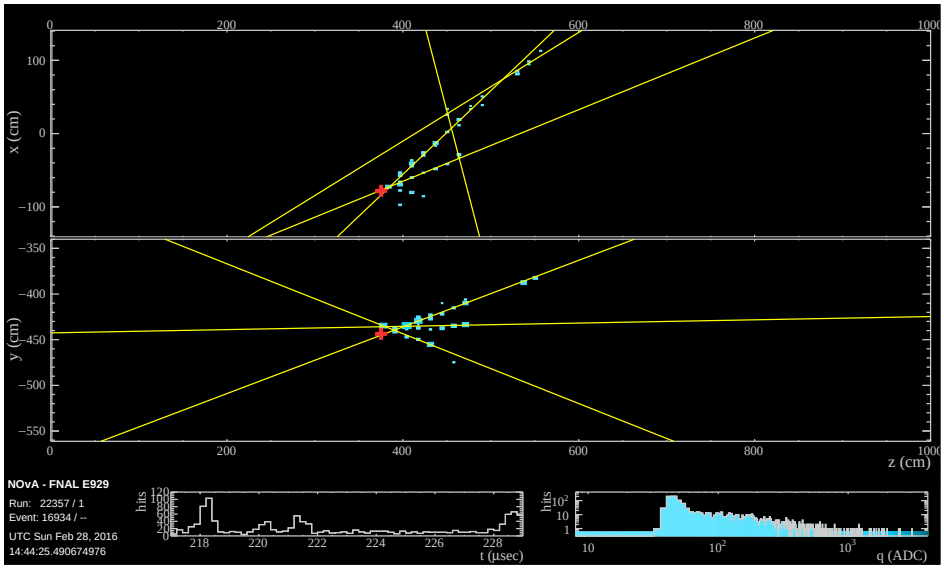

Figure 4.3: Result of finding Hough lines in yellow, and the vertex found with Elastic arms indicated with a red cross. This is from the same event depicted in Figure 4.2.

4.1.3 Clustering

By analyzing the slice hits and the interaction vertex, we can categorize the hits into distinct particle "prongs", which are clusters of hits with a defined starting point and direction. This process employs a possibilistic clustering algorithm known as *fuzzyk* [76, 77], derived from the Fuzzy k-means technique. The fuzzyk method, utilized by NOvA, enables hits to belong to multiple clusters, hence the term "fuzzy", and it is possibilistic as a hit does not have to possess a membership probability of on [75]. The prong formation process is done separately for each view, which results in the clusters of hits denominated as 2D prongs. The last step is to match clusters between the two views to form 3D prongs. Of course, not all of the 2D prongs can be matched into a 3D prong. The result of this step is shown in Figure 4.4.

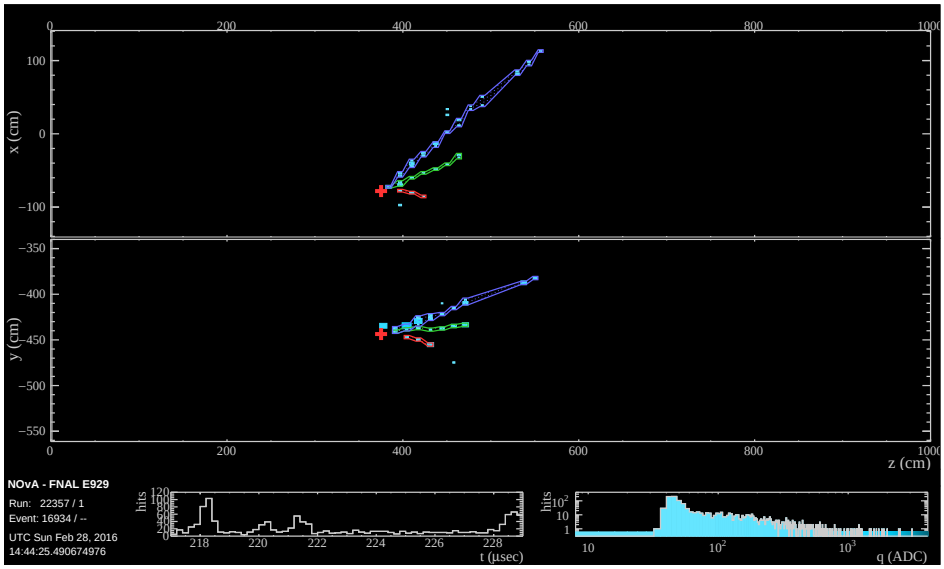

Figure 4.4: Result of the fuzzyk clustering procedure. The event display (same event as in Figure 4.3) shows three 3D prongs, with their corresponding matched 2D prongs indicated by the matching colors.

4.1.4 Tracking

Prongs are excellent units of information to describe particles that produce showers, such as photons and electrons. However one additional reconstruction method beyond prongs are the tracks, which in addition to start point and direction information, also contains an end point and a vector of trajectory points. NOvA uses a *Kalman Tracker* algorithm, based off of a multiple scattering model and a Kalman filter [78]. It takes as input the clusters of hits formed from the slicing algorithm and forms tracks in the xz and yz detector views separately. Each view produces 2D tracks which are later matched to produce a single 3D track [79]. Another tracking algorithm available in NOvA is called Break Point Fitter. This method takes input from the 3D prongs obtained from *fuzzyk*, and breaks the particle path at various points to allow for Coulomb scattering dependent on the particle mass and energy deposition rate. The output of this algorithm is again, a 3D track. In addition, the another tracking method, uses a sliding window algorithm to reconstruct expected tracks from cosmic rays. The *window tracker* [80] algorithm assumes that muons follow a straight trajectory within small sections or windows of their track, in other words, mostly in the downward direction and with single-track topologies.

4.2 Particle identification

In addition to obtaining reconstructed pieces of information from the detector,it is crucial to identify the particles produced in the interaction captured in a slice. The samples of the 3-flavor analysis search for ν_μ and ν_e , and minimize the content of NC, and other background events. The topologies of these events are displayed in Figure 4.5. The ν_μ events are easily identified by the tracks of the muon, which are typically long and straight. Analogously, ν_e events are identified by the electron produced, which leaves a shorter electromagnetic shower. NC events can mimic the topology of a low energy electron. Similarly, the two photons produced by a π_0 decay could also be mistaken for an electron if their opening angle is small enough that the showers overlap and the decay occurs close to the interaction vertex. The NC events can not be used to identify the flavor of the incoming neutrino because there is no lepton in the final state.

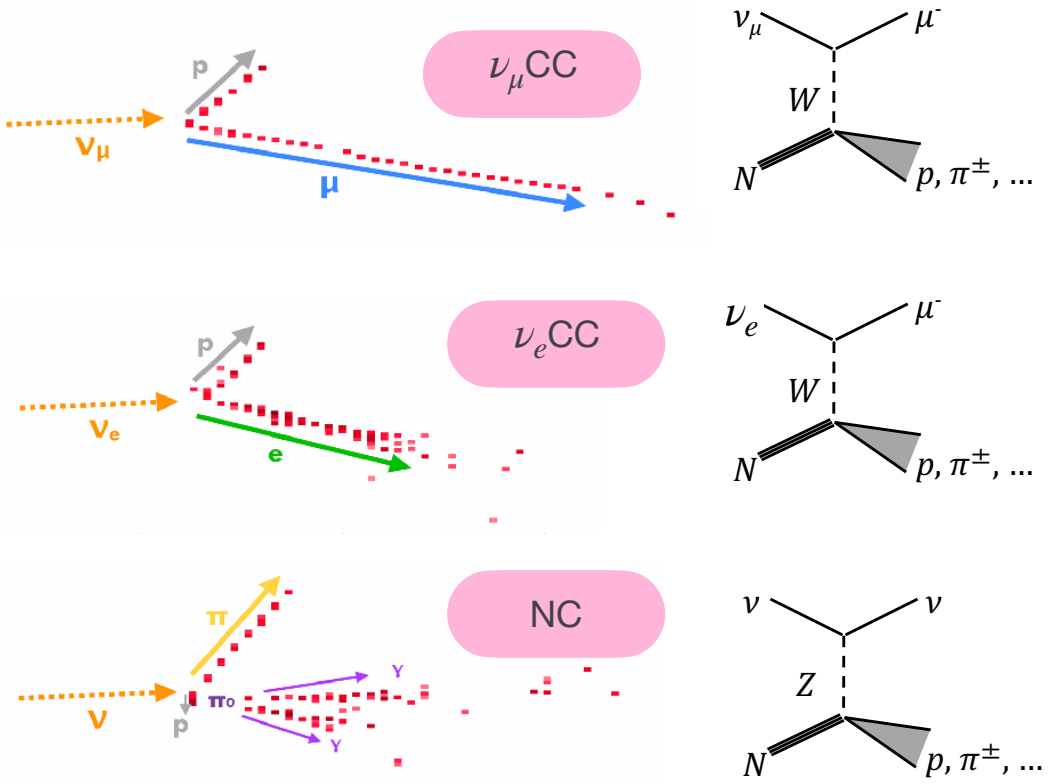

Figure 4.5: Three interaction topologies of interest for the 3-flavor oscillation analysis. From top to bottom: ν_μ CC, ν_eCC, and NC with a π_0 detached from the vertex.

NOvA has various algorithms to identify the particles at an event-level and at prong-level. For the particular case relevant to this thesis, both of these algorithms employ the deep-learning classifier known as Convolutional Visual Network (CVN) [81], which belongs to the Convolutional Neural Network (CNN) family of deep learning methods.

Event-level CVN The advantage of using a CVN method at an event-level, is its independence from the reconstruction algorithms, which removes any bias that could be introduced from those algorithms. CVN is based on techniques from the field of computer vision for image recognition, and in particular, this CVN's architecture is inspired by GoogleNet [82]. In the case of NOvA, the input image is a pixel map, where each pixel corresponds to the cell hits in

a slice. The network is trained over separate FHC and RHC samples of simulated beam events as well as cosmic ray data. The output of the classifier is a score from 0 to 1 of how likely is that the slice comes from a ν_eCC, ν_μCC, ν_τCC, NC interactions or cosmic activity. Figure 4.6 shows a *t-SNE* [83] visualization of the performance of this classifier.

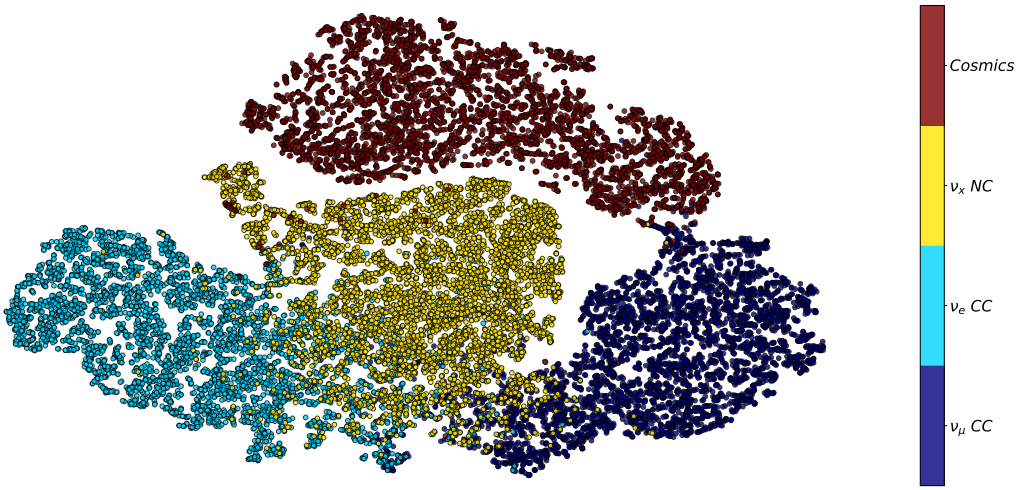

Figure 4.6: A t-SNE transformation of the feature vector from the event-level CVN classifier trained with the neutrino beam mode sample. Each color represents the interaction types. Good separation is observed.

Prong-level CVN This application of CVN, named *ProngCVN* [84], aims to classify the 3D prongs reconstructed with *fuzzyk*, such as the ones pictured in Figure 4.4. This classifier however is not independent of the reconstruction. It uses an analogous architecture as the event level CVN, with the additional input of the xz and yz pixel maps of the individual prongs. The output of the network is a vector of scores, from 0 to 1, that correspond to how likely is the prong to have originated from an electron, photon, muon, charged pion or proton. The purity and efficiency of this classifier is displayed in Figure 4.7. The sum of all these scores for a single prong is 1. In this work, the prong-level CVN is utilized partially in the energy estimation of the ν_e, to distinguish the electromagnetic component of the deposited energy. In addition, the particle

identification is used to create a selection of various topologies within the selection of ν_μ CC events, and evaluate various aspects of the NOvA simulation.

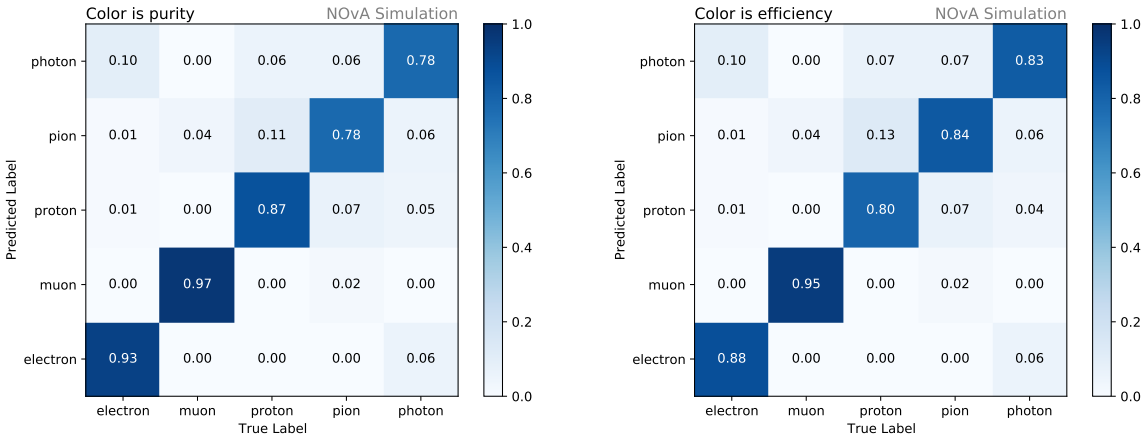

(a) Purity

(b) Efficiency

Figure 4.7: Performance evaluation matrices for the ProngCVN network trained on the neutrino beam mode sample. The predicted label on the y-axis is the highest scoring label from the network. The diagonal shows the purity (a) and efficiency (b) of each particle type while the off-diagonal shows background contamination and mis-classification respectively.

CNN cosmic veto The NOvA Far Detector, being on the surface, records an order of magnitude more cosmic data than it does beam data. This poses the advantage that we can directly measure cosmic backgrounds of the neutrino samples, however the volume of data is very large and therefore computationally expensive to process through the full reconstruction chain. To reduce the computational load, a CNN-based algorithm filters neutrino-like activity from cosmic activity [85]. The CNN cosmic veto uses pixel maps of the whole FD cell hits during 16μs windows within a slice, and each window overlaps 1μs with the previous and next windows. Hits not associated with neutrino-like activity, and the hits around then in time, are removed completely from the file.

Near Detector Rock filter Similar to the role of the CNN cosmic veto, the ND rock filter aids in removing unwanted rock muon events as early in the reconstruction chain as possible. The

filter runs after the MultiHough, ElasticArms and CosmicTrack algorithms. The filter removes cutting out events that had a reconstructed vertex within 21 cm of the detector walls, excluding the back wall.

Cosmic rejection Boosted Decision Trees A decision tree is a machine learning technique that classifies its input based on binary decisions trying to predict some feature. Boosting refers to creating multiple classifiers, where the subsequent one is trained to perform better on the samples that the previous one mis-classified. A boosted decision tree (BDT) combines multiple weak classifiers to form a strong classifier [86]. In NOvA, BDTs are utilized to identify muons. A separate network is trained for each beam mode, and for the ν_e and ν_μ samples.

Reconstructed Muon Identifier Reconstructed Muon Identifier (ReMId) is a Boosted Decision Tree (BDT) used to identify the muon tracks originated from a ν_μCC interaction, and distinguish them from background CC and NC events. Particularly, pion tracks are the main background. The BDT is trained using four reconstructed variables provided by the Kalman track algorithm: deposited energy per unit length (dE/dx) log-likelihood , scattering log-likelihood, track length, and fraction of planes used in dE/dx LLh [87]. These log-likelihood evaluations are done based on a sample of simulated muons and pions. The fact that pions interact with the strong force, in addition tot he weak force, allows to distinguish their tracks from muons as more deflection in their paths is expected, and the hadronic scattering affects their dE/dx. The score of the highest scoring track for a slice is taken used as a classification probability describing how likely that event is ν_μCC. Four separate versions are generated to account for the ND, FD, FHC and RHC sample.

4.3 Energy estimation

The oscillation analysis in NOvA depends on the observation of ν_e and ν_μ . In addition to correctly identifying these events, the quality of the oscillation parameters extracted depends on the energy measurement. Therefore it is essential to have a sensible estimate of the neutrino

candidates' energy. Accurate energy estimation depends on the calibration of the hits in the detector, a good reconstruction and good estimation of the energy deposits of the different particles that can be produced by the neutrinos, including muons, electrons and hadrons, such as pions or protons. Following the slicing step in the reconstruction, the hits are calibrated against standard candles to ensure their translation to energy units is consistent across detector elements and over time. The basic idea behind the energy reconstruction is adding up the energy from the lepton to the energy of additional hadronic activity in the slice. In order to develop and evaluate an estimator, simulated events are used. Different estimators are used to determine the energy of ν_μ and ν_e candidates, as the electrons and muons deposit energy in the detectors in different manners.

4.3.1 Muon neutrino energy reconstruction

After identifying an event corresponds to the ν_μ topology, the muon track is found using ReMID. Muons within a certain energy range ($0.2 - 2\text{GeV/c}$) have a consistent energy deposition as Minimum Ionizing Particles (MIPs). This implies that the length of the muon track is closely related to its initial energy. Therefore, the estimation of ν_μ energy involves determining the contribution of the muon based on its track length and then adding the energy of the hadronic system. In other words:

$$E_{\nu_\mu} = E_\mu + E_{HAD} \tag{4.1}$$

A piece-wise linear spline fit is applied to the reconstructed Kalman track length versus the true muon energy obtained from simulations. Figures 4.8 (a),(c) show that the distribution of this fit has a relatively small spread for true muon energies above 1 GeV. The spline fit involves determining the slopes, intercepts, and stitch points using the mean value of the distribution for each bin of track length. This approach yields a muon energy resolution of approximately 3%.

A similar fitting procedure is carried out to estimate the composition of the hadronic system. Unlike muon tracks, the energy depositions of hadrons are not as clean. Therefore, the total calorimetric energy of the hadronic system is used instead of the track length. All hits in the slice

that are not associated with the muon track are considered as part of the hadronic system. Since the objective is to estimate the neutrino energy rather than the true hadronic energy, the y-axis in the fit is defined as the true neutrino energy minus the previously determined reconstructed muon energy. Figures 4.8(b) and (d),show that the distribution has a significant spread, resulting in a hadronic energy resolution of approximately 26%. However, when combined with the accurate muon energy estimation, the average energy resolution for FD neutrinos (antineutrinos) is 9%(8%).

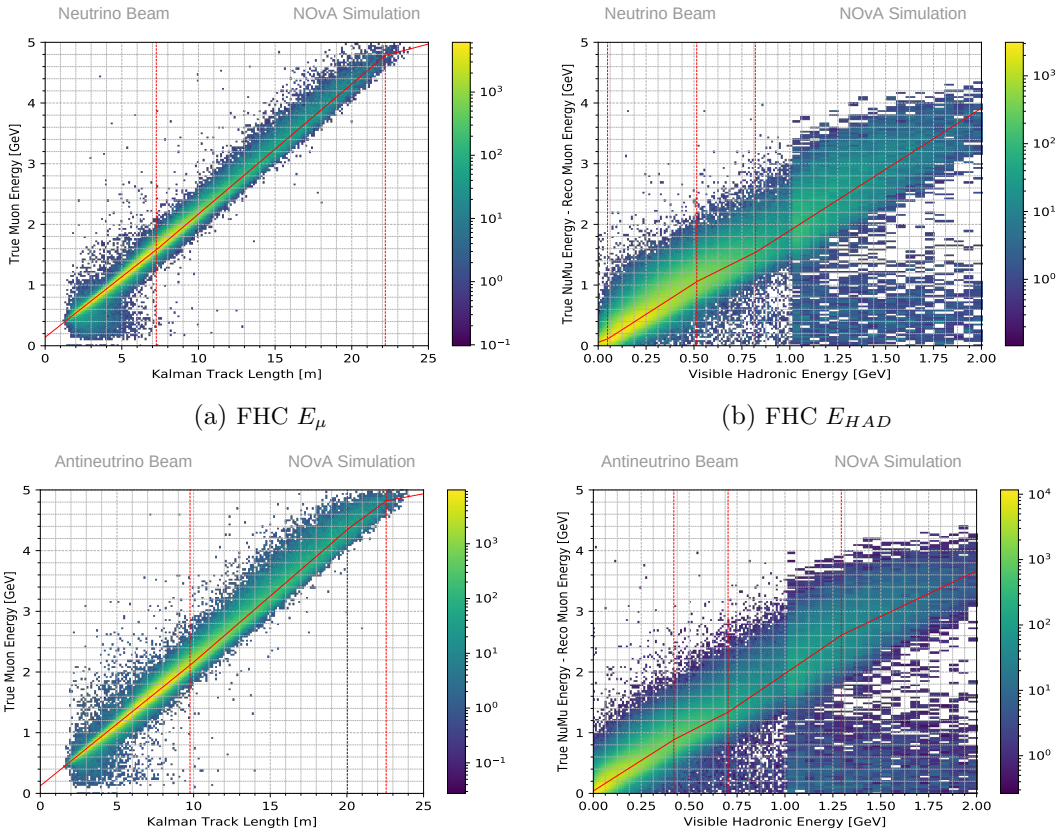

(a) FHC E_{μ}

(b) FHC E_{HAD}

(c) RHC $E_{\bar{\mu}}$

(d) RHC E_{HAD}

Figure 4.8: Linear spline is the red line. Red dashed lines indicate stitch points. Spline is overlaid with distribution of True Muon Energy vs Kalman Track Length for FHC(a) and RHC (c) or True Numu Energy - Reco Muon Energy) vs (Visible Hadronic Energy) (b) for FHC and (d) for RHC.

4.3.2 Electron neutrino energy reconstruction

Electron neutrino candidates are identified with the use of event-level CVN score. After reconstruction, ProngCVN is used to identify electromagnetic-like prongs, and distinguish them from the hadronic activity. The identity of each prong is specifically determined by calculating an EM score: adding the electron, photon and π^0 CVN scores, and a hadronic score using the sum of the proton and $\pi^{\pm}$ CVN scores. The larger of the EM or hadronic scores is chosen to classify them as EM or not. The total energy of the incident ν_e or $\bar{\nu}_e$ is calculated using the following expression:

$$E_\nu = \alpha_0(\alpha_1 E_{EM} + \alpha_2 E_{HAD} + \alpha_3 E_{EM}^2 + \alpha_4 E_{HAD}^2) \tag{4.2}$$

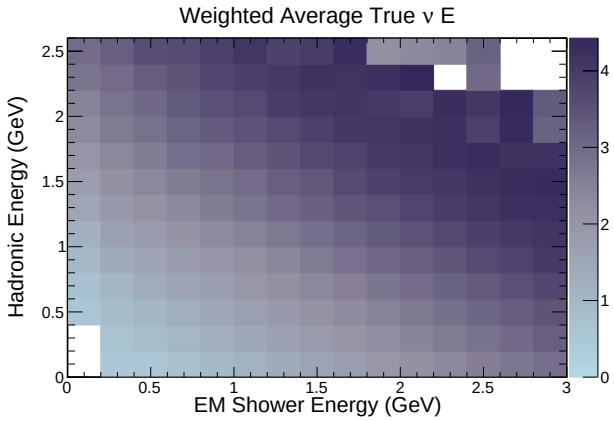

Figure 4.9: Distribution of E_{HAD} versus E_{EM} for simulated ν_e events from the neutrino beam mode. Color denotes the average true neutrino energy re-weighted to a flat flux.

E_{EM} is the sum of the calibrated energy deposits of EM prongs, and E_{HAD} the total energy of the slice minus E_{EM}. The constants α_i are fitted minimizing the variance of reconstructed neutrino energy from true neutrino energy in simulation. An additional consideration is that the simulated flux of ν_e peaks at 2GeV, if using this flux directly, the estimator would be biased to reconstruct most events towards this energy peak. Therefore the neutrino energy is re-weighted such that the fit has a flattened energy flux, shown in Figure 4.9, as input before fitting the quadratic equation 4.2. This procedure yields an energy estimation that is unbiased , and with

relatively flat resolution, across most of the energy range of interest, 1–4GeV, as shown in Figures 4.10 and 4.11. Neutrino and antineutrino functions are determined separately: the average energy resolution at the FD is 10% for the neutrino beam mode and 9.1% for antineutrino beam.

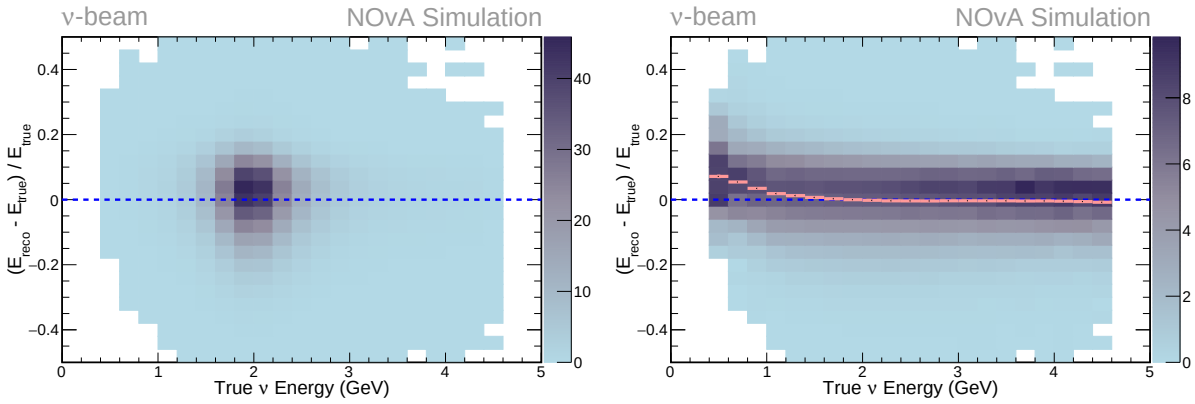

(a) (b)

Figure 4.10: Results of the ν_e energy estimator. Energy resolution vs true neutrino energy is shown with bias (a) and with true energy re-weight, pink line shows the mean in each bin (b).

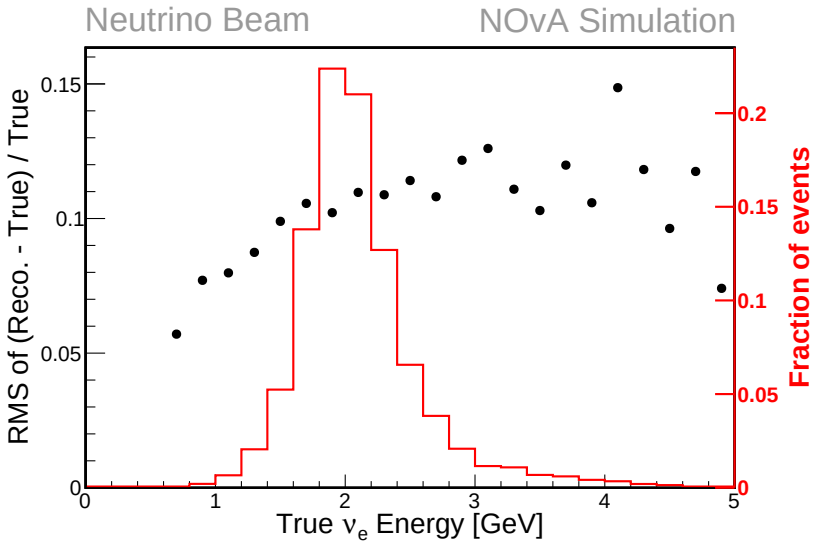

Figure 4.11: Results of the ν_e energy estimator: RMS of the energy resolution as a function of true neutrino energy where the red histogram shows the simulated neutrino flux. Both plots show the FD energy estimator trained on the neutrino beam mode sample.

4.4 Near and Far detector neutrino selections

The estimation of 3-flavor neutrino oscillation parameters relies on optimally selecting the events likely to be ν_μ or ν_e as well as estimating their energy. In NOvA, the selection of events consists on multiple *cuts*, or selection criteria, based on four functions, (quality, containment, cosmic rejection/ rock veto, and particle identification) which are tuned according to the type of neutrino (ν_e or ν_μ) and the detector [88].

Quality criteria In general, the quality cuts ensure that the beam was delivered as expected, detector was working properly and some basic criteria regarding reconstruction. This means removing events with problems in one or more DCMs (such as dropped DCMs, or out of sync). Additional cuts account for the timing of the beam spill, the current of the horn, the beam position relative to the target, and the width of the beam in x and y directions. The basic reconstruction cuts ensure that a vertex, a prong or track (depending on the neutrino type) is present in the slice. In addition slices with very few hits are removed.

Containment These cuts ensure that the energy deposited by all the products of a neutrino interaction is within the volume of the detector, in order to determine the total energy of the incident neutrino as accurately as possible. In addition, this helps to identify tracks that correspond to cosmic and rock muons in the FD and ND respectively.

The specific criteria for each detector and selection for rock veto, cosmic rejection and particle identification are described next. An overview diagram of the ν_e and ν_μ selections is shown in Figure 4.12.

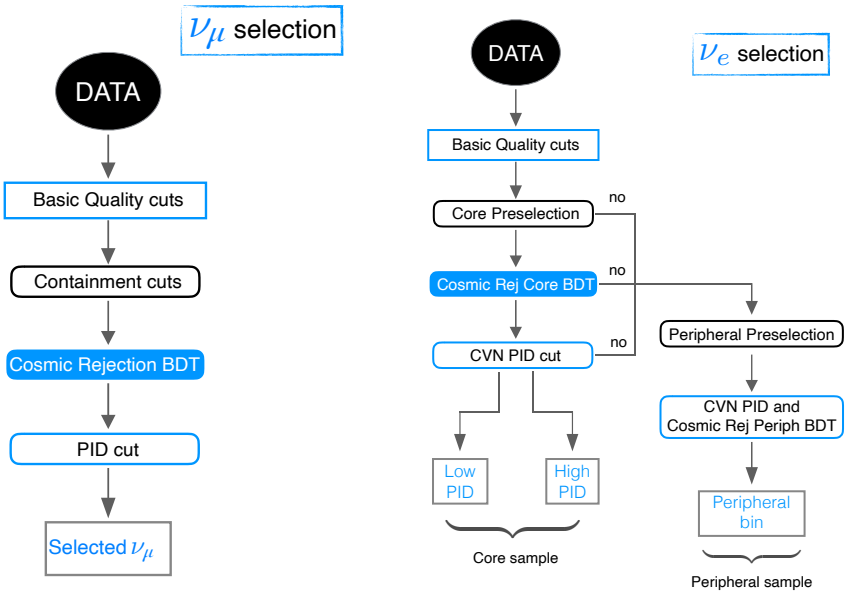

(a) (b)

Figure 4.12: Diagram of the two FD selection cut flows, from [89]. The ND ν_μ selection follows the same sequence, swapping cosmic rejection for the ND rock veto.

4.4.1 Far Detector selection

There are four selected samples at the Far Detector. As NOvA measures ν_e and $\bar{\nu}_e$ appearance as well as ν_μ and $\bar{\nu}_\mu$ disappearance, there are different selection criteria for each flavor sample. Note that the same criteria applies for neutrinos and antineutrinos, as NOvA can not distinguish the charge of the leptons.

The cosmic veto is the same for ν_μ and ν_e FD selections. As the rate of cosmic events is much higher than the neutrino interactions of interest, it would result computationally expensive to process the cosmic tracks through the whole reconstruction chain. Therefore it is preferred to remove this events before processing. This is achieved using the CNN cosmic veto or filter described in section 4.2. In addition the ν_e and ν_μ selections use a custom BDT for additional rejection of muon-like tracks that were not caught and removed by the CNN filter. The BDT

inputs are specific for the ν_e and ν_μ selection. The containment cuts specific for ν_e and ν_μ selections aim to remove the remaining slice activity from cosmics.

ν_e selection

The FD ν_e selection is divided into a core and peripheral selection. The core sample selects contained events separated into low and high Particle Identification (PID) regions. The peripherial sample accounts for uncontained events. This criteria is chosen in order to maximize the number of selected ν_e interactions, given that most ν_μ from the beam would have oscillated into ν_τ, so the rate of ν_e at the FD is actually quite low.

As mentioned above, the cosmic BDT takes specific variables to reject cosmic tracks. For the core sample, the reconstructed variables used are [90]:

- Number of hits in the event.
- p_T/p: fraction of the reconstructed momentum transverse to the beam direction.
- Sparsness asymmetry, which calculates the direction of the EM shower development determined by the relative hit density between the upstream and downstream ends of the slice.
- Minimum distances of any prongs start or end point to each side of the detector.
- Inelasticity, defined as $1 - E_{\text{shw}}/E_\nu$ or the proportion of the energy in the slice that corresponds to the identified electron shower.
- Width of the EM shower in the event.

The peripheral sample has a smaller set of input variables:

- $p_x/p, p_y/p$: reconstructed momentum in the vertical and horizontal directions transverse to the beam direction.
- Distance from the start or end position of any prong to the top of the detector.

- Event vertex location.

In addition , the containment criteria selects events with activity closer than 63 cm from the detector top, 12 cm from the bottom, east or west and 18 cm from the front or back are rejected from the core samples. With regards to the PID, slices with cosmic BDT greater than 0.49 (0.47) for FHC(RHC) are selected towards the core sample. The peripheral selection employs a separate cosmic BDT and events passing the threshold of 0.56 (0.57) are selected. The high PID selection picks events with CVN$\geq$0.97. The low PID selection accepts events between 0.84(0.85)$\leq$CVN$<$0.97. The peripheral bin cut is tighter, at $\geq$0.995.

ν_μ selection

The BDT for ν_μ samples evaluate the most muon-like track in the event using information from the following variables [91]:

- Cosine of the track angle with respect to beam direction
- Cosine of the track angle with respect to the vertical
- Highest vertical position of start or end of the track
- Track distance of closest approach to each side of the detector.
- Ratio of the number track hits to total hits in the slice.
- p_T/p: fraction of reconstructed transverse momentum relative to the beam direction.

The containment criteria selects events with prongs closer to 60, 12, 16, 12, 18 and 18 cm from the top, bottom, east, west, front and back detector sides respectively are rejected. In addition there must be no hits in the front and back detector planes.With respect to PID, the slices with a CVN muon identification score larger than 0.8, a ReMId score greater than 0.30, and a cosmic BDT score greater than 0.45 are accepted. This criteria is used for both ν_μ and $\bar{\nu}_\mu$ selections.

4.4.2 Near detector selection

The ν_μ ND selection is very similar to the FD selection, as its main feature is looking at the muon tracks. Instead of rejecting cosmics, the major background is the muons originating from neutrinos interacting with the surrounding rock. This is done using the rock veto described in section 4.2.

- Containment: All activity must be within the ranges $-180 < \{X, Y\} < 180$ cm and $20 < Z < 1525$cm. Also, only one track can enter the muon catcher and the event vertex cannot be located there. Any events with tracks that cross the air gap due (or Y position of the end of track < 55cm) to the differing muon catcher height are rejected. The kalman tracks are projected forwards and backwards from their end and start points: the projected track must cross more than 5 planes from the end point and more than 10 planes from the start point before reaching any detector edge to be accepted.

- PID: Same criteria as the FD ν_μ samples.

4.5 Near Detector topology selections

The Near Detector neutrino and antineutrino datasets are very large samples that have been used in NOvA's 3-flavor oscillation analysis to constrain the Far Detector predictions. This constrain depends on the ND sample having good agreement with the ND data, so it can accurately predict the FD spectrum. The ND simulation undergoes several adjustments to match the data, with the largest one done by modifying certain aspects of the cross section model, as it was describer in chapter 3. In the most recent 3flavor analysis [10], the ND data set was used to enhance the 2p2h contribution of the simulation. Without this adjustment, the simulation would show a large underprediction of events.

The tuning of 2p2h is made independent of other parameters in the cross section model and the uncertainties constructed are conservative as the exact interaction between the 2p2h and other cross section parameters has not been thoroughly understood.

As the overall agreement with the cross section adjustments is very good (yet not perfect throughout the whole phase-space), as seen in Figure 3.13, one way of further understanding the applied NOvA tune, is to subdivide the ND selection into samples that have different characteristics. A large data set, such as the ND $\nu_\mu + \bar{\nu}_\mu$ selection, has enough statistics ($\mathcal{O}(10^6)$ events), and different types of events, to obtain more information from the cross section model and other parameters. The distributions in Figure 3.13 can be observed with a different breakdown, by the true final state, in Figure 4.13. This chapter presents the study in which this data set is broken down into subsets that target different final states. This allows to observe different levels of agreement with data as well as other interesting features for each sample.

The purpose of this samples is to use them to constrain the model parameters via a ND fit, in order to propagate them to the FD oscillation fit. Details of this technique will be described in chapters 5 and 6.

4.6 Topology samples

To further examine the NOvA interaction model, a useful tool are the topology samples. These were developed with the purpose of dividing the ND data and simulation into subsets by discriminating different final states, in order to find distinctive features in the topology of the final state. This could aid in picking apart different aspects of the interaction model. The criteria that defines each sample is the identification of particles in the final state distinguishable by the 3D prong multiplicity and their *prongCVN* score. A prong is a collection of hits in the same time slice that are associated to a single particle that deposited this energy. The CVN score details were described in section 4.2.

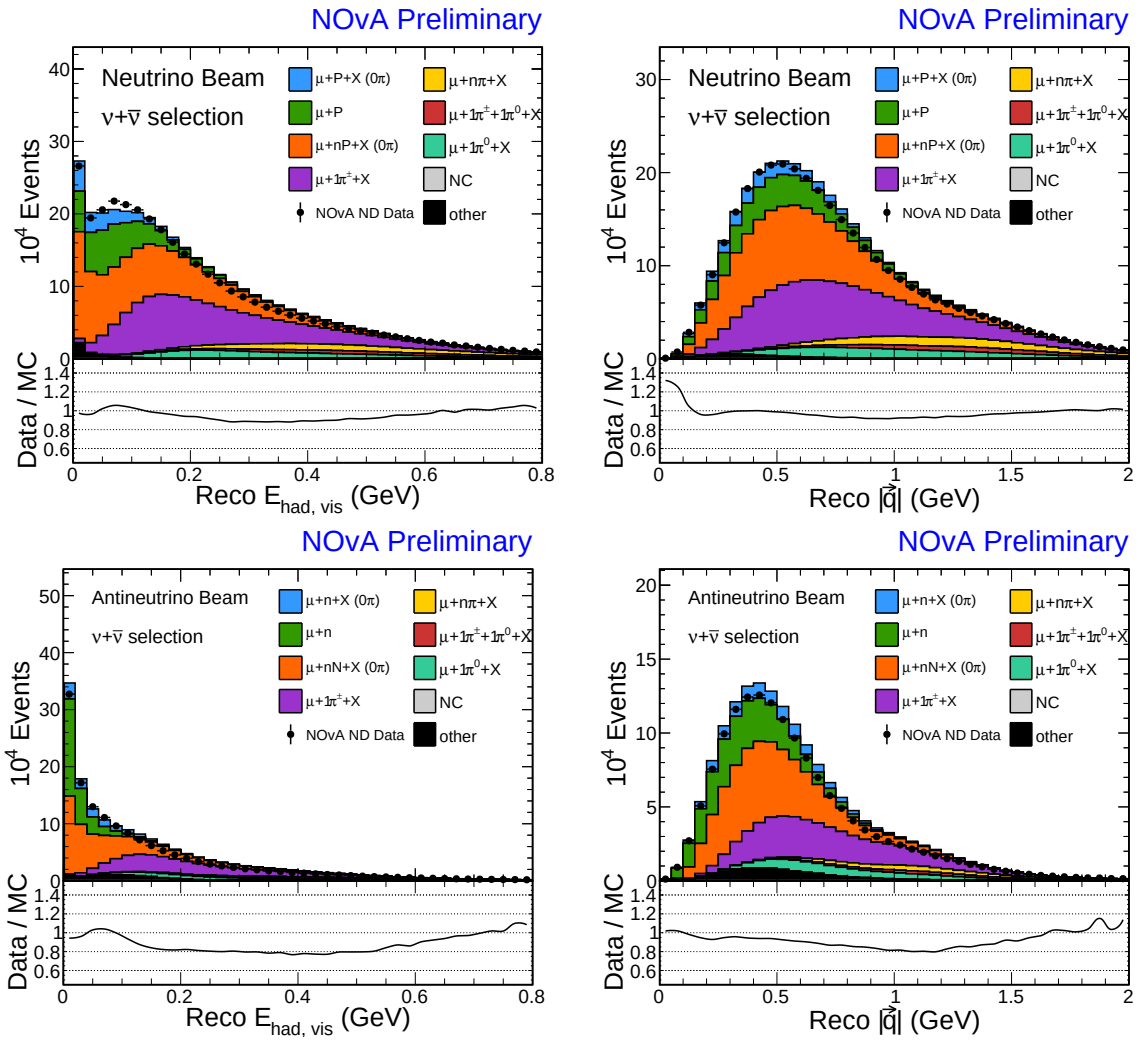

Figure 4.13: Neutrino(left) and antineutrino (right) beam distributions of $E_{had,vis}$ and $|\vec{q}_{reco}|$ with true final state categories breakdown.

Five topologies are defined for each beam mode. Their prong multiplicity and CVN score are summarized in table 4.1. The only difference of RHC with respect to the FHC samples is the $\mu + p + X(0\pi)$ classification. For RHC, this selection would yield a very low statistics sample. Therefore it was modified to not require a proton, fewer protons are expected antineutrino interactions. Essentially the selections divide the FHC and RHC datasets into five subsets of one

(muon), two (muon and proton), and three or more (muon and pion, protons, or other) distinguishable particles, as is pictured in Figure 4.14.

Table 4.1: Topology samples definition

Sample	**3D prong multiplicity**	**CVN score criteria**	**Notes**
μ	1	$\text{CVN}_\mu \geq 0.5$ or prong length $\geq$ 500cm	FHC and RHC
$\mu + P$	2	$\text{CVN}_\mu \geq 0.5$ or prong length $\geq$ 500cm $\text{CVN}_p \geq 0.5$	FHC and RHC
$\mu + P + X$	3 or more	$\text{CVN}_\mu \geq 0.5$ or prong length $\geq$ 500cm $\text{CVN}_p \geq 0.5$	FHC only
$\mu + X$	3 or more	$\text{CVN}_\mu \geq 0.5$ or prong length $\geq$ 500cm	RHC only
$\mu + \pi^\pm + X$	2 or more	$\text{CVN}_\mu \geq 0.5$ or prong length $\geq$ 500cm $\text{CVN}_\pi \geq 0.7$	FHC and RHC
Remaining FHC	any	Not fitting into previous categories	
Remaining RHC	any	Not fitting into previous categories	

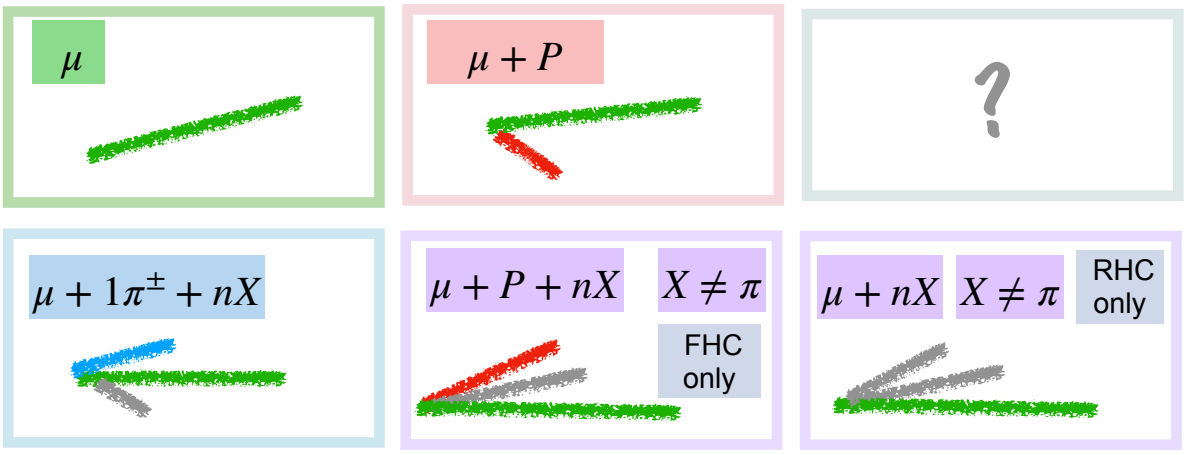

Figure 4.14: Cartoon that illustrates the expected topology for each cut. The green lines represent muon prongs, the red lines proton prongs, the blue lines pion prongs, and the gray lines are not identifiable 3D prongs, according to their CVN scores.

The samples have the following overall characteristics. Such features can be observed in figures 4.16 thorugh 4.19, and in tables 4.2 through 4.5.

- $\boldsymbol{\mu}$: Enhanced in QE and MEC interactions. Shows good agreement for both FHC and RHC modes, and these are the largest samples. It contains the least amount of true final states with pions.

- $\boldsymbol{\mu + P}$: QE and MEC enhanced. Shows a slight overprediction for both beam modes. It is dominated by interactions with multiple protons in the true final state. It also contains a significant amount of events with one charged pion in the true final state.

- $\boldsymbol{\mu + \pi^{\pm} + X}$: RES dominated and DIS enhanced. Slightly underpredicted for both FHC and RHC. It is the smallest RHC sample. In both beam modes, the sample has a high purity, as it is dominated by interactions with one charged pion in the true final state.

- $\boldsymbol{\mu + P + X}(0\pi)$: RES dominated and DIS enhanced. Large overprediction. It is the smallest FHC sample. Interestingly, it contains a large amount of interactions with final states with multiple pions, even though it contains a CVN score criteria to reject pions.
- $\boldsymbol{\mu + X}(0\boldsymbol{\pi})$: RES dominated and DIS enhanced. Large overprediction. Has a noticeable QE/RES content, and a large amount of events with true final states with one or more pions.
- **Remaining**: Better agreement with data for RHC than FHC. Mixture of all interaction type categories and true primaries categories.

There are two breakdowns used to display the samples, shown in Figure 4.15 including both the breakdown by interaction type and primary particles categories. Both categories are defined directly by the GENIE simulation. The primary final states categories are obtained according to the simulated particles resulting from the neutrino interaction, after FSI. No reconstructed information is used to define this categories.

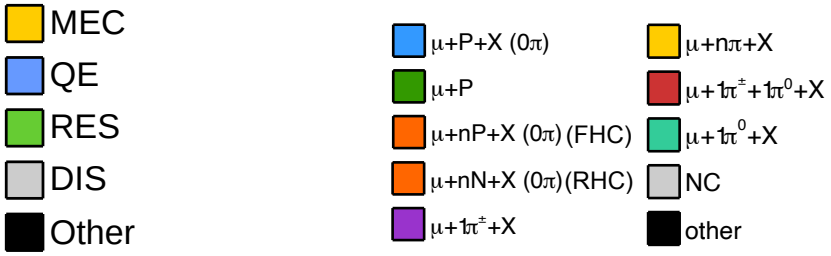

(a) Interaction type categories (b) Primary particles categories

Figure 4.15: Two categorizations by primary final states and neutrino interaction types

Note that for the primary particles categories, depending on the beam, one of the categories is $\mu + nP + X$ ($\mu + nN + X$) for FHC (RHC). The nP (nN) denotes any number of protons (neutrons), greater than one.

More detail about each sample is described in the following sections. The variables used to examine each sample are related to the observables for the individual prongs.

Table 4.2: Composition of FHC samples in categories of interaction type

Int. type %	μ	$\mu + P$	$\mu + P + X$	$\mu + \pi^{\pm} + X$	Remaining
QE	34.6	25.0	2.91	6.00	12.4
MEC	27.0	13.8	2.53	2.96	10.6
RES	30.5	50.0	62.4	59.6	50.9
DIS	6.33	10.8	31.5	27.4	24.8
Other	1.58	0.44	0.51	4.04	1.30

Table 4.3: Composition of RHC samples in categories of interaction type

Int. type %	μ	$\mu + P$	$\mu + X$	$\mu + \pi^{\pm} + X$	Remaining
QE	44.4	31.6	8.58	4.56	26.8
MEC	28.6	23.4	6.40	0.88	15.3
RES	20.3	34.6	59.2	58.0	39.5
DIS	4.80	9.90	24.1	26.3	15.5
Other	1.86	0.99	1.66	10.3	2.95

Table 4.4: Composition of FHC samples in categories of simulated primary particles in the final state category

Final State particles	μ	$\mu + P$	$\mu + P + X$	$\mu + \pi^{\pm} + X$	Remaining
$\mu + P + X$ (0π)	7.93	3.82	2.40	1.38	4.42
$\mu + P$	18.9	16.3	0.86	3.82	5.96
$\mu + nP + X$ (0π)	43.9	42.2	23.9	8.40	27.2
$\mu + 1\pi^{\pm} + X$	23.2	29.9	27.7	65.3	32.3
$\mu + n\pi + X$	1.19	3.07	12.3	11.2	9.84
$\mu + 1\pi^{\pm} + 1\pi^{0} + X$	0.48	0.89	8.95	4.57	5.72
$\mu + 1\pi^{0} + X$	2.25	3.07	22.5	3.96	12.2
NC	0.20	0.25	0.48	0.43	0.62
Other	1.97	0.54	0.88	0.88	1.65

Table 4.5: Composition of RHC samples in categories of simulated primary particles in the final state category

Final State particles	μ	$\mu + P$	$\mu + X$	$\mu + \pi^{\pm} + X$	Remaining
$\mu + P + X$	9.29	7.67	2.32	0.70	4.50
$\mu + P$	27.3	16.0	2.85	0.32	16.1
$\mu + nN + X$ (0π)	38.8	42.2	30.4	4.12	27.2
$\mu + 1\pi^{\pm} + X$	14.8	22.3	27.8	71.3	26.4
$\mu + n\pi + X$	0.72	2.02	8.74	9.83	4.91
$\mu + 1\pi^{\pm} + 1\pi^{0} + X$	0.32	0.62	5.92	4.39	3.21
$\mu + 1\pi^{0} + X$	2.42	2.35	18.0	4.44	12.2
NC	0.14	0.20	0.33	0.37	0.40
Other	6.10	6.67	3.60	4.53	5.09

- **Weighted calorimetric energy**: energy based on summed calibrated deposited charge (GeV) weighted to take into account hits shared between prongs.
- **Prong length**: track length in cm.
- **Number of hits**: Number of hits that compose the 3D prong. Closely related to the prong length
- **Weighted calorimetric energy per hit**: Ratio of the variables described above. Can be thought of as a crude estimation of the dE/dx of the prong.

4.6.1 Muon sample

The μ sample selection is the simplest, as it is choosing events with a single prong associated with a muon. The distributions of hadronic visible energy and $|\vec{q}|$ show a good agreement for RHC (Figure 4.21) and slightly worse agreement in FHC (Figure 4.20). Both beam distributions are dominated by QE and MEC interactions, with a larger but subdominant RES contribution in RHC.

Figures 4.22 show the properties of the muon prong for the RHC sample. The variables of calorimetric energy, prong length and number of hits agree very well with the data, whereas the energy per hits distribution shows a slight bias of the simulation towards higher values.

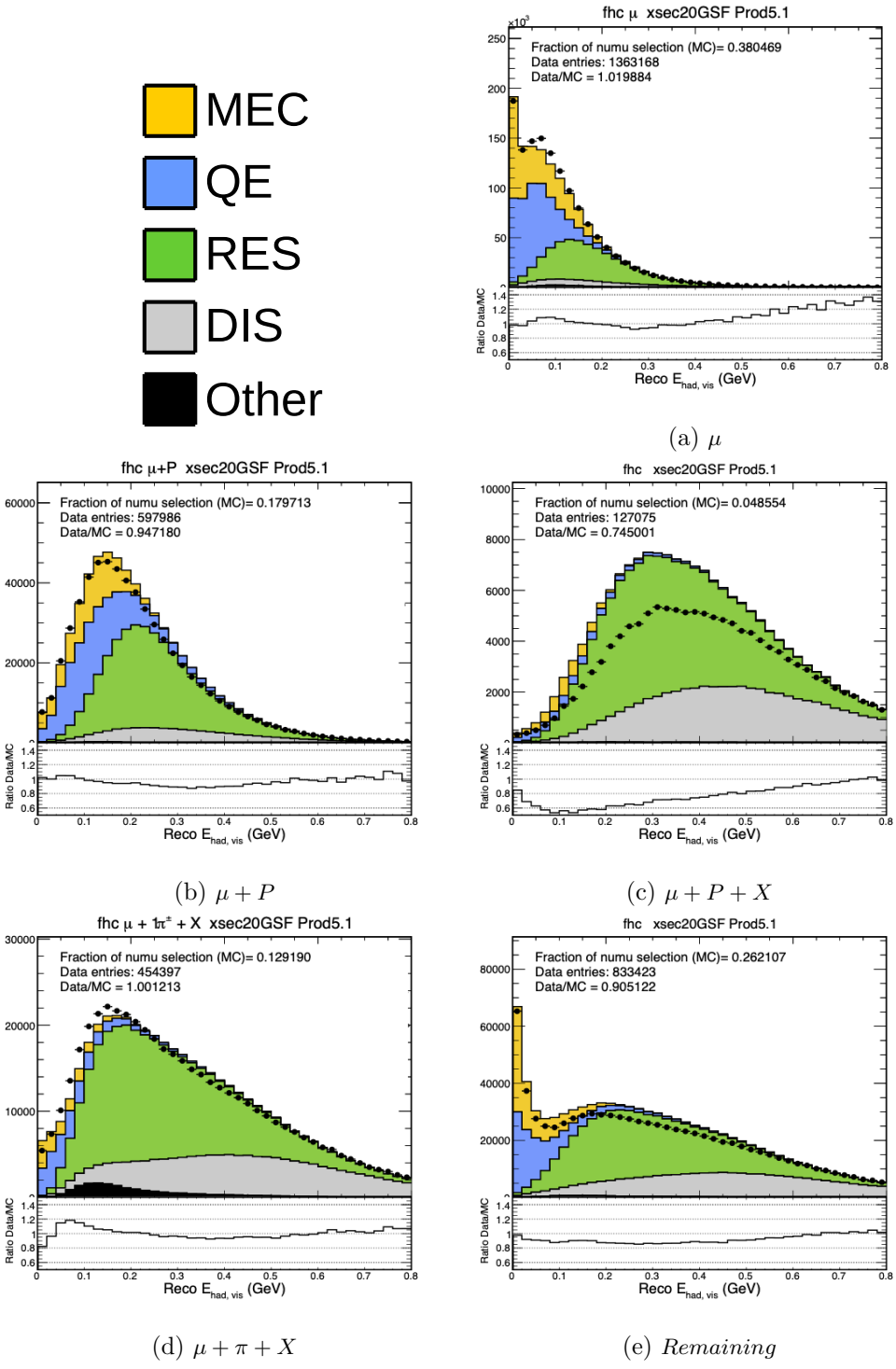

(a) μ

(b) $\mu + P$

(c) $\mu + P + X$

(d) $\mu + \pi + X$

(e) *Remaining*

Figure 4.16: FHC topologies with interaction type breakdown .

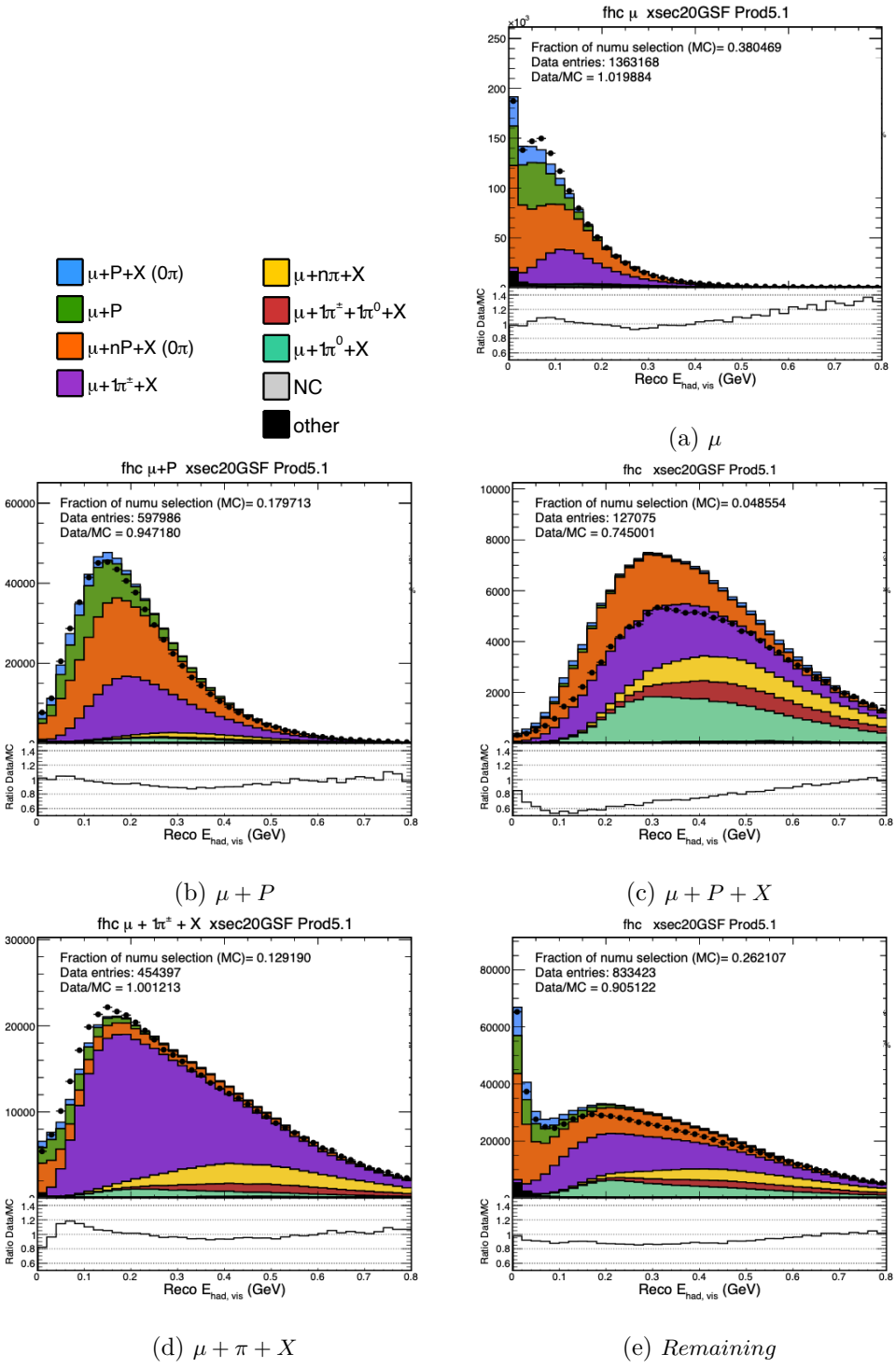

(a) μ

(b) $\mu + P$

(c) $\mu + P + X$

(d) $\mu + \pi + X$

(e) *Remaining*

Figure 4.17: FHC topologies with primaries content breakdown .

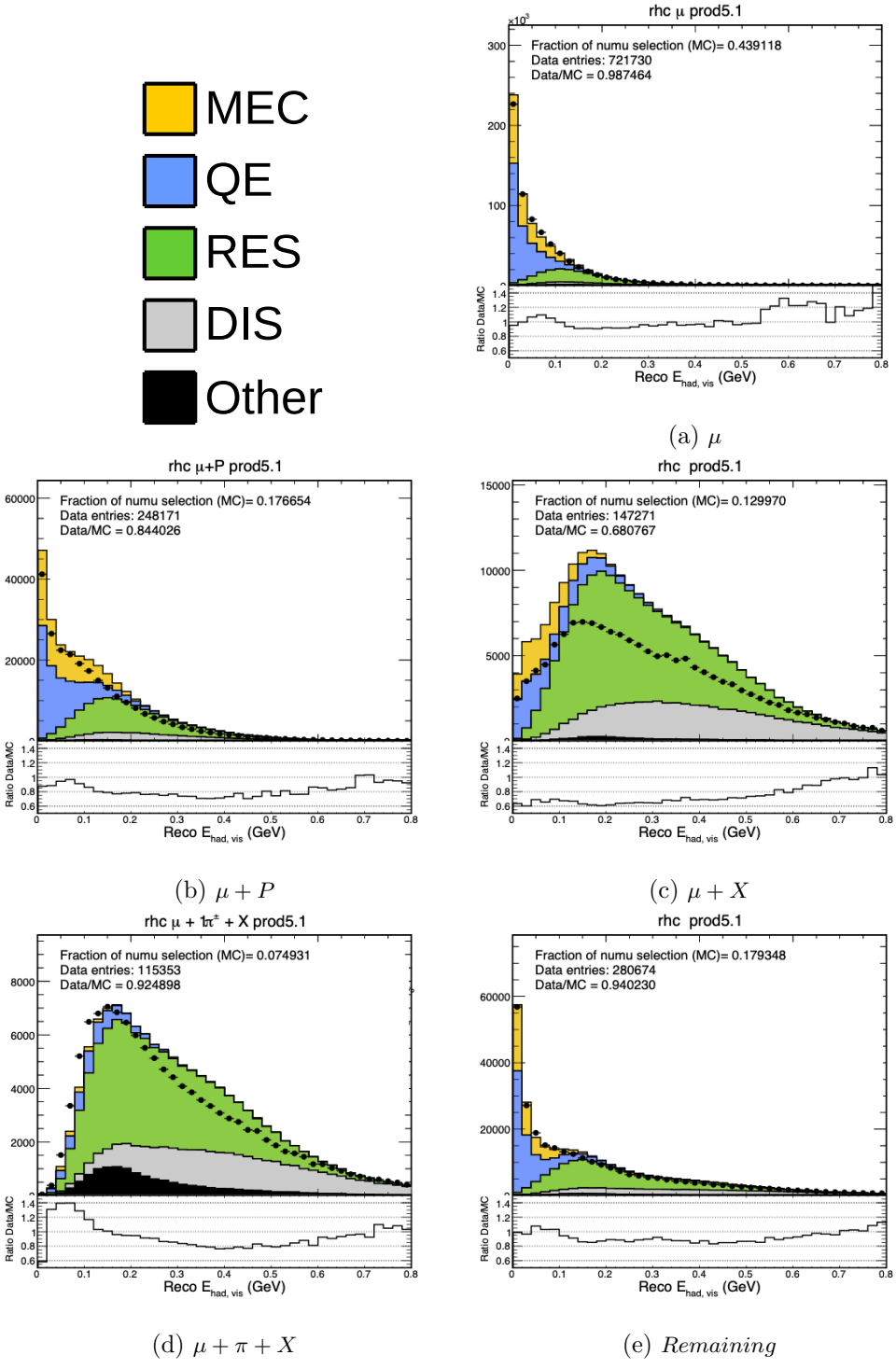

(a) μ

(b) $\mu + P$

(c) $\mu + X$

(d) $\mu + \pi + X$

(e) *Remaining*

Figure 4.18: RHC topologies with interaction type breakdown.

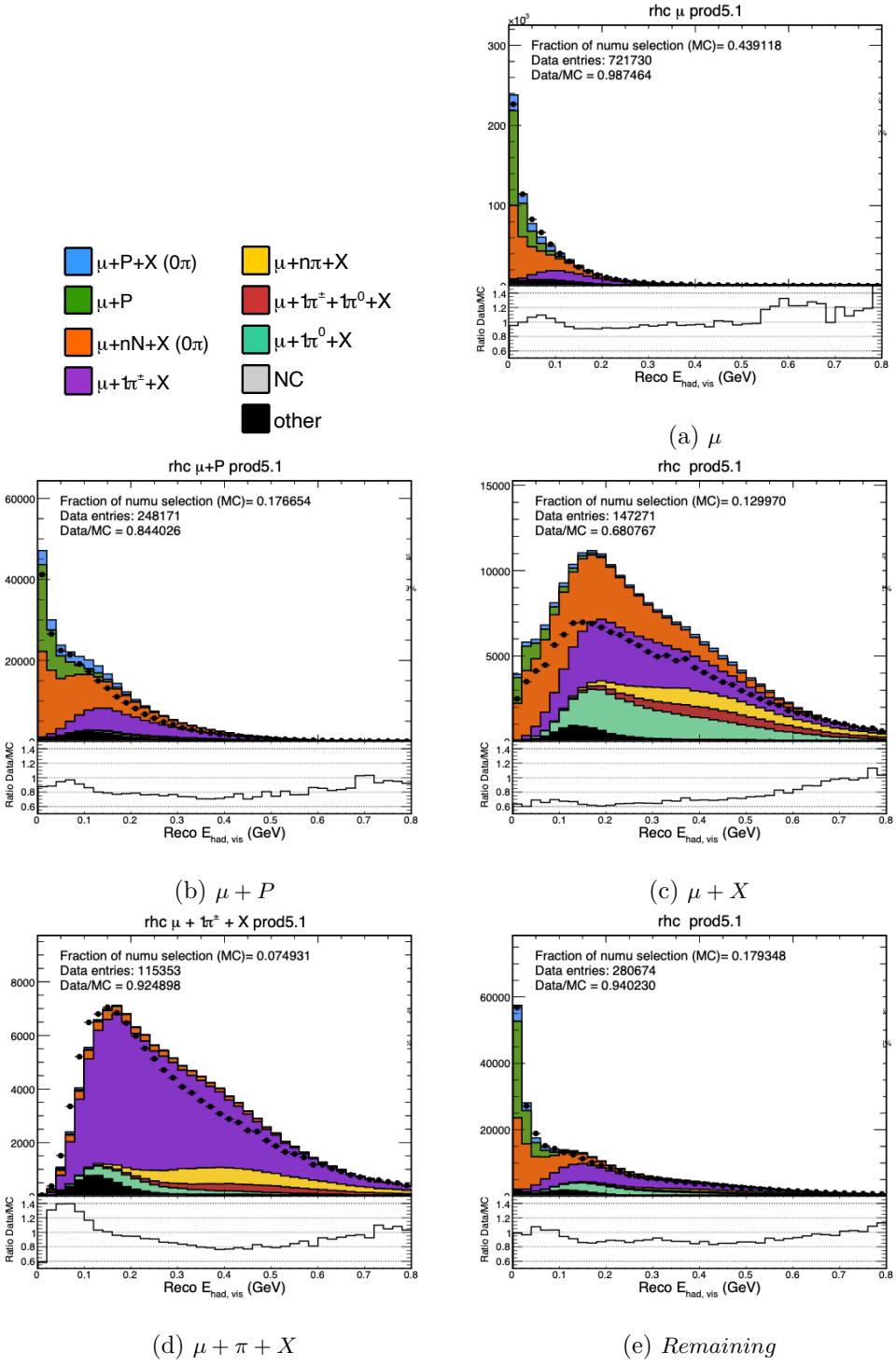

(a) μ

(b) $\mu + P$

(c) $\mu + X$

(d) $\mu + \pi + X$

(e) *Remaining*

Figure 4.19: RHC topologies with primaries content breakdown.

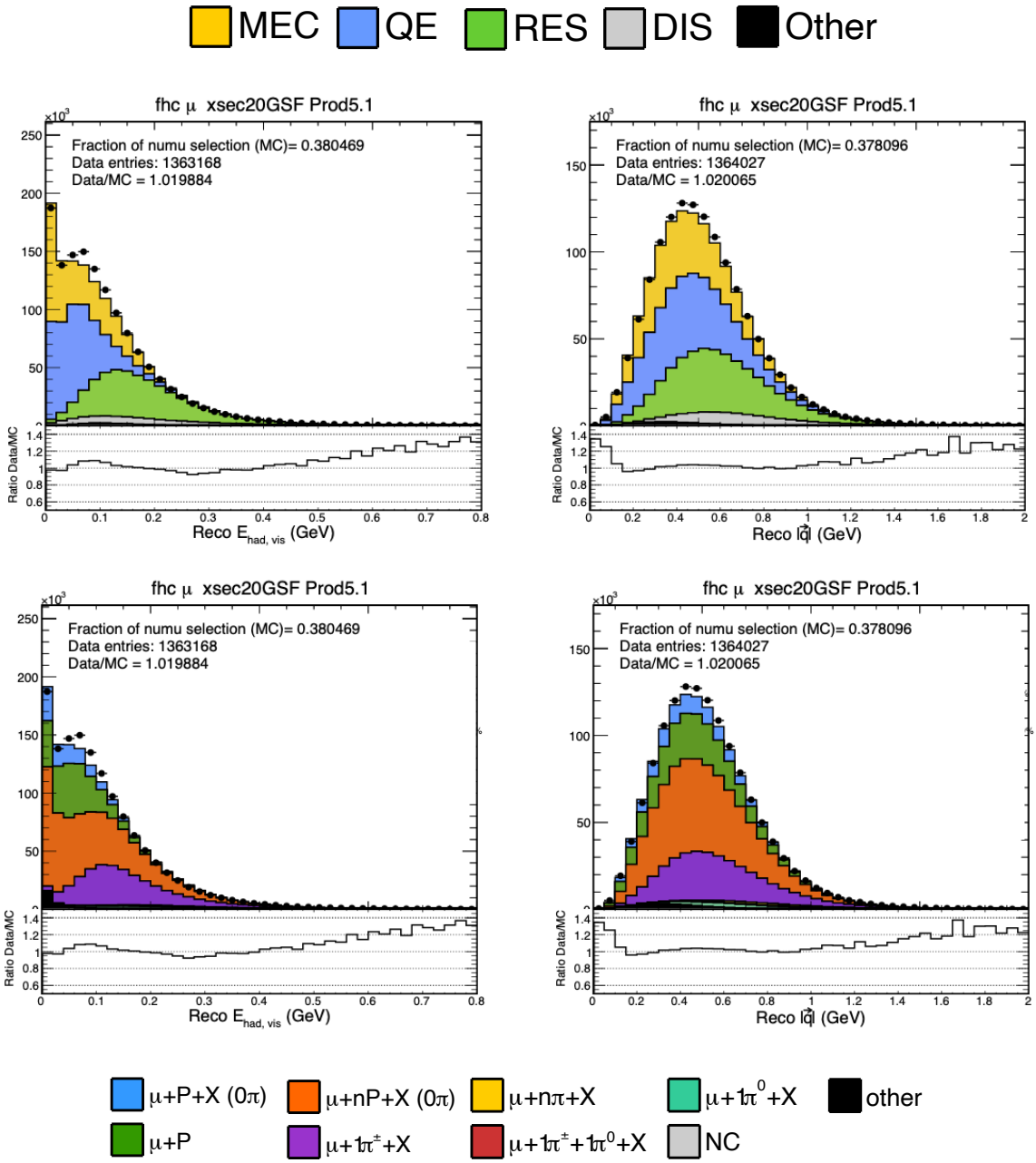

Figure 4.20: FHC distributions of visible hadronic energy (left) and reconstructed three momentum (right) with interaction type breakdown (top) and final state primaries (bottom).

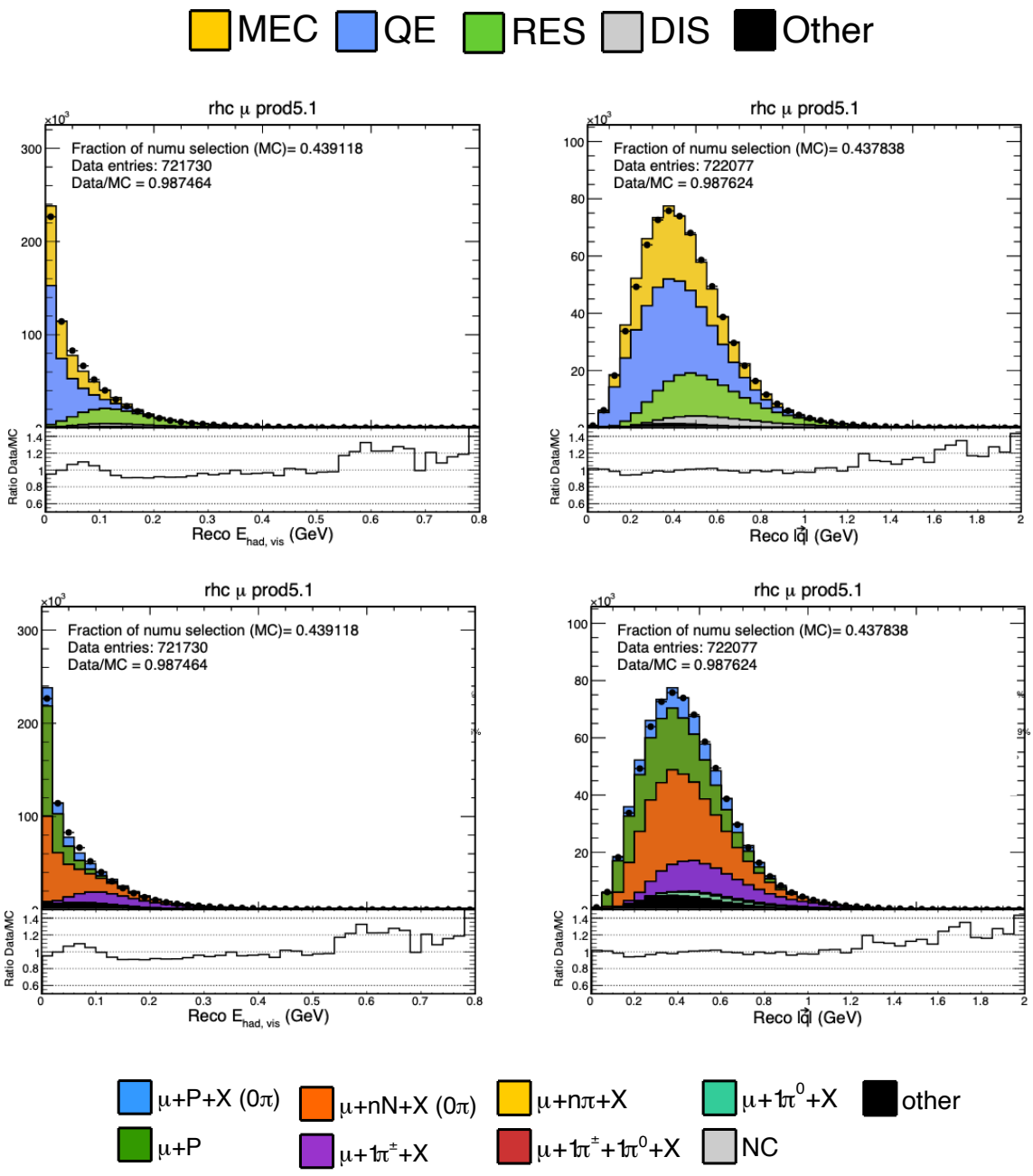

Figure 4.21: RHC distributions of visible hadronic energy (left) and reconstructed three momentum (right) with interaction type breakdown (top) and final state primaries (bottom).

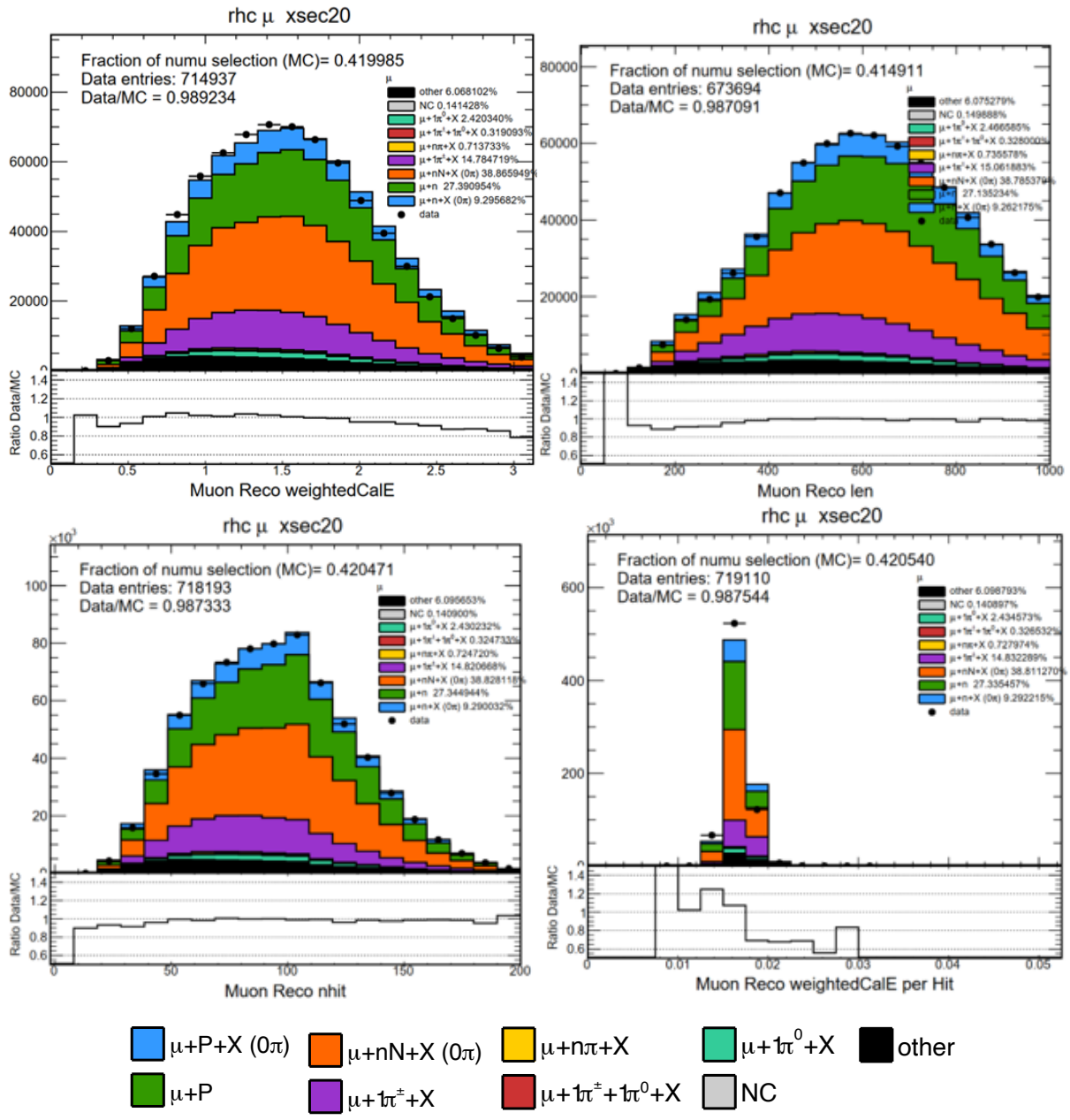

Figure 4.22: RHC distributions of weighted calorimetric energy (top left), length (top right), number of hits (bottom left), and weighted calorimetric energy per hit (bottom right).

4.6.2 Muon + Proton sample

This sample contains events with two 3D prongs, one identified as a muon and one as a proton as described in table 4.1. The agreement with data is very good for FHC, and the RHC sample is overpredicted. These samples contain a large fraction of RES interactions, but also contain a significant contribution from QE and MEC. In terms of the true final state particles, the samples are dominated by events with multiple protons (neutrons) and no pions, for FHC (RHC), which correspond to the orange contribution. These also contain a significant contribution of events with a single proton (neutron), shown in green, and with one charged pion shown as purple in the histograms.

Figures 4.23 through 4.26 show the characteristics of the muon and proton prongs for the FHC and RHC selections. The muon prong distributions are very similar for both FHC (Figure 4.23) and RHC (Figure 4.24). The RHC simulation is overpredicted with what seems mostly a normalization difference. In particular the calE/hit variable shows a bias for the muon prong, with the simulation predicting higher values than what is observed in data. This is more notorious in FHC.

For the proton prongs, the FHC distributions agree relatively well with data 4.25. The lowest bins of the number of hits and length distributions are slightly overpredicted. This is more evident for calorimetric energy. For the calE/hits distribution, the overprediction is located at the tail. In the case of RHC (see Figure 4.26, the overprediction is more notorious. The calorimetric energy distribution is quite different from FHC, with a lot of events in the first bin. In addition the calE/hits distribution is has two peaks, at 0.01 ant 0.03 GeV/cm, in contrast with FHC, which as only one peak at 0.03 GeV/cm. This lower peak is significantly overpredicted, and is dominated by the category of multiple neutrons and no pions in the final state (orange).

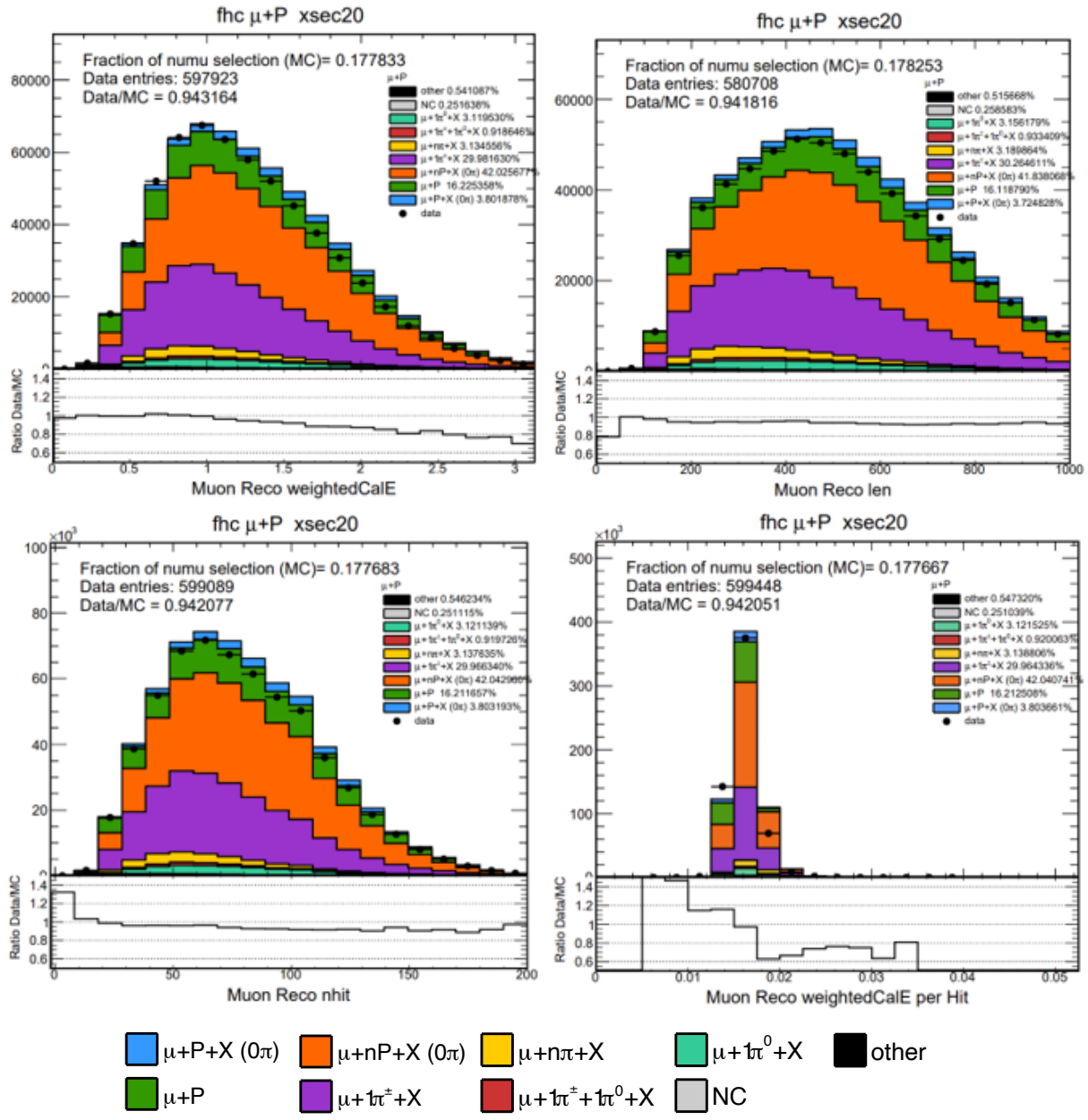

Figure 4.23: Weighted calorimetric energy, prong length, number of hits and energy per hits of muon prongs in the $\mu + P$ sample in FHC

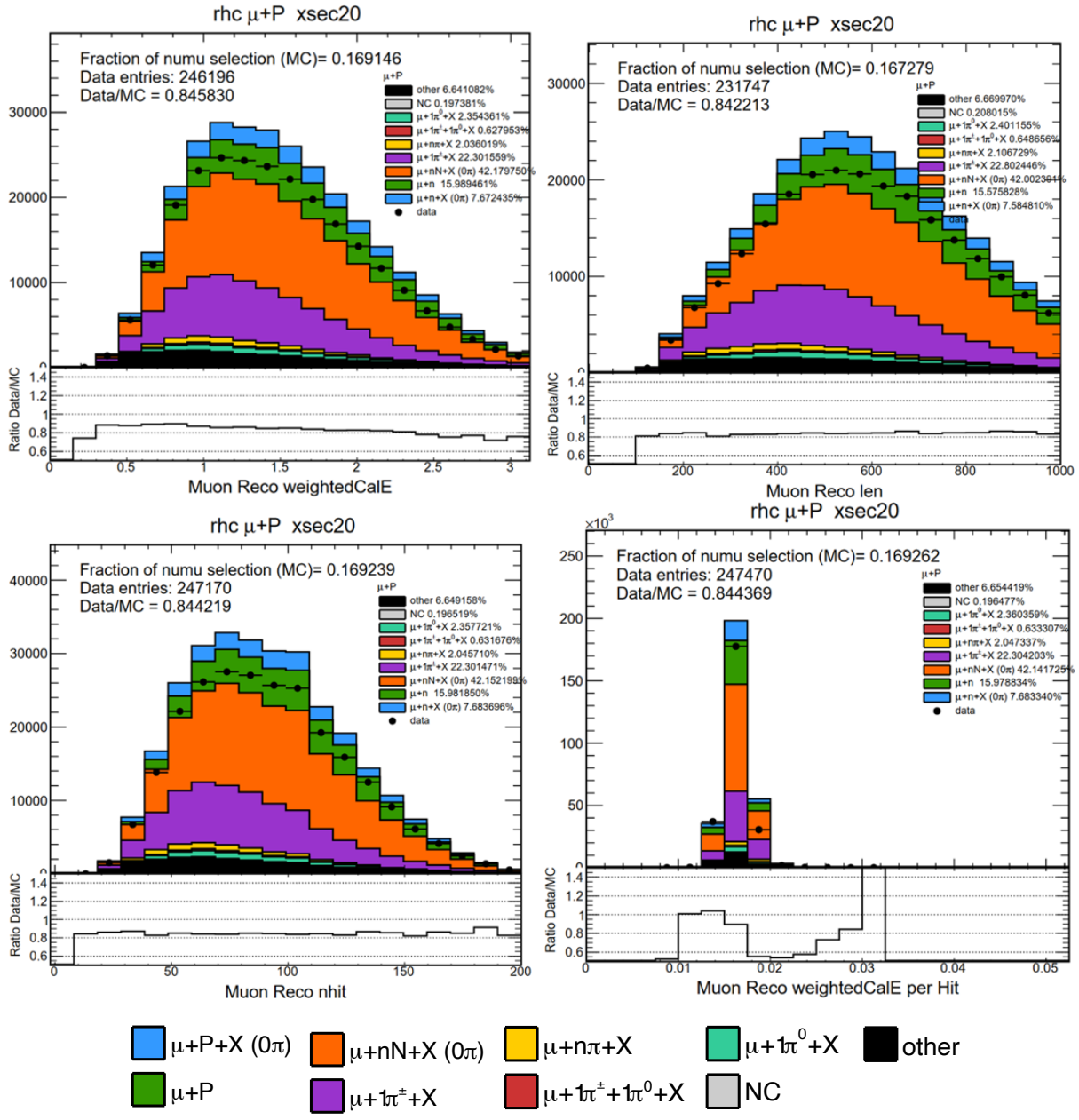

Figure 4.24: Weighted calorimetric energy, prong length, number of hits and energy per hits of muon prongs in the $\mu + P$ sample in RHC

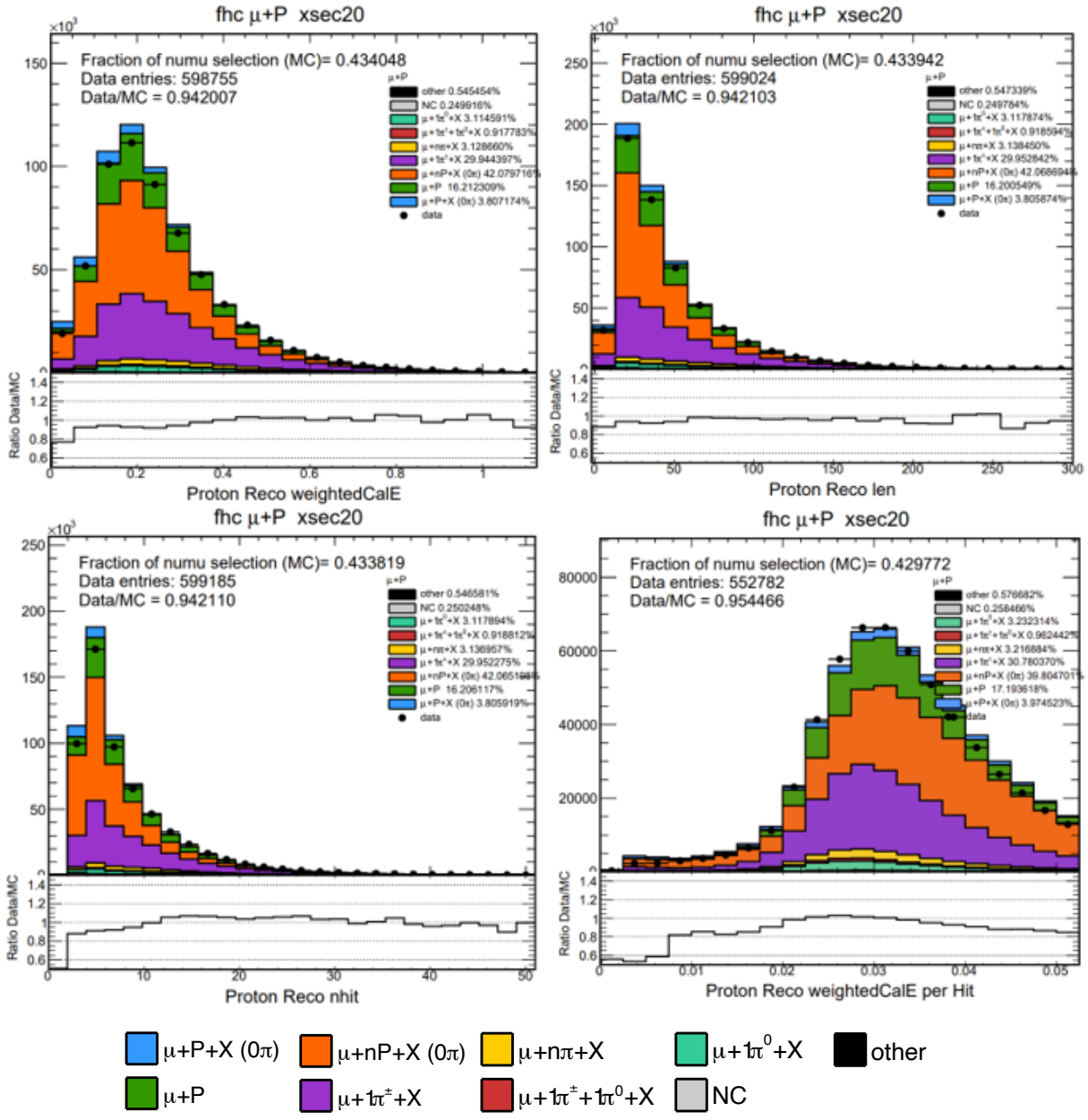

Figure 4.25: Weighted calorimetric energy, prong length, number of hits and energy per hits of proton prongs in the $\mu + P$ sample in FHC

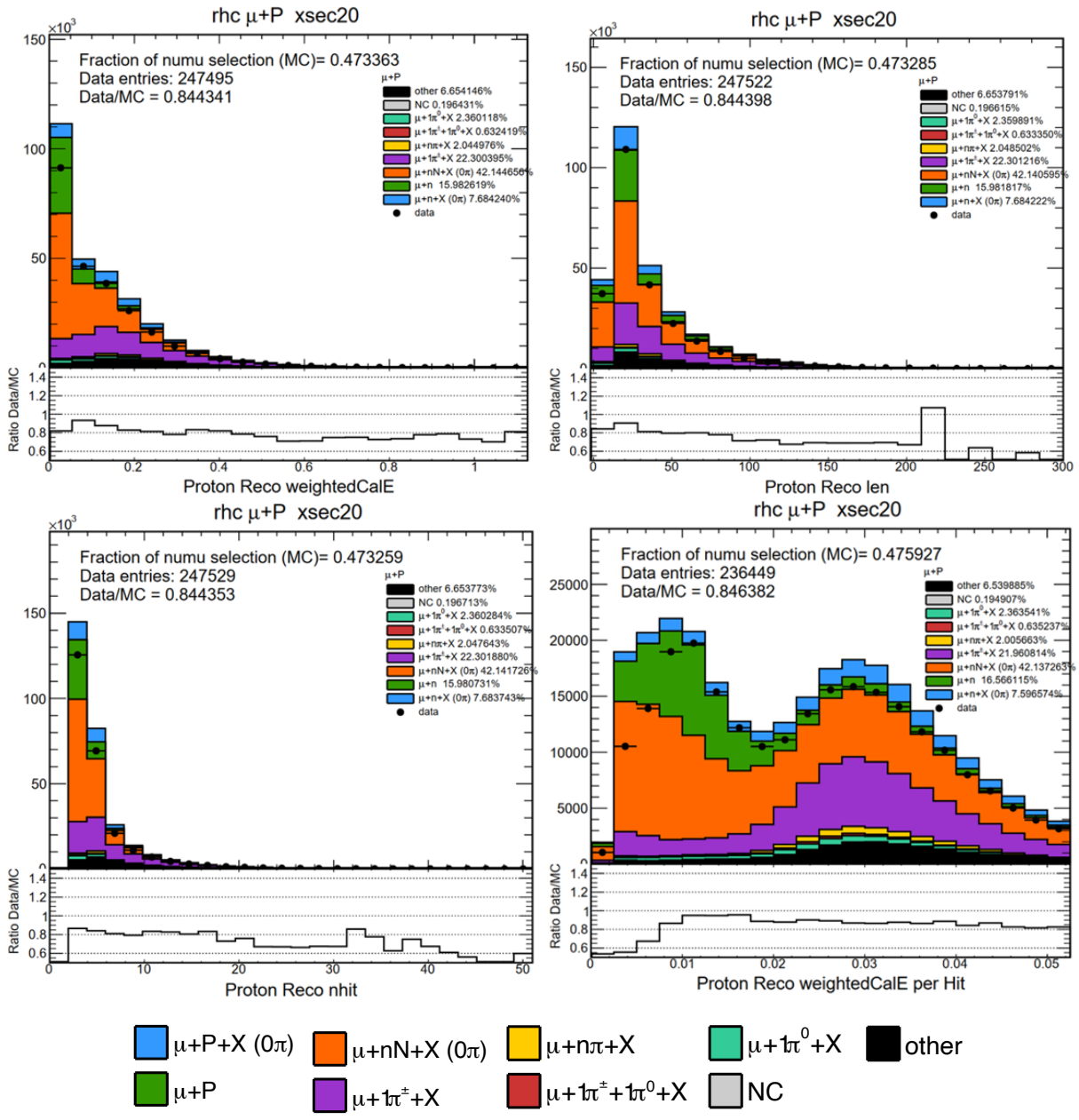

Figure 4.26: Weighted calorimetric energy, prong length, number of hits and energy per hits of proton prongs in the $\mu + P$ sample in RHC

4.6.2.1 Transverse Kinematic Imbalance

The $\mu + P$ sample is dominated by the MEC and QE interactions, which make it a good candidate to evaluate the adjustment made to 2p2h described in chapter 3.

The simple topology of two particles is useful to probe the interaction model because it allows for the reconstruction of the momentum of both particles. The momentum vector of the final state can be decomposed into longitudinal, and transverse momentum, with respect to the direction incoming neutrino. Assuming that the interaction has QE-like kinematics, the total transverse momentum vector should be close zero. This means all the momentum is transferred to the outgoing particles. However, in real neutrino-nucleus scattering there is an imbalance, $\delta\vec{p}$, between the neutrino and the outgoing lepton and hadron as a result of nuclear effects. This imbalance is the sum of Fermi motion and other effects including nucleon correlations and FSI[92]. Quantities based on these transverse momentum have been used by other neutrino experiments, such as T2K [93] and MINERvA [94] to study deficiencies in the neutrino interaction models.

Four of the Transverse Kinematic Imbalance (TKI) variables are pictured in Figure 4.27, where $\vec{p}_T^{\,p}$and $\vec{p}_T^{\,\mu}$are the components of proton and muon momenta in the plane perpendicular to the neutrino direction. The proton transverse momentum is decomposed along x and y axis $(\delta p_{Tx}, \delta p_{Ty})$:

$$\delta\vec{p}_T \equiv \vec{p}_T^{\,p} + \vec{p}_T^{\,\mu} \tag{4.3}$$

$$\delta\alpha_T \equiv \arccos\left(- \hat{p}_T^{\mu} \cdot \delta\hat{p}_T^{\mu}\right) \tag{4.4}$$

$$\delta p_{Tx} = \left(\hat{p}_\nu \times \hat{p}_T^{\mu}\right)\delta\vec{p}_T \tag{4.5}$$

$$\delta p_{Ty} = -\hat{p}_T^{\mu} \cdot \delta\vec{p}_T \tag{4.6}$$

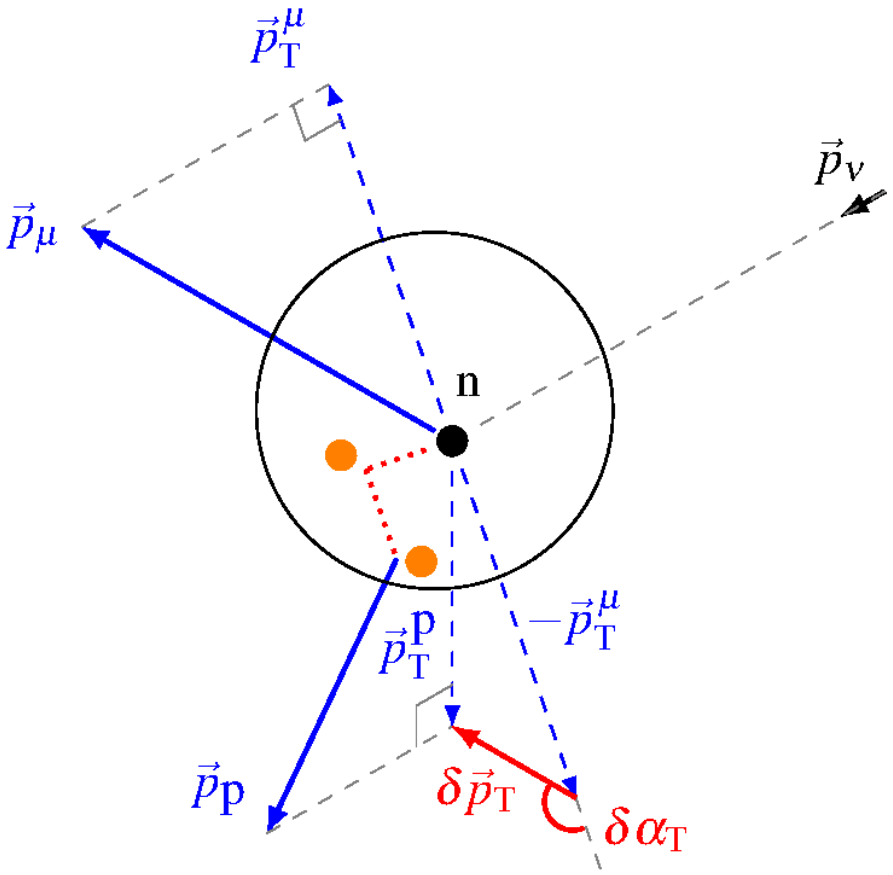

Figure 4.27: Schematic definition of the transverse kinematics. taken from [92].

The shapes of δp_{Tx} and δp_{Ty} are affected by nuclear effects. For QE δp_{Tx} is expected to be symmetric around zero. The distributions of $\delta\alpha_T$ and $\delta\vec{p}_T$ provide insight into nuclear effects affecting the cross section, such as FSIs, the Fermi motion and 2p2h processes [94][92].

The TKI variables are not directly related to the $(|\vec{q}|, E_{had,vis})$, phase space used for the tuning. This makes them a potential probe to evaluate the NOvA cross section model. Figures 4.28 through 4.31 display the different TKI variables for the $\mu + P$ sample, on the left, without

the cross section model adjustments, and on the right with both the FSI and 2p2h adjustments[1]. In most cases, the rate of events is enhanced in a way that both the shape and the normalization agree very well with the data. The distribution of $\delta\alpha_T$ agrees well with the data under 80°, and afterwards there is a slight over prediction (Figure 4.28). $\delta\vec{p}_T$ agrees very well in the peak of the distribution (Figure 4.29). Moreover, the distribution of δp_{Tx} shows the expected symmetry around zero, and δp_{Ty} shows a tail towards the negative values. The four variables show a distribution similar to what was observed in [94], which provides a cross check that the tuning made to 2p2h is a sensible enhancement to the simulation. These distributions however, are only for the evaluation of the NOvA cross section model, and not a measurement of said TKI quantities.

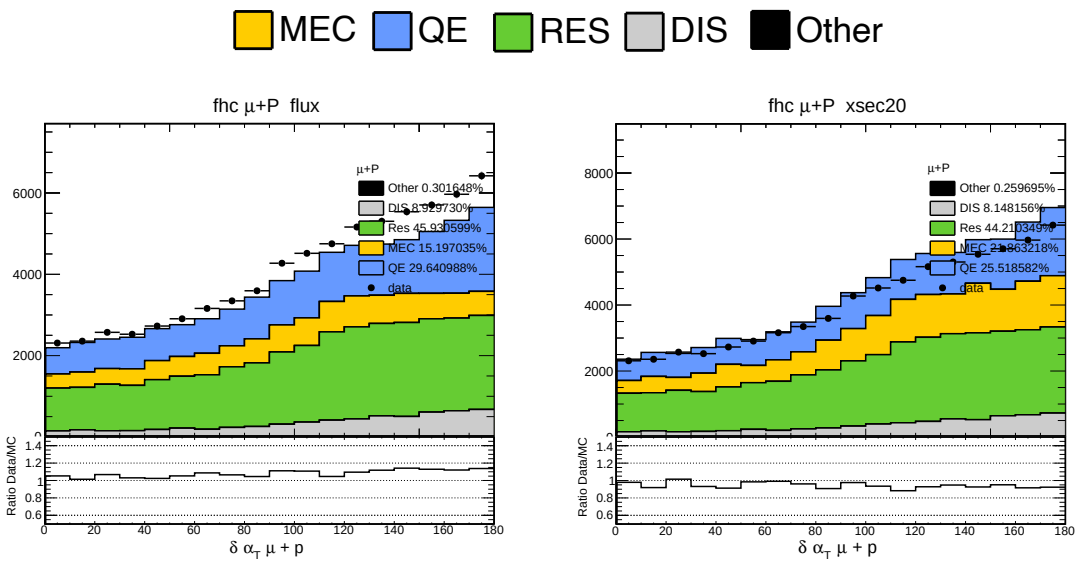

Figure 4.28: Angle for $\mu + P$ sample with (bottom) and without (top) cross section weights. The plots on the right represent the subset of $\mu + P$ sample that does not have 2D prongs.

[1]These distributions were made with a different version of the GENIE model described on chapter 3. However, the QE and MEC interactions were not affected by this change, and the 2p2h adjustment made is the same.

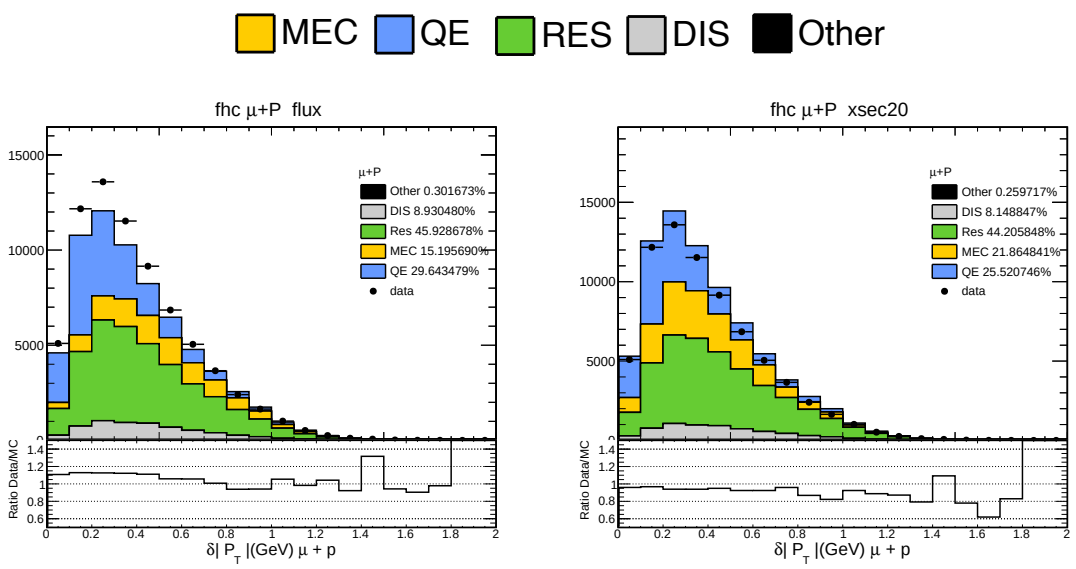

Figure 4.29: Missing transverse momentum of proton for $\mu + P$ sample with (left) and without (right) cross section weights

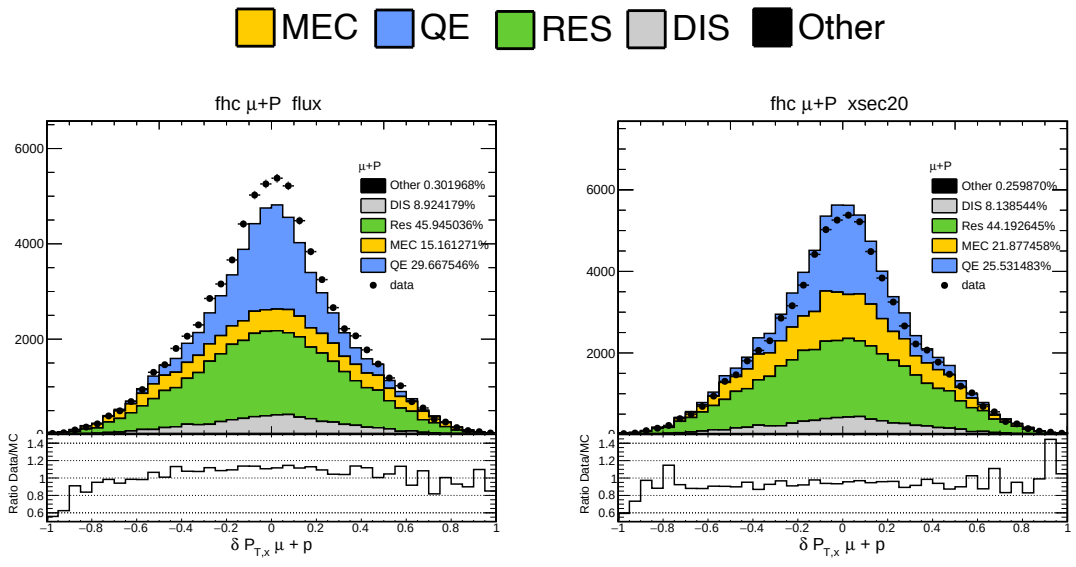

Figure 4.30: Angle for $\mu + P$ sample with (left) and without (right) cross section weights

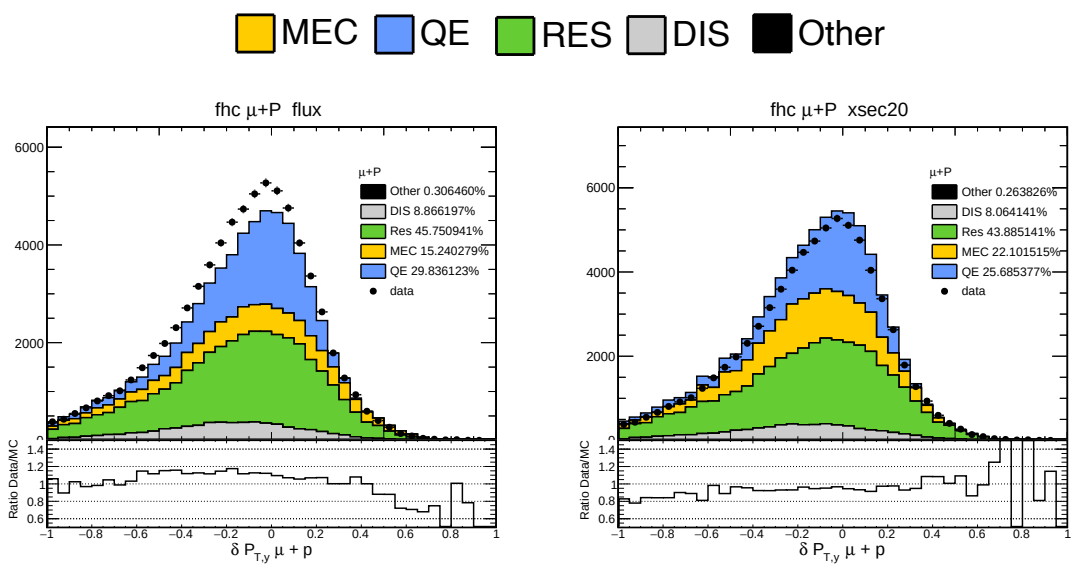

Figure 4.31: Angle for $\mu + P$ sample with (left) and without (right) cross section weights

4.6.3 Muon + Pion + X sample

The agreement between data and simulation for the FHC sample (Figure 4.32) is good and the purity of the sample is $\approx 65\%$, based on the true final state primaries categories (purple). Also this sample is dominated by interactions which produce a resonance. In the case of RHC the agreement is slightly worse, as can be seen in Figure 4.33. The higher E_{had} tail is overpredicted, as well as the 2nd bump in $|\vec{q}|$. The purity of this sample is also high, with $\approx 71\%$ of interactions having actually one charged pion in the simulated final state (purple category).

4.6.3.1 Pion and X prong characterization

One of the most interesting findings after studying this sample, is that the agreement is affected by the number of additional non-pion (X) prongs. The sample requires at least 2 prongs, one which is associated with the muon and one with a charged pion (both by their respective CVN scores). Additional X prongs in the event are allowed, as long as they are not identified as charged pions by the CVN score criteria. One of this sample's features, is the observation of two

subcategories of events with charged pions, defined by the presence (or not) of X prongs. The main difference between the two subcategories is :

- Undersimulating when there are no X prong
- Oversimulating when there are X prongs

In other words, the overall good agreement seen in the sample can be inferred as the average of the behavior of the events with different prong multiplicity. When there are 0 X prongs there is undersimulation for FHC, and good agreement in RHC (see Figure 4.34); for 1 and 2 X prongs there is a slight oversimulation, which is more prominent for RHC. Most of the X prongs are associated with simulated protons, followed by photons, and a few pions and muons, as shown in the top row of Figure 4.35.

The study of the pion CVN score of the prongs in this sample is relevant to evaluate how robust is the selection of pions. The distributions of pion CVN score of all the prongs (bottom of Figure 4.35), shows a good agreement with data, especially at the regions between 0.6 and 1. In the FHC distribution, there is an accumulation of the $\mu + nP + X$ (orange) category of primaries in the final state, between ≈ 0.5 and 0.8 CVN score. For RHC, a larger fraction of the true $\mu + 1\pi + X$ (purple) final state category events are located in the bins of 0.6 and higher. When these distributions are broken up in categories of the true pdg of the prongs (Figure 4.36), it is evident that the accumulation observed in FHC, comes from the protons that have a high pion CVN score. In other words, there is a considerable amount of prongs associated with an actual (simulated) proton that are being selected as pions. This is the case for both FHC and to a smaller extent in RHC. In the case of prongs associated to simulated photons (rightmost distributions in fig. 4.36), there is a bump at around 0.8 pion CVN score, that contains a significant amount of the neutral pion final state category (teal/turquoise), especially for RHC.

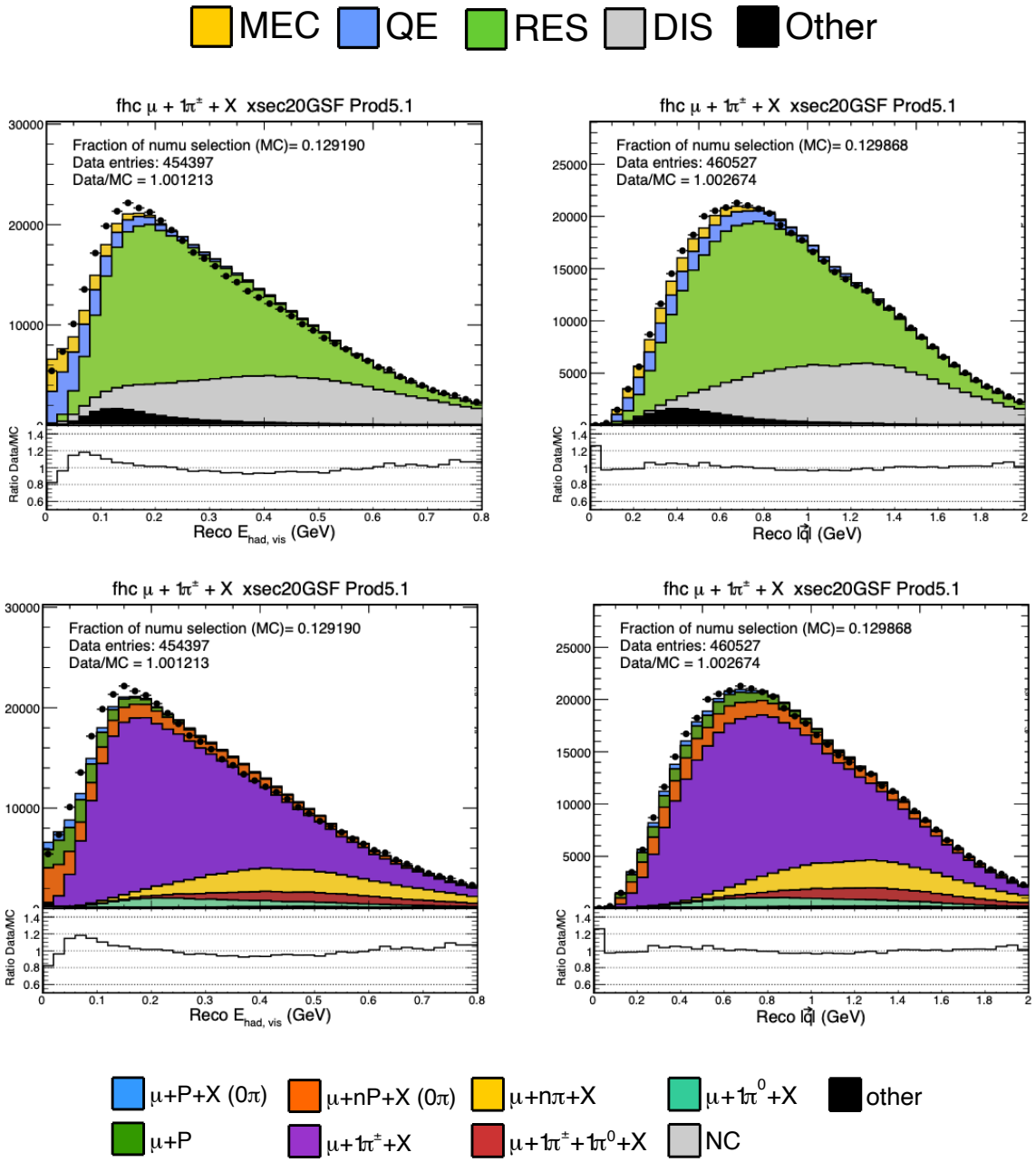

Figure 4.32: Distributions of visible hadronic energy (left) and reconstructed three momentum (right) with interaction type breakdown (top) and final state primaries (bottom).

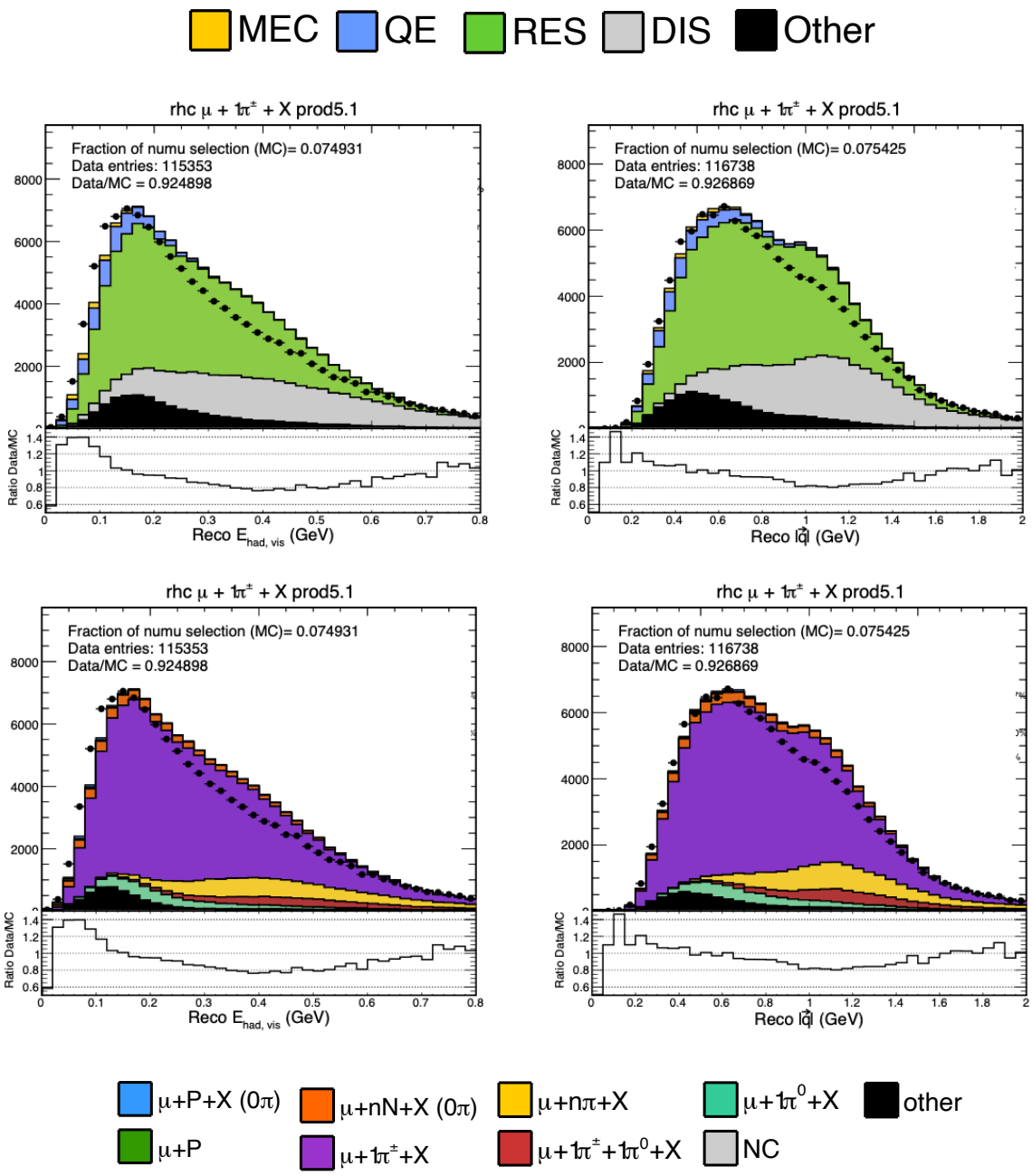

Figure 4.33: Distributions of visible hadronic energy (left) and reconstructed three momentum (right) with interaction type breakdown (top) and final state primaries (bottom).

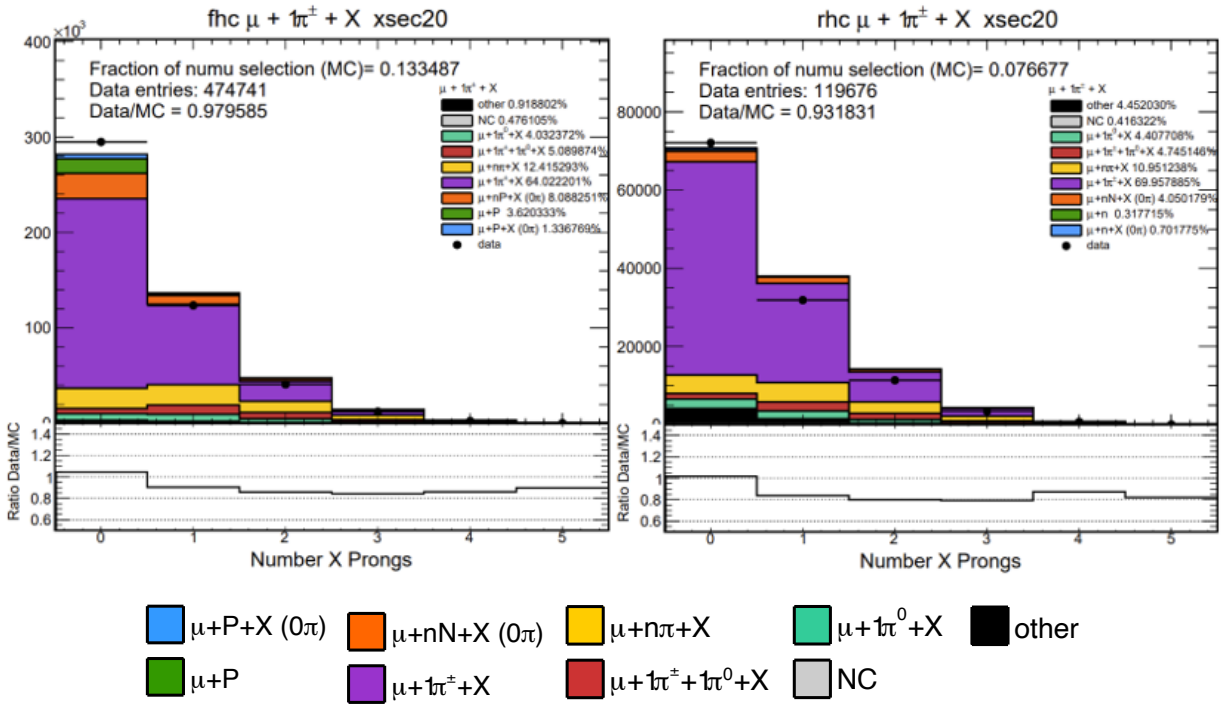

Figure 4.34: Number of X prongs for FHC (left) and RHC (right) $\mu + \pi^{\pm} + X$ samples.

In the bottom Figure 4.35, the individual prongs calorimetric energy distribution, shows that the muon and pion prongs are very well simulated, as the data and MC ratio is mostly flat and very close to 1. However the X prongs show oversimulation at lower energies. Knowing that there is a different agreement for events that include an X prong, versus those that do not, and that we have a significant contamination of proton prongs identified as pions, it is of interest to look at the characteristics of the pion prongs when we vary the pion CVN score criteria to select this sample.

The distributions in figures 4.38 through 4.40 show the FHC sample pion prongs as selected by various CVN score criteria, and divided into categories according to the presence or lack of X prongs. The first feature that stands out is the slight overprediction when there are X prongs, and underprediction when there are not. The length and calorimetric energy for the pions from 0.5 to 0.7 CVN score have the most $\mu + P + nX$ true final state (orange) contamination, which is consistent with the bump observed in the pion CVN score plot (Figure 4.36). In this case the pion

prongs have a lower energy and are shorter than in the more strict selections above 0.7 or 0.8 score.

4.6.4 Muon + Proton + X sample

This sample shows a large overprediction of around 24%, specially between 0.1 and 0.7 GeV in E_{had}, and below 1.8 GeV of $|\vec{q}|$. It is dominated by resonance and deep-inelastic scattering interactions. In terms of the true final state, the sample contains mostly final states with pions, including both charged (purple, yellow, red categories) and neutral pions (teal, red and yellow categories), plus a significant contribution of $\mu + nP + X$(orange).

Figures 4.46 to 4.47 show distributions of the different prong variables for the muon, proton and X prongs. The overprediction observed in the overall sample looks different for each of the prongs. The muon prong has a slight bias towards lower CalE/hit. The proton prongs distributions show a flat ratio for length, number of hits and calorimetric energy. The calE/hit shows a larger overprediction at the lowest values, although there are very few events in these bins. For the case of the X prong, all the variables show the excess at the low values of each of these four variables.

This sample was defined in order to reject prongs that are likely associated with a pion, by using a criteria of rejecting any 3D prongs that have a score larger than 0.5. This criteria was decided, as it allows for a the largest possible rejection of pion prongs. In contrast to the $\mu + \pi + X$ sample, where the goal was to get as pure of a selection of pion prongs by restricting the pion score, in this sample a looser pion score criteria discards more events with pion prongs, at the cost of a smaller sample.

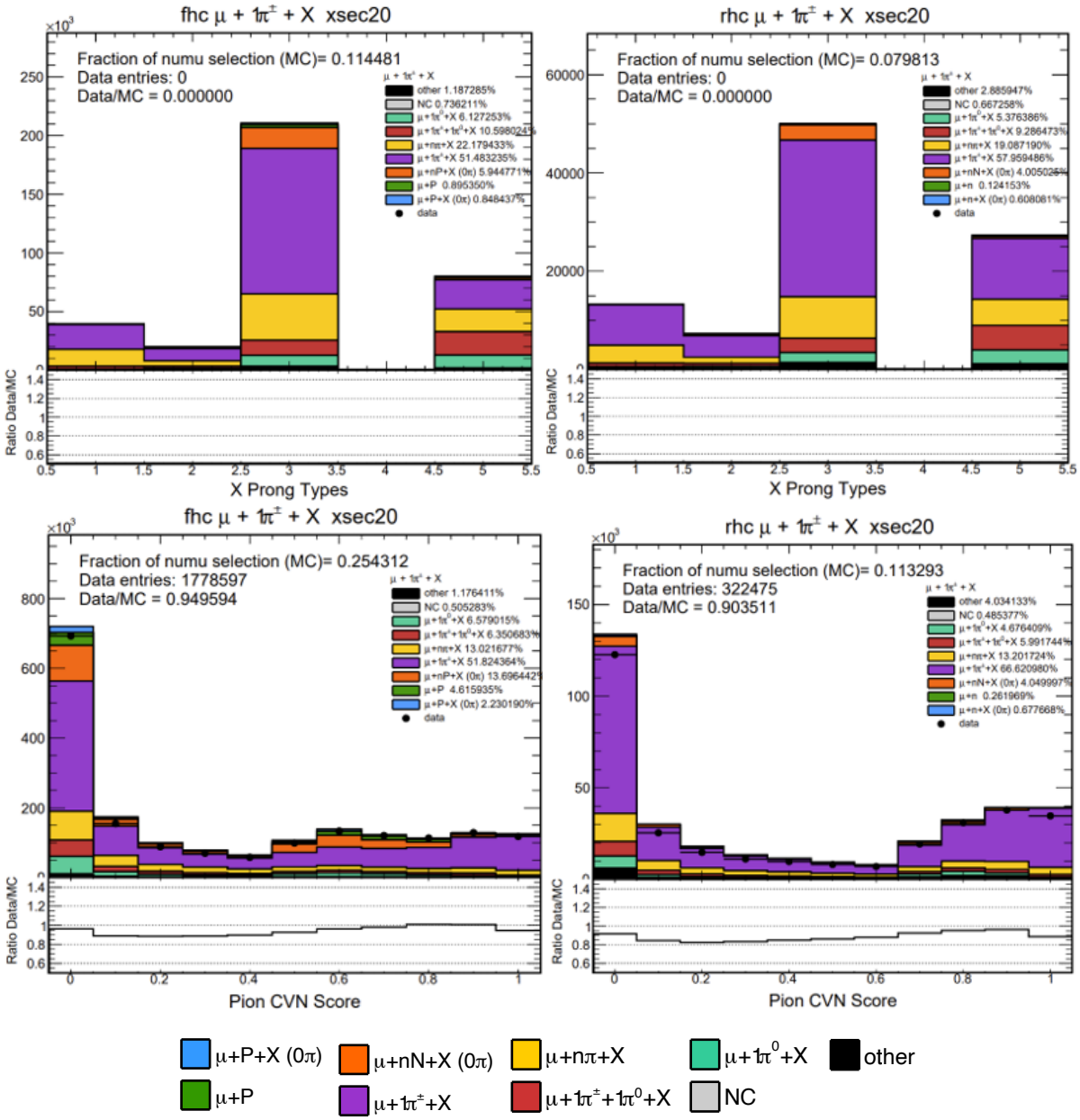

Figure 4.35: Top: PDG of X prongs for FHC (left) and RHC (right) $\mu + \pi^{\pm} + X$ samples. Bin 1= $\pi^{\pm}$, Bin 2= μ, bin 3= P, bin 4= π^0, bin 5= γ. Bottom: Pion CVN score of all prongs for FHC (left) and RHC (right) $\mu + \pi^{\pm} + X$ samples.

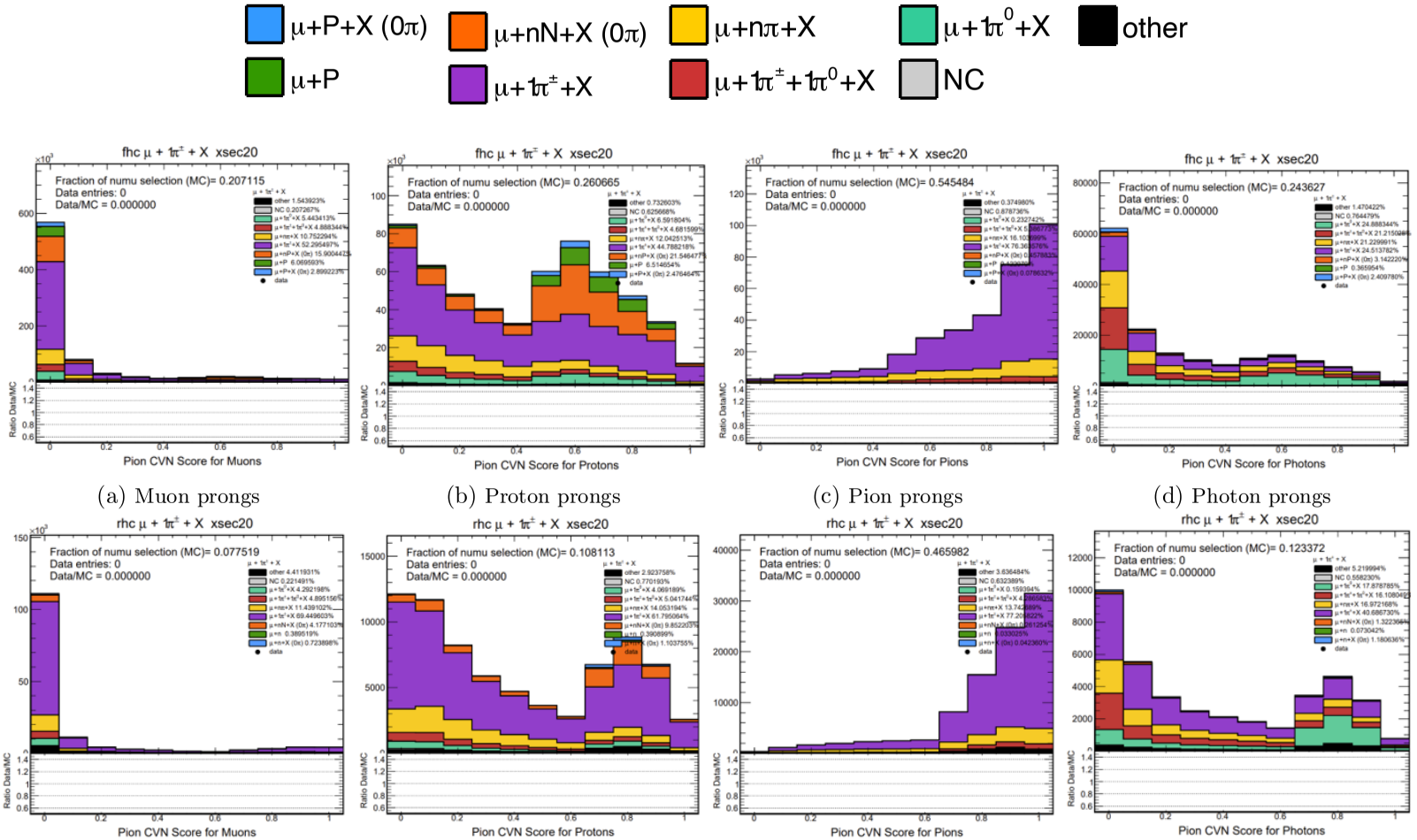

(a) Muon prongs (b) Proton prongs (c) Pion prongs (d) Photon prongs

(e) Muon prongs (f) Proton prongs (g) Pion prongs (h) Photon prongs

Figure 4.36: Pion CVN score of all prongs, divided by their true prong pdg, for FHC (top) and RHC (bottom) $\mu + \pi^{\pm} + X$ samples.

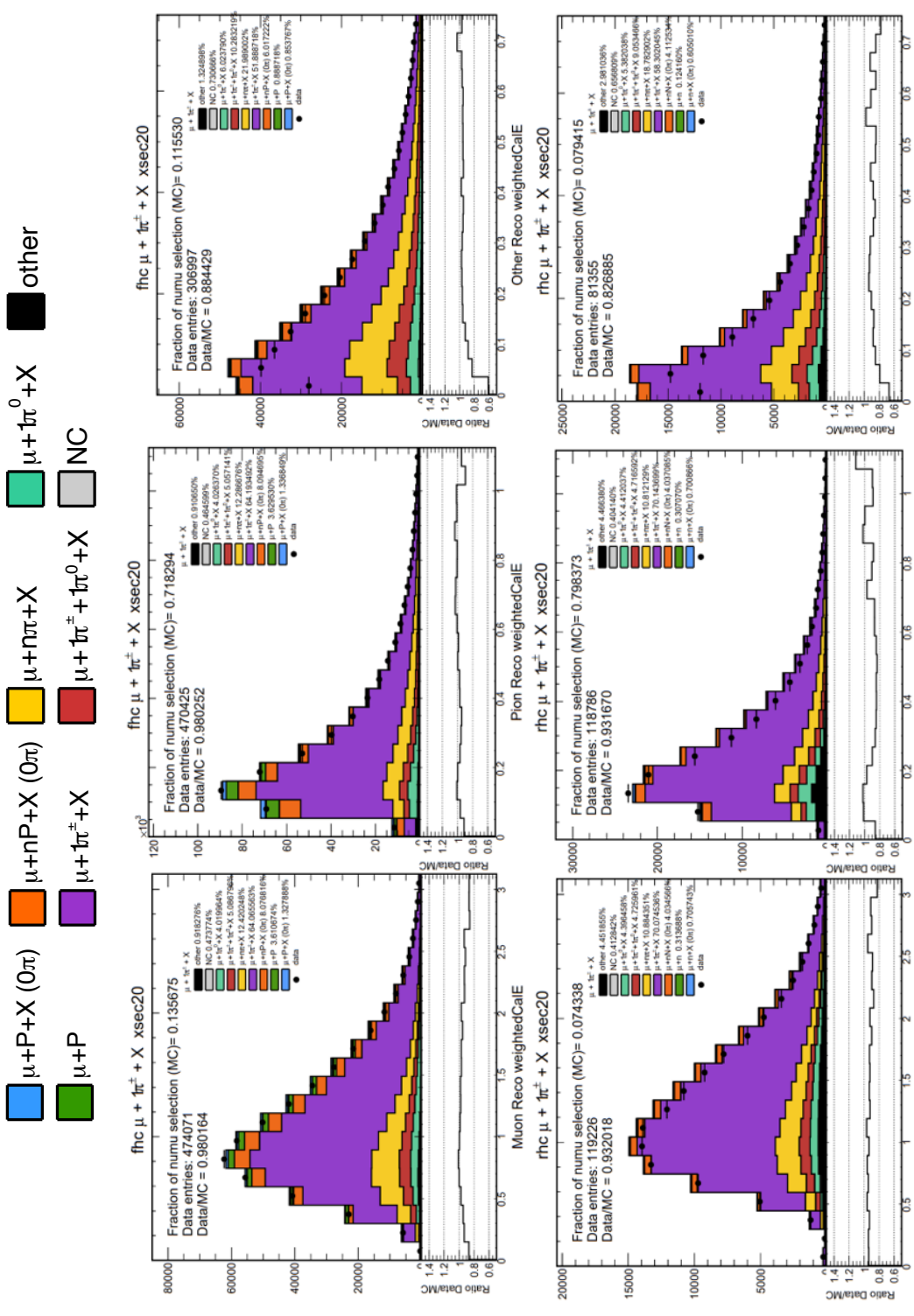

Figure 4.37: Weighted calorimetric energy for muon, pion and other prongs for FHC (top) and RHC (bottom) $\mu + \pi^{\pm} + X$ samples.

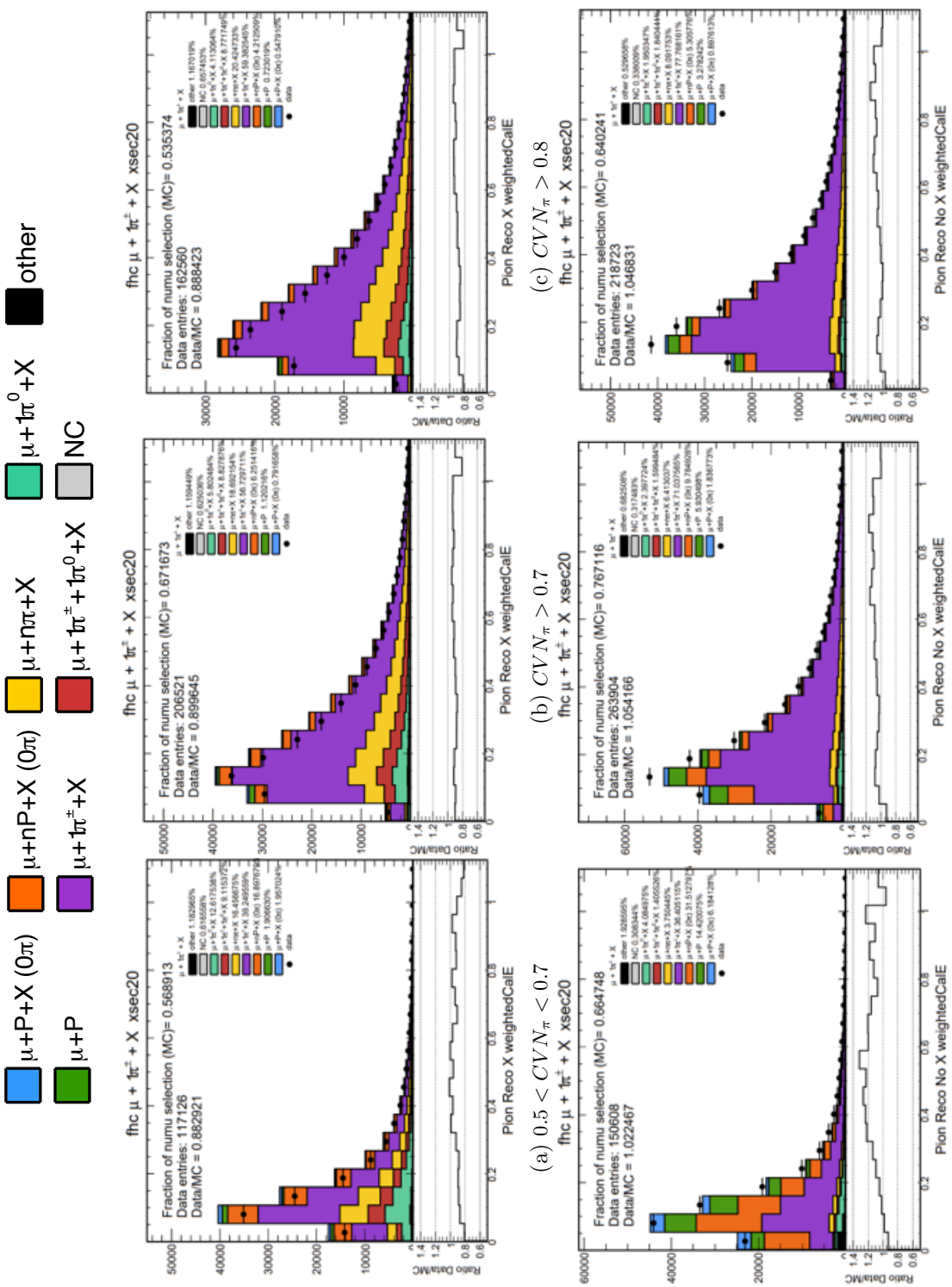

(a) $0.5 < CVN_\pi < 0.7$

(b) $CVN_\pi > 0.7$

(c) $CVN_\pi > 0.8$

(d) $0.5 < CVN_\pi < 0.7$

(e) $CVN_\pi > 0.7$

(f) $CVN_\pi > 0.8$

Figure 4.38: Weighted calorimetric energy for pion prongs identified by different CVN score ranges within the $\mu + \pi + X$ sample for FHC, when the event contains X prong (top) or not (bottom).

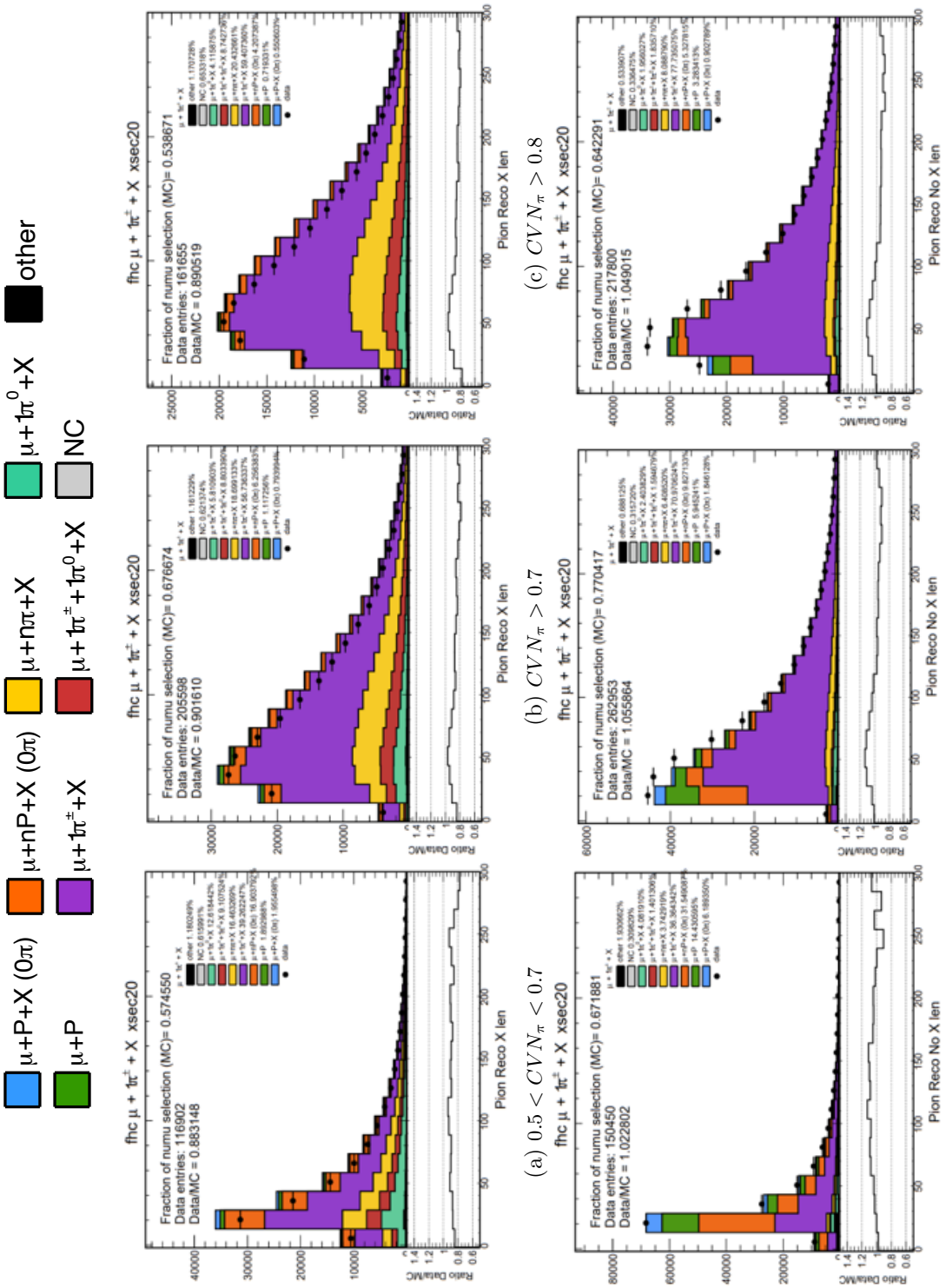

(a) $0.5 < CVN_\pi < 0.7$ (b) $CVN_\pi > 0.7$ (c) $CVN_\pi > 0.8$

(d) $0.5 < CVN_\pi < 0.7$ (e) $CVN_\pi > 0.7$ (f) $CVN_\pi > 0.8$

Figure 4.39: Prong length for pion prongs identified by different CVN score ranges within the $\mu + \pi + X$ sample for FHC, when the event contains X prong (top) or not (bottom).

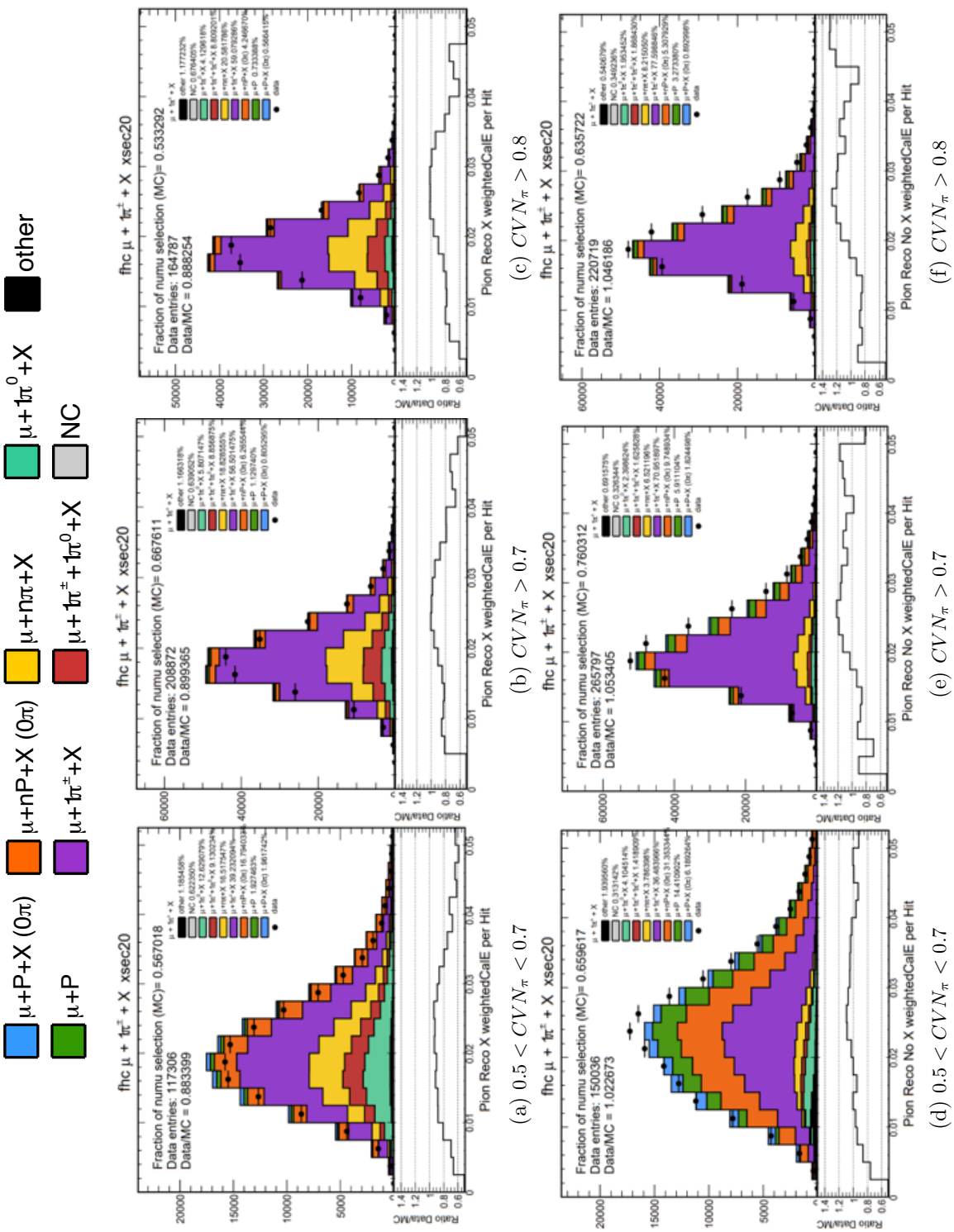

(a) $0.5 < CVN_\pi < 0.7$

(b) $CVN_\pi > 0.7$

(c) $CVN_\pi > 0.8$

(d) $0.5 < CVN_\pi < 0.7$

(e) $CVN_\pi > 0.7$

(f) $CVN_\pi > 0.8$

Figure 4.40: Weighted calorimetric energy per hit for pion prongs identified by different CVN score ranges within the $\mu + \pi + X$ sample for FHC, when the event contains X prong (top) or not (bottom).

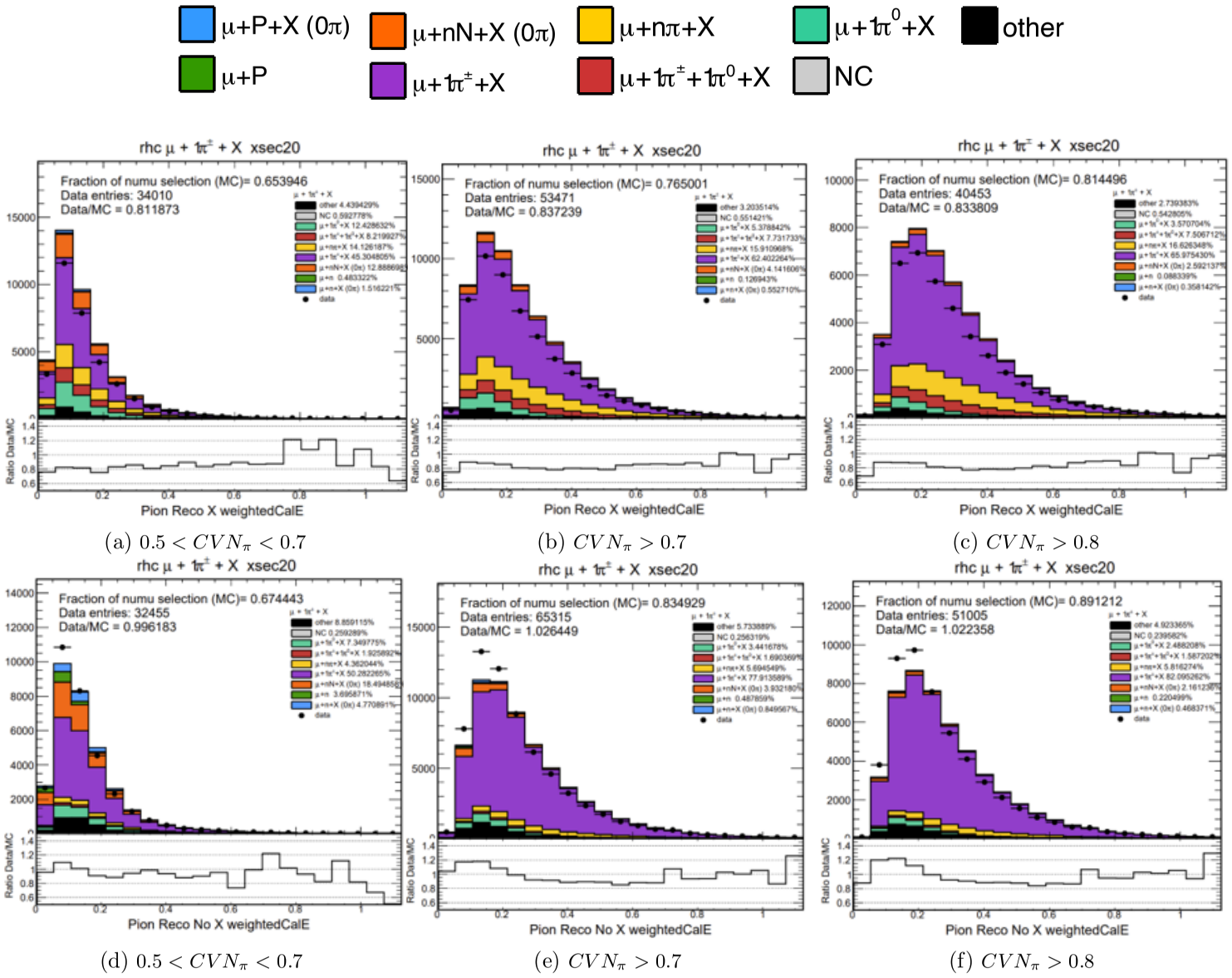

(a) $0.5 < CVN_\pi < 0.7$ (b) $CVN_\pi > 0.7$ (c) $CVN_\pi > 0.8$

(d) $0.5 < CVN_\pi < 0.7$ (e) $CVN_\pi > 0.7$ (f) $CVN_\pi > 0.8$

Figure 4.41: Weighted calorimetric energy for pion prongs identified by different CVN score ranges within the $\mu + \pi + X$ sample for RHC, when the event contains X prong (top) or not (bottom).

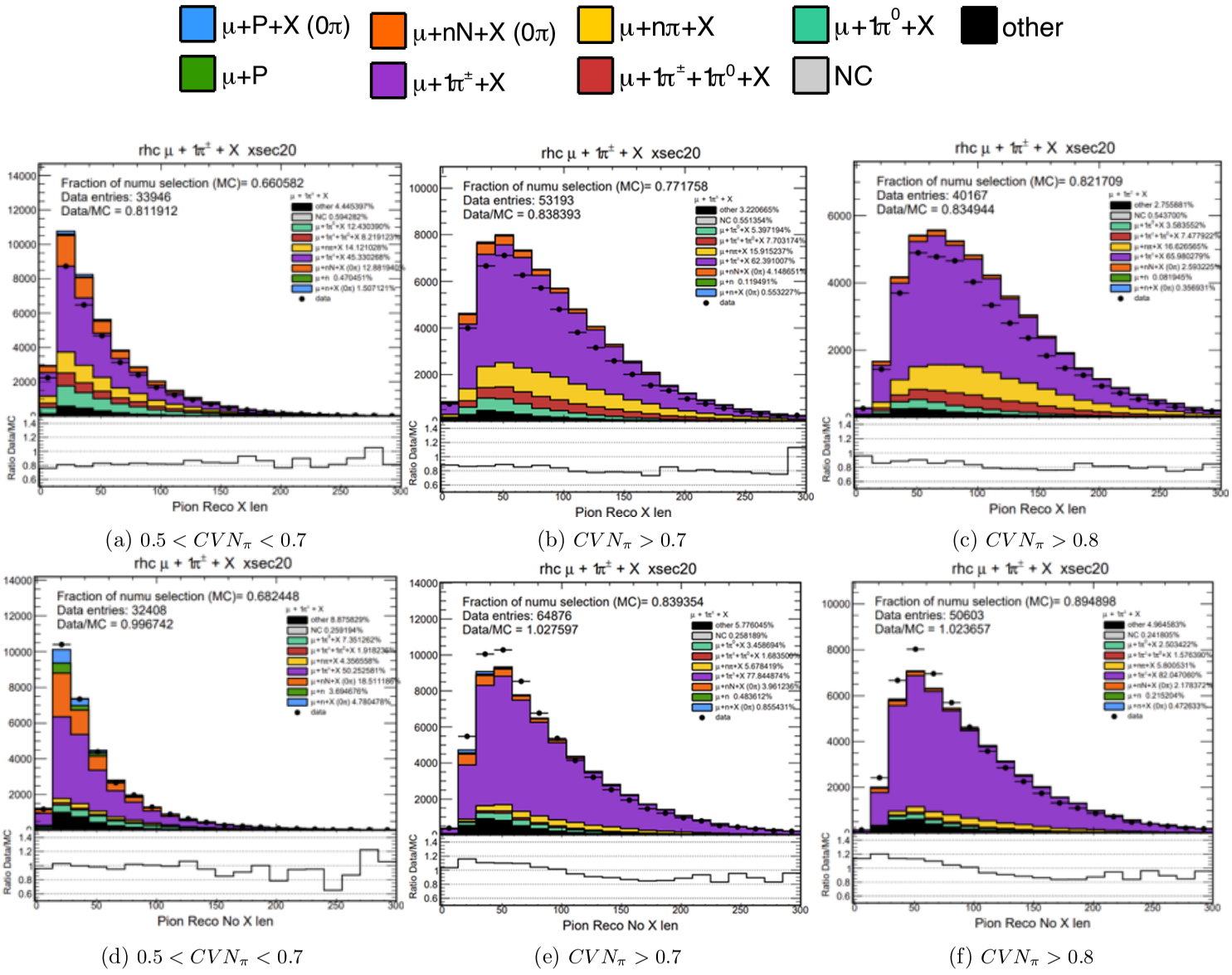

(a) $0.5 < CVN_\pi < 0.7$ (b) $CVN_\pi > 0.7$ (c) $CVN_\pi > 0.8$

(d) $0.5 < CVN_\pi < 0.7$ (e) $CVN_\pi > 0.7$ (f) $CVN_\pi > 0.8$

Figure 4.42: Prong length for pion prongs identified by different CVN score ranges within the $\mu + \pi + X$ sample for RHC, when the event contains X prong (top) or not (bottom).

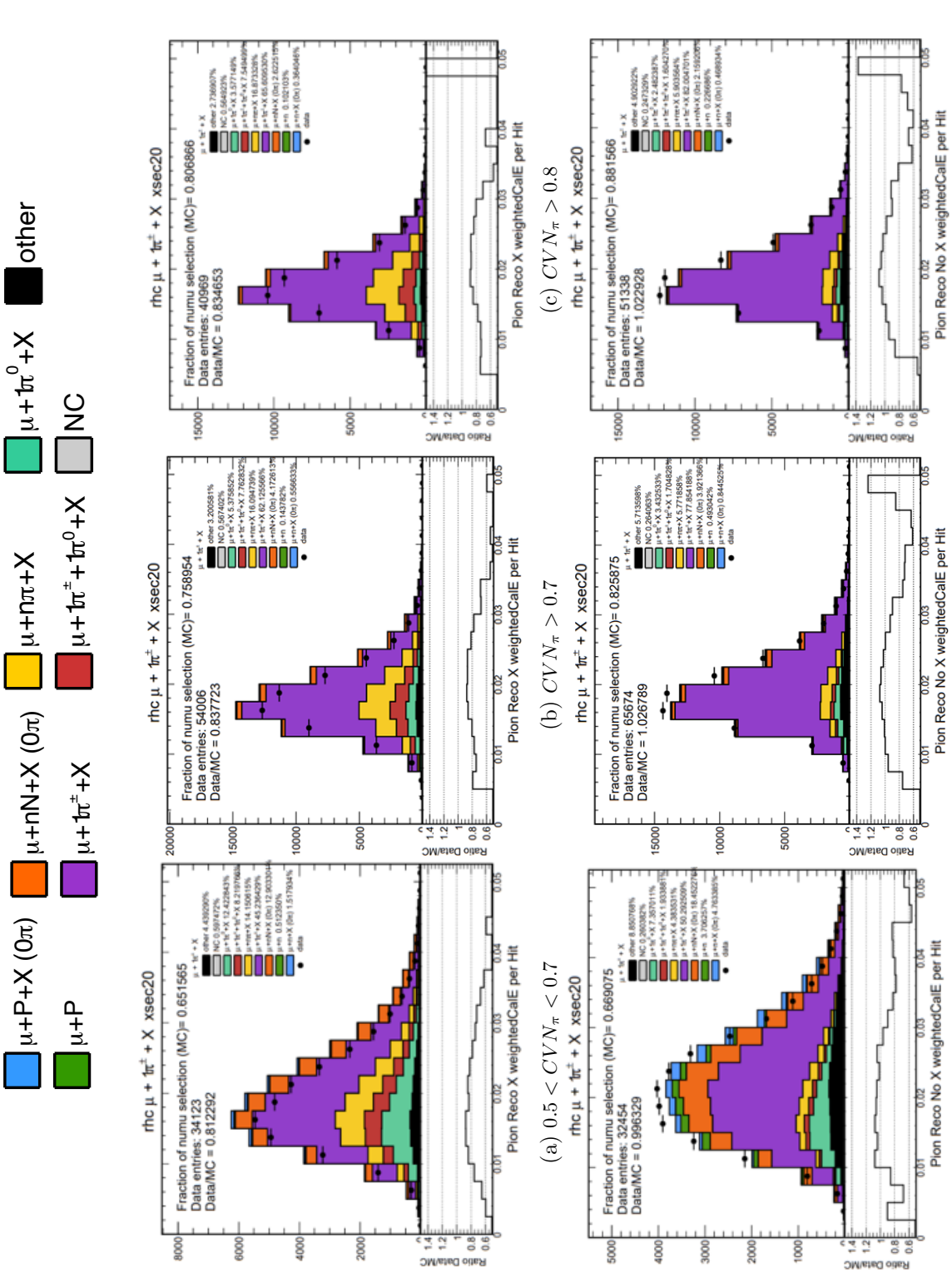

(a) $0.5 < CVN_\pi < 0.7$ (b) $CVN_\pi > 0.7$ (c) $CVN_\pi > 0.8$

(d) $0.5 < CVN_\pi < 0.7$ (e) $CVN_\pi > 0.7$ (f) $CVN_\pi > 0.8$

Figure 4.43: Weighted calorimetric energy per hit for pion prongs identified by different CVN score ranges within the $\mu + \pi + X$ sample for RHC, when the event contains X prong (top) or not (bottom).

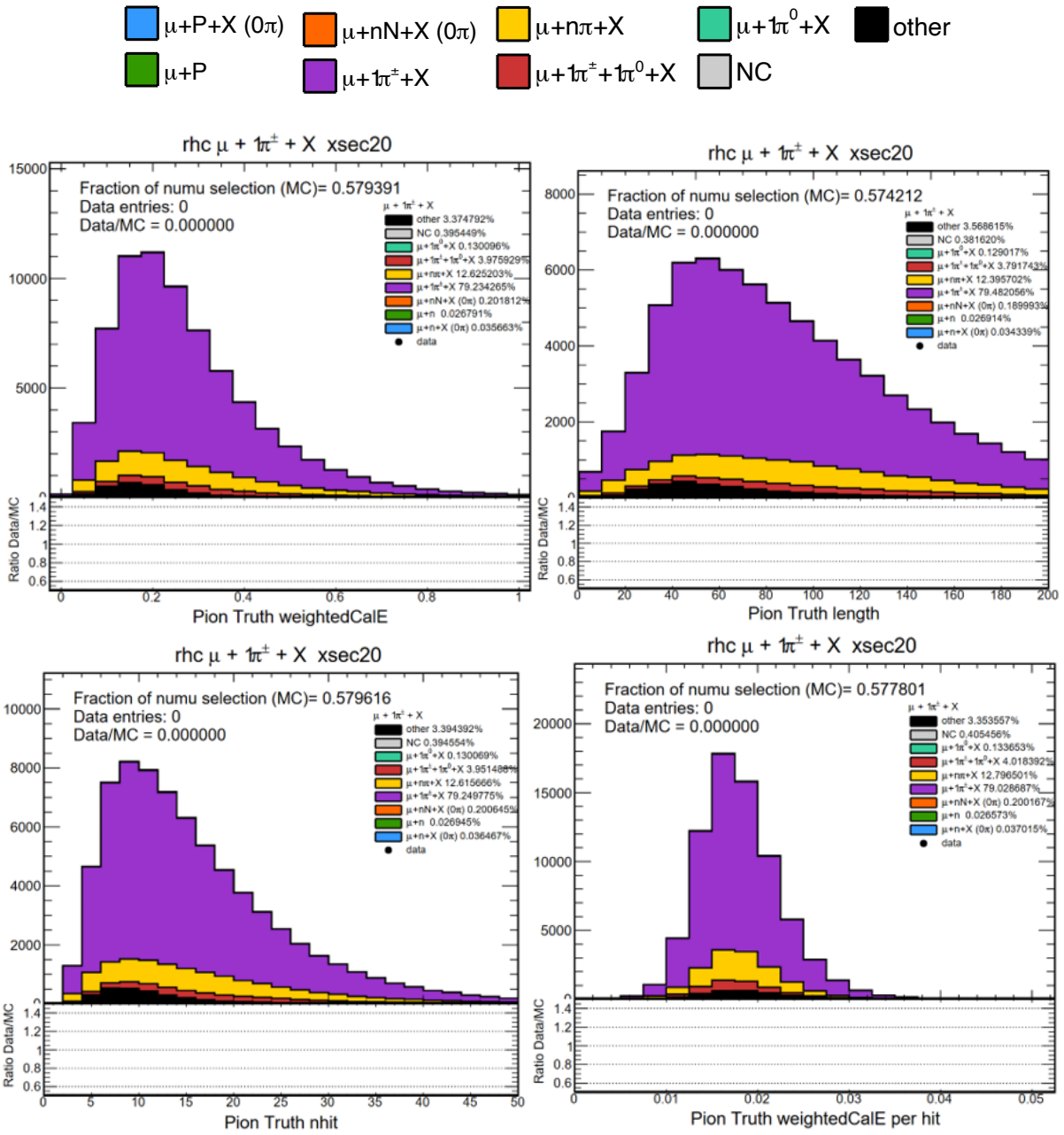

Figure 4.44: Weighted calorimetric energy (top left), length (top right), number of hits (bottom left), and weighted calorimetric energy per hit (bottom right) for truth pion prongs for RHC $\mu + \pi + X$ sample

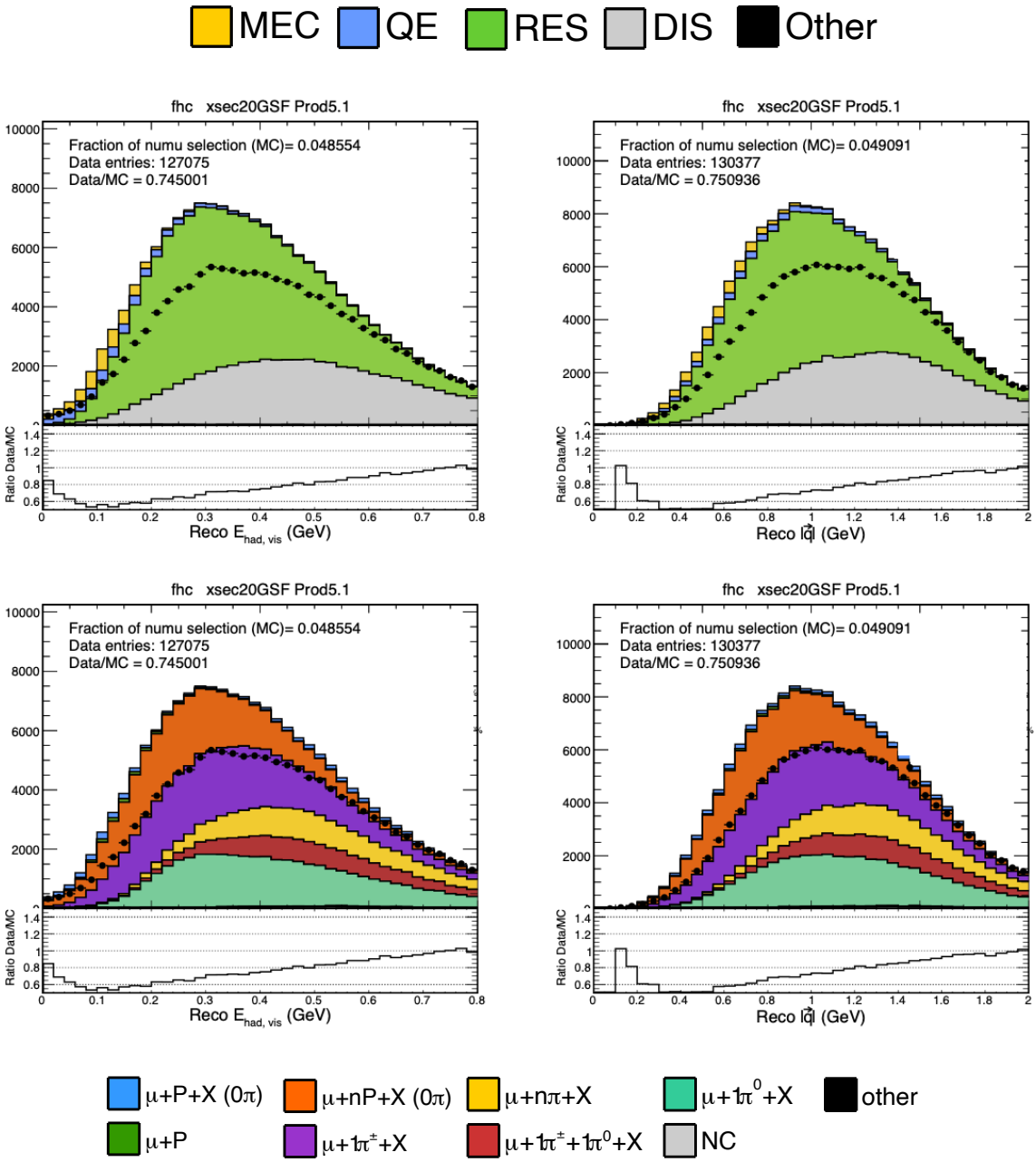

Figure 4.45: Distributions of visible hadronic energy (left) and reconstructed three momentum (right) with interaction type breakdown (top) and final state primaries (bottom).

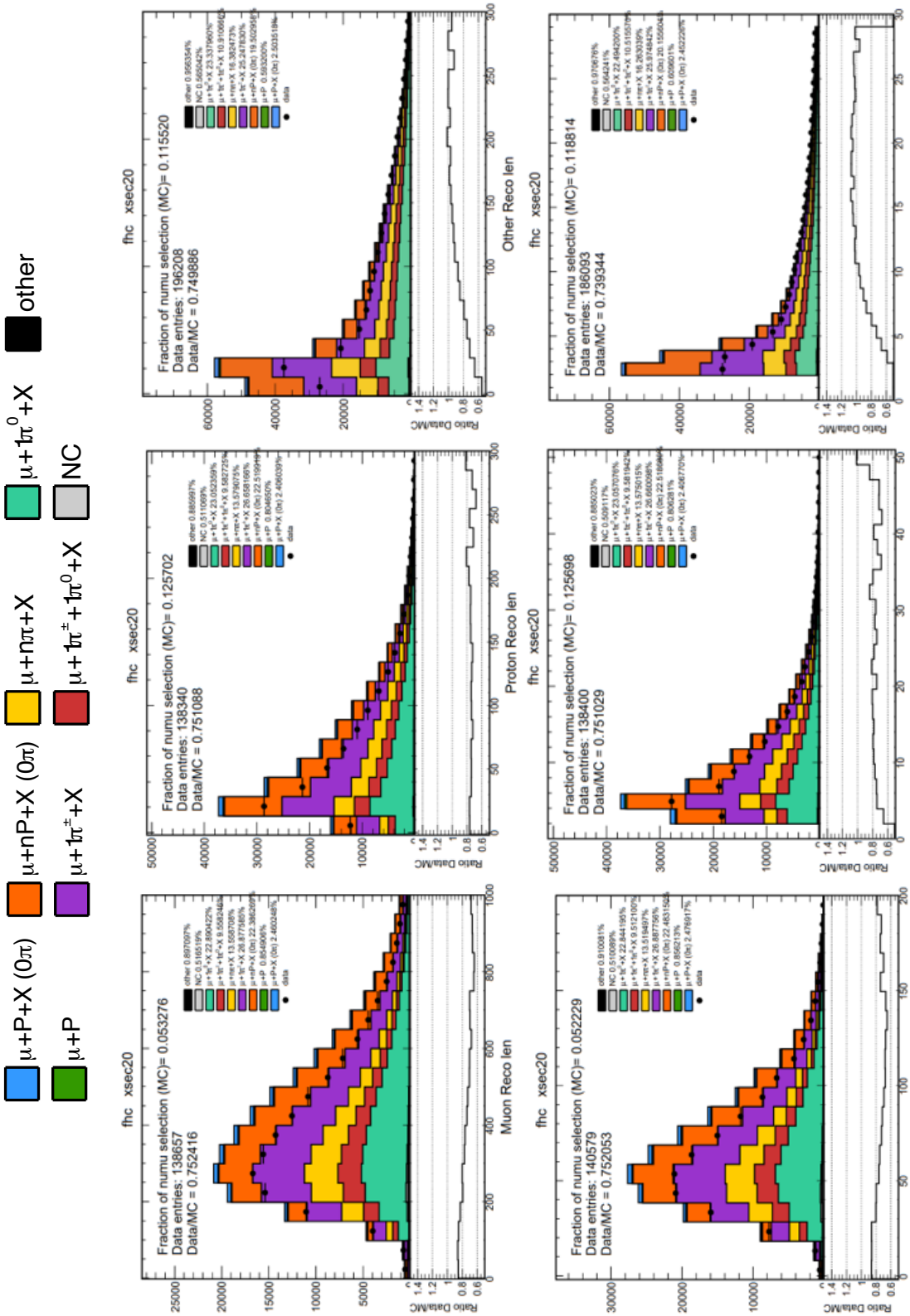

Figure 4.46: Prong length (top) and number of hits (bottom) for muon, proton, and other prongs for FHC $\mu + P + X$ samples

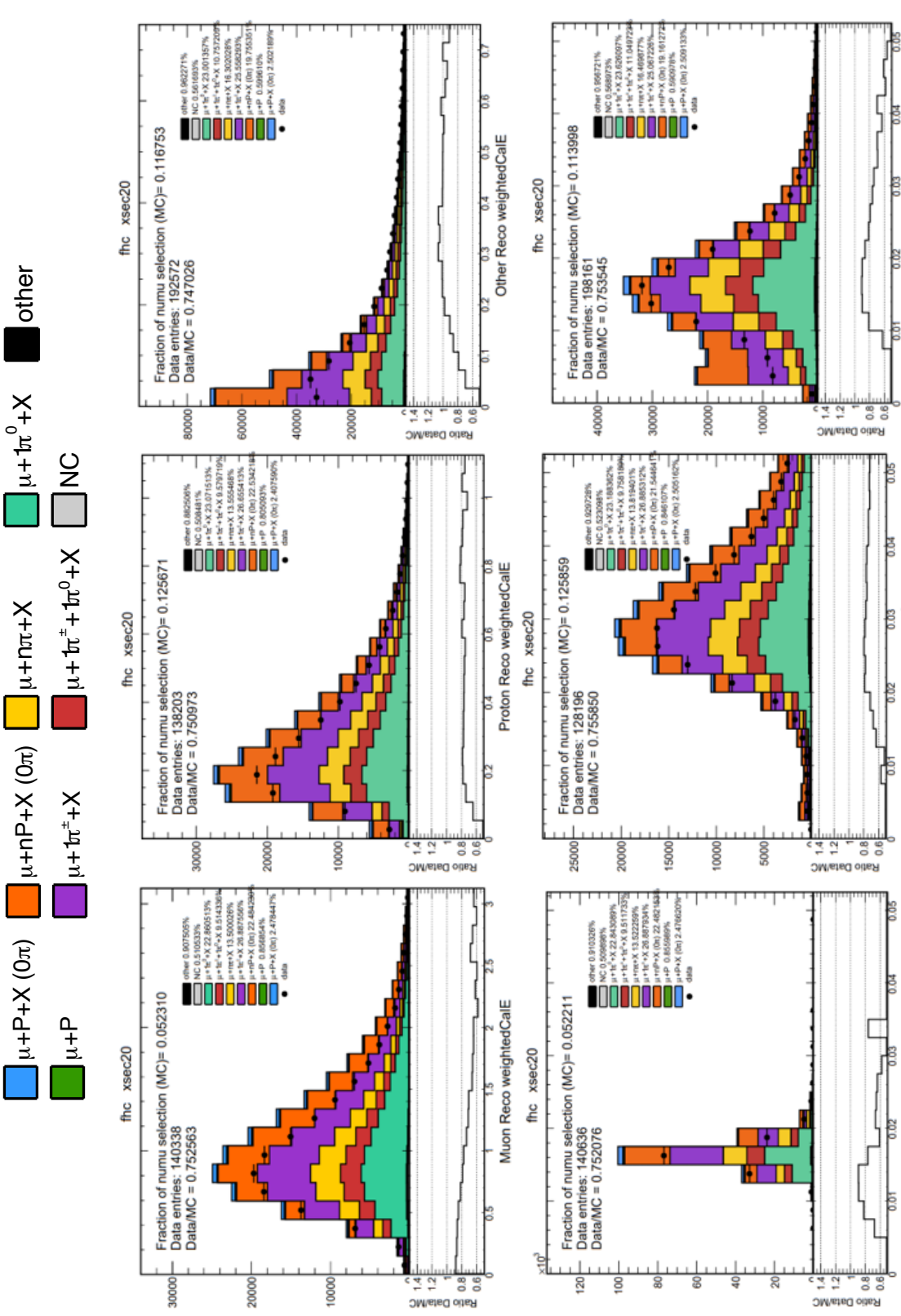

Figure 4.47: Weighted calorimetric energy (top) and weighted calorimetric energy per hit (bottom) for muon, proton, and other prongs for FHC $\mu + P + X$ samples

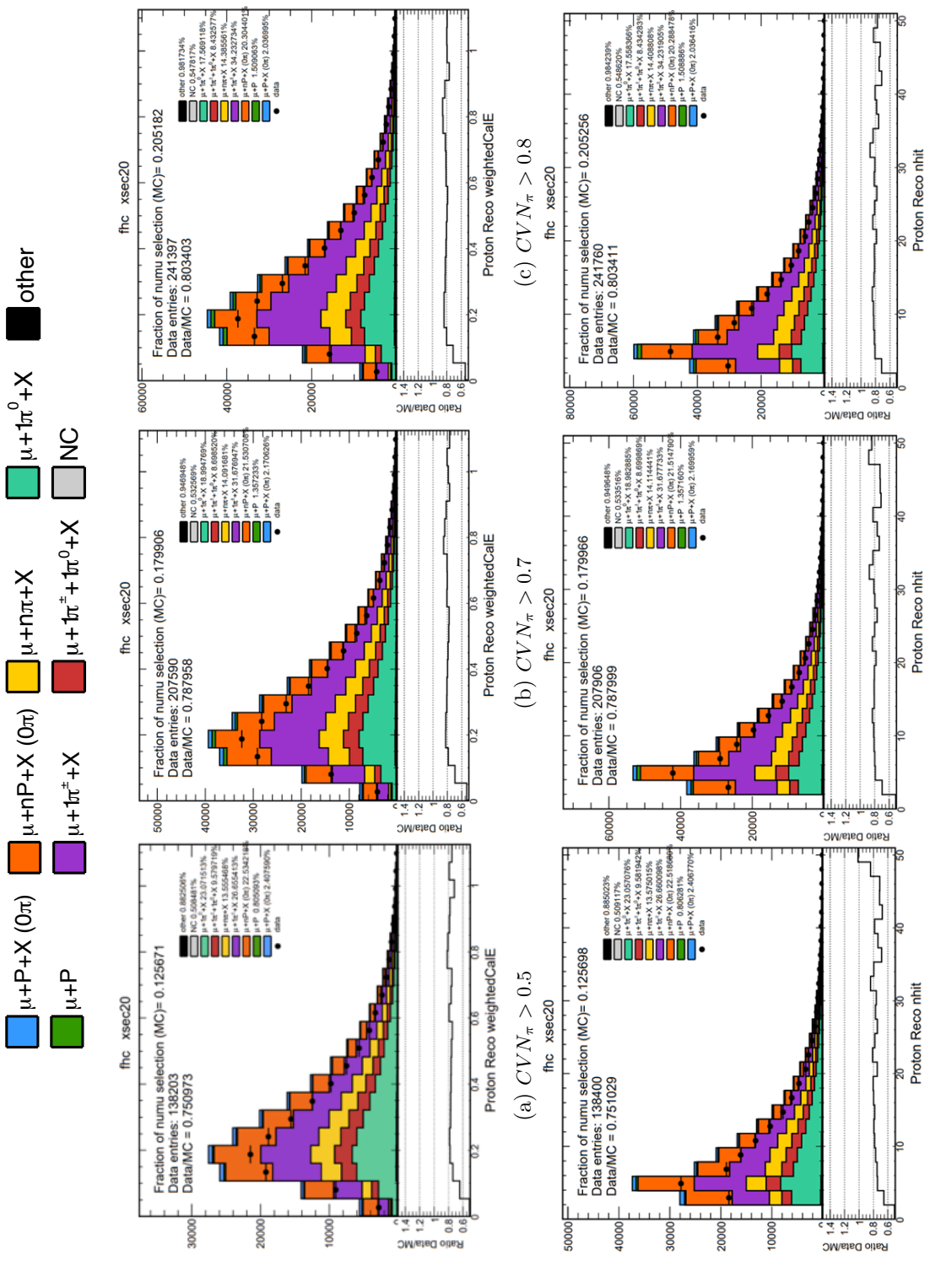

(a) $CVN_\pi > 0.5$ (b) $CVN_\pi > 0.7$ (c) $CVN_\pi > 0.8$

(d) $CVN_\pi > 0.5$ (e) $CVN_\pi > 0.7$ (f) $CVN_\pi > 0.8$

Figure 4.48: Weighted calorimetric energy per hit (top) and number of hits (bottom) for proton prongs when excluding different pion CVN score ranges for the X prongs in the $\mu + P + X$ sample in FHC

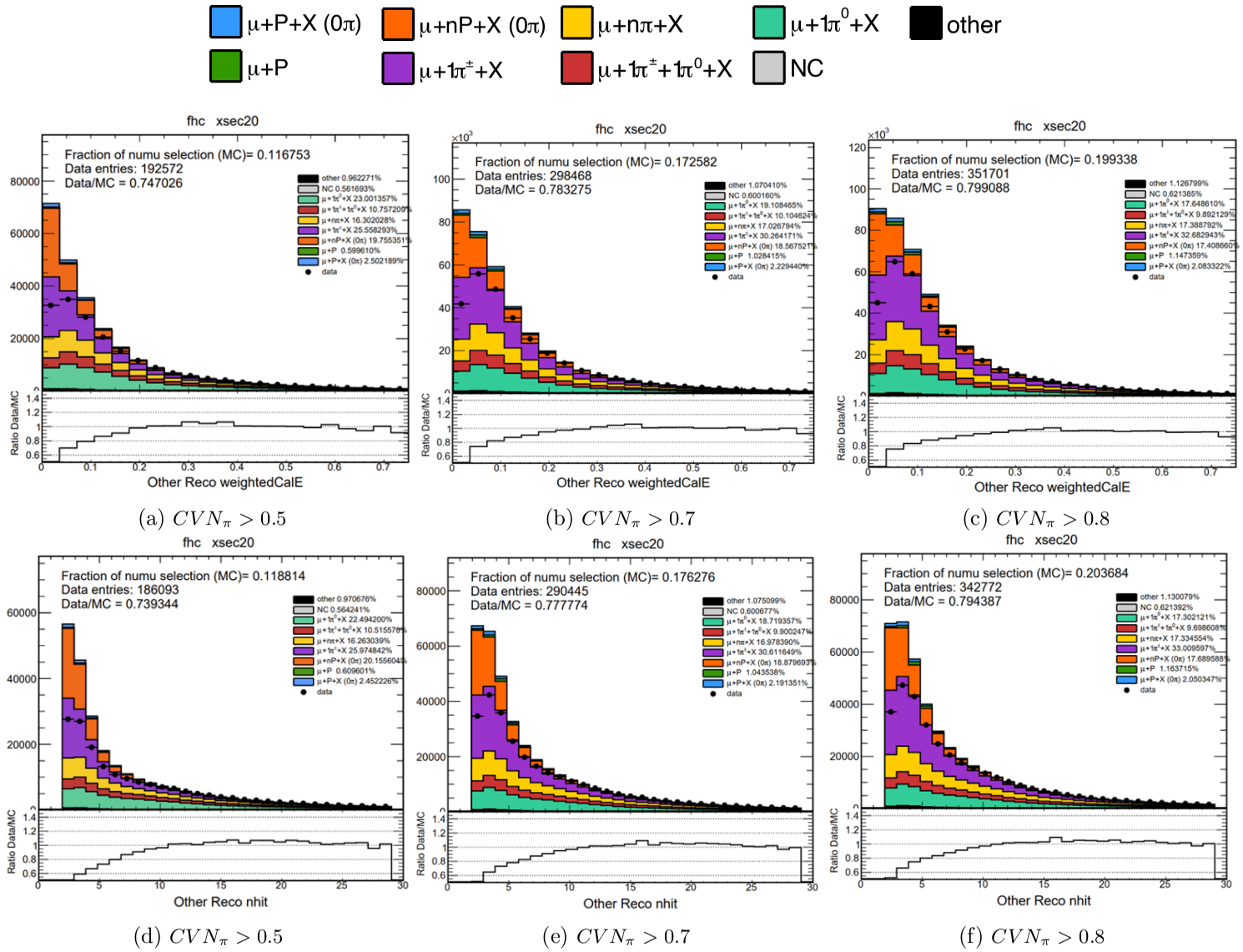

(a) $CVN_\pi > 0.5$ (b) $CVN_\pi > 0.7$ (c) $CVN_\pi > 0.8$

(d) $CVN_\pi > 0.5$ (e) $CVN_\pi > 0.7$ (f) $CVN_\pi > 0.8$

Figure 4.49: Weighted calorimetric energy per hit (top) and number of hits (bottom) for X prongs when excluding different pion CVN score ranges for the X prongs in the $\mu + P + X$ sample in FHC

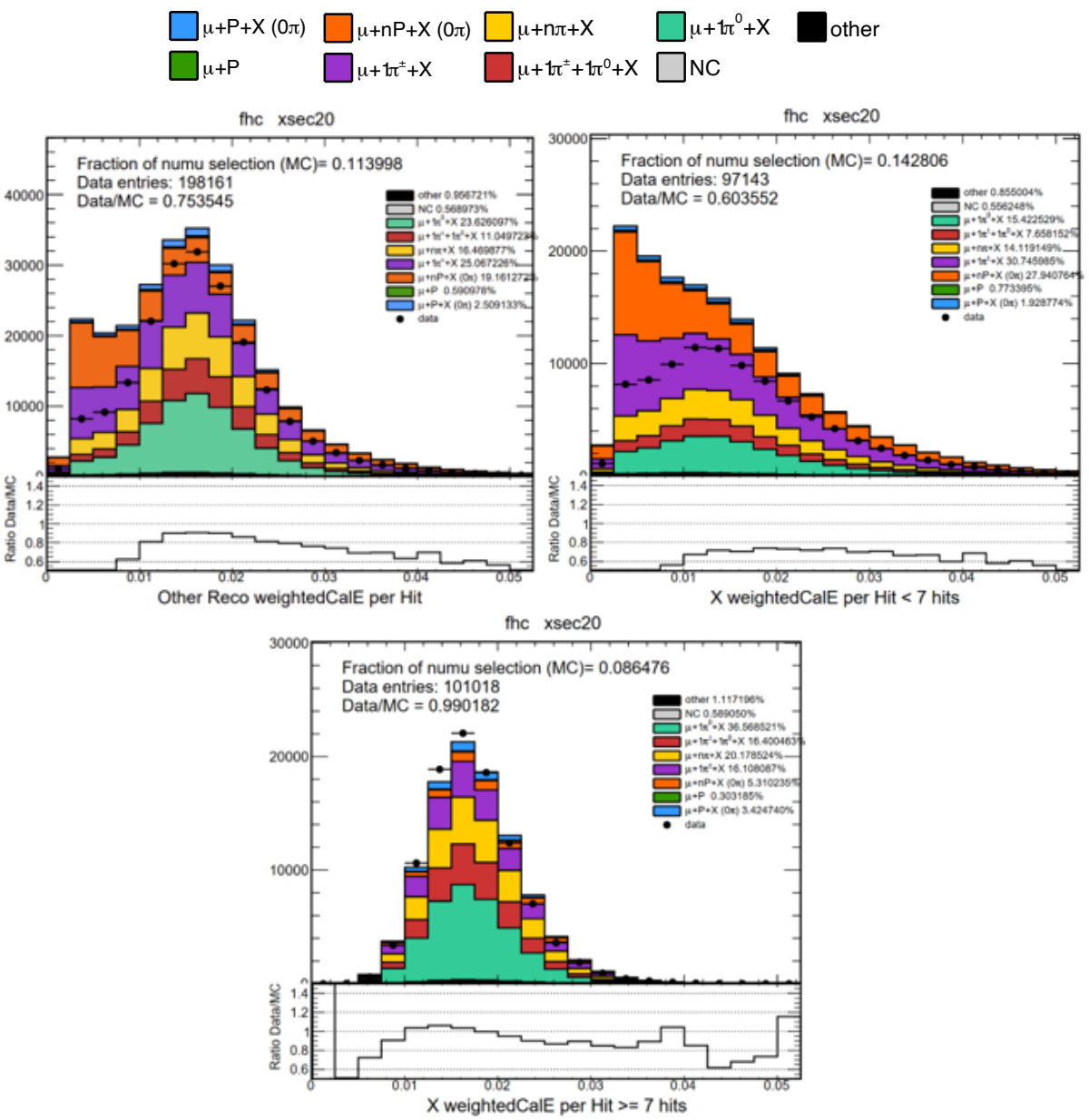

Figure 4.50: Weighted calorimetric energy per hit of X prongs overall, when the X prong has less than 7 hits, and when the X prong as at least 7 hits in the $\mu + P + X$ sample in FHC

Figures 4.48 and 4.49 show the characteristics of the proton and X prongs, when the pion CVN score for pion rejection is varied (rejecting pions with $CVN_{\pi} > 0.5$, 0.7 and 0.8). The data and simulation agreement for the proton prongs is similar in these three variations, as can be seen

in the ratios. For the proton prongs, the ratio is mostly flat at 0.8 after 0.2 weighted CalE and above 5 hits; for the X prongs, the simulation significantly overpredicts the rate of events with weighted calE smaller than 0.3 GeV and fewer than 10 hits, while the rest of the distribution matches the data, independent of the criteria to reject pions. However the percentage of events with a true single charged pion in the final state is reduced, when the rejection criteria is 0.8 the percentage of this category is 33 whereas with the criteria of 0.5 the percentage is reduced to 25. The variation in pion CVN affects the size of the sample as well.

When observing the length or number of hits for the X prongs, as shown in figures 4.46 and 4.46, it is noticeable that the underprediction in this sample, is especially bad for the cases where the X prong is shorter than $\approx$ 100cm or less than $\approx$ 7 or 8 hits. Figure 4.50 shows the distributions of calorimetric energy per hit of the X prongs split in two categories, whether prong has less or more than 7 hits. Clearly the longer prongs have a very different distribution that agrees well with the data, whereas the shorter prongs have an excess at low CalE/hit. Also note that most of the orange category corresponds to the shorter prongs.

4.6.5 Muon + X sample

Similar to the $\mu + P + X$ sample, this sample aims select events with multiple hadrons, while rejecting prongs likely associated with a pion. In contrast with the FHC $\mu + P + X$ sample, this one does not select a proton, as fewer protons are expected for RHC beam data. The most notorious characteristic of these distributions (Figure 4.51) is the large overprediction. In terms of the composition, the sample is dominated by RES events followed by DIS, and small percentages of QE and MEC. In the breakdown by true final state categories, there is a similarity with $\mu + P + X$, as there is a significant amount of final states with charged and neutral pions (purple, yellow, red, teal) and also a significant amount with multiple neutrons (0π, orange). Note that the shape of the simulated visible hadronic energy is reminiscent to the RHC pion sample, with a peak close to 0.2 GeV, but with a higher rate of events at the lowest energies.

Figures 4.52 to 4.53 show the characteristics of the muon prong on the left panels. The features that stand out are the very first bin for the muon prong calorimetric energy, length and hits distributions, as these are more populated than the subsequent bins, which was not observed in the muon prongs of the $\mu + \pi + X$ or $\mu + P$ RHC samples. However this bins match well with the data. Also, the calorimetric energy per hit for the muon prong is very similar to the other samples. The rest of the distribution is overpredicted, with no significant bias in any calorimetric energy, length or hits. The more interesting features of the X prong are discussed in the next section.

4.6.6 X prong characterization

The right panel of figures 4.52 to 4.53 show the same variables for the X prong. It is especially noticeable in the number of hits distribution, that the overprediction is concentrated for events where the X prong is short. It also stands out that the fraction of true final states with multiple neutrons (orange) or one charged pion (purple) correspond to about the amount that is overpredicted in the sample ($\approx 27\%$). Another highlight of the X prongs is their calorimentric energy per hit distribution. The overprediction concentrates at the lower values, with most of it coming from the events with multiple neutrons in the true final state (orange).

On the right panel of Figure 4.54 , it is also interesting to show that most of the events in the sample have 2 X prongs, and as the events have more prongs the overprediction gets worse. Most of these prongs have a true pdg of protons followed by pions, which can be observed in the left panel of Figure 4.54. The events where X is a proton contain more of the orange category, whereas events where X is a photon contain a larger fraction of the teal (true final state with one neutral pion). This hints at two kinds of events in this sample.

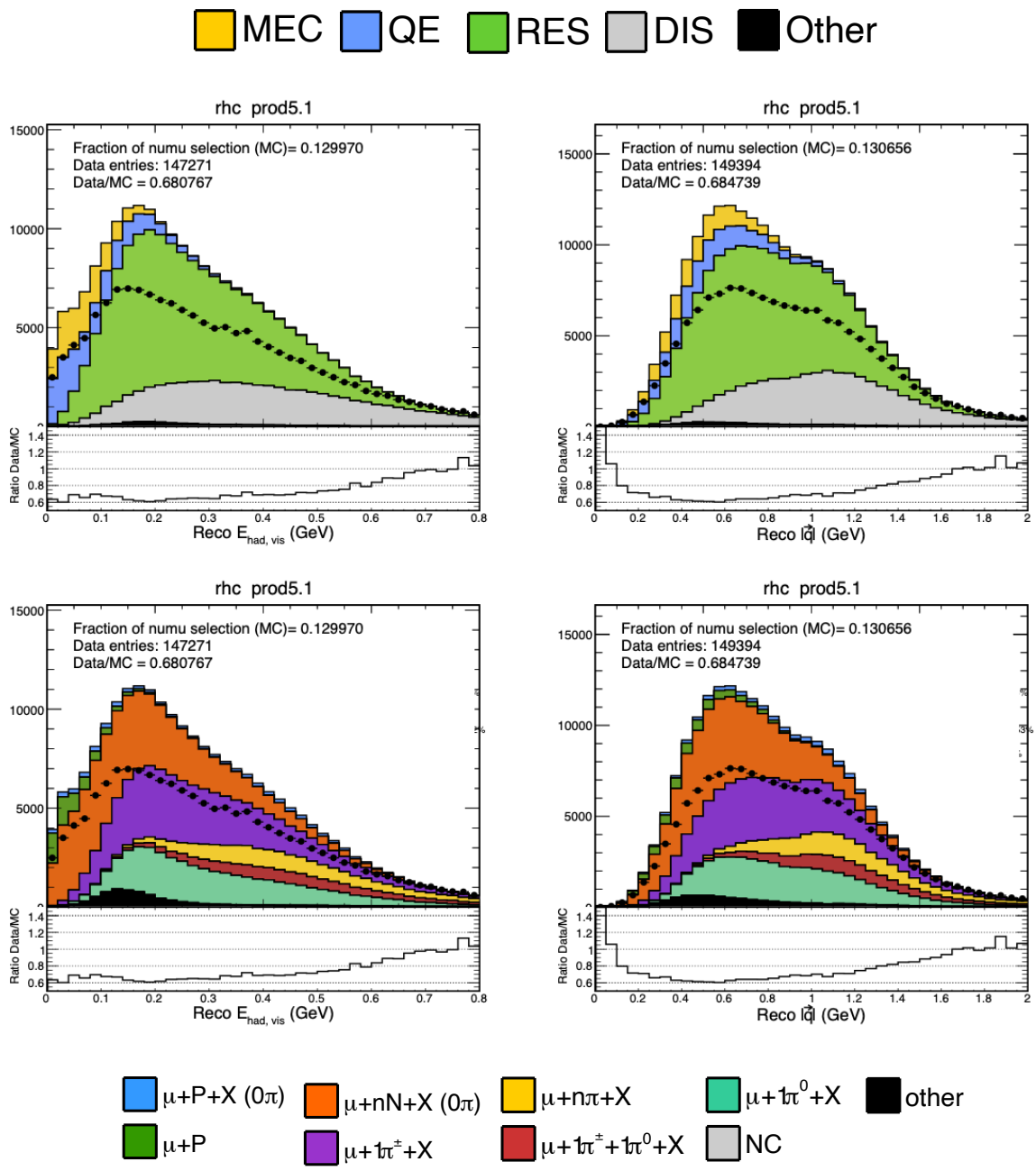

Figure 4.51: $\mu + X$ sample distributions of visible hadronic energy (left) and reconstructed three momentum (right) with interaction type breakdown (top) and final state primaries (bottom).

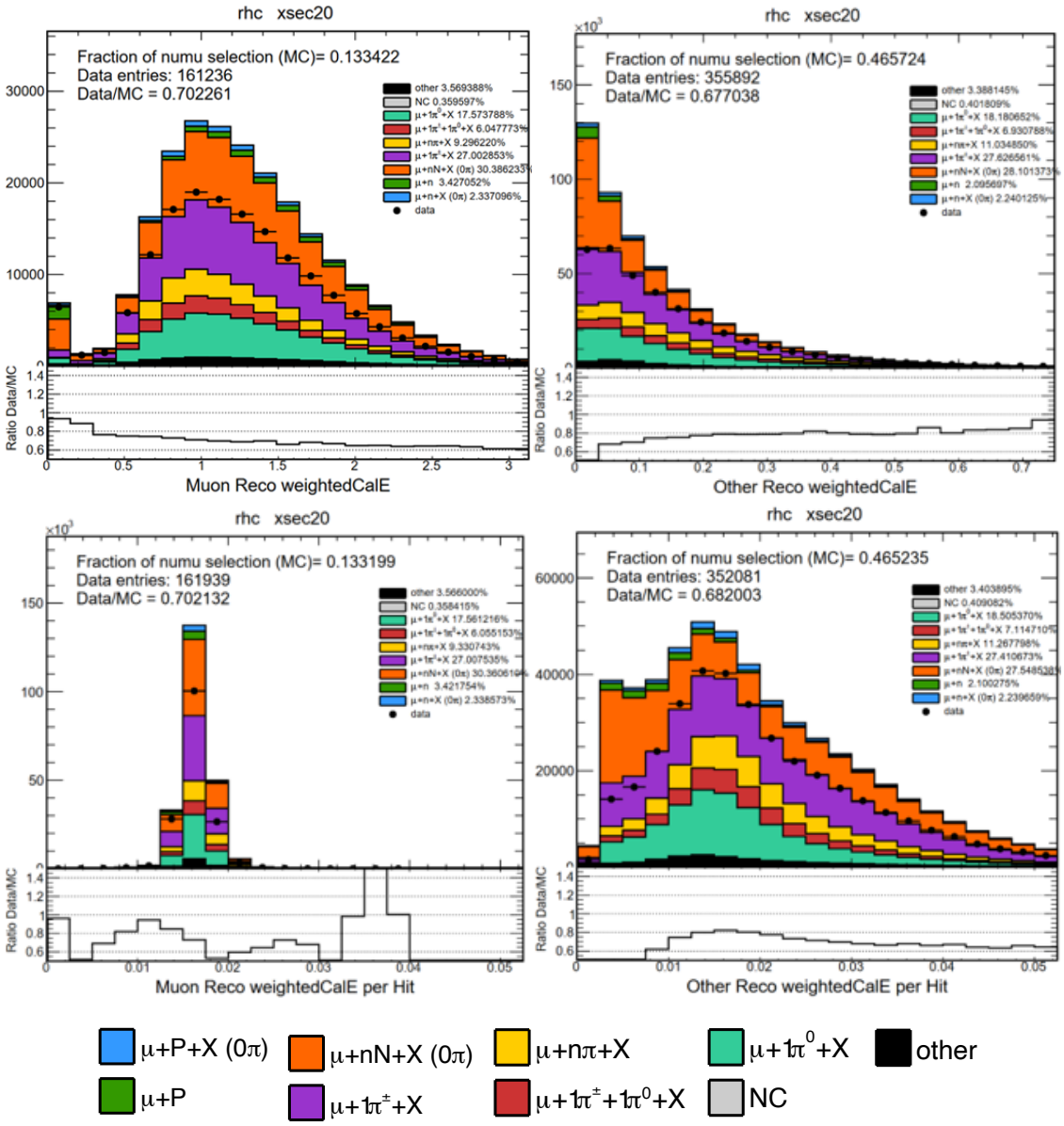

Figure 4.52: Weighted calorimetric energy (top) and Weighted calorimetric energy per hit (bottom) for muon and other prongs for RHC in the μ + X sample

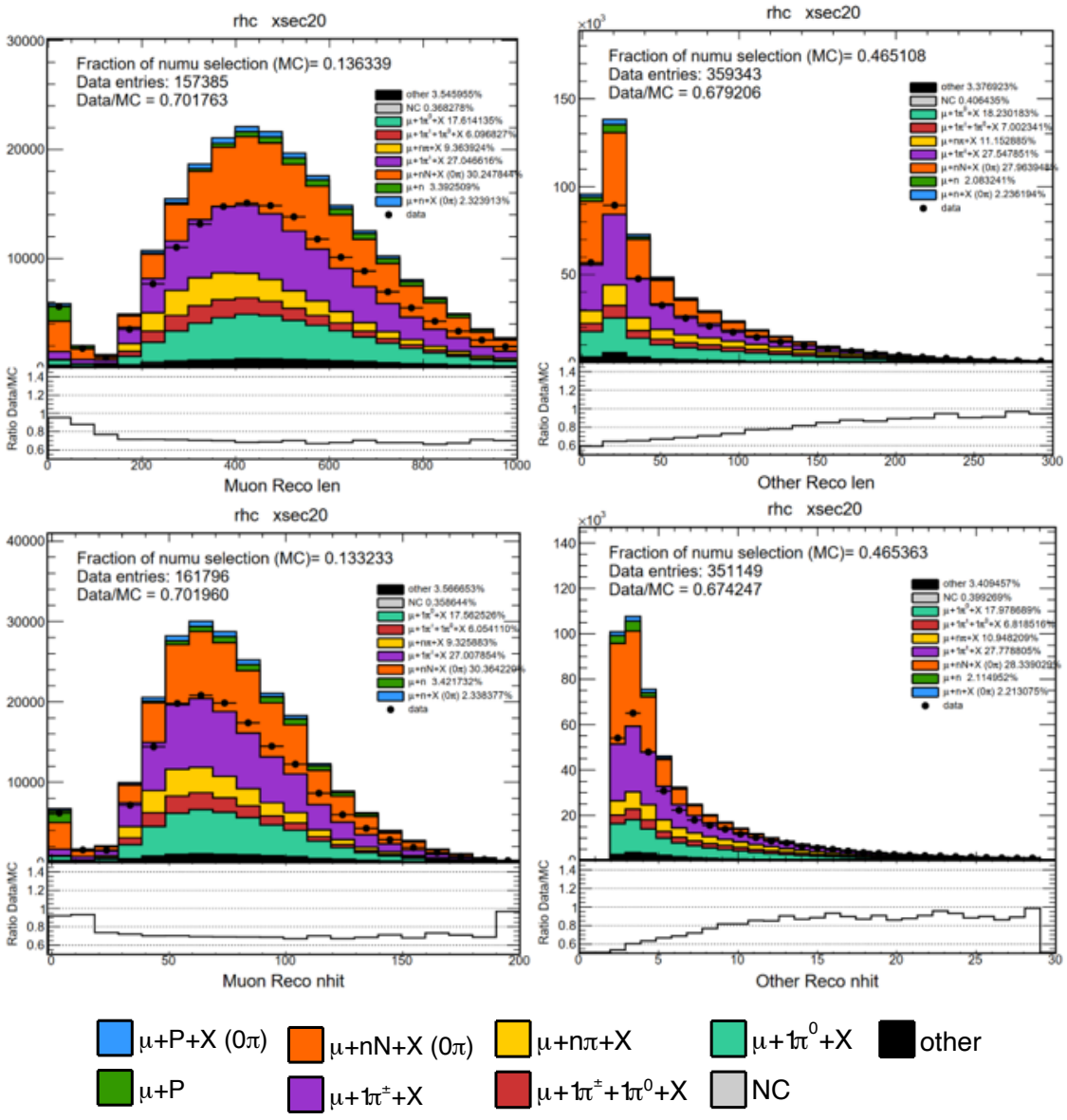

Figure 4.53: Length (top) and hits (bottom) for muon and other prongs for RHC in the μ + X sample

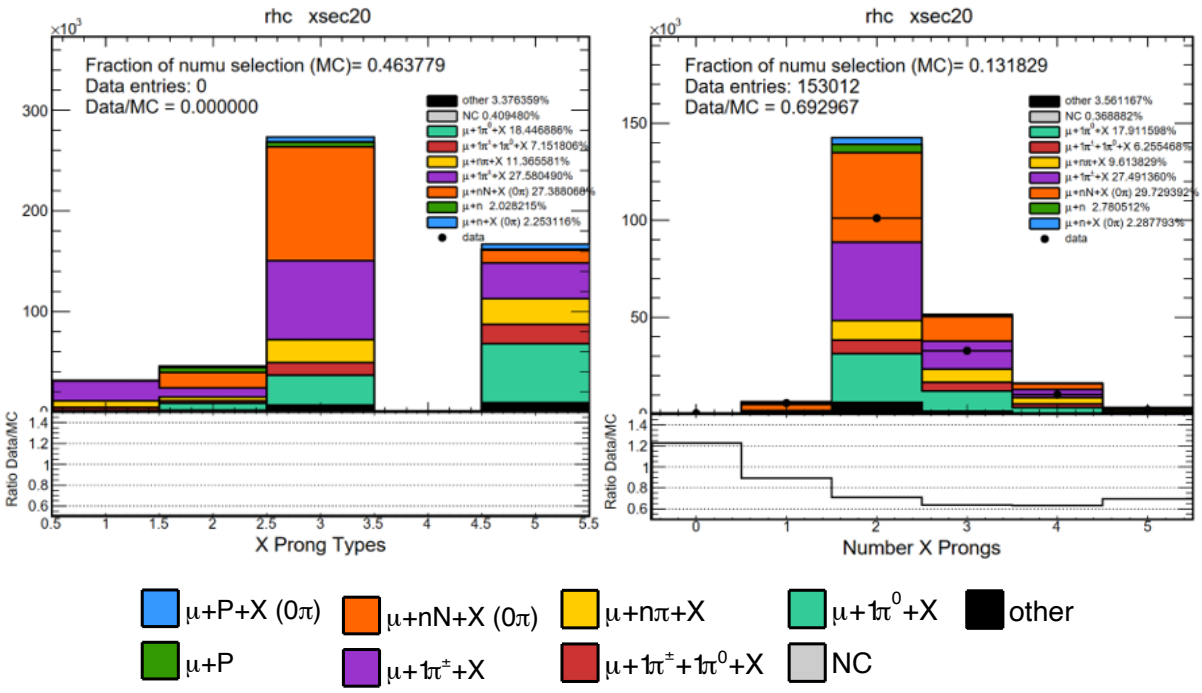

Figure 4.54: X prong types (left) and number of X prongs (right) for the RHC in the μ + X sample. Bin 1= $\pi^{\pm}$, Bin 2= μ, bin 3= P, bin 4= π^0, bin 5= γ

One way to subdivide this sample is by using the criteria of number of hits. Figure 4.55 shows the calorimetric energy per hit distribution for the whole sample and divided according to the nhits of X. Similar to the observation in the $\mu + P + X$ sample, the distribution agrees very well with the data for longer X prongs, however in contrast to the mentioned FHC case, the tail of this distribution is longer towards higher energy/hit values. The calE/hit for the shorter X prongs shows a very large overprediction corresponding to the excess seen at low calE/hit in the total sample distribution. Another interesting distribution is the true invariant mass of the events in these two categories. Figure 4.55 shows the breakdown, and clearly for the events with longer X prong the invariant mass second peak is much larger.

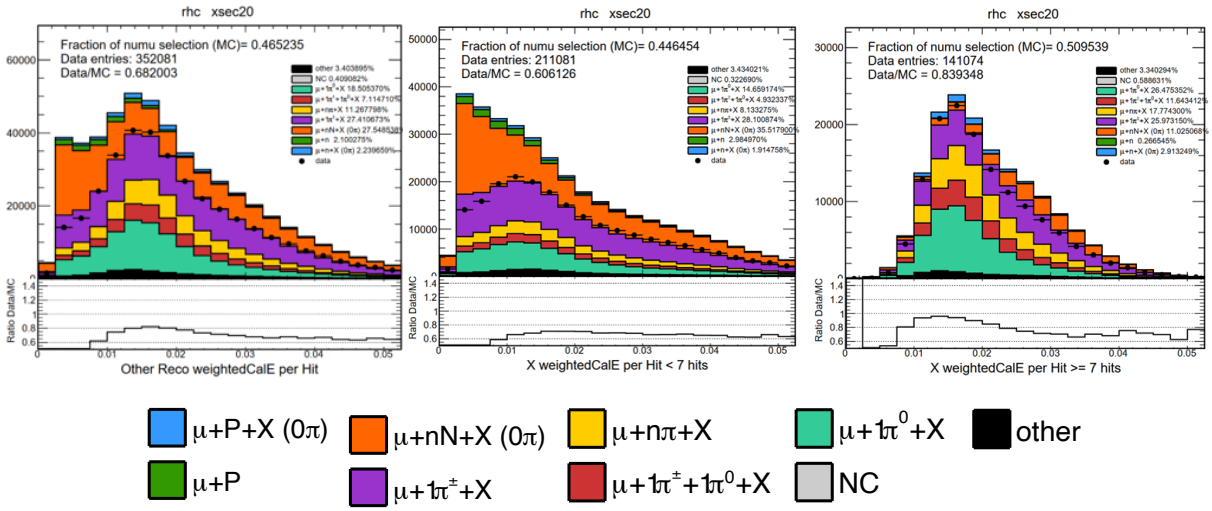

Figure 4.55: Weighted calorimetric energy per hit for other prongs for RHC in the μ + X sample total (left), when there are less than 7 hits (center), and when there are greater than or equal to 7 hits (right)

4.6.6.1 Comparison of pion prongs

Although the fraction of X prongs that have a true pdg of pions is small (see first bin in Figure 4.54), it is of interest to learn what kind of pions pass the selection, which rejects pions with $\text{CVN}_\pi > 0.5$. Figure 4.57 shows the characteristics of these pion prongs. Notice how the tails of the distributions of number of hits and weighted CalE are very short, up to $\approx$ 15 hits and $\approx$ 0.4 GeV. The length goes up to about 140-120 cm. In contrast, the true pion prongs in the $\mu + \pi + X$ sample for RHC go up to $\approx$ 0.8 GeV, $>$ 50 hits and $>$ 200 cm in length (Figure 4.44). The other striking difference is the broad CalE/hit distribution for this sample, compared to the narrow one in the $\mu + \pi + X$ sample . Both have the same approximate peak at $\approx$ 0.018 GeV/hit. So in summary, less energetic pions are selected in this sample.

4.6.7 Remaining sample

This sample contains, for both FHC and RHC, the events that did not match any of the other categories described before.

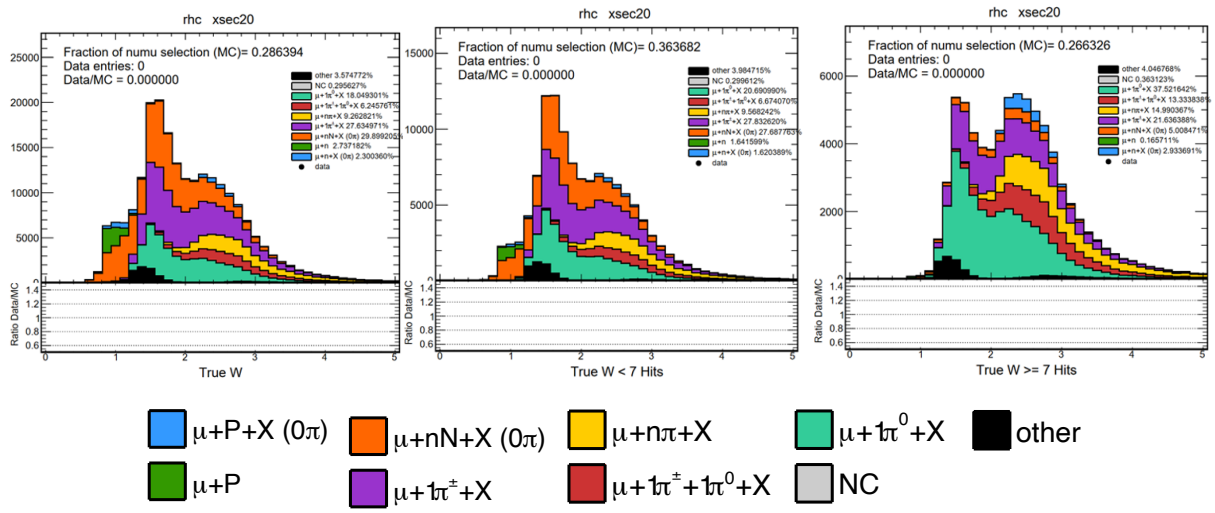

Figure 4.56: True W for RHC in the μ + X sample total (left), when there is an X prong with less than 7 hits (center), and when there is an X prong with greater than or equal to 7 hits (right)

The FHC sample is dominated by RES and DIS interactions. In the hadronic visible energy distribution, there are two peaks, the lower one contains most of the MEC and QE which are subdominant in the sample. Overall there is an overprediction of about 10%. The true final state categories that dominate are the single charged pion (purple) and multiple protons with no pions (orange) . However there is a significant fraction of the other categories with pions. For RHC, the overprediction is much smaller, at about 6%. This sample contains more QE and MEC than the RHC version, however RES events dominate. The $|\vec{q}|$ distribution has a peak at around 0.4 GeV and a longer tail. It is also notorious that there is a large fraction of events with only a muon and a neutron in the final state (green). These populate the lowest hadronic visible energy bins, along with the events with multiple neutrons and no pions (orange). The tail of this distribution is dominated by interactions with pions i n the final state.

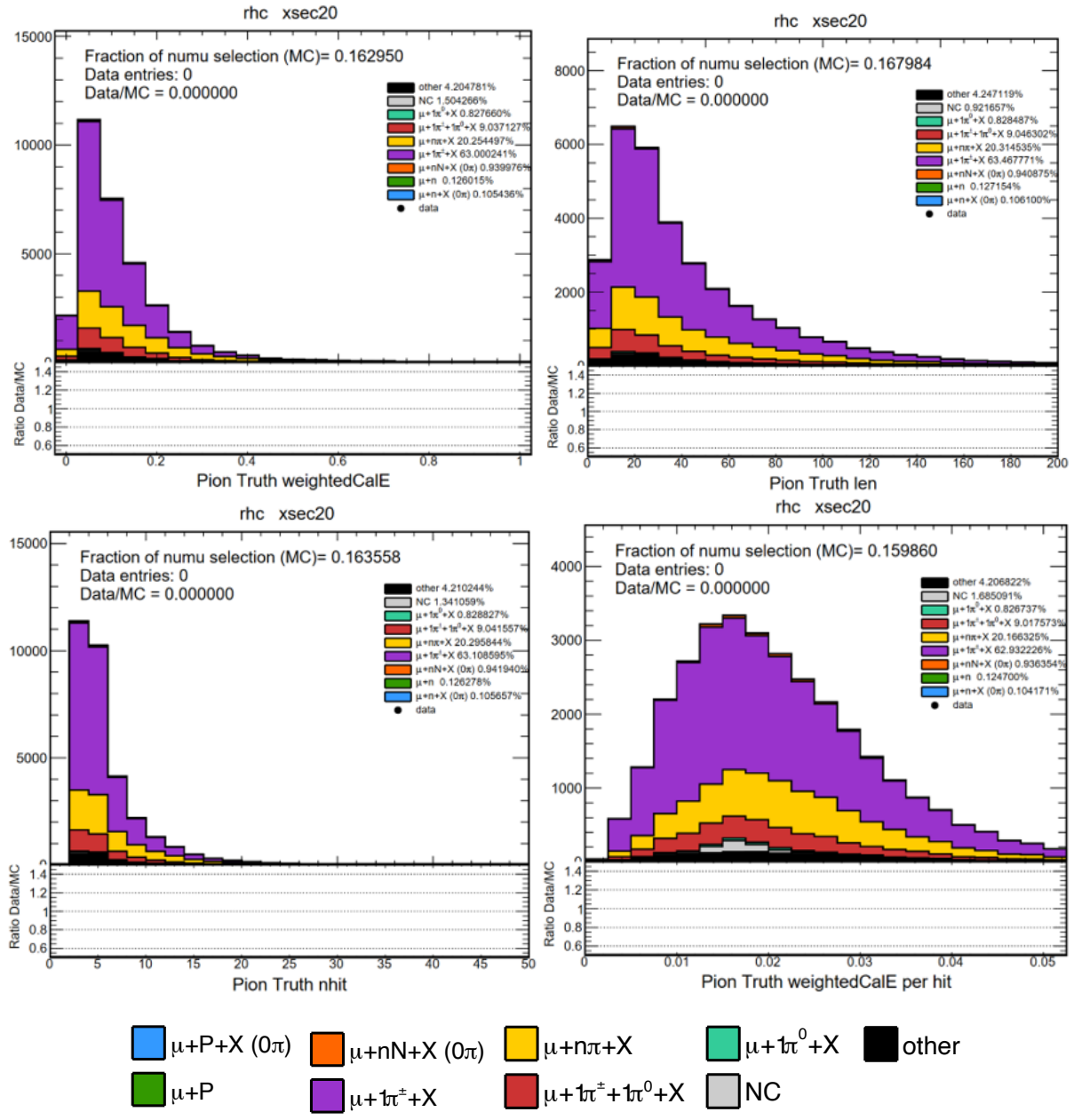

Figure 4.57: Weighted calorimetric energy (top left), length (top right), number of hits (bottom left), and weighted calorimetric energy per hit (bottom right) for truth pions for RHC μ + X sample

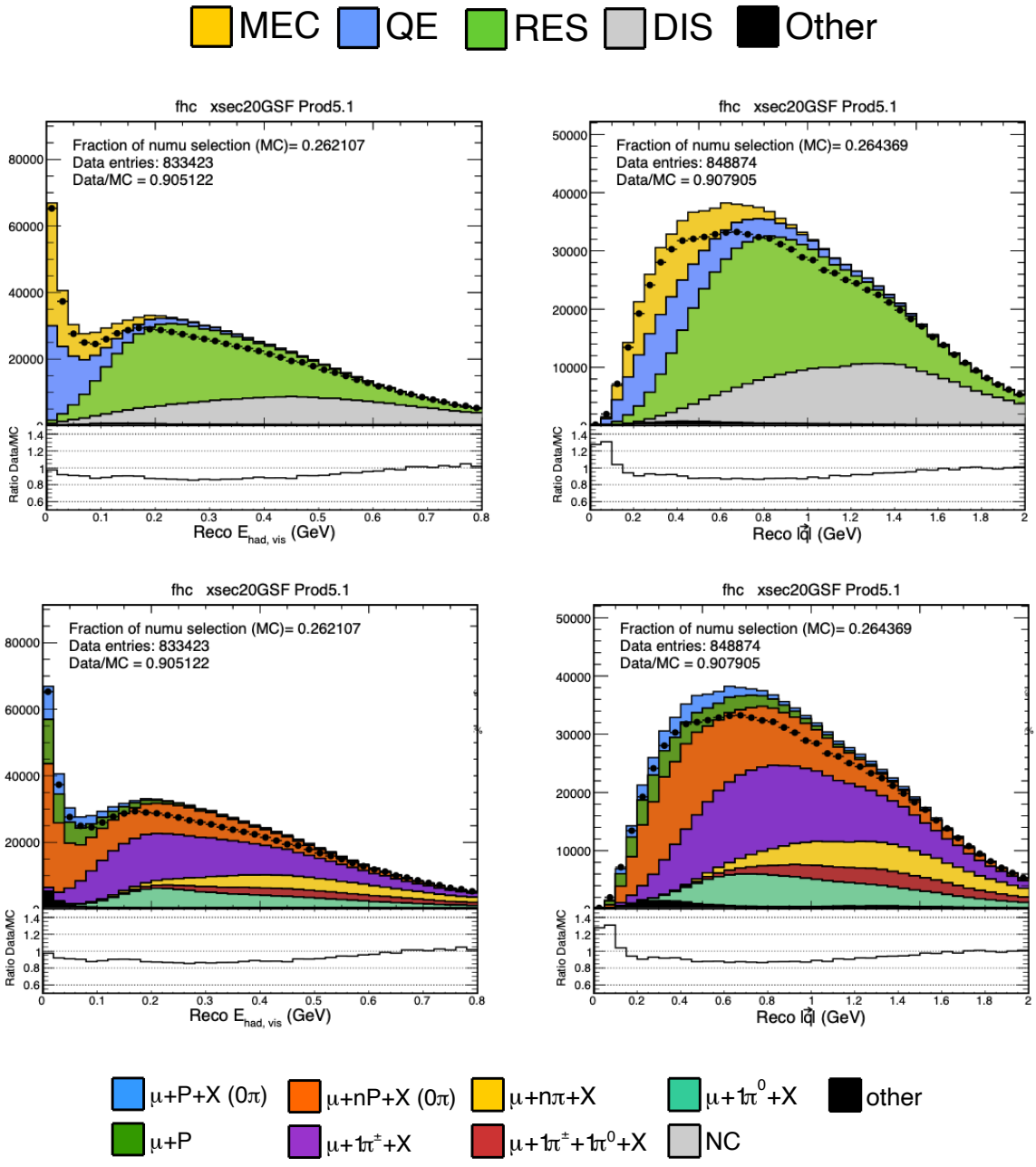

Figure 4.58: Distributions of visible hadronic energy (left) and reconstructed three momentum (right) with interaction type breakdown (top) and final state primaries (bottom).

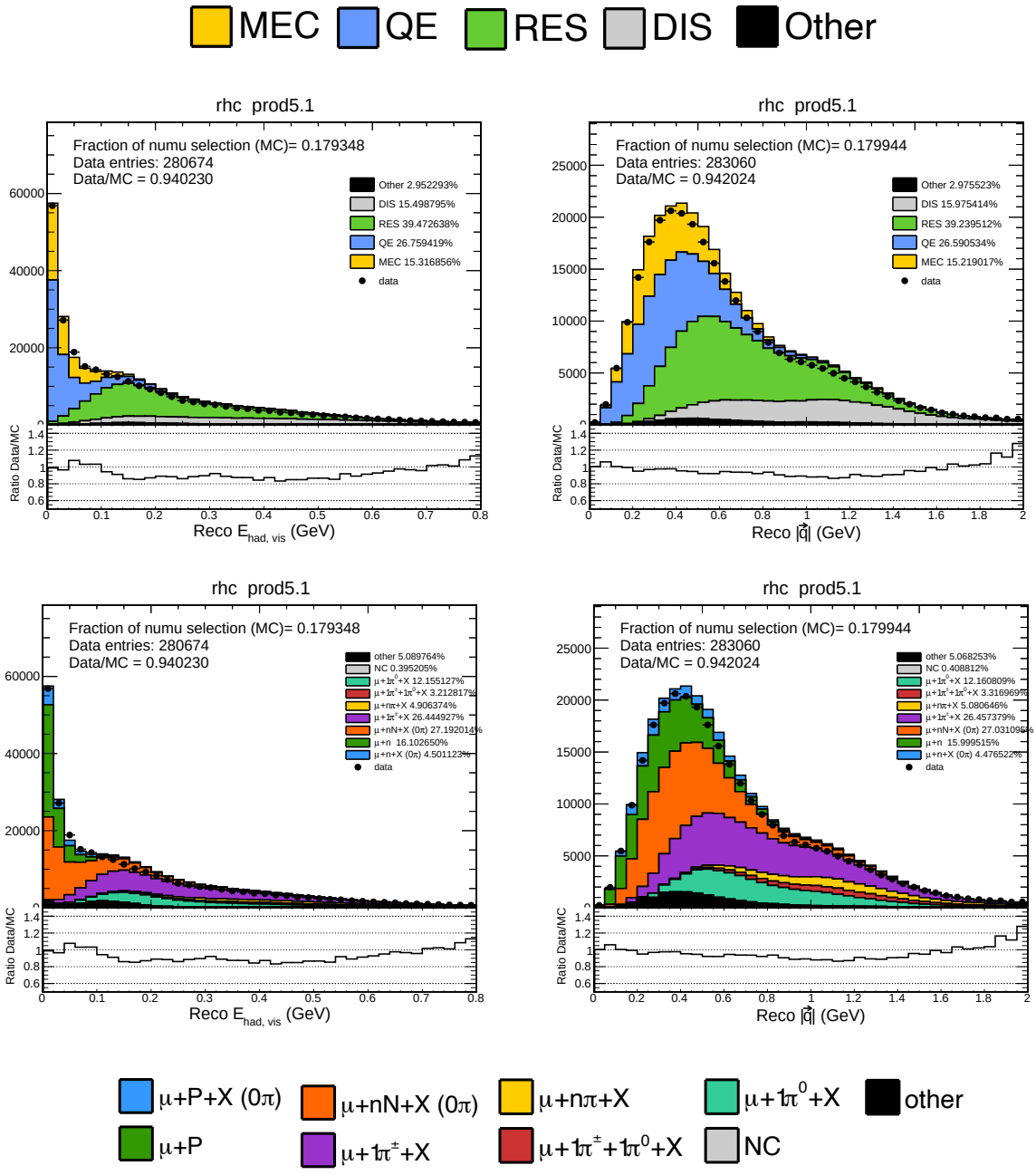

Figure 4.59: Distributions of visible hadronic energy (left) and reconstructed three momentum (right) with interaction type breakdown (top) and final state primaries (bottom).

4.6.8 Summary

The NOvA tune shows an overall good agreement with the ND data, as seen in Figure 3.13. A further look into the data and simulation via the topology samples revealed that this is still true for some of these samples. The FHC μ and $\mu + P$ samples show good agreement, well within the cross section uncertainties. The $\mu + \pi + X$ sample is slightly underpredicted for the lower bins of hadronic visible energy and three momentum transfer. The *Remaining* sample is overpredicted at higher energy/momentum. The most notorious disagreement is for the $\mu + P + X$ sample, which in addition is very far from the cross section uncertainty range, as shown in Figure 4.60. For the RHC samples, the agreement is very similar, with a slight overprediction in the $\mu + P$, and also some overprediction at the higher visible hadronic energy bins of the $\mu + \pi + X$ sample. The $\mu + X$ sample is analogous to the FHC $\mu + P + X$ sample, as it also shows a significant overprediction outside of the uncertainty range (see figure 4.60).

In addition to these overall features, the pion samples had two subcategories of events. With the presence of additional prongs to the pions (X prongs) the distributions were oversimulated, and undersimulated otherwise. The pion selection was found to increase the amount of background when varying the pion score criteria from 0.8 to 0.5, with most background from proton prongs and photons that are confused as pions by their CVN score.

The very overpredicted $\mu + P + X$ FHC sample showed different features for the different prongs. The proton prongs had an approximate flat data/MC ratio, pointing towards a normalization difference. However the X prongs had a different level of agreement depending on the length or number of hits. The short X prongs(less than 7 hits) in this sample were oversimulated, while the rest of the X prongs had a good agreement and reconstruction (energy/hit). Most of the X prongs have a true id of protons or photons.

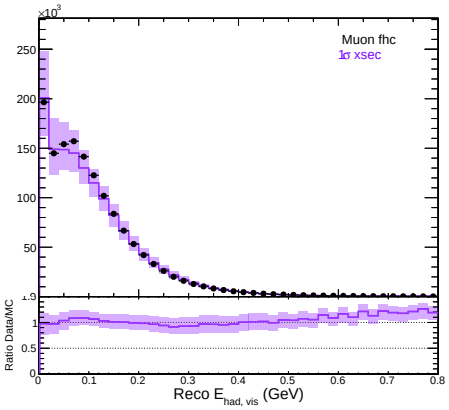

(a) μ

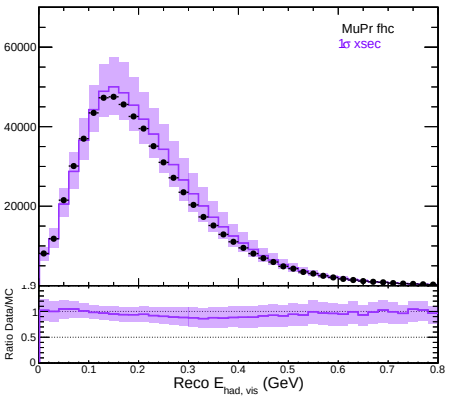

(b) $\mu + P$

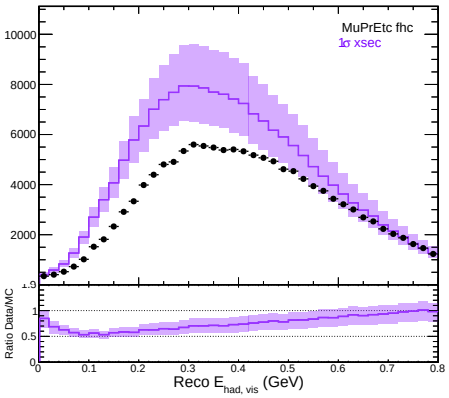

(c) $\mu + P + X$

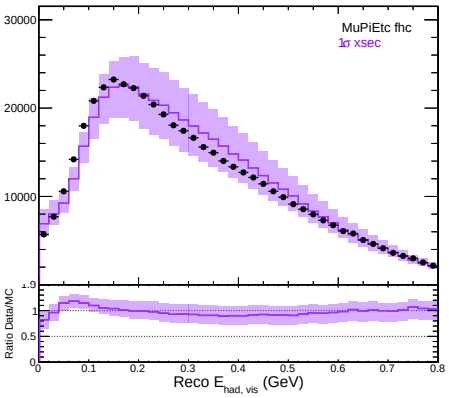

(d) $\mu + \pi + X$

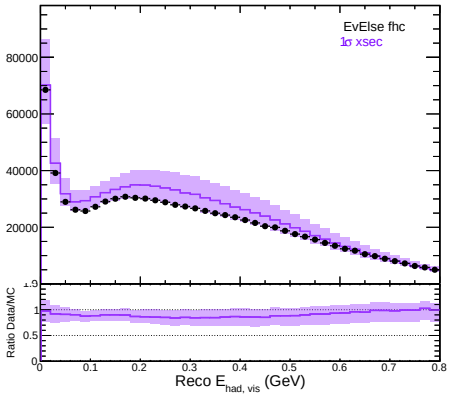

(e) *Remaining*

Figure 4.60: FHC with 1σ cross section uncertainties

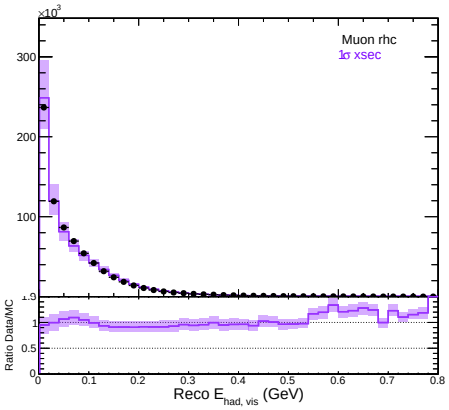

(a) μ

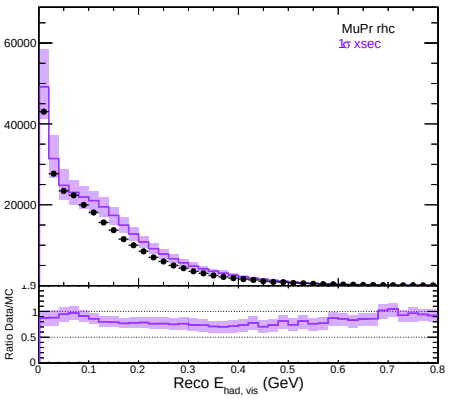

(b) $\mu + P$

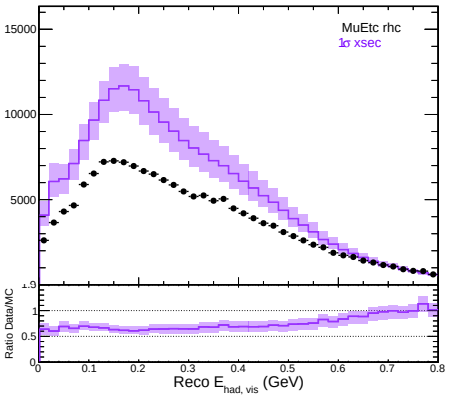

(c) $\mu + X$

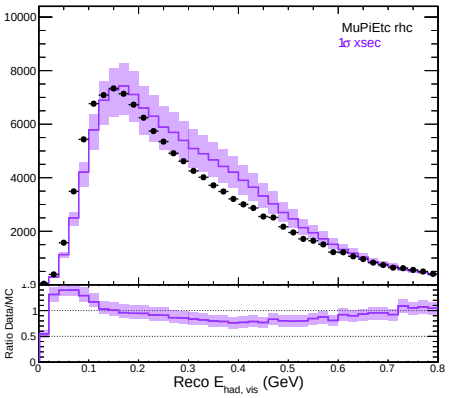

(d) $\mu + \pi + X$

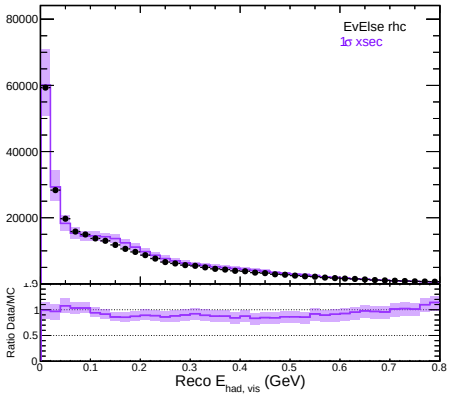

(e) *Remaining*

Figure 4.61: RHC topologies with 1σ cross section uncertainties

This study mainly focused on describing the pion and X prongs in the $\mu + \pi + X$, $\mu + P + X$ and $\mu + X$ samples, as these are the most complex topologies, and the worse data/MC agreement. This has led to the development of additional uncertainties related to the Resonant and DIS events, which will be described in chapter 5. The disagreement is most likely not entirely explained by the cross section model, there are other aspects that impact the data/MC agreement, such as effects of reconstruction, but such studies are out of the scope of this work. In addition the samples are used to constrain cross section parameters, as well as flux and detector systematics with a fit which will also be described in Chapter 5 .

CHAPTER 5. CONSTRAIING MODEL PARAMETERS USING NEAR DETECTOR DATA

The oscillation analysis in NOvA essentially requires measuring the rate and energy spectrum of ν_e and ν_μ interactions at the Far Detector. This measurement requires a good understanding of the neutrino interactions, so that the rate measured can be compared to predicted rates, based on simulations, and extract the oscillation parameters. As described in the previous chapters, there are a number of aspects that affect the predictions, including but not limited to the cross section model, beam simulation and detector response. The Near Detector selection of ν_μ does not undergo oscillations, and therefore it can be used to understand the behavior of the predictions as a function of said model parameters, without the additional shape change expected from the neutrino oscillations.

As seen in the previous chapter, the selected samples present distinct features depending the topology of the final state. These selections are a proxy for approximately separating the ND data set into subsets enhanced in the interaction types or true final states. This translates to sensitivity to different model parameters of the current NOvA simulation for each topology. This chapter describes the use of these samples to obtain constrains for the model parameters, with both fake data and real Near Detector data.

5.1 Fitting procedure

The method to constrain systematic uncertainties using the Near Detector data is via minimization of the Poisson log-likelihood function summed over all bins N and all systematic uncertainties, or model parameters, S:

$$\mathrm{L}(\vec{\delta}) = \ln \lambda(\vec{\delta}) = -2 \sum_{i=1}^{N} \left[N_i(\vec{\delta}) - O_i + O_i \ln \frac{O_i}{N_i(\vec{\delta})} \right] + \sum_{j=1}^{S} \frac{\delta_j^2}{\sigma_j^2} \tag{5.1}$$

with O_i is the observed number of events in bin i, N_i is the predicted number of events in the bin i. The vector $\vec{\delta}$ represents all the systematic parameters. The second term, also referred as *penalty term*, contains δ_j is the fitted value of systematic j and σ_j is its error.

A detailed description of the systematic parameters included in the fit are described in the following section. Specifically, this minimization procedure is done using MINUIT [95].

5.2 Systematic uncertainties for ND fit

The NOvA software allows to implement systematic uncertainties, which encode the variation allowed by the different model parameters embedded in the simulation. We call deviations from the central value *systematic shifts*. The majority of the uncertainties in the NOvA simulation are related to the cross section model, based on the GENIE simulation, described in chapter 3. A subset of these uncertainties are taken directly from GENIE, some need to be customized and new ones have to be implemented in accordance to the adjustments described as well in chapter 3. Not all of the uncertainty shifts produce significant changes in the distributions of the ND simulation in reconstructed variables, and therefore can not be constrained. Other uncertainties produce very small variations in the samples, and therefore are difficult to constrain. Each of the systematic uncertainties accounts as a degree of freedom in the fit, so it is relevant to only keep the ones that can be constrained.

To optimize the number of degrees of freedom of the fit, only the most relevant systematic uncertainties are considered. The specific metric to discriminate relevant systematics is the change in χ^2, with respect to the nominal simulation, when shifting by $\pm\sigma$ each systematic parameter. The nominal simulation refers to the central value, or the NOvA tune, produced by the adjustments in MEC interactions and FSI, from chapter 3. Only the systematic uncertainties which produce a $\Delta\chi^2 > 100$, summed over the 10 samples, are considered relevant for this analysis. The average $\Delta\chi^2$ for $\pm1\sigma$ shifts of all samples, for each systematic uncertainty considered, is displayed in Figure 5.1.

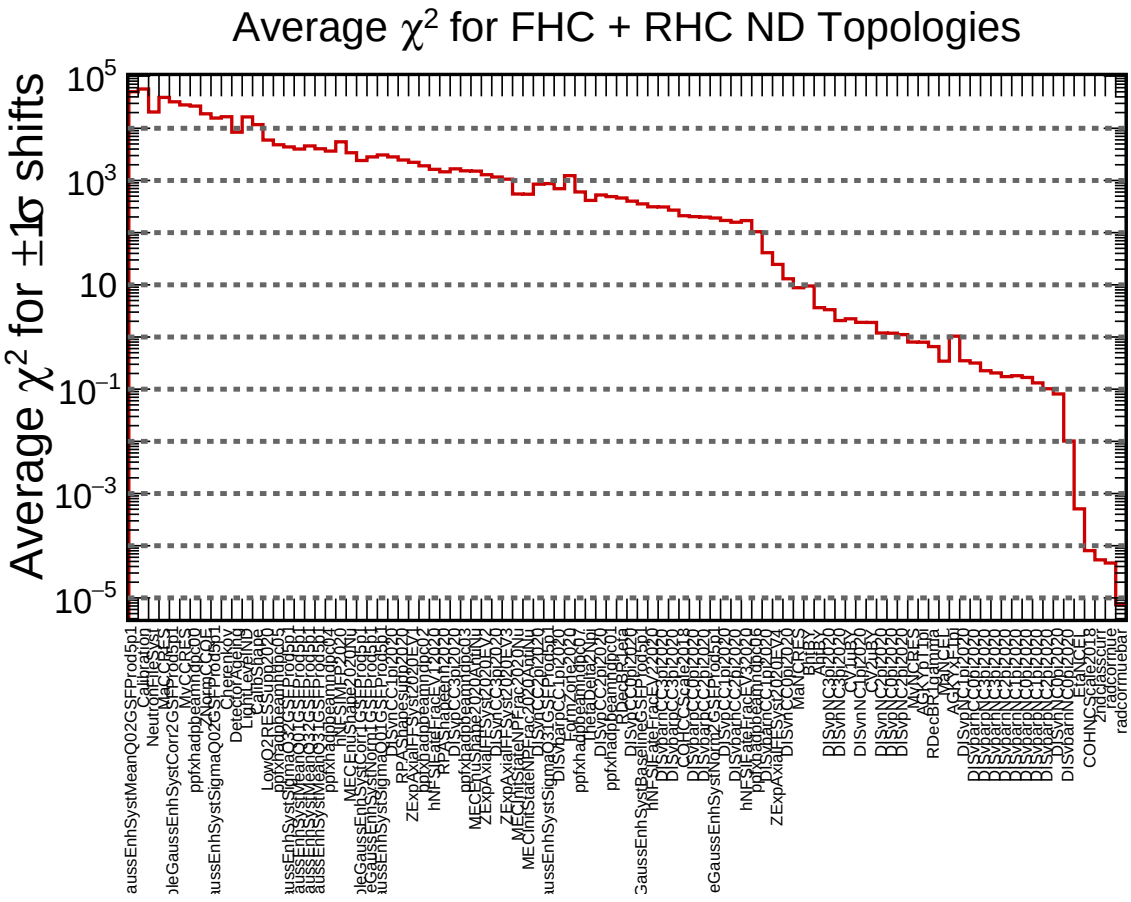

Figure 5.1: Average χ^2 for $\pm1\sigma$ shifts over all samples.

The cutoff at 100 excludes mostly systematic uncertainties related to neutral current cross section parameters, whereas the systematic uncertainties with the largest $\Delta\chi^2$, which translates to larger impact in the samples, are related to the MEC adjustment and detector response, such as Calibration. The next section details the selected uncertainties that can be constrained using ND data. Indicated in parenthesis is the abbreviated parameter name. Special emphasis is put in the *Resonance scale, Resonance neutrino-nucleon* and *DIS Hadronization model*, as these parameters were specifically developed for this analysis and were not part of the *NOvA tune* previously used in [10].

5.2.1 Cross section systematic uncertainties

5.2.1.1 Quasi-Elastic interactions

Z-expansion Normalization : represents a simple $+20\%/-15\%$ QE normalization factor(`ZNormCCQE`) .

Z-Expansion eigen vectors :4 shape parameters corresponding to the $a_1 - a_4$ parameters from the z expansion formalism, as described in chapter 3. These are function of Q^2. Although four parameters are available, only the first 3 are relevant for this analysis(`ZExpAxialFFSyst2020_EV1,2,3`).

QE RPA :This uncertainty represents how well the Random Phase Approximation (RPA) effect, long-range nuclear correlations resulting in weak nuclear charge screening, is understood [96]. There are two uncertainty knobs that control the enhancement at large Q^2 and suppress it at low Q^2 (`RPAShapeenh2020,RPAShapesupp2020`) .

5.2.1.2 Resonance interactions

Ma CC Affects $\frac{d^2\sigma(\text{CCRES})}{dWdQ^2}$ in both shape and normalization(`MaCCRES`).

Mv CC Affects $\frac{d^2\sigma(\text{CCRES})}{dWdQ^2}$ in both shape and normalization(`MvCCRES`).

Branching ratio of η decay Tweaks the branching ratio of the decay $R \to X + \eta$, for instance $N^+(1440) -> p + \eta$, only considered for fake data fits (`RDecBR1eta`).

$\theta\Delta$ to $N\pi$ Distorts the π angular distribution in the decay $\Delta \to N + \pi$ (`Theta_Delta2Npi`).

Q^2 suppression The GENIE CMC selected does not require a weight correction for the resonant interaction rate, however in a previous version of the NOvA simulation (which we call *prod*4) a discrepancy in low Q^2 was observed. This required a reweight correction. An uncertainty is taken into account, constructing it from the difference of *prod*4 with a MINOS-like

Q^2 suppression [97], with the current one. The difference between these two simulations is fit to the function $1 - Ae^{-bQ^2}$. The difference between the result of this fit and the nominal simulation constitutes this one-sided uncertainty (`LowQ2RESSupp2020`).

Table 5.1: Parameters for RES low-Q^2 suppression systematic uncertainty

Parameter	**FHC**	**RHC**
A	0.391	0.429
b	12.9	20.9

Resonance scale This is a custom uncertainty developed for this analysis. The rate of events coming from resonance decays can vary with the two uncertainties developed for this purpose:

- Delta Resonance scale: event is reweighed by $1 + n$, where 1 is 20%(`RESDeltaScaleSyst`).
- Other Resonances scale: event is reweighed by $1 + n$, where 1 is 20%(`RESOtherScaleSyst`).

Figure 5.2 shows the simulated invariant mass distribution for the total FHC selection, with these systematic shifts applied. This translates into the reconstructed variables shown in figures 5.3 and 5.4. The systematic uncertainties are applied to the $\mu + \pi + X$ sample, which is dominated by resonance interactions. The Delta scale systematic afffects lower values of E_{had} and $|\vec{q}|$, in contrast with the non-Delta case (Figure 5.4) where the higher E_{had} and $|\vec{q}|$ bins are affected. Notice that this knob allows the model to have enough freedom to match the ND data in both the FHC and RHC sample.

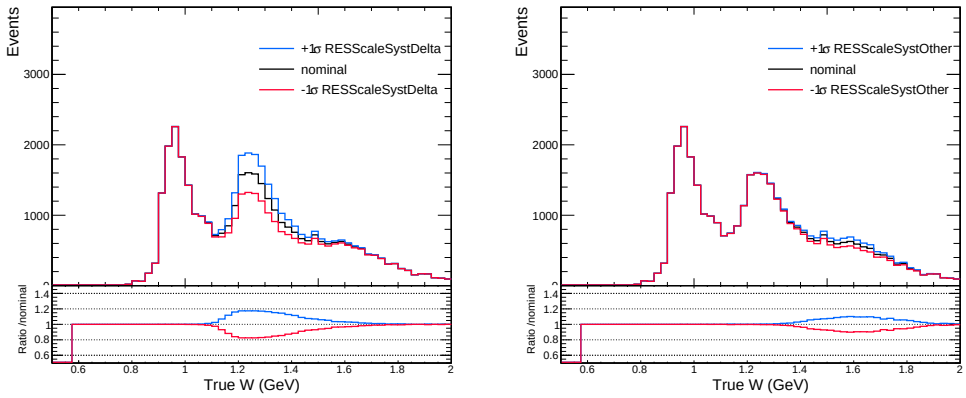

Figure 5.2: True invariant mass distribution of neutrino selection with Delta (left) and non-delta Resonance (right) scale systematic uncertainty

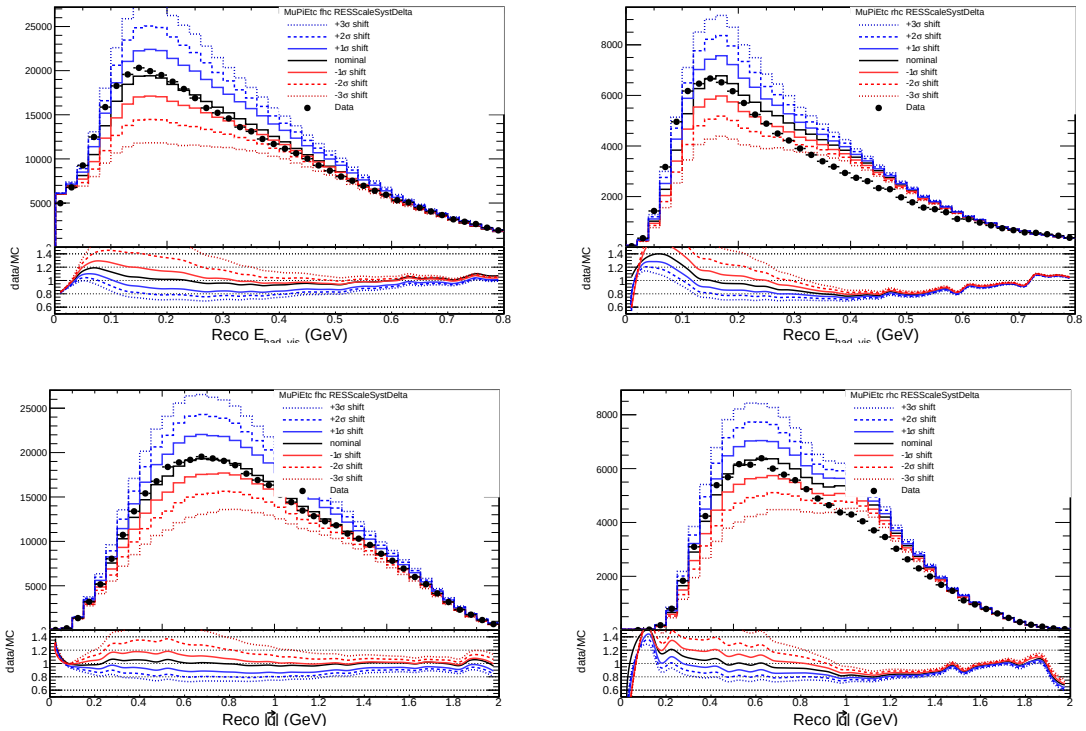

Figure 5.3: Distributions of simulation and data $\mu + \pi + X$ samples with Delta Resonance scale systematic uncertainty for FHC (left) and RHC (right) reconstructed variables $E_{had,vis}$ (left) and $|\vec{q}$ (right).

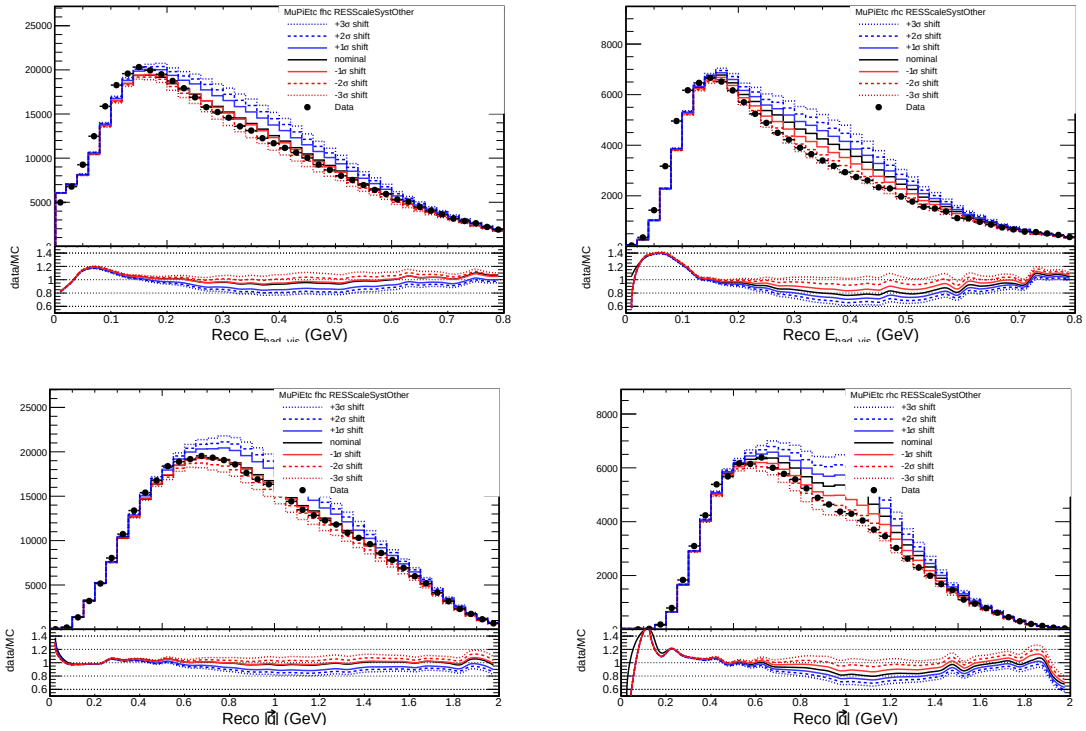

Figure 5.4: Distributions of simulation and data μ+π+X samples with non-Delta Resonance scale systematic uncertainty for FHC (left) and RHC (right) reconstructed variables $E_{had,vis}$ (left) and $|\vec{q}$ (right).

Resonance neutrino-nucleon ratio This is a custom uncertainty developed for this analysis. A parameter that introduces flexibility on the model to vary the $\nu p/\nu n$ and $\bar{\nu}p/\bar{\nu}n$ cross section rations. This implies the introduction of two weights:

- $r_{\nu p/\nu n}$: The $w_p = (1.0 + f_\nu)$ weight is applied to all resonance events with νp initial state, and $w_n = (1.0 - f_\nu)$ is applied to those with νn in the initial state. The default value for f_ν is zero, and 1σ value is 0.05.

- $r_{\bar{\nu}p/\bar{\nu}n}$: The $w_p = (1.0 + f_{\bar{\nu}})$ weight is applied to all resonance events with $\bar{\nu}p$ initial state, and $w_n = (1.0 - f_{\bar{\nu}})$ is applied to those with $\bar{\nu}n$ in the initial state. The default value for $f_{\bar{\nu}}$ is zero, and 1σ value is 0.05.

The effect of this uncertainties is shown in Figure 5.5 for the samples where they have the most impact: the $\mu + \pi + X$ FHC sample with $\pm 1, 2, 3\sigma$ shifts for ratio$_{\nu p/\nu n}$ and the $\mu + \pi + X$ RHC sample with the $\pm 1, 2, 3\sigma$ shifts for ratio$_{\bar{\nu} p/\bar{\nu} n}$ (`RES_vpvn_Nu_ratio_xsec_syst, RES_vpvn_NuBar_ratio_xsec_syst`).

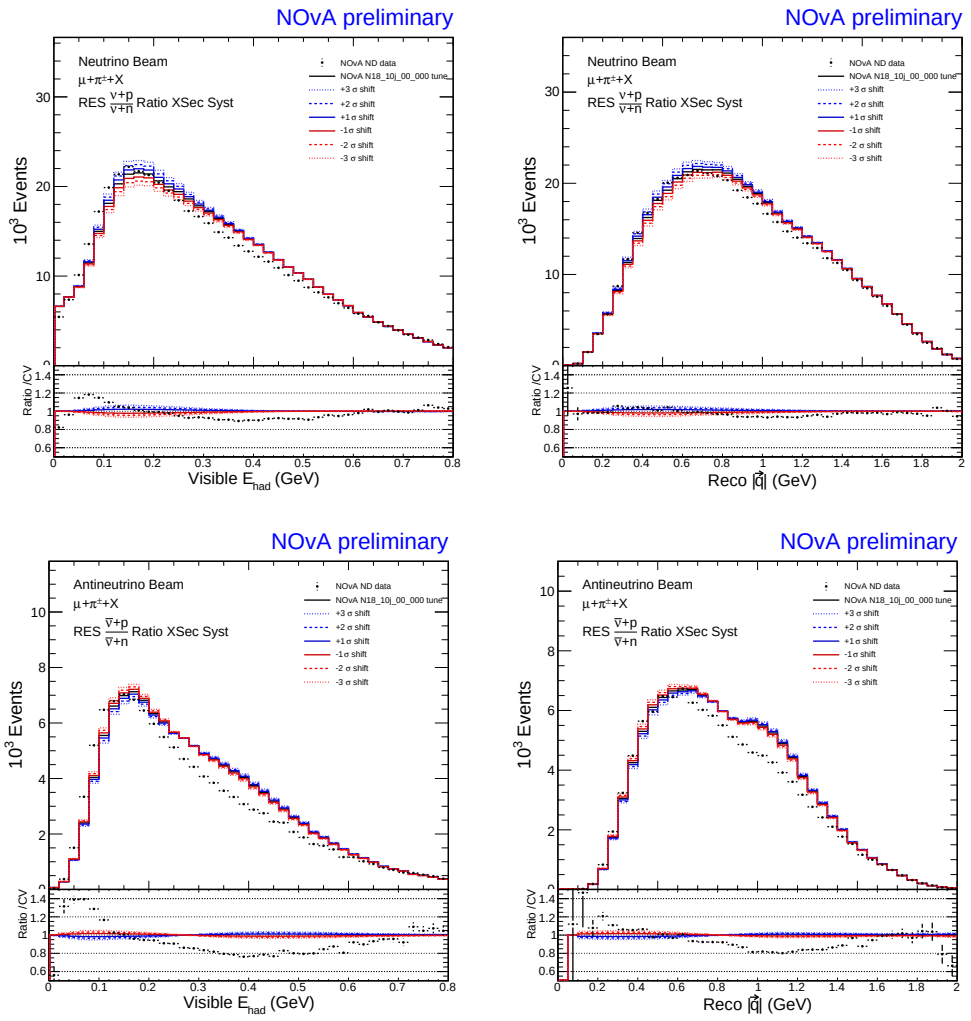

Figure 5.5: $\mu + \pi + X$ FHC (RHC) samples with resonance neutrino(antineutrino)-nucleon ratio systematic uncertainty.

5.2.1.3 Deep-Inelastic Scattering interactions

Nonresonant Nπ normalizations GENIE recommends a 50% normalization uncertainty for transition-DIS events (DIS events with high W, $1 < W < 2$ GeV and $Q^2 < 1$). We implement a separate normalization systematic for each (0, 1, 2, 2+) pions, neutrinos vs anti-neutrinos, CC vs NC, and whether interacting on a neutron or proton, for 4x2x2x2 = 32 different individual systematics. The uncertainty linearly decreases from 50% at W = 3 GeV to 5% at W = 5 GeV, and 50% for $W < 3$ GeV. Although this results in 32 individual systematics knobs, for the present analysis, the most relevant ones are selected, 9 out of 32, based on their impact of the χ^2 in the topology samples:

- DIS$\bar{\nu}$nCC3pi
- DISνnCC1pi
- DISνpCC0pi
- DIS$\bar{\nu}$pCC1pi
- DISνnCC2pi
- DISνpCC2pi
- DIS$\bar{\nu}$pCC3pi
- DISνnCC3pi
- DISνpCC3pi

DIS formation zone During the process of forming hadrons from the quarks that are modeled as the outgoing particles from a DIS scattering, partons may propagate some distance within the nuclear medium before they coalesce into hadrons. The "formation zone" is the distance constant in a decaying exponential distribution from which hadrons' pre-hadronization propagation is sampled [98]. GENIE provides two knobs, for pions and nucleons. A single uncertainty was created, with alternate simulation to compare with the base simulation, such that both the pion an nucleon formation zone are shifted simultaneously(`FormZone2020`).

DIS Hadronization model This is a custom uncertainty developed for this analysis. It consists in two systematic parameters that control final state hadron production for events with a multiplicity of 2. By default, a DIS interaction with initial state $\nu + n$, with a final state of hadronic charge state $Q = +1$, the default probability of the outgoing particles is 1/3 for $\pi^0 + p$ and 2/3 for $n + \pi^+$. Comparably, for antineutrino interactions with initial state $\bar{\nu} + p$, the final

state with $Q = 0$ has the default probability of 2/3 for a $\pi^- + p$ final state and 1/3 for $n + \pi^0$. To allow these probabilities to vary, two weights are introduced: f_0 and f_1. The weight should be applied based on the identity of the final state (pre-FSI hadron) as indicated in table 5.2.
Figure 5.6 displays the effect of this systematic uncertainty in the muli-hadron topology sample

Table 5.2: Parameters for DIS hadronization systematic uncertainty

Q	0	1
Weight for events with protons	$1 + 1.5f_0$	$1 + 3f_1$
Weight for events with neutrons	$1 - 3f_0$	$1 - 1.5f_1$
New hadronization fraction	$f_0 = 0.0 \pm 1/3$	$f_1 = 0.0 \pm 1/3$
Physical bounds	$(-2\sigma, +1\sigma)$	$(-1\sigma, +2\sigma)$
Parameter name	`DIS_nubar_hadro_Q0_syst`	`DIS_nu_hadro_Q1_syst`

$\mu + \pi + X$.

5.2.1.4 2p2h interactions

Central value parametrization We keep 10 out of the 13 parameters in table 3.4, except for the *Normalization, Mean q_0 and Correlation* of Gaussian 2. One of these is excluded due to their small impact in the χ^2 of the samples and the other two after concluding that these parameters are degenerate. In other words that they overconstrain the shape of the reconstructed variables. More of this will be explained in the fake data fits section (5.4.2)
(`MECDoubleGaussEnhSyst{Baseline, SigmaQ3_2, SigmaQ0_2, MeanQ3_2, Corr_1, SigmaQ3_1, SigmaQ0_1, MeanQ3_1, MeanQ0_1, Norm_1}_GSFProd5p1`)

Nucleon pair fraction One uncertainty for neutrinos and one for antineutrinos, as detailed in Chapter 3.2.3 (`MECInitStateNPFrac2020Nu, MECInitStateNPFrac2020AntiNu`).

Neutrino Energy dependence Two uncertainties (for neutrinos and antineutrinos) as described in Chapter 3.2.3 (`MECEnuShape2020Nu,MECEnuShape2020AntiNu`).

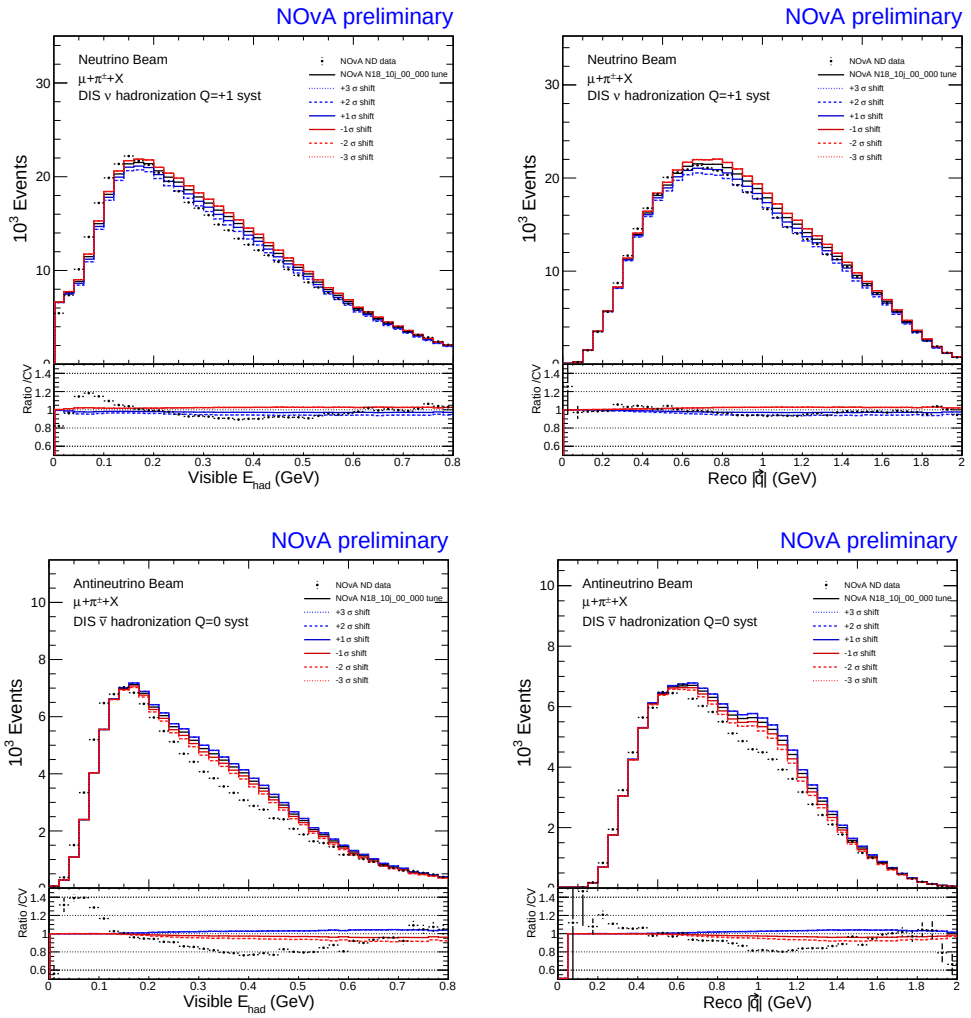

Figure 5.6: $\mu + \pi + X$ samples with DIS hadronization systematic uncertainites applied. Top is Q_1 and bottom is Q_0.

5.2.1.5 Additional cross section uncertainties

Final State interactions We keep one of the fate fractions and the Mean Free Path parameter described in table 3.3. For fake data fits, the whole set of parameters are used (`hNFSI_FateFracEV{1,2,3}_2020, hNFSI_MFP_2020`).

Radiative corrections These include an uncorrelated 2% uncertainty on the ν_e/ν_μ and $\bar{\nu}_e/\bar{\nu}_\mu$ cross section ratios to account for radiative corrections, based on T2K's simple model [99] (`radcorrnue,radcorrnuebar`).

2nd Class Currents An additional 2% uncertainty which is fully anticorrelated between ν_e and $\bar{\nu}_e$ to allow for second class currents, also based on [99] (`2ndclasscurr`).

5.2.2 Flux and Beam uncertainties

The categories of neutrino flux uncertainties are hadron production and beam transport [100]. The first refers to the intermediate chain of particles produced by the protons incident in the graphite target which eventually decay to neutrinos. The second refers to the optics of the beam, such as the target position, magnetic field in the decay pipe and the amount of current in the focusing horns [101]. The effects of these uncertainties are correlated between true neutrino energy bins. To reorganize these into uncorrelated systematic uncertainties, these are treated with a technique called Principal Component Analysis (PCA) [102]. This method starts from a statistical ensemble of randomly generated variations in these uncertainties in order to estimate the variance in each neutrino energy bin as well as the correlations between different bins. A covariance matrix is then obtained and diagonalized, and the 5 eigenvectors with the largest eigenvalues are considered for this analysis, as they capture 97.5% of the variance(`ppfx_hadp_pc0{0,1,2,3,4}`).

5.2.3 Detector response

Light Level The number of photons produced by an energy deposition in scintillator is calculated using the parametrization

$$N_\gamma = F_{\text{view}}(Y_s E_{\text{Birks}} + \epsilon_C C_\gamma) \tag{5.2}$$

An alternate sample was generated to investigate the overall number of photons collected by the fiber. A separate systematic for ND and FD. For both detectors, the light level uncertainty was set as $\pm 5\%$.

Cherenkov This uncertainty was defined as a two-sided systematic, with the absolute value of ϵ_c (an overall scaling factor for Cherenkov energy) shifted by ± 0.05 ($\pm 6.2\%$).

Calibration Determined by studying the differences in data and MC in energy response for various candidate particles. The absolute and relative calibration systematics were determined by studying data- MC differences in the energy response for various candidate particles. Then data-MC comparisons were made for each sample by comparing the dE/dx as a function of position along the track. From these studies, the proton sample showed the largest discrepancy at 5%, which is taken as a conservative estimate for the calibration uncertainty across all samples and both detectors.

Calibration Shape The systematic uncertainty was defined based on data/MC differences. The uncertainty was the with a linear shape, with different slopes in the middle of the detector vs the edges, determined by linear fits to data MC ratios [103].

Detector Aging The uncertainty is implemented as a simple linear drift downward in light level as a function of time, and a corresponding drift upward in the overall calibration scale to compensate. This is intended to mimic the impact of the number of hits above thresholds falling over time, while the overall calorimetric energy remains the same [103].

Neutron systematic The uncertainty is obtained from a QE-like neutron prong subset of $\bar{\nu}_\mu$ CC candidates at the ND. A low energy MC neutron prong excess and a mid to high energy neutron prong MC deficit were identified. A 1σ shift in this uncertainty randomly selects 47% of simulated neutrons with visible energy below 20 MeV, and removes their energy contribution. These two numerical values were chosen to achieve good agreement in the calorimetric energy of said neutron prong candidates [104] (`NeutronEvisPrimariesSyst2018`).

Muon Energy Scale Characterizes the uncertainty associated with using reconstructed muon length in the detectors to determine muon energy. For the ND the variation is 0.15% and

for the FD 0.13%. These uncertainties are mostly for *mass accounting*, which includes uncertainty in the volume or density of the detector components (scintillator, steel, PVC) (`CorrMuEScaleSyst2020, UnCorrFDMuEScaleSyst2020`).

Tau Scale A 60% uncertainty is placed on the ν_τCC cross section. The origin of this uncertainty is the OPERA measurement [105] of $\sigma_\tau = (1.2^{+0.6}_{-0.5}) \times \sigma_{\text{GENIE}}$. Their error bars are applied to the 88% of the ν_τ sample which is CC. This results in a 57% uncertainty which is rounded to 60%(`NuTauScale`).

5.3 Samples

5.3.1 Binning

The 2D space of $(E_{had,vis}, |\vec{q}|)$, applied to the topological samples described in Chapter 4, results in very finely grained samples, as shown in Figure 5.7. In consequence, a significant number of bins have very low statistics. When looking at data, these bins are susceptible to high statistical fluctuations, and this is difficult to accurately represent by varying the systematic parameters in the NOvA simulation. For this reason, it was decided to modify the samples by removing the region of the $(E_{had,vis}, |\vec{q}|)$ phase space with large statistical fluctuations. This corresponds to the red bins displayed in Figure 5.8, where the $z-$axis displays $1\sqrt{N}$. In addition, the total number of non-empty bins for the 10 samples is 8776, which means the fit will include more than 8000 degrees of freedom. This translates to a computationally expensive fit. A variable size of bins was chosen to reduce the number of degrees of freedom, while preserving the distinctive features of each sample. This can be observed in Figure 5.9. The specific number of bins for each sample, before and after applying said modifications are specified in table 5.3. These adjustments greatly reduce the number of degrees of freedom from more than 8000 to fewer than half without significant loss of information.

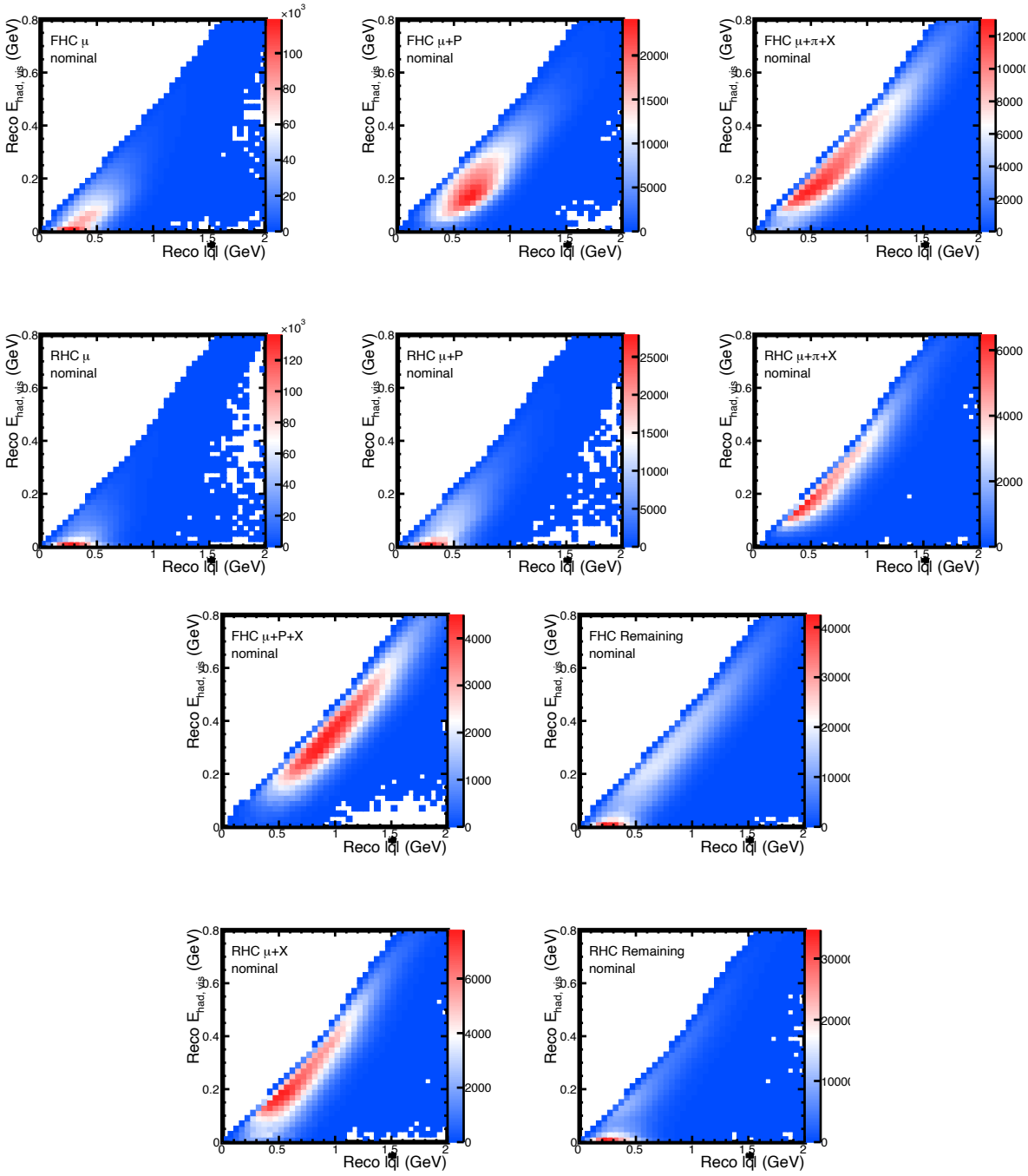

Figure 5.7: Topological samples with uniform binning in $(|\vec{q}|, E_{had})$ space

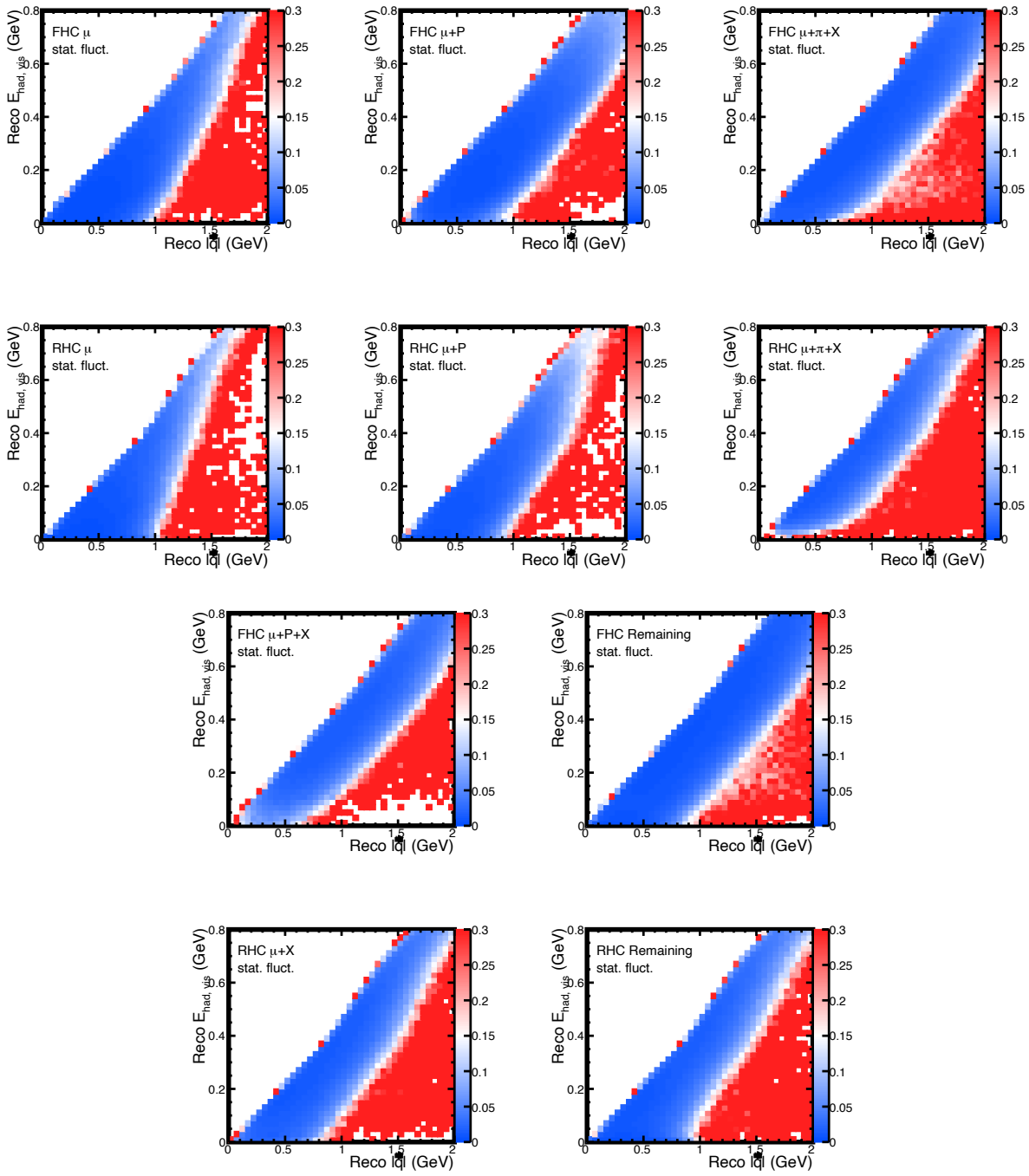

Figure 5.8: Topological samples statistical fluctuations with uniform binning in $(|\vec{q}|, E_{had})$ space

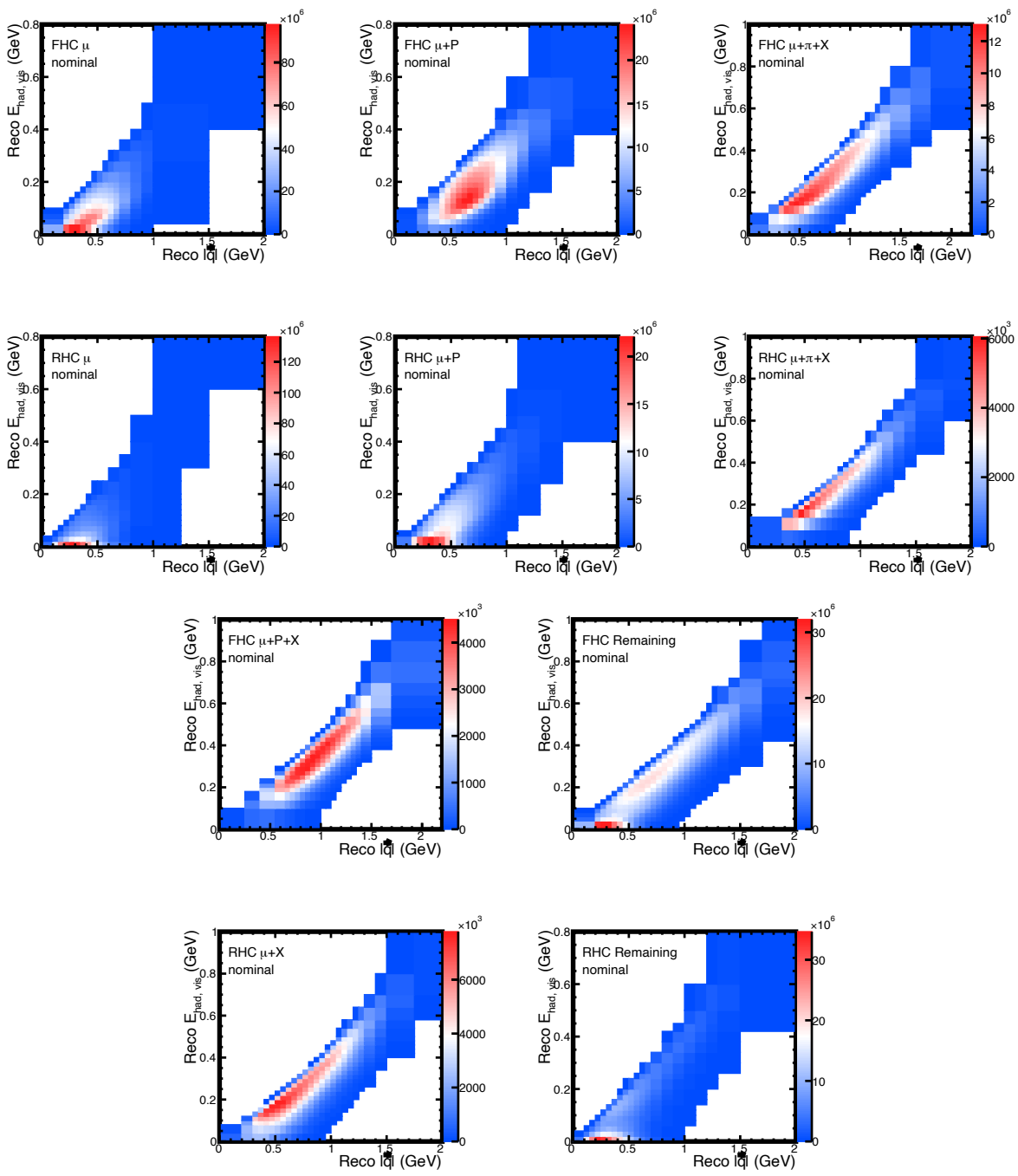

Figure 5.9: Topological samples with specialized binning in $(|\vec{q}|, E_{had})$ space

Table 5.3: Topology samples binning before and after removing the high $|\vec{q}$ and low $E_{had,vis}$ phase space and implementing variable bin size for each sample. The number in parenthesis represents the number of bins with large statistical fluctuations, calculated as $1/\sqrt{N}$, with N representing the number of events in each bin.

Sample	**Uniform (high-fluct)**	**Variable**
μ	874 (297)	155
$\mu + P$	887 (216)	252
$\mu + P + X$	834 (240)	278
$\mu + \pi^{\pm} + X$	936 (168)	299
Remaining FHC	925 (143)	406
μ	780 (292)	141
$\mu + P$	797 (239)	225
$\mu + X$	905 (320)	341
$\mu + \pi^{\pm} + X$	921 (382)	240
Remaining RHC	917 (325)	202
Total	8776 (2622)	2539

5.4 Fake Data Studies

This section focuses on fake data studies created to understand the behavior of most of the interaction model parameters described in section 5.2. In the various iterations of these studies, the procedure is similar: fake data is created by shifting the systematic parameters with random values within the allowed $\pm 3\sigma$. Then the samples are fitted using the same systematic uncertainties as fit parameters. The expectation is that the fit result should yield a $\chi^2 = 0$ when finding the correct value for the input parameters. To test the robustness of this method, the fits are performed multiple times, with each iteration starting from a different seed, where the parameters that are being fitted are assigned random values. This is done to ensure the whole parameter space is probed.

5.4.1 Quasi-Elastic, Resonance and Final State Interactions fake data study

The first fake data study has the goal of testing different possible values for a subset of the neutrino interaction parameters. The fake data is generated by assigning random values within

the $\pm 3\sigma$ variations allowed for each parameter. The fit minimizes the χ^2 between the fake data and the simulation in the 2D space of reconstructed three momentum transfer and visible hadronic energy ($|\vec{q}|E_{had}$), as displayed in Figure 5.7. Two sets of such fake data are presented in tables 5.4. These fake datas labeled 1 and 2, are fitted multiple times starting from random values of each systematic parameter. For fake data 1, 5.10 shows in the $z-$axis the number of fits that converged in a certain parameter value. The lighter shades of violet indicate that a handful of fits did not converge at the correct fake data value, however these are very few of the total cases. This indicates that most of these parameters can be well constrained, except for the case of `Theta_Delta2Npi`, which approximately half of the fits find an alternate value. For fake data 2, the results of the fit, shown in Figure 5.11, are very consistent for the 200 iterations made. In this case, the Quasi-Elastic interaction parameters Z-Expansion form factors 2, 3 and 4, are consistently found to be close to zero, instead of the randomly assigned value of the fake data. This is an indication that these particular parameters can not be constrained with the topology samples defined in Chapter 4.6. The fits to real data exclude these parameters, which in addition have a low impact in the ND topologies, as indicated in Figure 5.1, where parameter 4 has a χ^2 impact of $\mathcal{O}(10)$.

Figures 5.12 and 5.13 show the E_{had} projection of fake data sets 1 and 2 respectively. The fake data is indicated in green markers, while the blue and red lines indicate the fitted predictions when the fitter converged and failed in blue and red respectively. The purple lines show the different randomly seeded parameters where each fit started, which also depicts the range of shapes that these parameters are able to model.

5.4.2 Correlations of QE and MEC parameters

Given that the largest adjustment to the NOvA central value is related to MEC interactions, and this involves 13 parameters that overlap in the $(|\vec{q}|, E_{had})$ with QE interactions, it is interesting to understand how well can the QE and MEC parameters be constrained with the topology samples presented in the Chapter 4. To study this, a fake data fit is constructed, where

Table 5.4: Parameter shift values for two ND fake datasets

Parameter	**Fake data 1**	**Fake data 2**
RPA Shape Enhancement	0.98	0.5
RPA Shape Suppression	-0.50	1.10
Z-Expansion Axial Form Factor		
Eigen Vector 1	-0.38	0.52
Eigen Vector 2	-2.00	0.10
Eigen Vector 3	0.43	-0.90
Eigen Vector 4	-0.18	-2.40
CCQE normalization	-0.60	-2.60
Low Q2 Suppression	-0.29	-0.25
Ma CC Resonance	-1.86	0.35
Mv CC Resonance	0.65	-1.05
ThetaDelta2Npi	0.66	2.00
Res Decay B.R. 1	0.45	2.52
hN FSI Fate Fraction		
Eigen Vector 1	-0.53	-3.00
Eigen Vector 2	1.63	2.15
Eigen Vector 3	-0.82	0.15
Mean Free Path	-1.03	0.45

the 13 parameters that compose the two 2D gaussians of the MEC weights and the QE cross section parameters are randomly shifted. For this fit, only the μ and $\mu + P$ samples are included, as these are the most enhanced in QE and MEC interactions. Figure 5.14 shows the true fake data values and the results obtained from various fits. It is noticeable how for this particular choice of parameter values, the fit results show degeneracies: most parameters have multiple values that can describe the fake data. This is further noticeable in Figure 5.15, as the two samples post-fit (blue lines) match the fake data closely, even having these multiple-valued cross section parameters.

To better understand if the degeneracy observed in QE and MEC parameters is inherent of the phase-space overlap, or the model parameters themselves, another fake data was created. For this study, the samples μ and $\mu + P$ are further separated by their true interaction type, and excluding other interaction types, resulting in 4 samples: μ-QE, $\mu + P$-QE, μ-MEC and

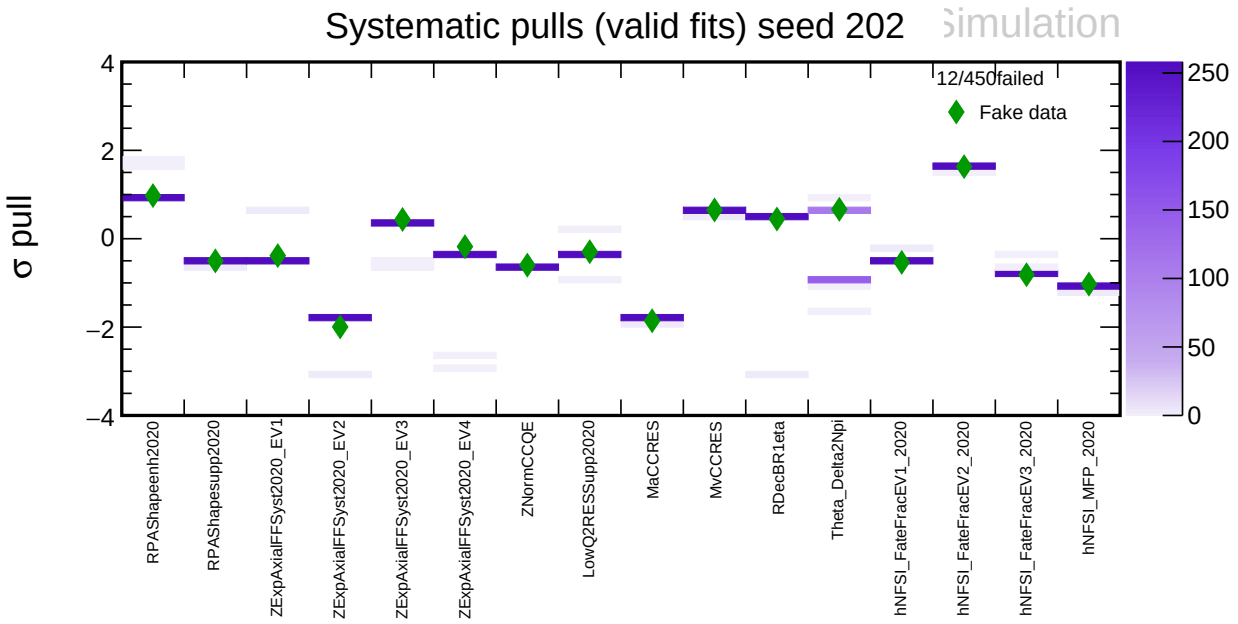

Figure 5.10: Fake data 1 random parameters (indicated with green markers). Fit results of 250 randomly seeded fits are shown in shades of purple.

$\mu + P$-MEC. The fake data is generated in the same manner as before, applying random shift to the model parameters. Then the same samples are fitted with the expectation of getting back the same parameter values. Figure 5.16 shows the fake data generated and fitted with these four samples. The Quasi-Elastic parameters are very well constrained, while the MEC parameters do not return the correct fake data value consistently. This is a clear indication that these parameters are highly correlated, and this is not a consequence of the overlap with Quasi-Elastic interaction phase space.

The same experiment, with only the μ and $\mu + P$ full samples, is repeated (fake data generated with random values of the 13 MEC parameters and QE parameters) but removing two of the parameters that compose the 2D gaussian from the fit. These correspond to the mean in q_0 and the correlation parameter for gaussian 2 (as indicated in table 3.4), which enhance the region of very low values of (q_3, q_0). A fake data fit with this modification is displayed in Figure 5.17. In this particular data set, the degeneracies were lifted, as no more multiple-valued results show up.

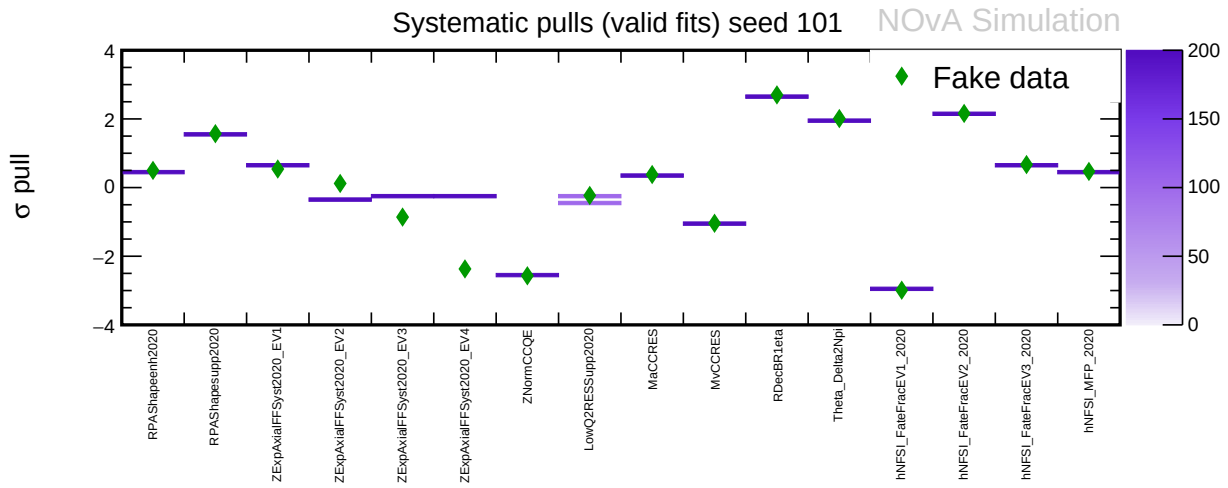

Figure 5.11: Fake data 2 random parameters (indicated with green markers). Fit results of 200 randomly seeded fits are shown in shades of purple.

One noticeable feature is that three of the MEC parameters, although well constrained, are not fit to the exact value with which the fake data was generated. This is an explainable feature, as the parameters excluded form the fit are compensated by these additional shifts. In other words, 11 out of the 13 MEC gaussian parameters can describe the same shape in the distributions. Therefore these parameters can safely be removed from the fit. This change is implemented in the next fake and real data fits.

5.4.3 Change of MEC model

Given that the largest adjustment to the NOvA central value is related to MEC interactions, it is of interest to understand if the parameters that construct this central value have sufficient freedom to reproduce data which that contains a different 2p2h model. For this purpose, the alternative scenarios accessible to evaluate within the NOvA framework are the MINERvA MEC tune, and the extremes of the NOvA 2p2h, which are labeled QE-like and RES-like. The Minerva MEC tune is a different parametrization of an adjustment to the Valencia model utilizing an

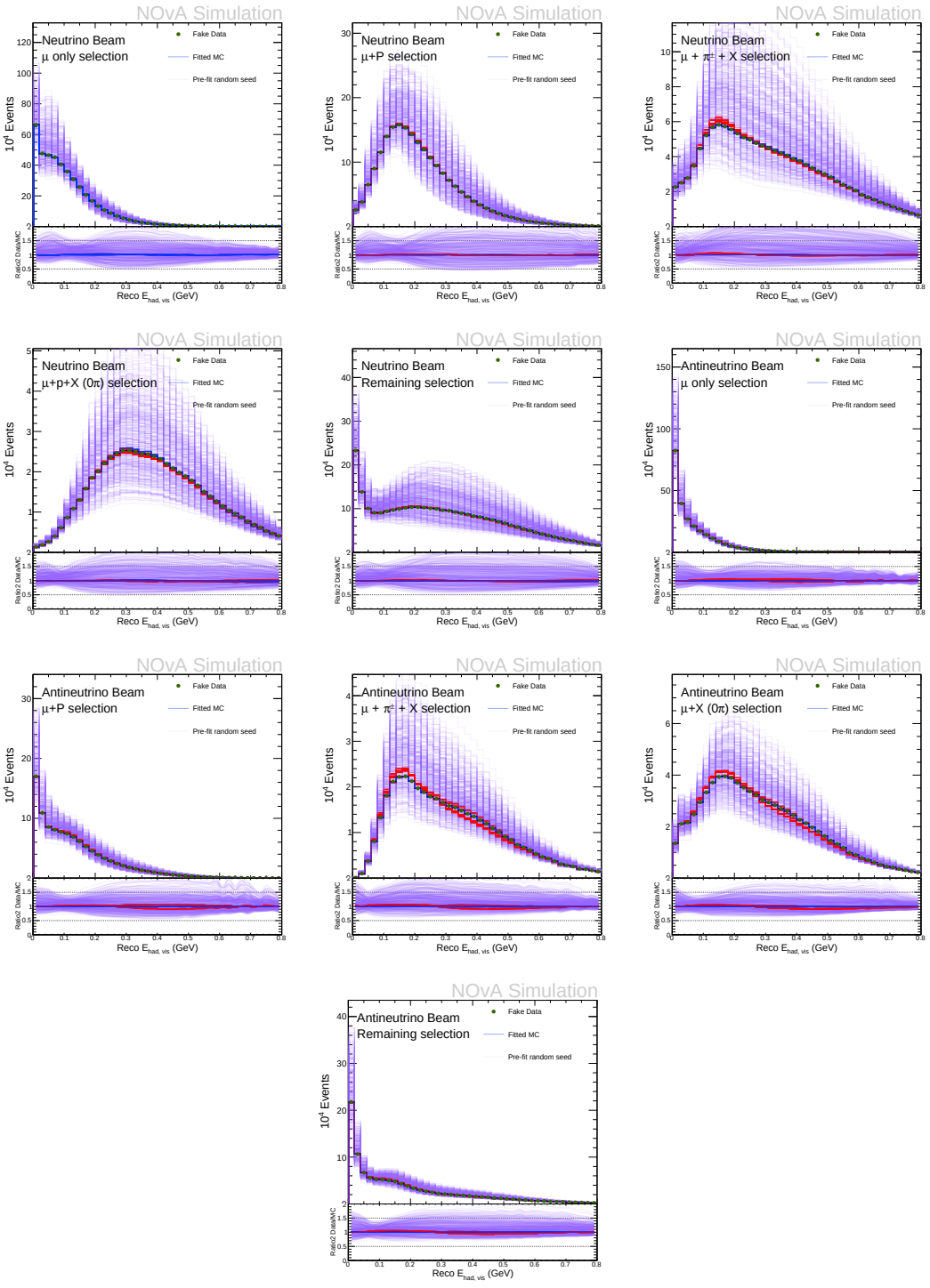

Figure 5.12: Fake data 1 predictions with fit results. The top(bottom) row shows the FHC(RHC) samples projected in the E_{had} axis.

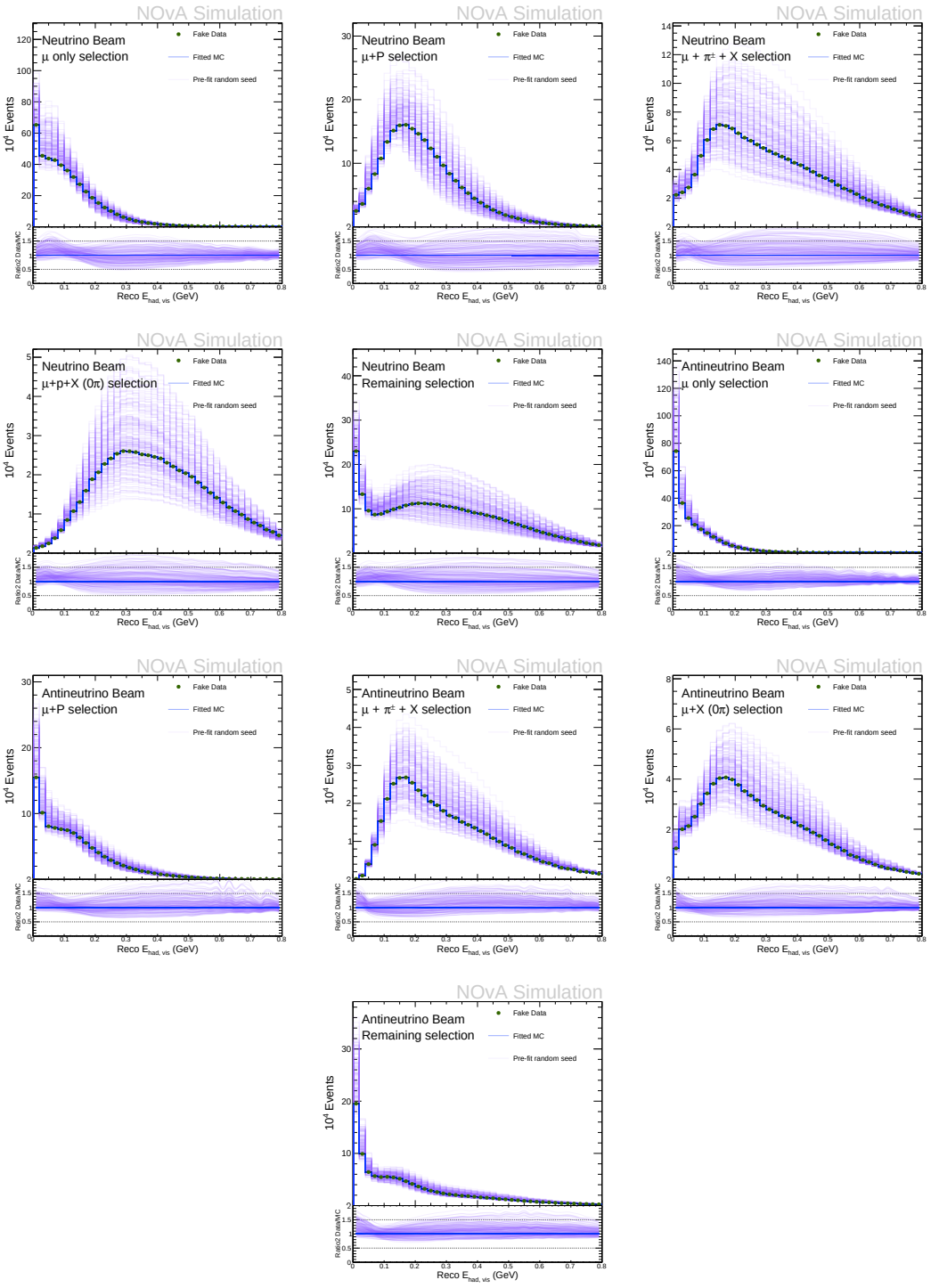

Figure 5.13: Fake data 2 predictions with fit results. The top(bottom) row shows the FHC(RHC) samples projected in the E_{had} axis.

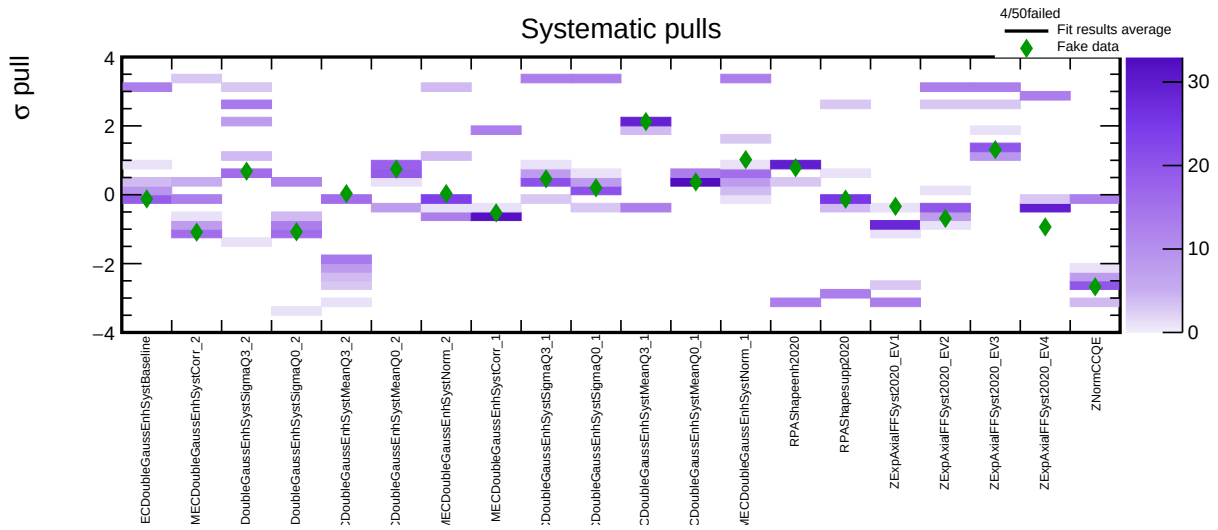

Figure 5.14: Fake data with MEC and QE random parameters(indicated with green markers). Fit results of 50 randomly seeded fits are shown in shades of purple.

enhancement shaped as one 2D-gaussian in (q_3, q_0) [106], but based on the data from the MINERvA experiment, which studies neutrinos from the same beam, but on axis.

Figures 5.18 through 5.20 display the topology samples for FHC and RHC in the two-dimensional space of $(|\vec{q}|, E_{had}$. As the μ, $\mu + P$ and *remaining* samples encapsulate most of the MEC phase-space, these are the samples that show a significant shape and normalization change. The case of MINERvA weight shows a smaller enhancement at the lowest $(|\vec{q}|, E_{had}$ bins, while the QE and RES-like weights show a notorious shift in the distribution peak, particularly for the FHC $\mu + P$ sample.

These fake data fits include a total of 53 systematic uncertainties, which describe the cross section model, detector response and neutrino flux as detailed in section 5.2. Figures 5.21 through 5.23 show the result of 50 fits randomly seeded in those 53 parameters. Highlighted in blue is the particular fit result which produced the best fit to the fake data, which is determined as the smallest overall χ^2. For the case of the MINERvA weight fake data, most of the parameters seem to be well constrained, as most of the fit results coincide with the best fit. Although the fitted parameters can very well describe these fake data, there are a number of parameters which are

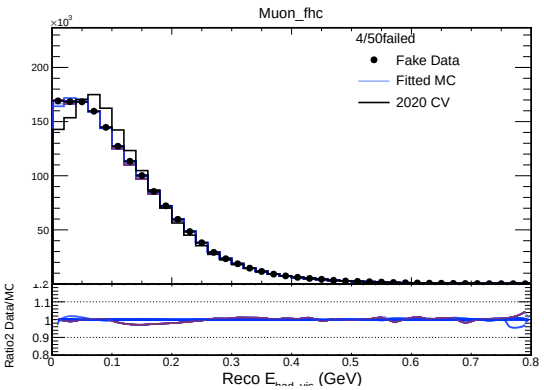

(a) μ sample E_{had} projection

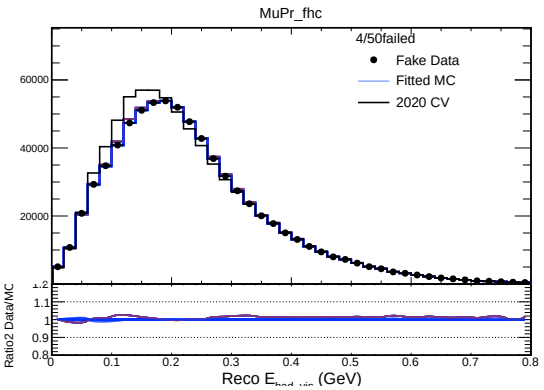

(b) $\mu + P$ sample E_{had} projection

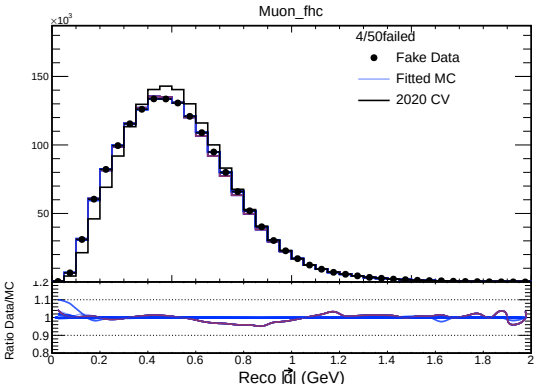

(c) μ sample $|\vec{q}|$ projection

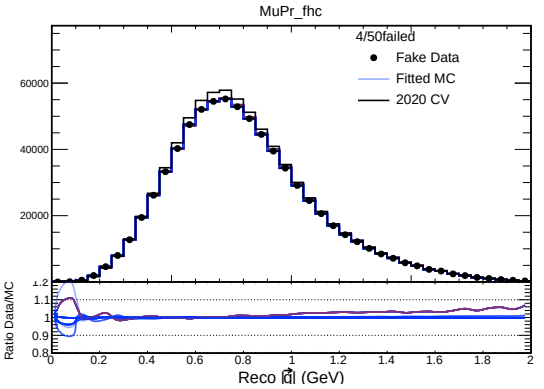

(d) $\mu + P$ sample $|\vec{q}|$ projection

Figure 5.15: Fake data with MEC and QE random parameters predictions with fit results. The top(bottom) row shows the $E_{had}(|\vec{q}|)$ samples projected in the E_{had} axis.

pulled to very large values, outside of the $\pm 3\sigma$ uncertainty range, such as `DISvbarpCC3pi_2020`, `MECInitStateNPFrac2020AntiNu`, and `MECEnuShape2020Nu`. The good agreement of this fake data fit result is shown in Figure 5.24.

The case of QE-like and RES-like MEC fake data sets is similar. Most of the parameters included in the fit are well constrained, as most fit results coincide with the best fit. For the QE-like fake data, 3 parameters show large values `DISvnCC3pi_2020` `DISvpCC3pi_2020` and `GussEnhSystNorm_1` For the RES-like fake data most of the systematic parameters show values within the $\pm 3\sigma$ range. However ambiguities in the DIS parameters for a small fraction of the fits

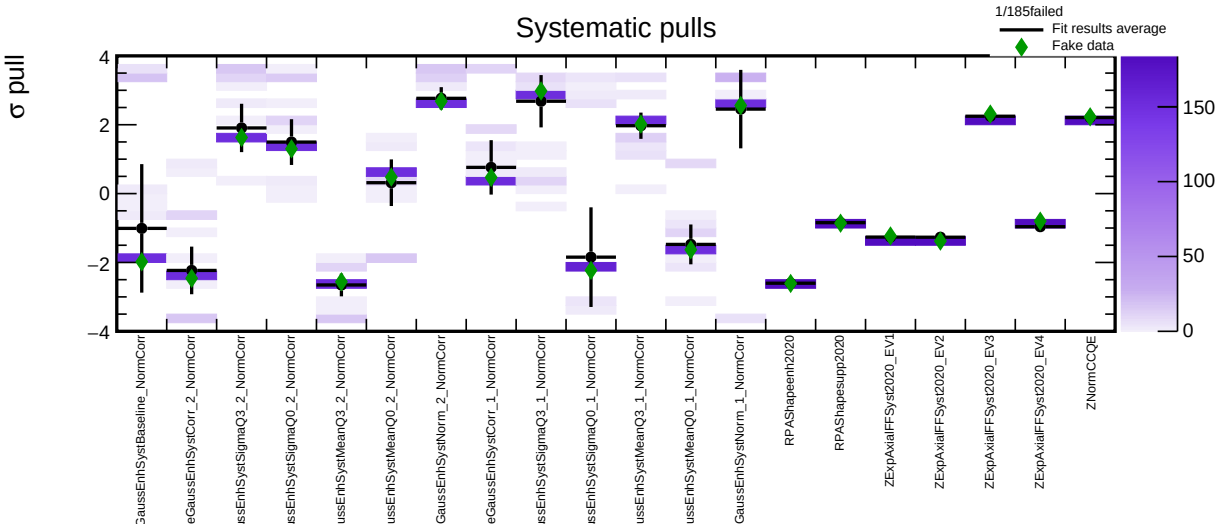

Figure 5.16: Fake data with MEC and QE random parameters(indicated with green markers). Fit results of 185 randomly seeded fits, on QE and MEC separated μ and $\mu + P$ samples, are shown in shades of violet.

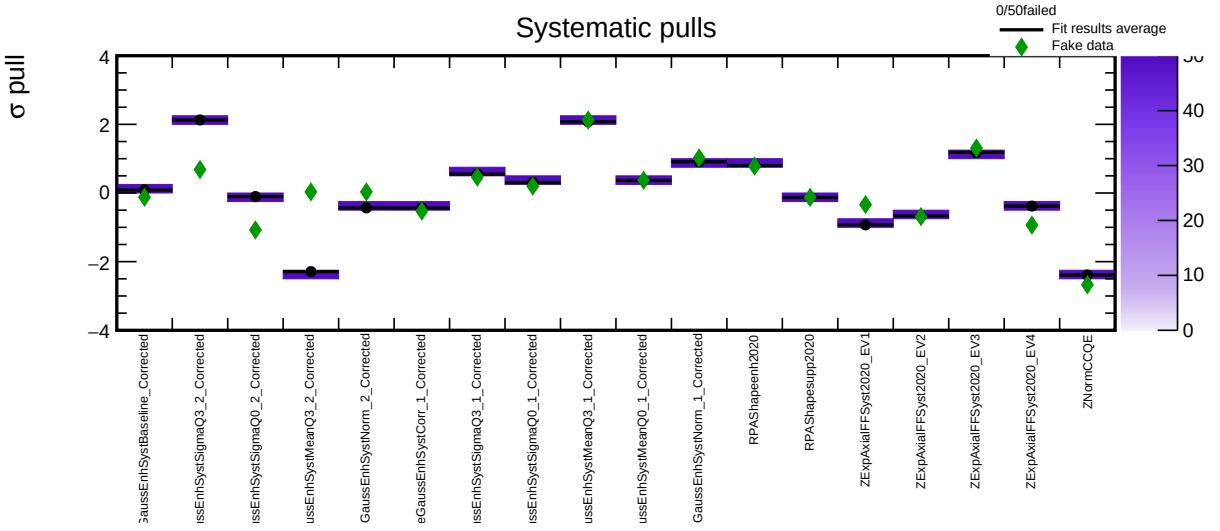

Figure 5.17: Fake data with reduced MEC and QE random parameters(indicated with green markers). Fit results of 50 randomly seeded fits are shown in shades of purple.

is observed. In both cases, the best fits match these fake data very closely, as can be observed in figures 5.25 and 5.26 .

5.5 Data fits

After performing various fake data studies the finalized list of parameters and binning, real data can be fitted. In addition to the χ^2 cut criteria to exclude parameters which which can not be constrained via this fit, an additional modification is made: the penalty term is adjusted in to ensure the parameter constrains stay within the physically understood range of $\{-3, 3\}\sigma$. Initially, it was observed that fits where poorly constrained parameters were included, resulted in values very far outside of this range. This modified penalty term, in addition to the reduced list of parameters, ensures that the fits do not result in highly unphysical values. Equation 5.4 describes the modified penalty term $\mathcal{P}(\sigma_i)$, where outside of $\pm 3\sigma$, the function increases exponentially instead of the original quadratic shape.

In summary the data fits minimize:

$$\chi^2(\vec{\theta}) = \min\left(\chi^2(\vec{\theta}, \vec{s}) + \sum_i \mathcal{P}(\sigma_i)\right) \tag{5.3}$$

,

and the penalty term can be written as:

$$\mathcal{P}(\sigma) = \begin{cases} \sigma^2 & \text{if } |\sigma| < 3 \\ \exp[(\sigma - a)^4] + b & \text{if } \geq 3 \end{cases} \tag{5.4}$$

where $a = 2.081453945311349$ and $b + 6.676273112395464$, as depicted in Figure 5.27

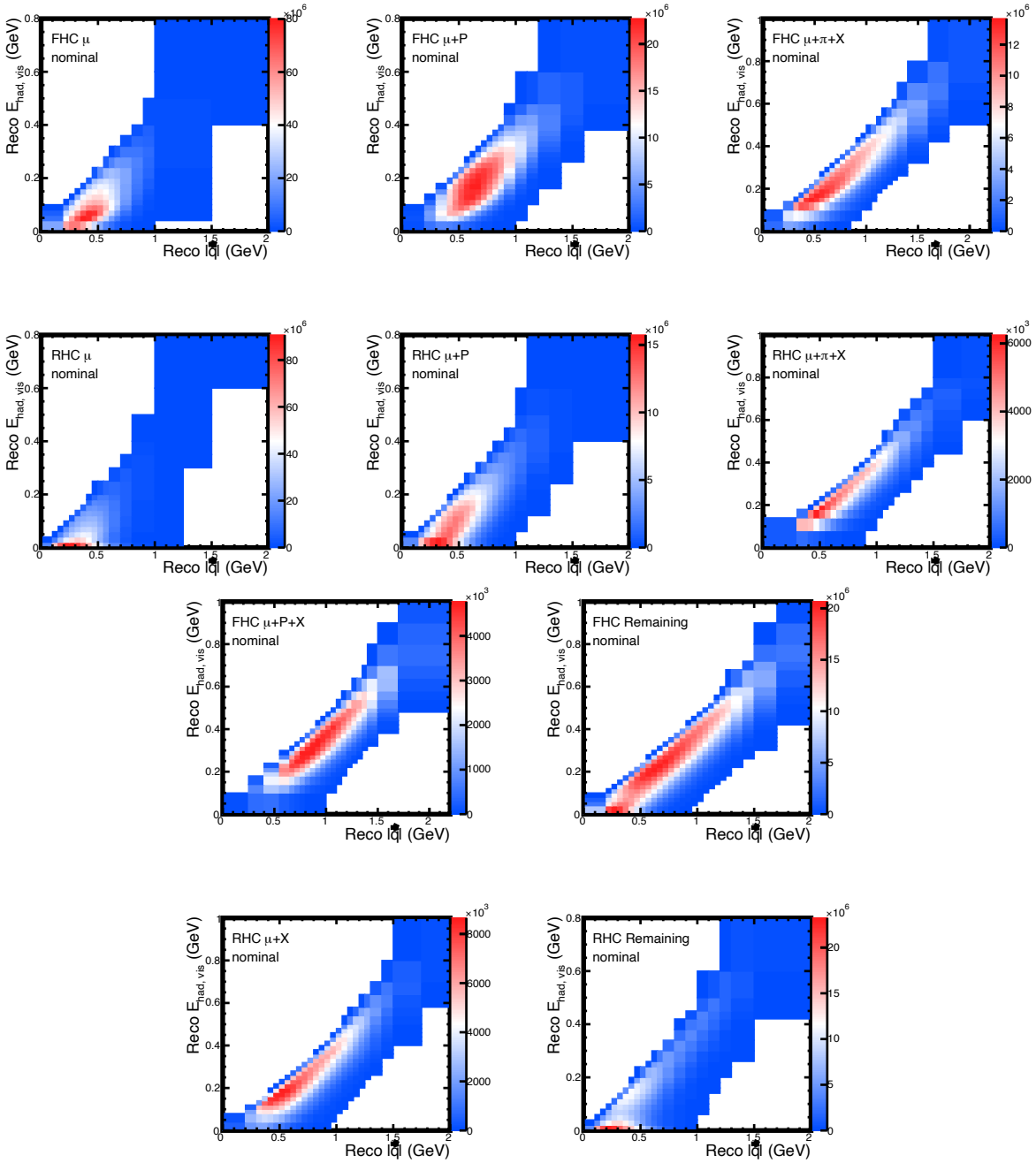

Figure 5.18: Minerva tune ND fake data

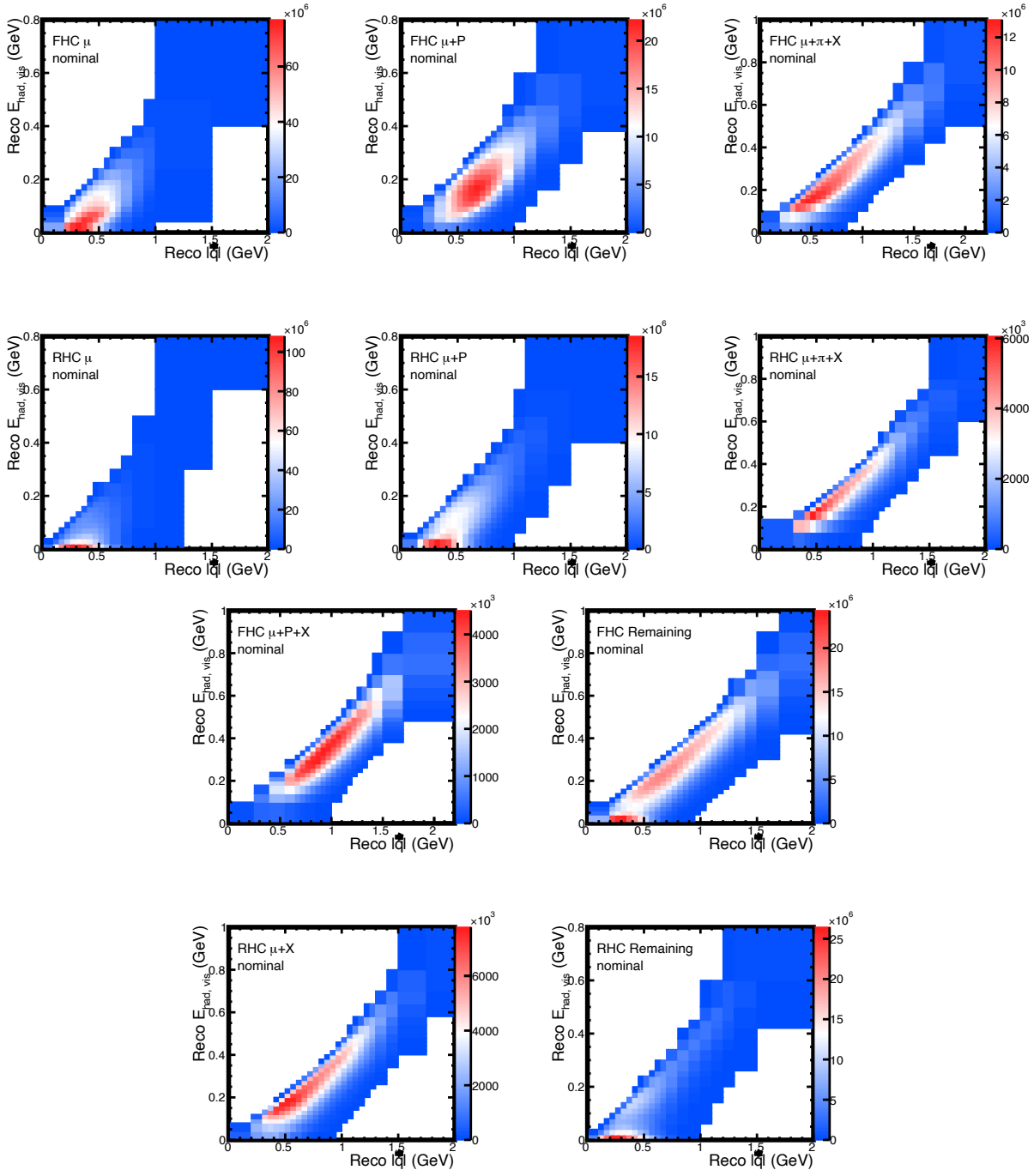

Figure 5.19: QE-like ND fake data

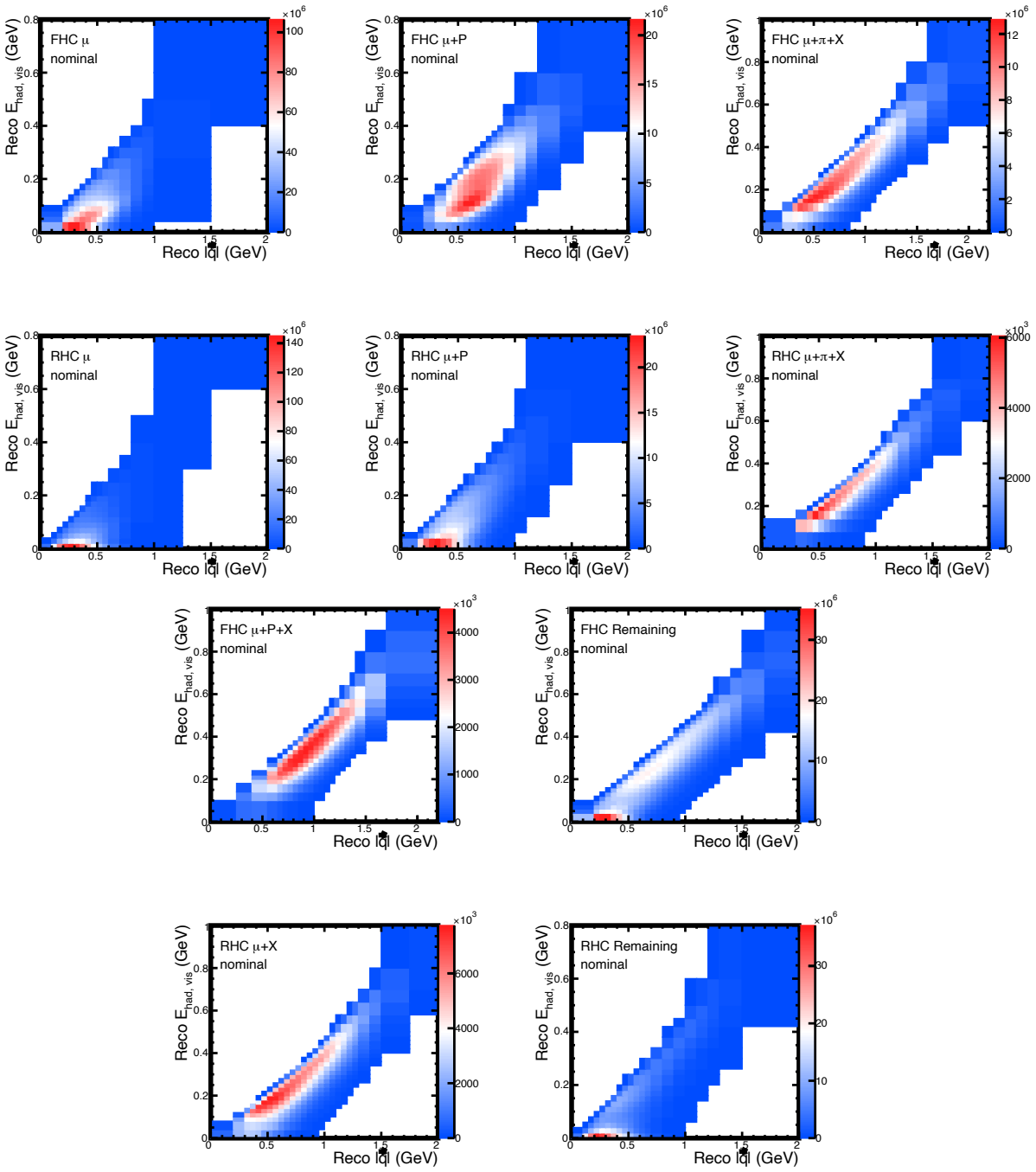

Figure 5.20: RES-like ND fake data

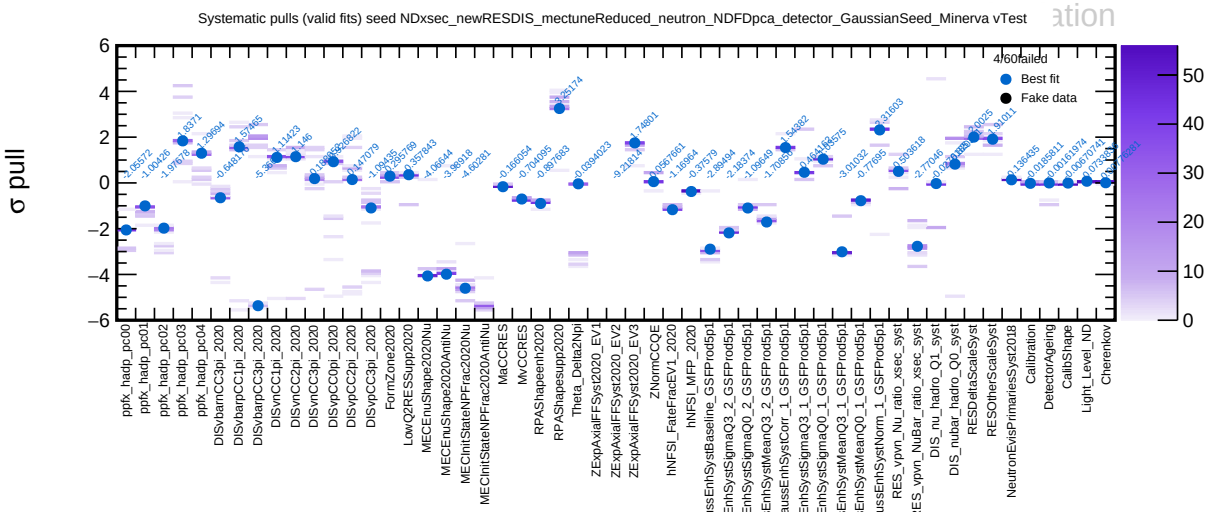

Figure 5.21: Systematic uncertainty shifts after Minerva tune ND fake data fit.

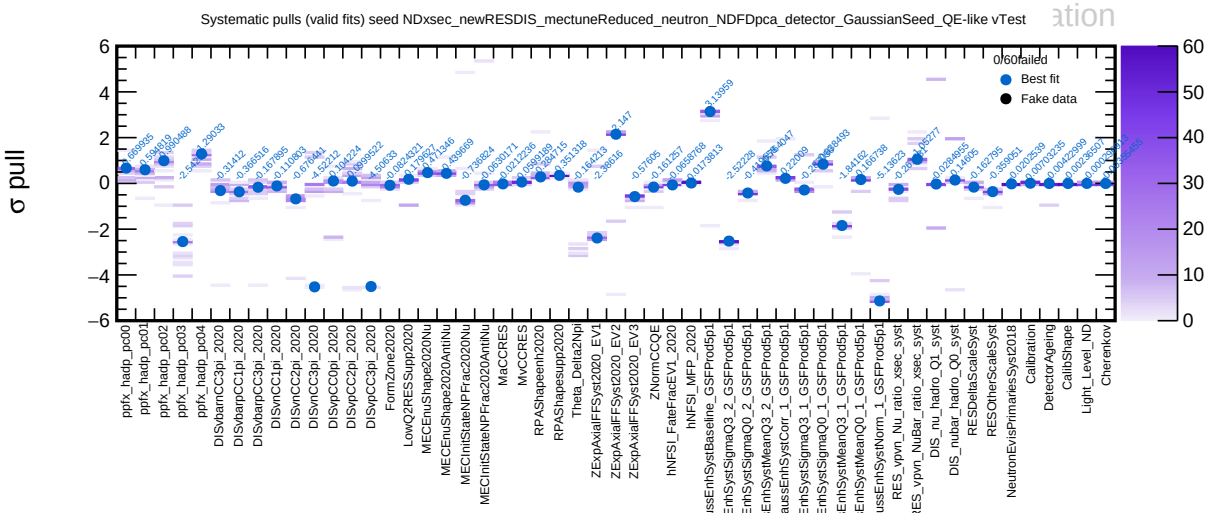

Figure 5.22: Systematic uncertainty shifts after QE-like tune ND fake data fit.

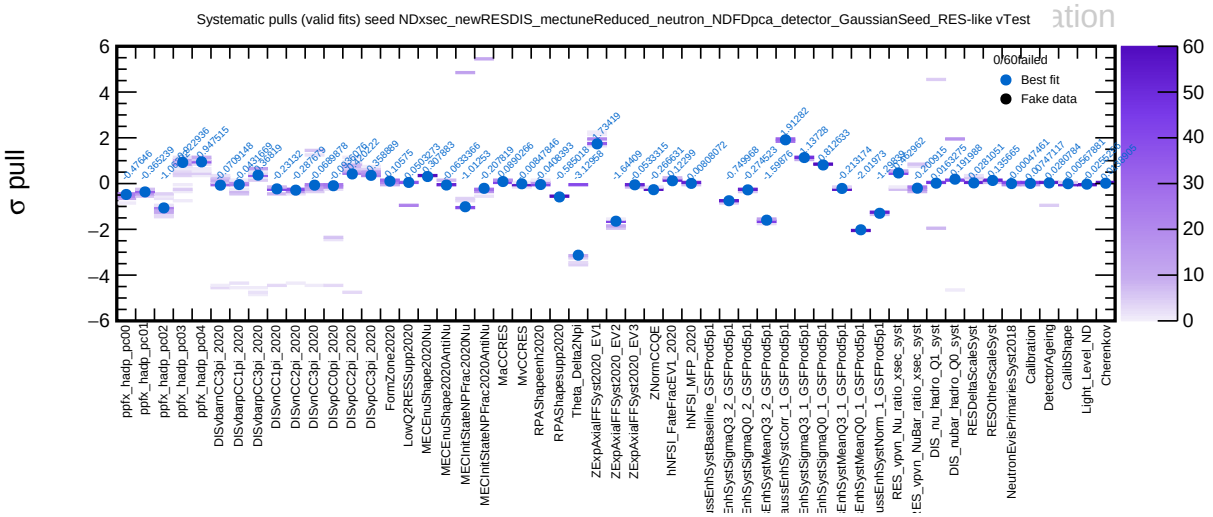

Figure 5.23: Systematic uncertainty shifts after RES-like tune ND fake data fit.

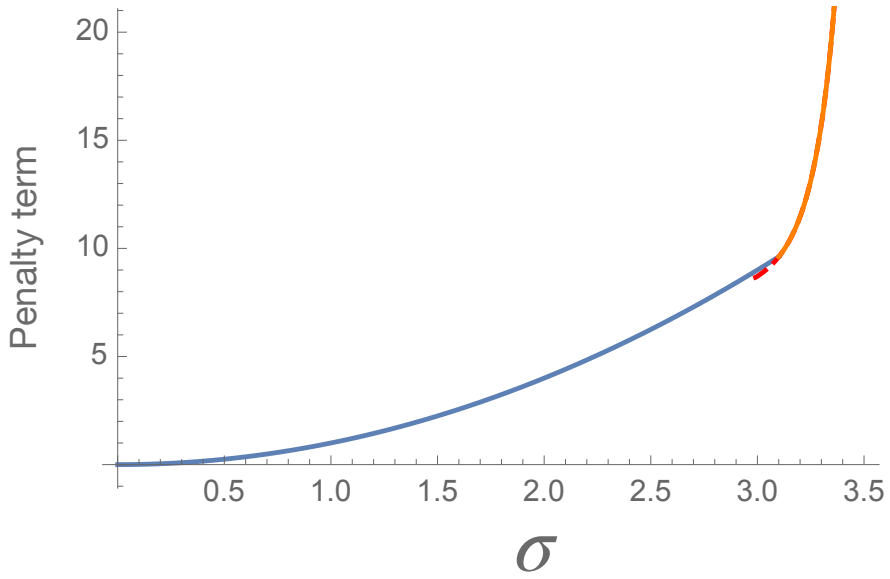

Figure 5.27: Modified penalty term function

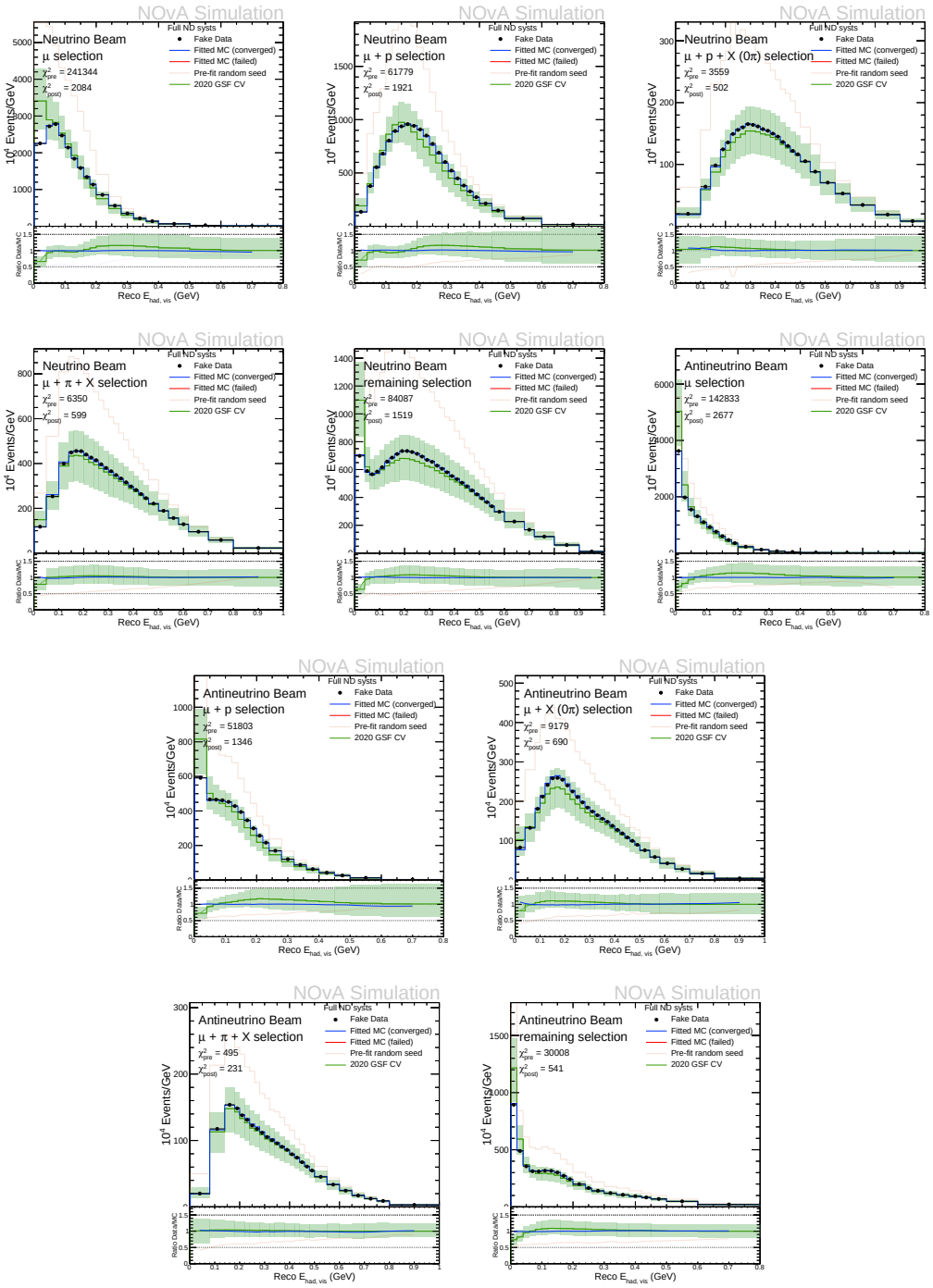

Figure 5.24: Visible hadronic energy distributions of ND fit using Minerva MEC fake data.

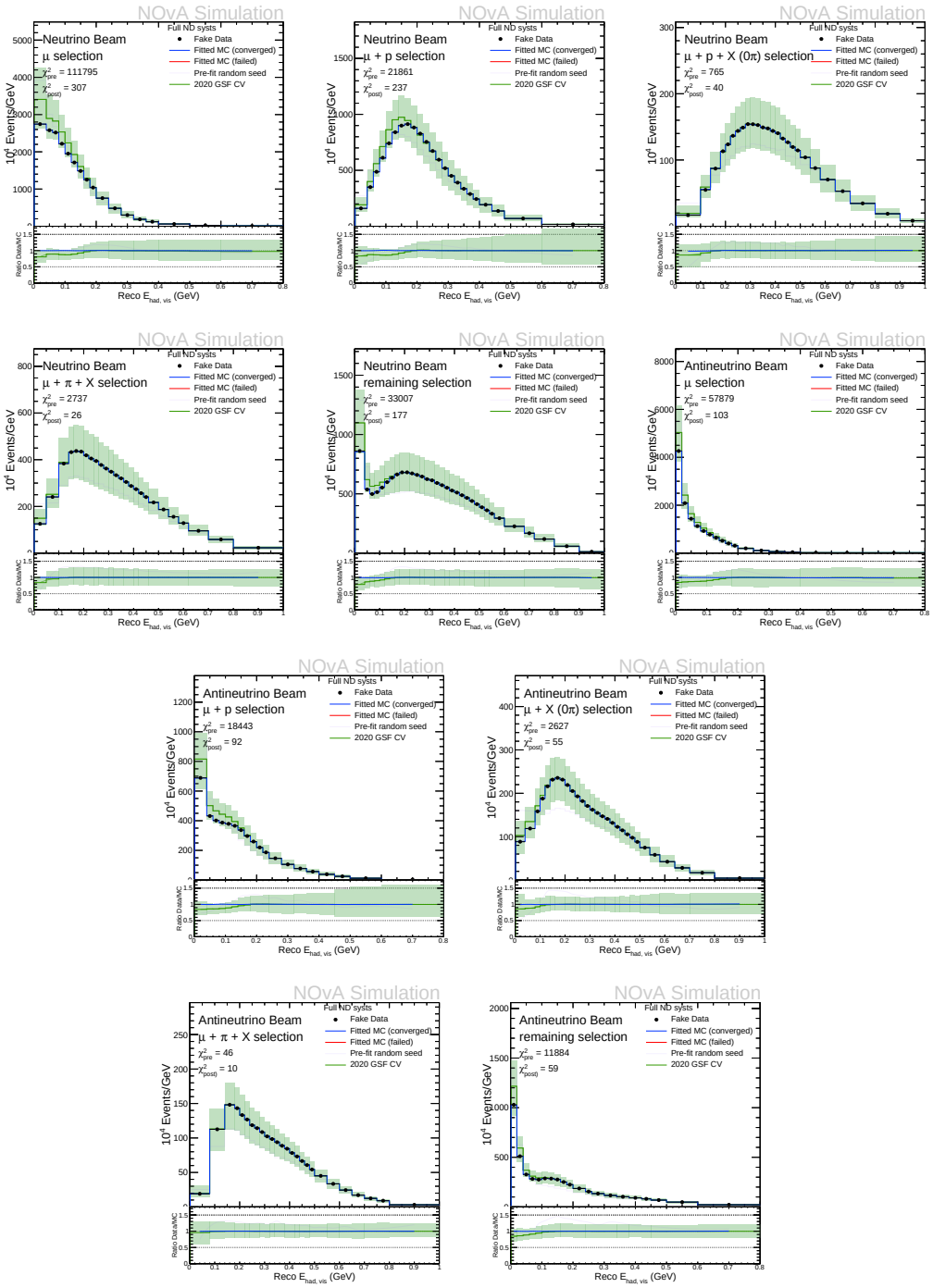

Figure 5.25: Visible hadronic energy distributions of ND fit using QE-like MEC fake data.

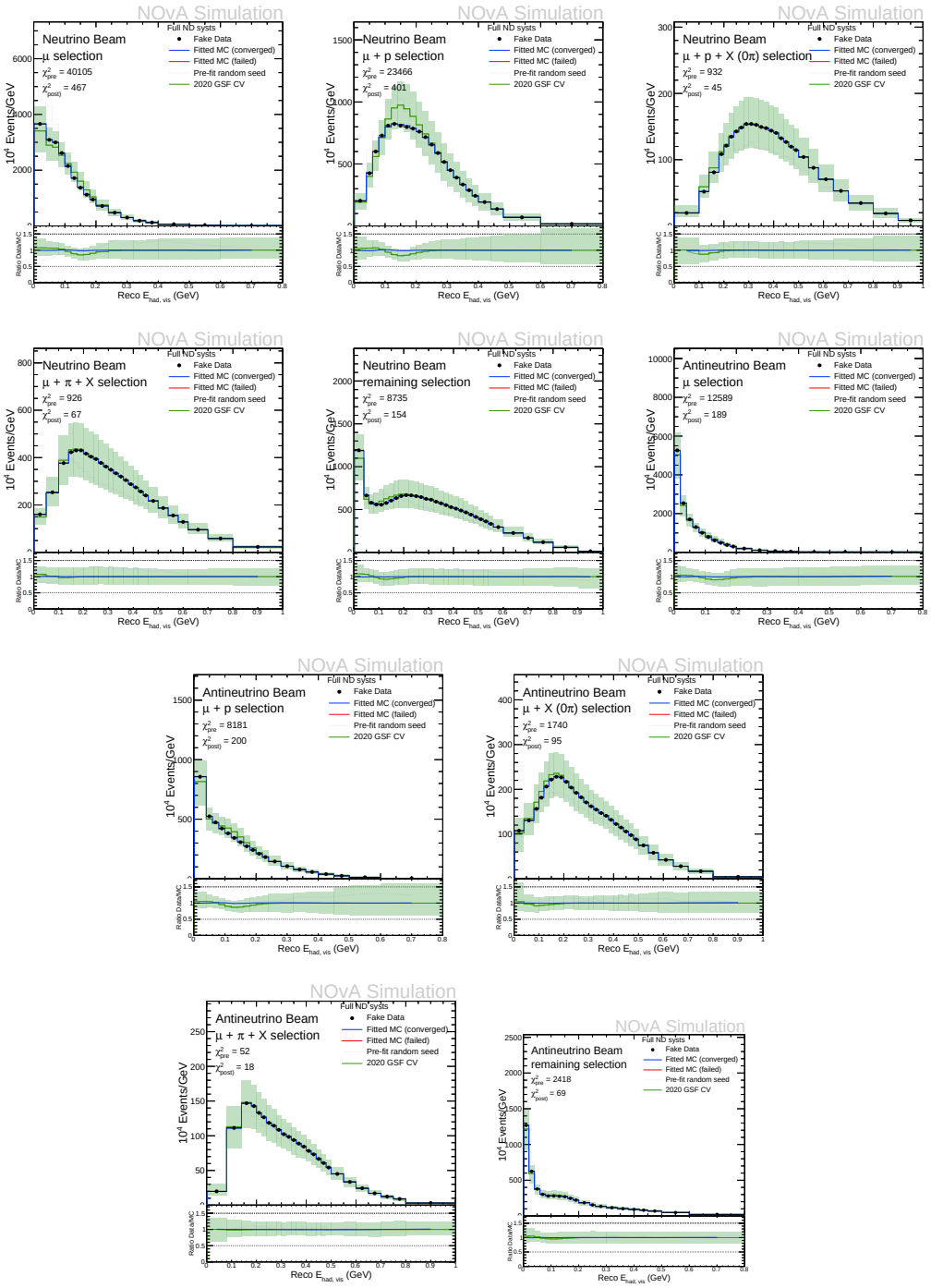

Figure 5.26: Visible hadronic energy distributions of ND fit using RES-like MEC fake data.

As described in section 5.4.2, the MEC tuning parameters show degeneracies with the QE parameters. This is a concern with regards to fitting real data, as it is possible to obtain multiple valued results, or different constrains, without being able to discern if the resulting parameters fit are the "true" best fit. To understand how these parameters interact, the procedure is repeated two times, with and without the MEC tune parameters. In both cases, the criteria to consider the best fit is the set of parameter values that results in the smallest χ^2 between simulation and data.

5.5.1 Data fit without MEC adjustment uncertainties

Figure 5.28 shows the result of fitting data with the finalized list of parameters, excluding the MEC tune parameters. Note that the nucleon pair fraction and energy dependent MEC systematics are still included. Most of the parameters have multiple values that are considered a valid, by the MINUIT framework, as noted by the shades of purple displayed in Figure 5.28. The best fit, indicated with blue markers, and specified in table 5.5, presents its largest pull on the `MECInitStateNPFrac2020Nu` parameter. This is a strong indicator that the data in the samples is better described with the freedom to reshape the MEC enhancement of the NOvA tune, as the MEC-related parameters included (nucleon pair fraction and energy dependent shape) are limited. There are also large ($> |\pm 2\sigma|$) shifts for three out of five beam parameters, enhancement on RES parameters and suppression in the DIS parameters. Table 5.6 shows the χ^2 of the samples after the fit. Note that all the samples' χ^2 is significantly reduced, except for the μ RHC sample. The E_{had} projection of the distributions are displayed in 5.29. The ratio to data in these plots shows that the post-fit distribution are much closer to a ratio of 1. In the case of the RHC μ samples, the slightly larger χ^2 is coming from the higher E_{had} bins, which are less populated. The $\mu + \pi + X$, $\mu + P + X$ and $\mu + X$ samples have a significantly improved agreement with data.

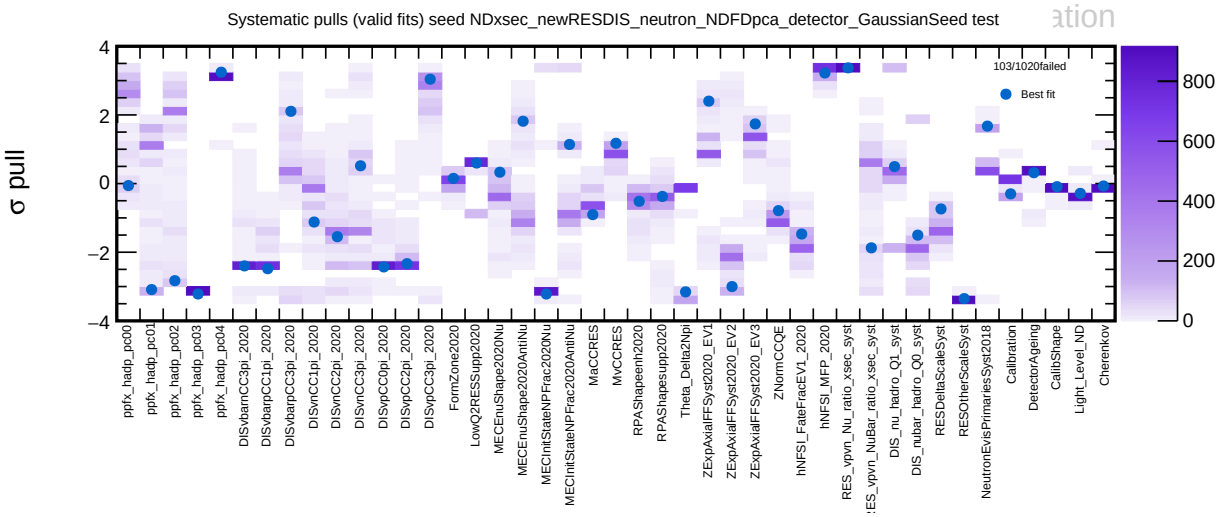

Figure 5.28: ND data fit results excluding MEC tune parameters. Fit results of 1020 randomly seeded fits. The systematic uncertainty shift values highlighted in blue produce the smallest χ^2.

5.5.2 Data fit with MEC adjustment uncertainties

The summary of fits to data including the final list of parameters is displayed in Figure 5.30. In this case, similar to the version without MEC parameters, most parameters have multiple values that are considered a valid fit, and which result in a significantly improved data-MC agreement. The values that yield the smallest χ^2 are highlighted with blue markers, and specified in table 5.7. In this case, the largest pull is in the `hNFSI_MFP_2020` parameter. Two of the five beam parameters show large pulls (larger than $\pm 2\sigma$), as well as six of the ten MEC 2D gaussian parameters. The pulls on the DIS systematics are consistent with the fit with no MEC parameters, and the agreement of this best fit is better than the case without MEC uncertainties, as shown in the χ^2 per sample, and total, displayed in table 5.8. The χ^2 table also shows that the agreement of most samples is improved with respect to the fit with no MEC parameters, as all samples have a smaller χ^2 than the pre-fit prediction. Particularly the μ and $\mu + P$ samples show a significant χ^2 reduction, and the case of $\mu + \pi + X$, $\mu + P + X$ and $\mu + X$ have better agreement than without MEC parameters, even when these samples have a small fraction of MEC

Table 5.5: Systematic uncertainty shifts found after fitting ND data with final list of parameters, excluding MEC parameters. The degrees of freedom (D.o.F.) are obtained from the number of non-empty bins - number of fit parameters, which in this case is 43. The parameters are in descending order from the absolute value.

MECInitStateNPFrac2020Nu	3.46689	DIS_nubar_hadro_Q0_syst	-1.28424
RES_vpvn_Nu_ratio_xsec_syst	3.37198	MECEnuShape2020AntiNu	1.18491
RESOtherScaleSyst	-3.32401	MvCCRES	1.16973
ppfx_hadp_pc04	3.21662	DISvnCC1pi_2020	-0.974499
ppfx_hadp_pc03	-3.21379	MECInitStateNPFrac2020AntiNu	0.883228
RPAShapesupp2020	-3.17053	MaCCRES	-0.868173
ZExpAxialFFSyst2020_EV2	-3.05043	RESDeltaScaleSyst	-0.724567
DISvpCC3pi_2020	3.00051	hNFSI_FateFracEV1_2020	-0.570488
RES_vpvn_NuBar_ratio_xsec_syst	-2.74347	LowQ2RESSupp2020	0.549788
DISvbarpCC3pi_2020	2.69446	DISvnCC3pi_2020	0.520858
hNFSI_MFP_2020	2.69059	ppfx_hadp_pc02	-0.517568
DISvbarpCC1pi_2020	-2.46874	MECEnuShape2020Nu	-0.426671
DISvpCC0pi_2020	-2.44671	DetectorAgeing	0.374979
DISvpCC2pi_2020	-2.40213	Calibration	-0.371329
DISvbarnCC3pi_2020	-2.35136	DIS_nu_hadro_Q1_syst	0.352824
ppfx_hadp_pc01	-2.06811	ppfx_hadp_pc00	0.237072
NeutronEvisPrimariesSyst2018	1.78924	Light_Level_ND	-0.22776
ZExpAxialFFSyst2020_EV1	1.78607	CalibShape	-0.213041
ZExpAxialFFSyst2020_EV3	-1.58607	FormZone2020	0.134465
ZNormCCQE	1.5533	Theta_Delta2Npi	-0.0397713
RPAShapeenh2020	-1.5506	Cherenkov	-0.0355075
DISvnCC2pi_2020	-1.48229		

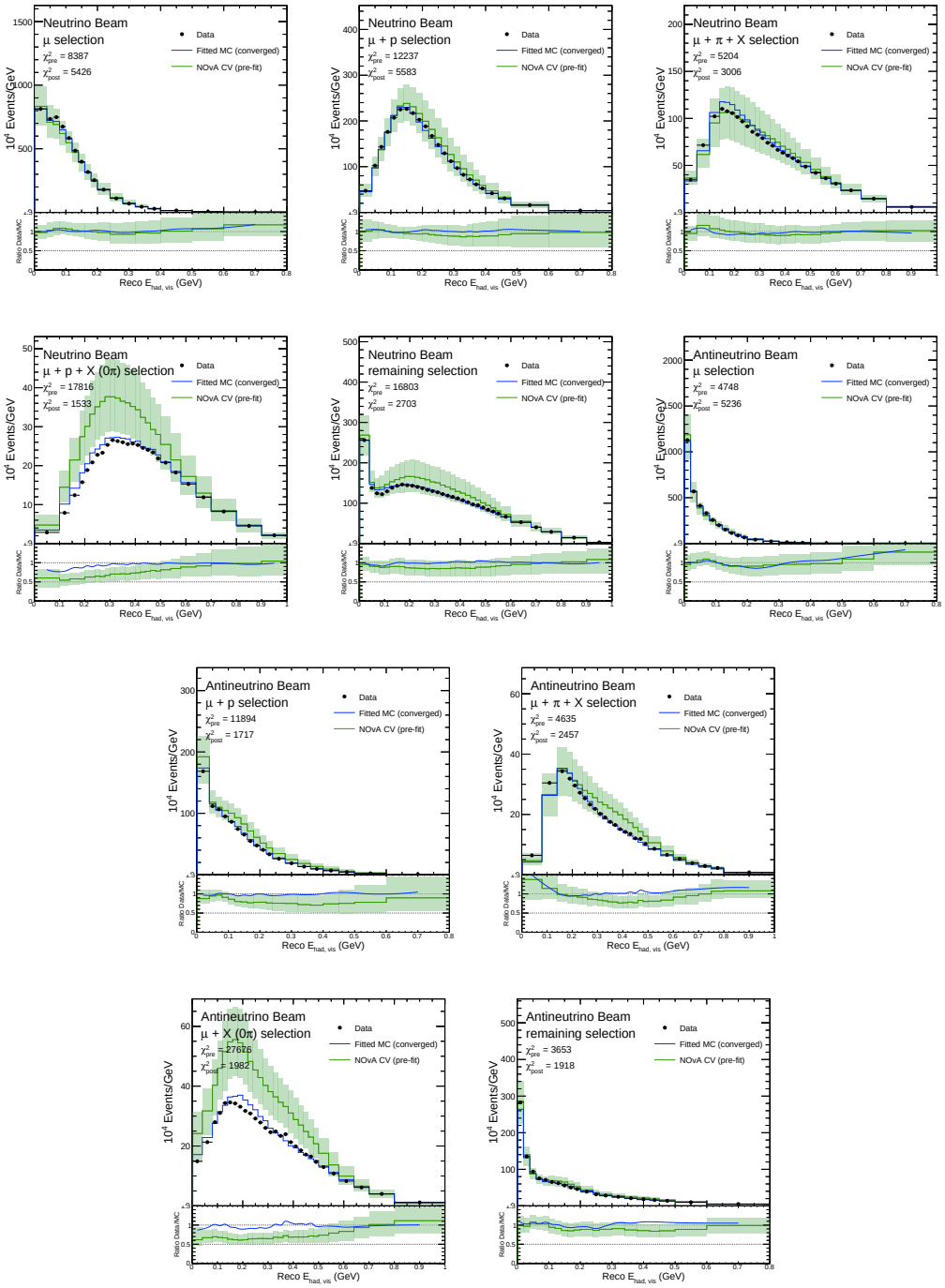

Figure 5.29: Visible hadronic energy distributions of ND fit to data with final list of parameters, excluding MEC.

Table 5.6: χ^2 summary of ND data fits excluding MEC tune parameters

Sample	χ^2 **pre-fit**	χ^2 **post-fit**
FHC		
Muon	8387.77	5426.1
MuPr	12238	5583.6
MuPiEtc	5204.8	3006.99
MuPrEtc	17816.7	1533.88
EvElse	16803.5	2703.23
RHC		
Muon	4748.5	5236.04
MuPr	11894.9	1717.12
MuPiEtc	4635.8	2457.91
MuEtc	27676	1982.09
EvElse	3653.12	1918.62
Total per D.o.F.	113059 / 2496 = 45.2961	31565.6 / 2496 = 12.6465

interactions. These is further shown in Figure 5.31, where the ratios of data ans simulation for all samples are very close to 1.

5.6 Summary

Although all the systematic parameters can not be unambiguously constrained in the ND topology samples, the best fit found describes the data significantly better than the initial CV, which was already obtained from ND inclusive selection (i.e. the NOvA tune). Excluding the MEC gaussian parameter does not seem to significantly improve the degeneracy in the parameters fit, and in turn the agreement to data is worsened significantly, as seen by the overall χ^2 per degree of freedom, which increases to 12.5 when excluding MEC parameters and 8.12 when they are included. Figure 5.32 shows the χ^2 per sample comparing the pre-fit and post-fit result in both cases, with and without MEC parameters. As mentioned earlier, in both cases agreement improves significantly, but it shows more improvement, particularly for the μ and $\mu + P$ samples with the full list of parameters. Also note that in both cases the $\mu + P + X$, $\mu + X$ and remaining

Table 5.7: Systematic uncertainty shifts found after fitting ND data with final list of parameters. The degrees of freedom (D.o.F.) are obtained from the number of non-empty bins - number of fit parameters, which in this case is 53. The parameters are in descending order from the absolute value.

Parameter	σ **fit**	**Parameter**	σ **fit**
hNFSI_MFP_2020	3.35261	MECDoubleGaussEnhSystCorr_1_GSFProd5p1	1.31436
RES_vpvn_Nu_ratio_xsec_syst	3.28734	DISvnCC2pi_2020	1.27616
MECDoubleGaussEnhSystMeanQ3_2_GSFProd5p1	3.27453	MvCCRES	1.22933
RPAShapesupp2020	-3.19987	DISvnCC1pi_2020	-1.20307
DISvpCC3pi_2020	3.16785	MECDoubleGaussEnhSystSigmaQ0_2_GSFProd5p1	1.16527
ZExpAxialFFSyst2020_EV1	3.13154	ppfx_hadp_pc02	1.13716
ppfx_hadp_pc04	3.09569	MECInitStateNPFrac2020AntiNu	1.11151
ppfx_hadp_pc03	-3.08906	RESDeltaScaleSyst	-1.0149
MECDoubleGaussEnhSystBaseline_GSFProd5p1	3.06513	ZNormCCQE	-0.974822
MECDoubleGaussEnhSystSigmaQ3_2_GSFProd5p1	2.99876	LowQ2RESSupp2020	0.931927
MECDoubleGaussEnhSystMeanQ3_1_GSFProd5p1	-2.87638	DIS_nu_hadro_Q1_syst	0.883863
MECDoubleGaussEnhSystSigmaQ3_1_GSFProd5p1	2.84315	RPAShapeenh2020	0.783787
RESOtherScaleSyst	-2.81116	MaCCRES	-0.758212
DISvbarpCC1pi_2020	-2.45765	ppfx_hadp_pc01	-0.727715
MECDoubleGaussEnhSystMeanQ0_1_GSFProd5p1	-2.37943	ppfx_hadp_pc00	0.504349
DISvpCC0pi_2020	-2.37836	MECDoubleGaussEnhSystNorm_1_GSFProd5p1	0.421419
DISvnCC3pi_2020	-2.32937	MECDoubleGaussEnhSystSigmaQ0_1_GSFProd5p1	-0.344117
DISvbarnCC3pi_2020	-2.31426	Calibration	-0.323817
DISvbarpCC3pi_2020	2.09573	FormZone2020	0.308344
DISvpCC2pi_2020	-1.99658	DetectorAgeing	0.28919
ZExpAxialFFSyst2020_EV3	1.98773	Light_Level_ND	-0.269208
ZExpAxialFFSyst2020_EV2	-1.94584	MECInitStateNPFrac2020Nu	0.262973
DIS_nubar_hadro_Q0_syst	-1.90389	MECEnuShape2020Nu	0.188463
hNFSI_FateFracEV1_2020	-1.86746	CalibShape	-0.0900407
RES_vpvn_NuBar_ratio_xsec_syst	-1.77528	Cherenkov	-0.0674833
NeutronEvisPrimariesSyst2018	1.61042	Theta_Delta2Npi	-0.0368933
MECEnuShape2020AntiNu	1.33858		

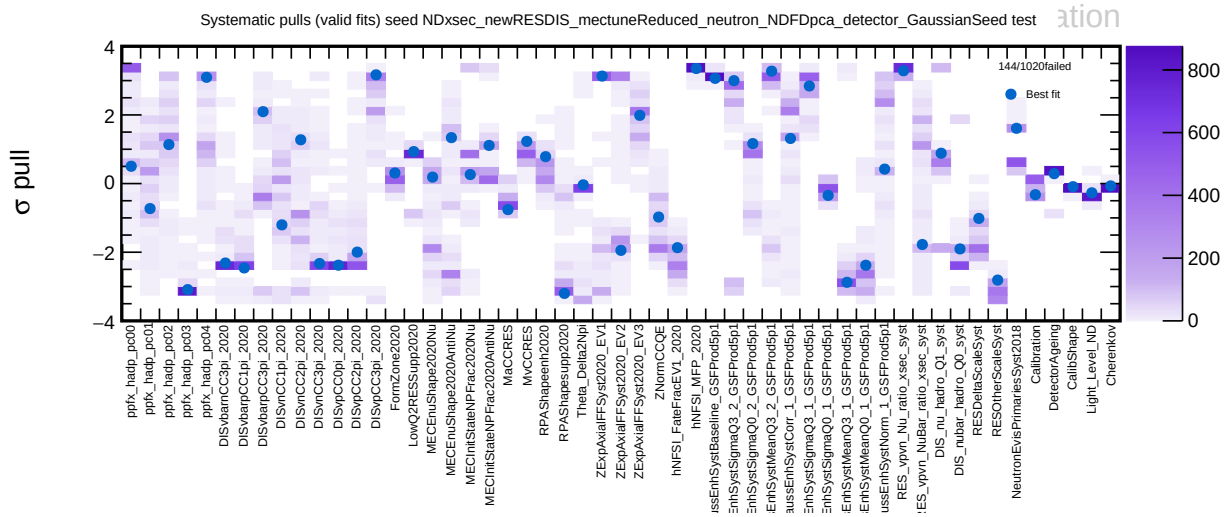

Figure 5.30: ND data fit results including all relevant parameters. Fit results of 1020 randomly seeded fits. The systematic uncertainty shift values highlighted in blue produce the smallest χ^2.

FHC are the samples with the most reduction of χ^2. The effects of by sample of different parameters is displayed in appendix A.

The level of agreement achieved with this fit is considered to be a good description of the ND data. The constrain obtained from this fit is implemented in the FD oscillation fit. As the remaining data-MC differences remain a concern, this is addressed in an additional robustness study in Chapter 6.

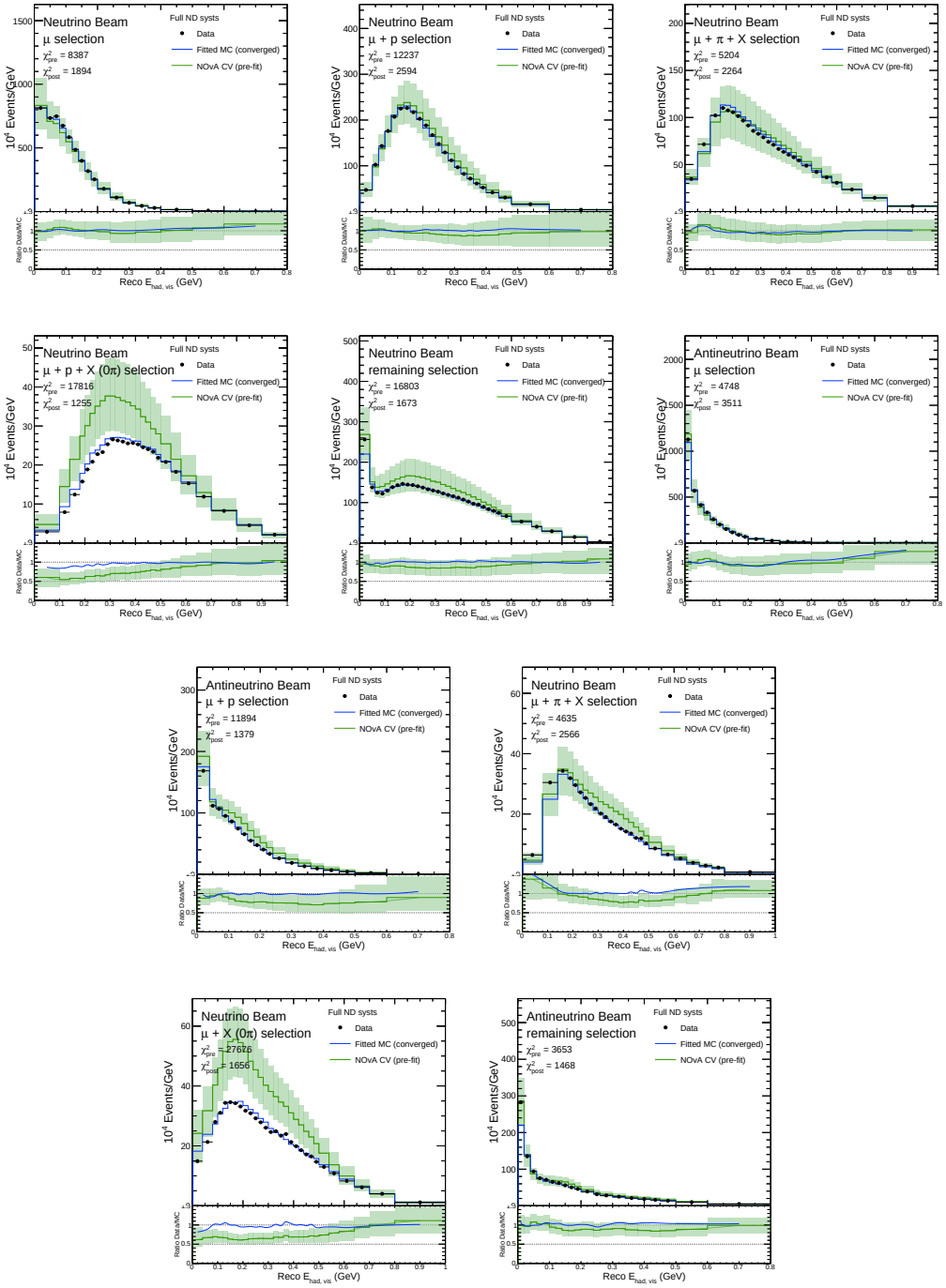

Figure 5.31: Visible hadronic energy distributions of ND fit to data with final list of parameters

Table 5.8: χ^2 summary of ND data fits including all parameters

Sample	χ^2 **pre-fit**	χ^2 **post-fit**
FHC		
Muon	8387.77	1894.56
MuPr	12238	2594
MuPiEtc	5204.8	2157.14
MuPrEtc	17816.7	1344.32
EvElse	16803.5	1942.24
RHC		
Muon	4748.5	3511.17
MuPr	11894.9	1379.67
MuPiEtc	4635.8	2613.83
MuEtc	27676	1626.07
EvElse	3653.12	1453.9
Total per D.o.F.	113059 / 2486 = 45.4783	20517.2 / 2486 = 8.25308

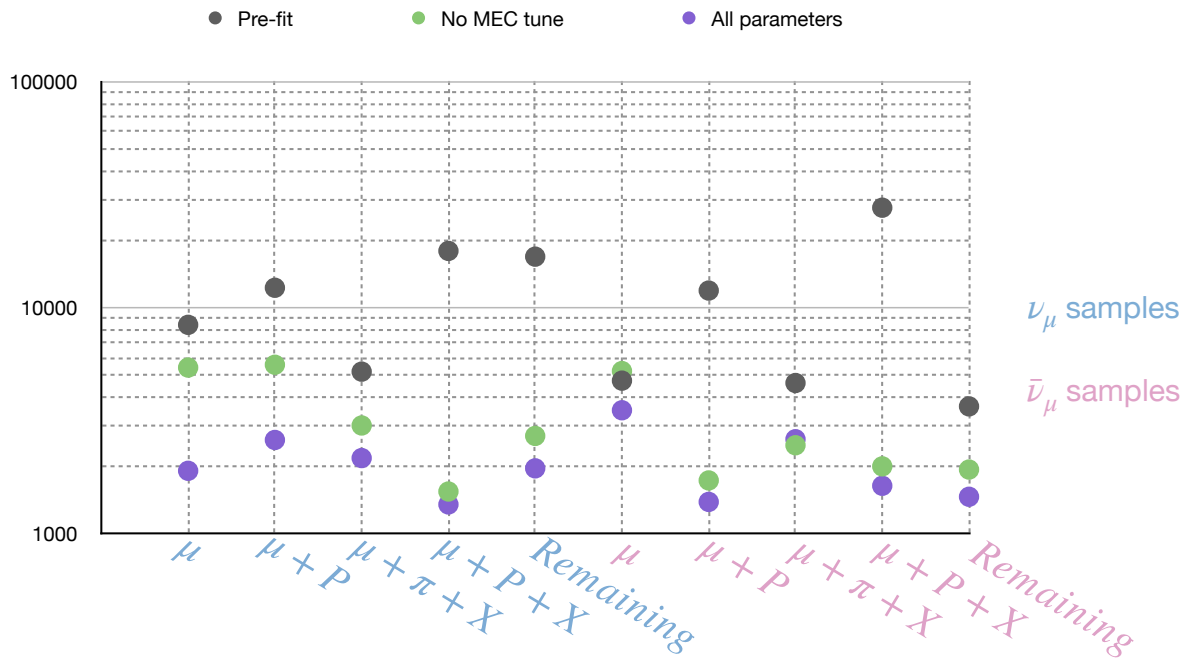

Figure 5.32: Summary of χ^2 pre and post fit per sample. The nominal, or NOvA tune, predictions' χ^2 is shown with the grey markers. Fits with MEC tune parameters are in purple and without in green.

CHAPTER 6. IMPACT OF ND CONSTRAIN IN 3 FLAVOR OSCILLATION ANALYSIS

In chapters 4 and 5, we defined ND samples that are used to constrain the systematic uncertainty parameters of the NOvA cross section model. It was shown that the current model with constrained parameters can describe the actual ND data better than the nominal NOvA weight from chapter 3. In this chapter we introduce the ν_μ FD predictions that correspond to the same topologies as the ND ones, as well as the ν_e selection that are used to measure oscillation parameters. A method to include the ND constrain from chapter 5 in the oscillation fit is described with an Asimov fake data fit. Various studies to test the robustness of this fitting method are presented. We conclude with the residual difference fake data fits, which address the concern of the remaining difference that still exists after the ND fit is finalized.

6.1 Far Detector predictions

Section 4.4.1 detailed the selection criteria for the ν_μ and ν_e selection in the FD. For the fitting method os this thesis, the constrain from the ND relied on the topology selections, which were defined in table 4.1. The FD ν_μ and $\bar{\nu}_\mu$ selections are subdivided using that same criteria. This adds up to 12 FD samples: 5 ν_μ (FHC), 5 $\bar{\nu}_\mu$ (RHC), 1 ν_e (FHC) and 1 $\bar{\nu}_e$ (RHC) selections. The distributions of these samples are shown in figures 6.1 and 6.2. Notice that the cosmic background is included in this distributions. The estimation of the background is made by overlaying cosmic events from real data taking scaled to the time (livetime) that corresponds to the POT when beam data was collected. These predictions assume oscillation parameters as the latest NOvA results [10] (see table 6.1). The systematic uncertainty band displayed includes the unconstrained systematic variation from the list of parameters in table 5.7, plus additional FD-only systematics described in section 6.2.1. The different topologies for the ν_μ and $\bar{\nu}_\mu$ samples

show different shapes in E_ν, where we see the oscillation dip (between 1 and 2 GeV) more pronounced for the μ and $\mu + P$ samples.

6.2 Fitting method

In order to obtain a measurement of oscillation parameters from the NOvA FD data, we continue using a frequentist statistical approach, similar to the approach used to obtain a constrain in the ND, as described in chapter 5. We start from the Poisson log-likelihood function for a binned prediction of neutrino events parametrized by the vector of oscillation parameters $\vec{\theta}$:

$$-2\ln\lambda(\vec{\theta}) = -2\sum_{i=1}^{N}\left[N_i(\vec{\theta}) - O_i + O_i\ln\frac{O_i}{N_i(\vec{\theta})}\right], \tag{6.1}$$

where O_i is the observed number of events in bin i, N_i is the predicted number of events in the bin i. These bins account for 12 the samples: 5 ν_μ , 5 $\bar{\nu}_\mu$, 1 ν_e and 1 $\bar{\nu}_e$. According to Wilk's theorem, $-2\ln\lambda$ follows a χ^2 distribuion, provided certain regularity conditions are met [107], so we use the "Gaussian approximation" $-2\ln\lambda(\vec{\theta}) = \chi^2(\vec{\theta})$. The set of oscillation parameters $\hat{\theta}$ that best describes the data is obtained by minimizing 6.1: $\chi^2_{\text{best fit}} \equiv \chi^2(\hat{\theta}) = \min\big(\chi^2(\vec{\theta})\big)$.

The test statistic $\Delta\chi^2$ is defined as

$$\Delta\chi^2 = \chi^2(\vec{\theta}) - \chi^2(\hat{\theta}) \tag{6.2}$$

which is always non-negative.

6.2.1 ND Constrain and Systematic Uncertainties

As described in chapter 5, the high statistics sample from the ND is used to constrain the systematic parameters in the underlying model used to simulate the data. The FD predictions are also described by these constrained model parameters ($\vec{\delta}_{\text{ND}}$), as well as additional systematic uncertainties that are unique to the FD ($\vec{\delta}_{\text{FD}}$). Equation 6.1 is then modified to include a covariance matrix penalty term V_{ND} as well as an unconstrained penalty term, similar to that of equation 5.1:

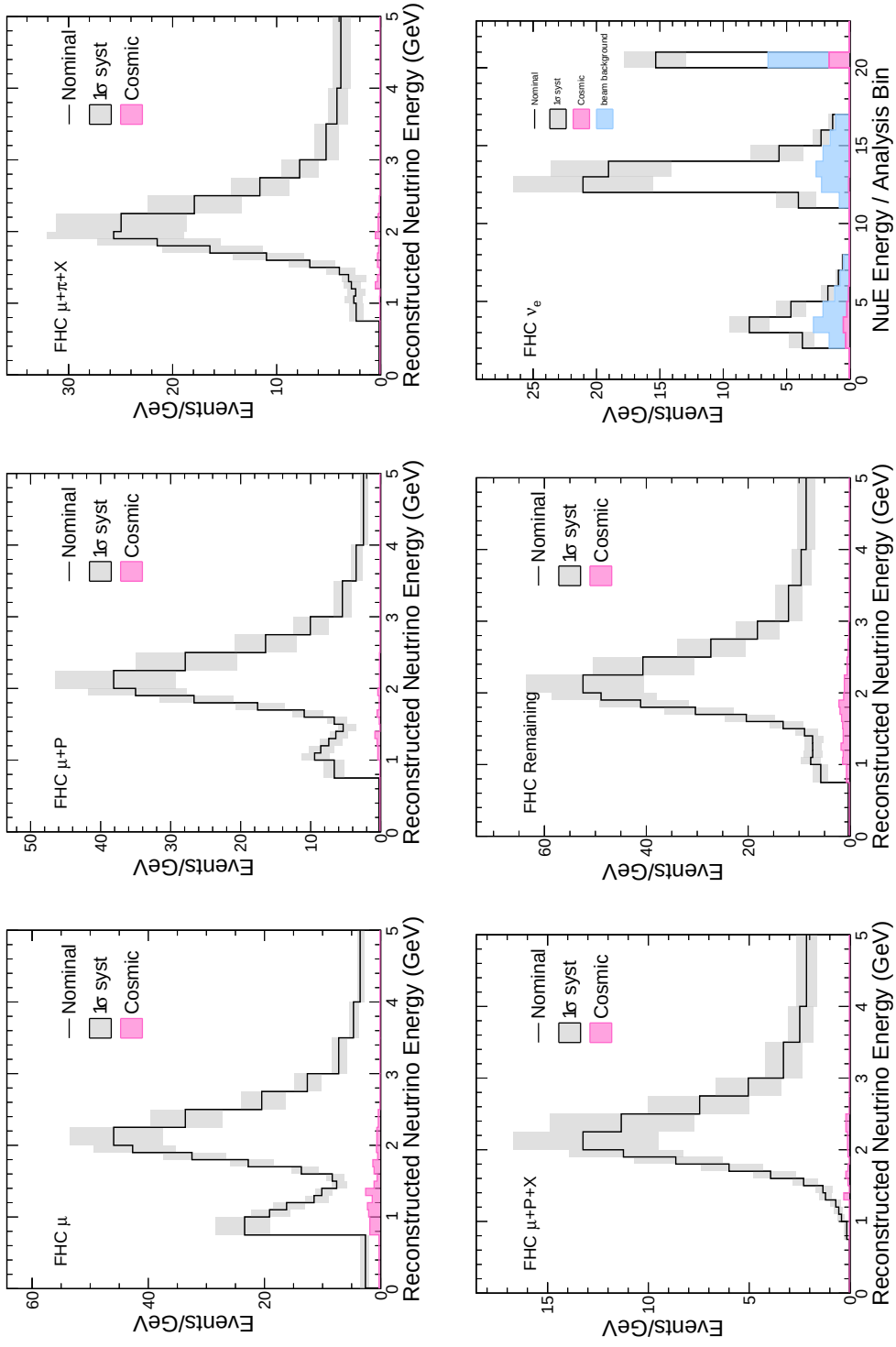

Figure 6.1: Far Detector FHC $\nu_\mu + \bar{\nu}_\mu$ topology and $\nu_e + \bar{\nu}_e$ distributions expected at oscillation parameters from [10].

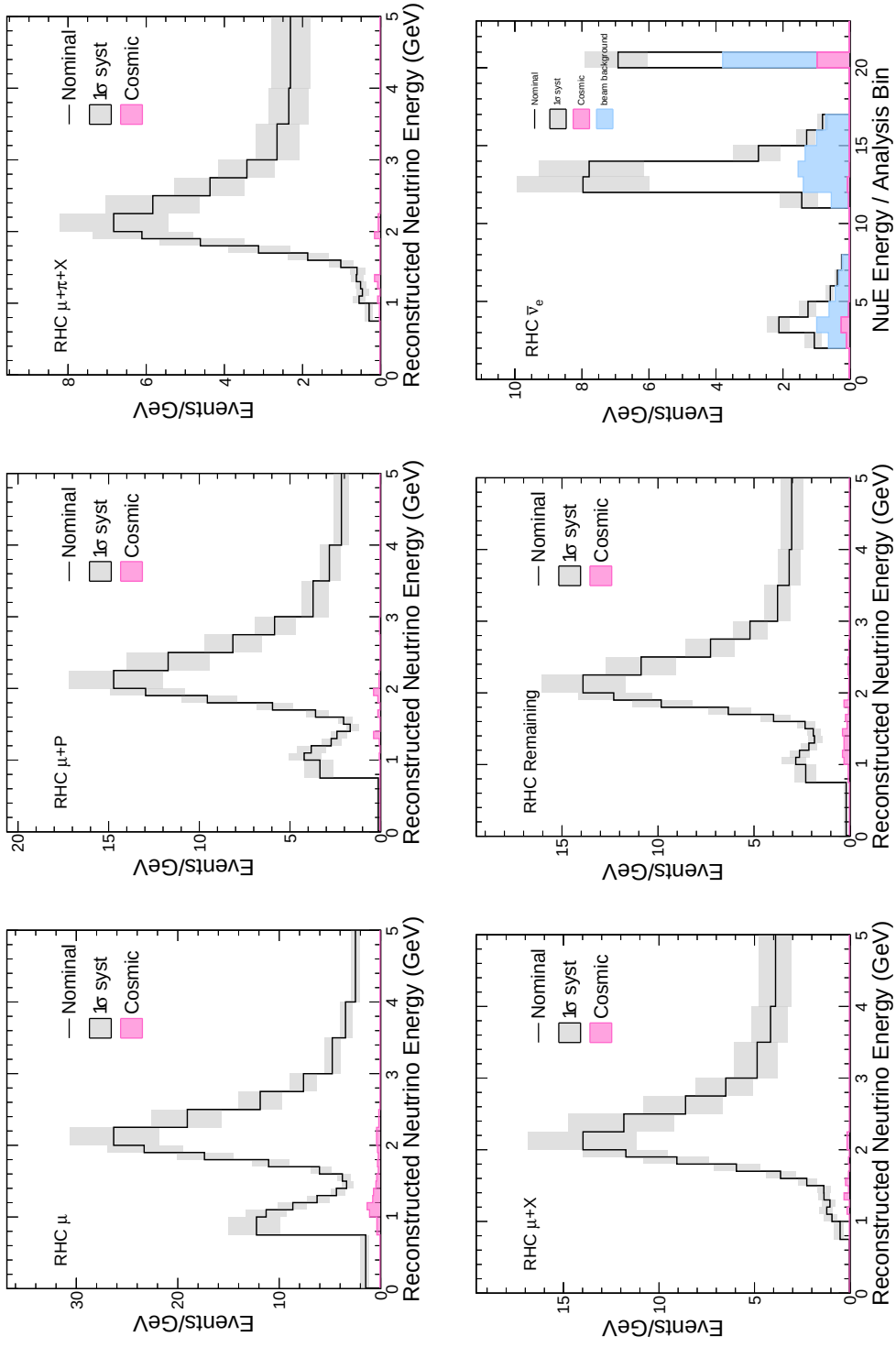

Figure 6.2: Far Detector RHC $\nu_\mu + \bar{\nu}_\mu$ topology and $\nu_e + \bar{\nu}_e$ distributions expected at oscillation parameters from [10].

$$-2\ln\lambda(\vec{\theta},\vec{\delta}) = \chi^2(\vec{\theta},\vec{\delta}) \tag{6.3}$$

$$= -2\sum_{i=1}^{N}\left[N_i(\vec{\theta},\vec{\delta}) - O_i + O_i\ln\frac{O_i}{N_i(\vec{\theta},\vec{\delta})}\right] + \sum_{j=1}^{S}\frac{\delta^2_{\mathrm{ND},j}}{\sigma^2_j} + \vec{\delta}^{\,T}_{\mathrm{FD}}V^{-1}_{\mathrm{ND}}\vec{\delta}_{\mathrm{FD}}. \tag{6.4}$$

Unlike equation 5.1, a subset of the systematic parameters $\vec{\delta}$ are not independent of each other, but instead constrained by the values and covariance found in the ND best fit. The additional S systematic parameters, which are unique to the FD predictions remain considered independent, and therefore preserve the quadratic penalty term. A schematic of the workflow of this fit is shown in Figure 6.3.

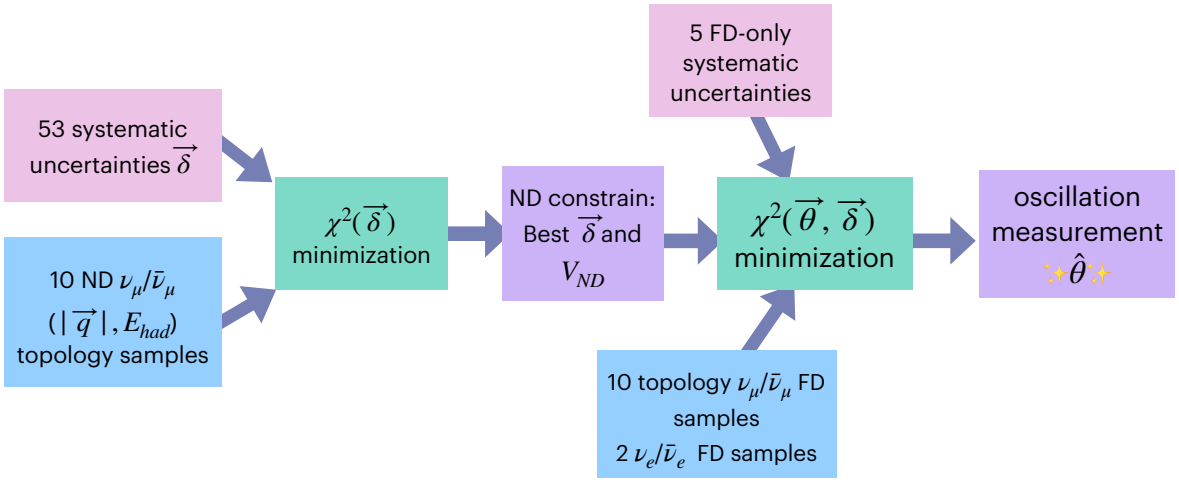

Figure 6.3: Diagram depiction of the oscillation fit with ND constrain

In section 5, 53 sources of systematic uncertainty were included in the ND fit. These included parameters in the categories of cross section, neutrino flux and detector response. Of these 53 systematic parameters, 48 are included in the oscillation fit. The systematic uncertainties removed are of the category of detector response, specifically calibration, calibration shape, light level, and Cherenkov parameters. The Far and Near detectors, although functionally identical, in practice has different response, so independent parameters are used for the FD. The covariance

matrix found from the ND constrain is then reduced by removing the rows and columns that correspond to these five parameters. Figures 6.5 and 6.4 show the covariance and correlation matrices obtained from the ND fit. The correlation matrix, with elements C_{ij} is included as it is easier to read. It is computed from the elements of the covariance matrix V:

$$C_{ij} = C_{ji} = \frac{V_{ij}}{\sqrt{V_{jj}V_{ii}}}. \tag{6.5}$$

Notice very strong correlations and anticorrelations among the 2D gaussian MEC parameters. The matrices from Figure 6.5 and 6.4 include the detector response covariance and correlations from the ND parameters (top 5 rows and last 5 columns), which are omitted when introducing this constrain to the FD fit.

The additional parameters that were not included in the ND fit (as described in section 5.2) are Muon Energy Scale, Tau neutrino scale, radiative corrections and Neutral Current versions of RES Ma and Mv, totaling 62 systematic uncertainty sources. These are particularly relevant for ν_e interactions, which were not possible to constrain using the ND ν_μ and $\bar{\nu}_\mu$ data. The muon energy scale systematics were also included only for the FD fit, given that a separate study pointed out the variables used in the ND were not as sensitive to the muon kinematics [108].

6.3 Asimov data fit

Fits to fake data are done prior to unblinding the actual FD data. The fake data used in this study, also called Asimov prediction [109], refers to histograms produced from the high statistics simulation, scaled down to the expected exposure of the real data. This translates to bins which not necessarily have an integer number of events, but do have the expected statistical errors of real data. The Asimov prediction in this study incorporates the oscillation parameter values for δ_{CP}, $\sin^2\theta_{23}$ and Δm^2_{32} measured in the latest NOvA analysis from [10], specified in table 6.3. In addition, the ND constrain described in the previous chapter is also implemented in the FD predictions. The exposure used to scale the FHC samples is (14.2×10^{20}) and for RHC $(12.5 \times 10^{20}$) POT-equiv.

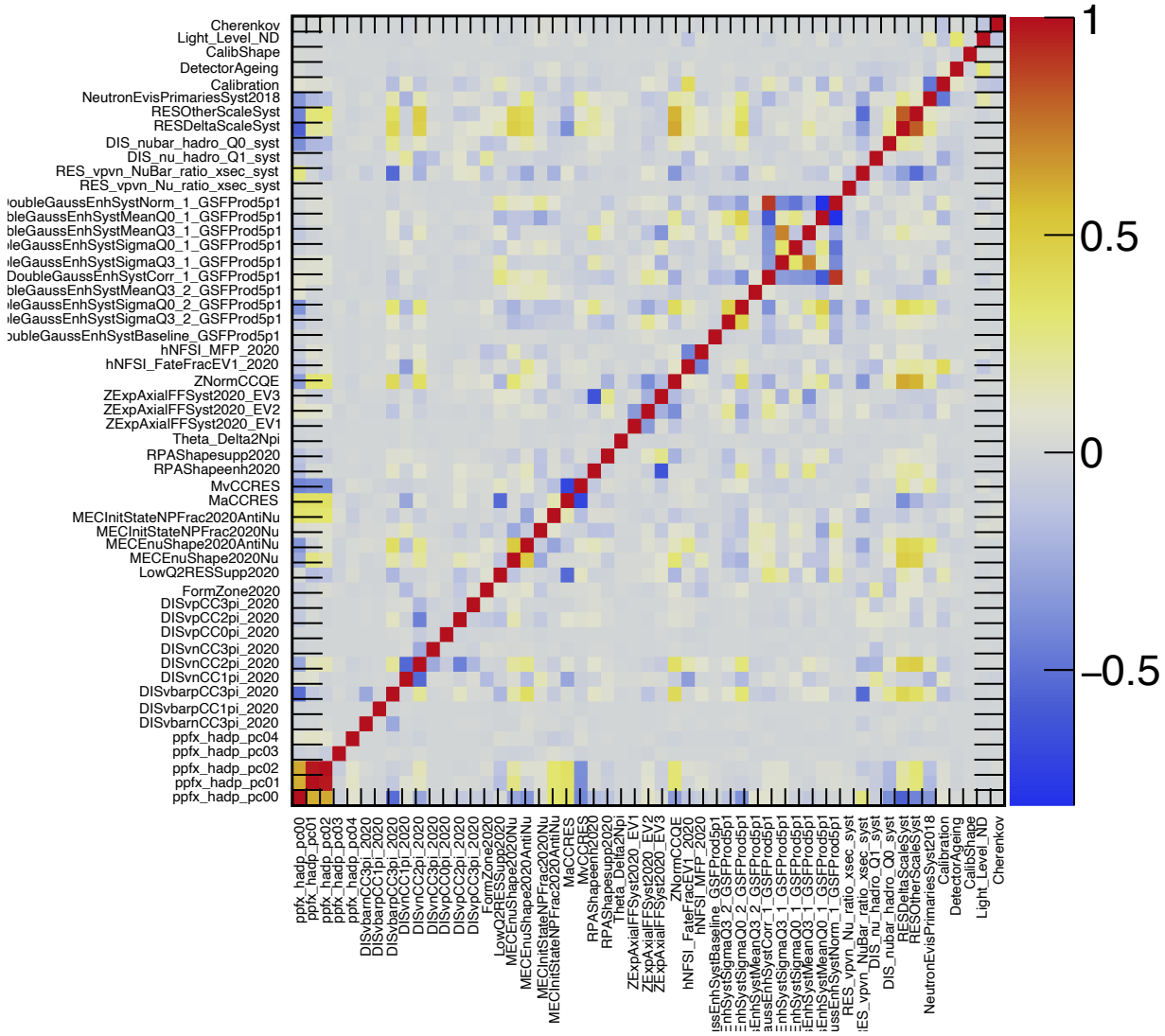

Figure 6.4: ND fit correlation matrix of systematic parameters obtained from ND fit.

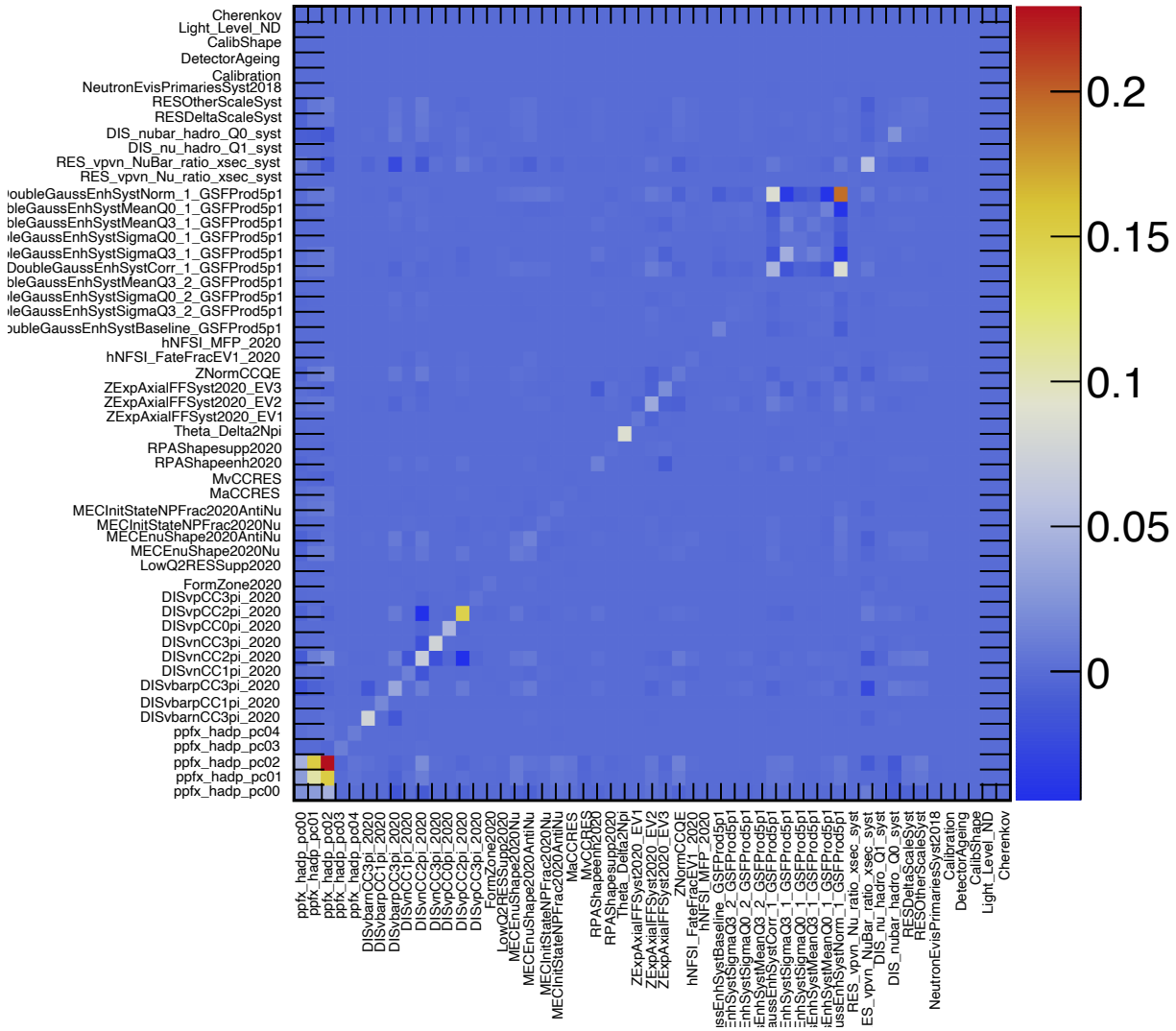

Figure 6.5: ND fit covariance matrix of systematic parameters obtained from ND fit.

Thus the fitted predictions and sensitivities are constructed following the procedure described before and summarized in Figure 6.3. The oscillation parameters δ_{CP} $\sin^2\theta_{23}$ and Δm^2_{32} are simultaneously fit, as free parameters. Note that the χ^2 minimization includes the constrained oscillation parameter θ_{13}, which has been measured by reactor neutrino experiments with higher precision than what is feasible with long baseline experiments. This is treated as a nuisance parameter, in a similar fashion as the systematic uncertainties, having a quadratic penalty term with 1σ as indicated in table 6.3.

Table 6.1: Asimov oscillation parameters from NOvA best fit [10] and external constrains [110].

Parameter	**Value**
NOvA best fit	
Δm^2_{32}	$2.41\ \times 10^{-3}\text{eV}^2$
$\sin^2\theta_{23}$	0.57
δ_{CP}	0.82π
External constrains	
Δm^2_{21}	$7.53\ \times 10^{-5}\text{eV}^2$
$\sin^2\theta_{12}$	0.2807
$\sin^2\theta_{13}$	$0.0210\pm\ 0.0011$
ρ	$2.84\ g/cm^3$

Figures 6.6 and 6.7 show the fake data which is generated with the oscillation parameters listed and using the constrain from the ND for the list of systematic uncertainties from chapter 5. The ratio plots include the statistical uncertainties, which are dominant with the current exposure. These predictions are also overlaid with the nominal prediction (which does not include any constrain), and the total unconstrained uncertainty. Notice the blue error bands display the reduced uncertainty as it is constrained by the ND fit.

Figure 6.8 shows the 1-dimensional slices of the oscillation parameters fit, which also show the 1σ uncertainties for each parameter at the global best fit. Note in this case the best fit is in the Normal Ordering, Upper Octant. The resulting values are identical to the parameters assigned to the Asimov point as expected.

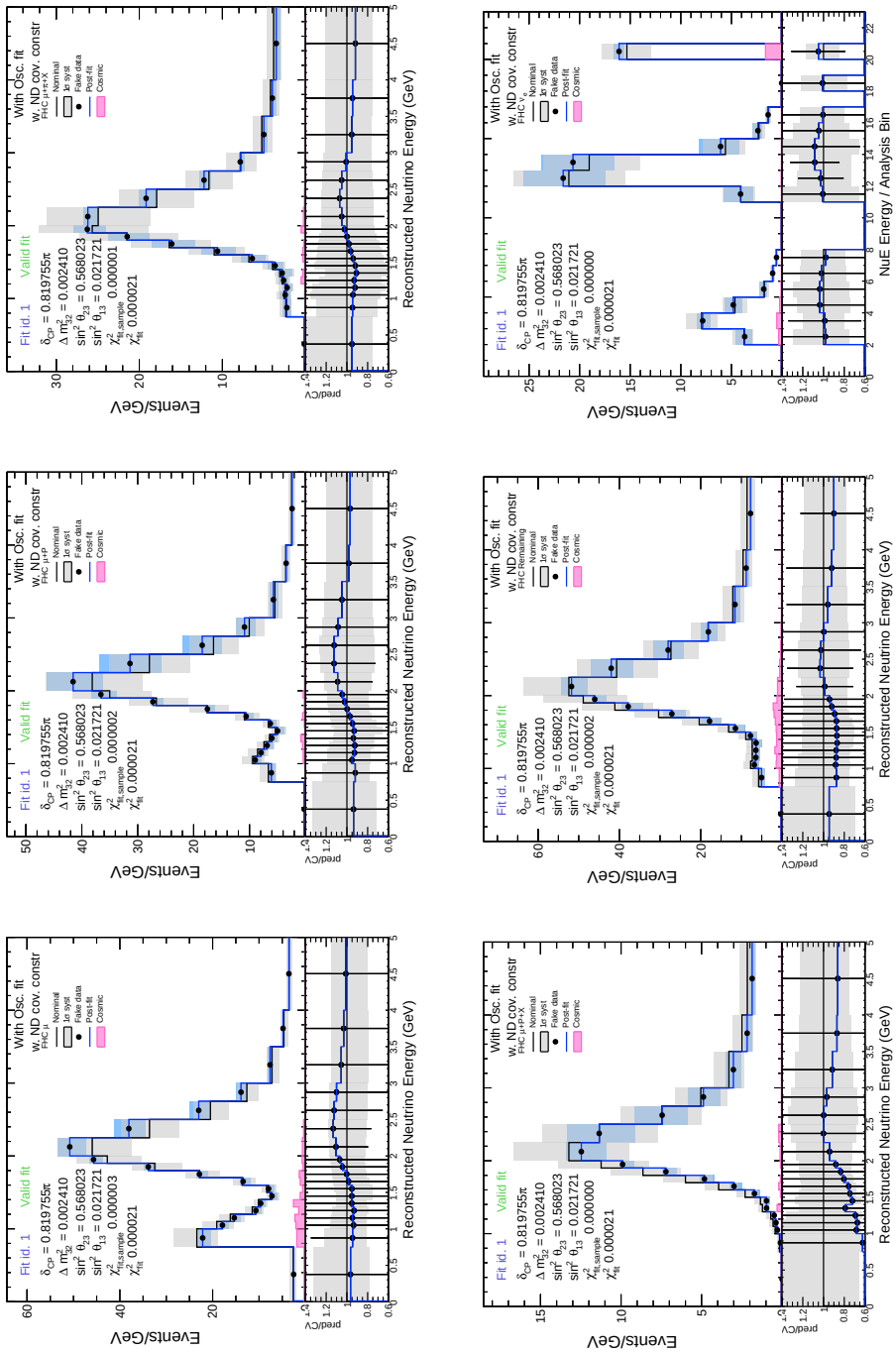

Figure 6.6: FHC predictions fit to Asimov data (black markers). The nominal prediction with unconstrained uncertainties is indicated with black and grey error bands. The fitted predictions with reduced uncertainty are indicated in blue. Statistical errors are displayed in the ratio.

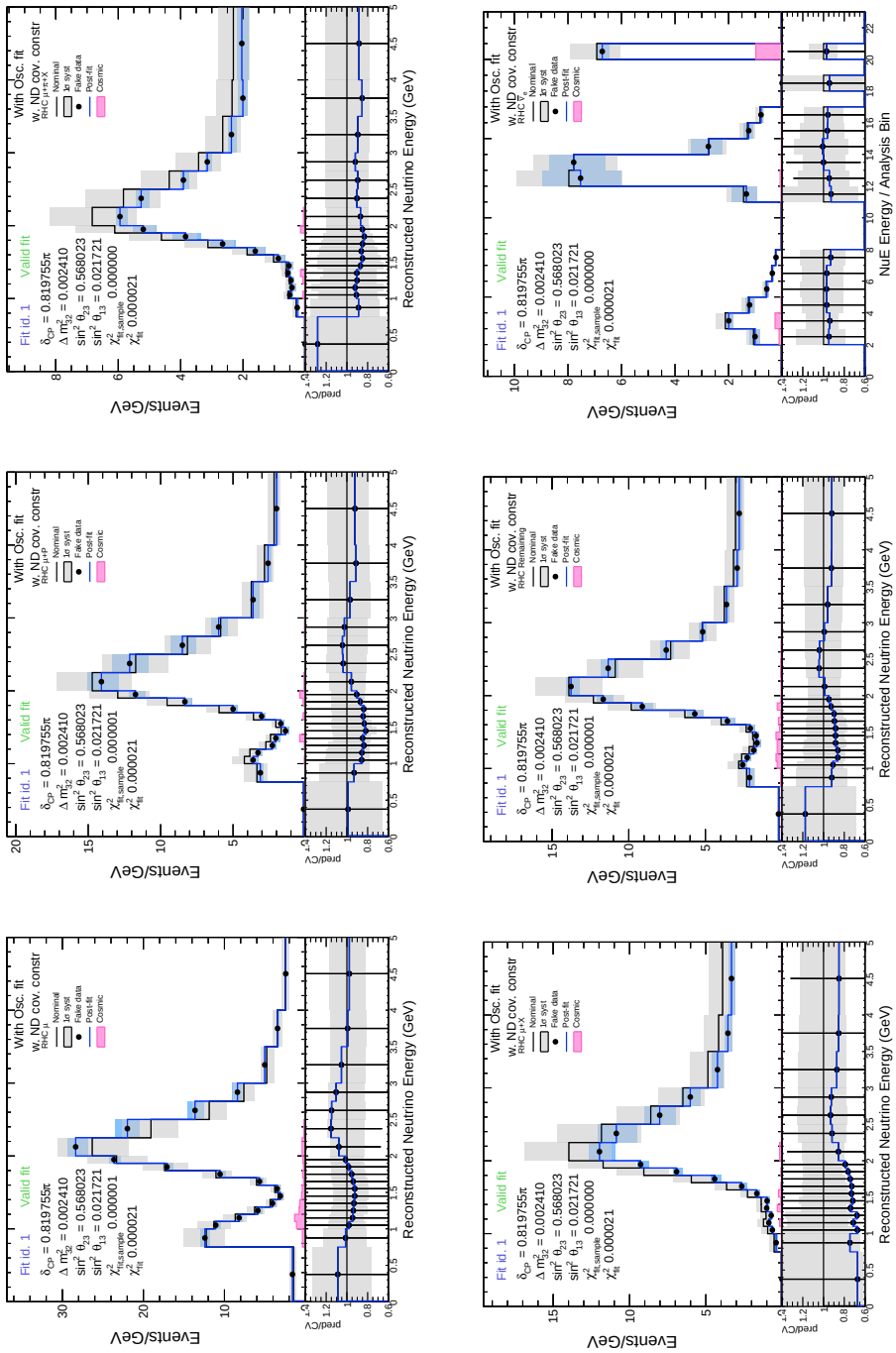

Figure 6.7: RHC predictions fit to Asimov data (black markers). The nominal prediction with unconstrained uncertainties is indicated with black and grey error bands. The fitted predictions with reduced uncertainty are indicated in blue. Statistical errors are displayed in the ratio.

Table 6.2: Asimov fit result. The 1σ uncertainty is given by Figure 6.8

Parameter	**Value**
$\Delta m^2_{32}(\times 10^{-3}\mathrm{eV}^2)$	$+2.41^{+0.058}_{-0.060}$
$\sin^2\theta_{23}$	$0.568^{+0.025}_{-0.124}$
$\delta_{CP}(\pi)$	$0.82^{+0.21}_{-0.80}$

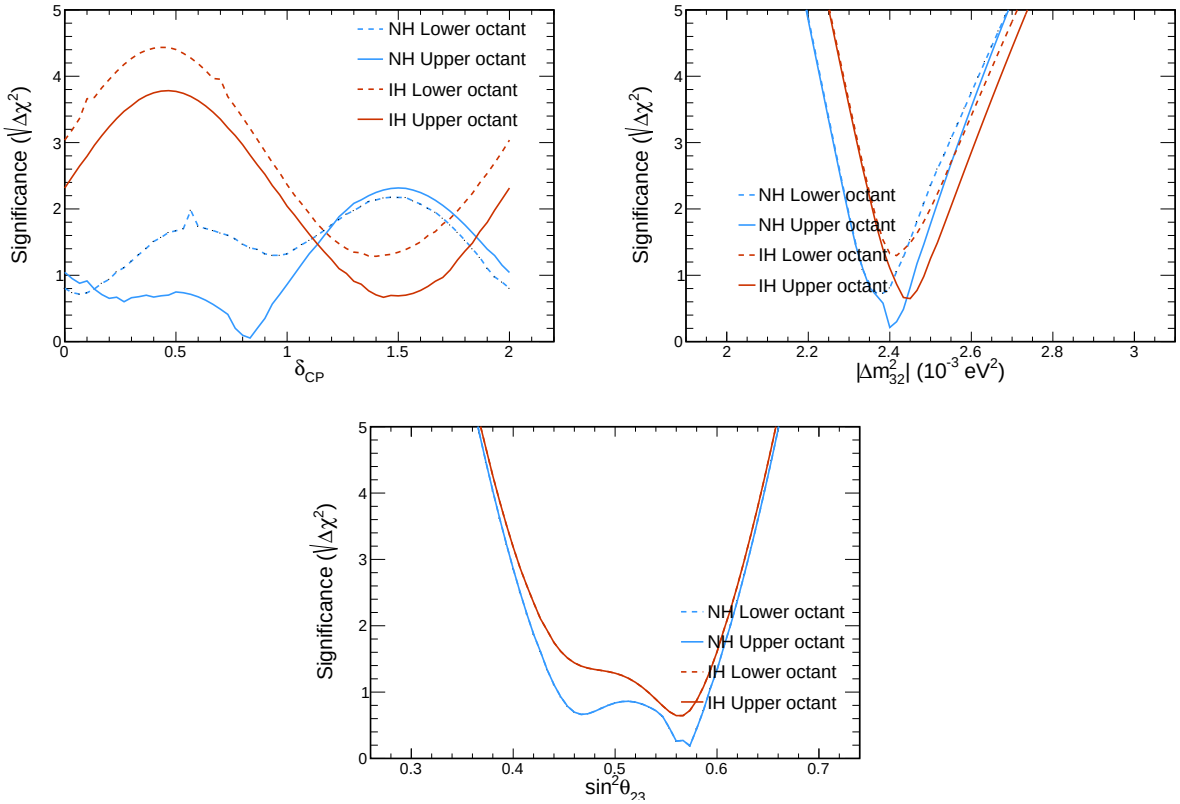

Figure 6.8: One-dimensional significance for δ_{CP} , $\sin^2\theta_{23}$ and Δm^2_{32} in the Asimov fit, shown for Normal (blue) or inverted (red) mass ordering/hierarchy, and for upper (solid line) or lower (dashed line) octants.

6.3.1 Contours

Figure 6.9 shows the contours in $(\delta_{CP}, \sin^2\theta_{23})$ and $(\Delta m^2_{32}, \sin^2\theta_{23})$ spaces, profiling over the two other variables not shown (including $\sin^2\theta_{13}$), asuming Normal Ordering/Hierarchy and Inverted Ordering/Hierarchy for the masses. The 1,2 and 3 σ contours are drawn, which correspond to $\sqrt{\Delta\chi^2} = 2.280$, 6.18 and 11.83 respectively.

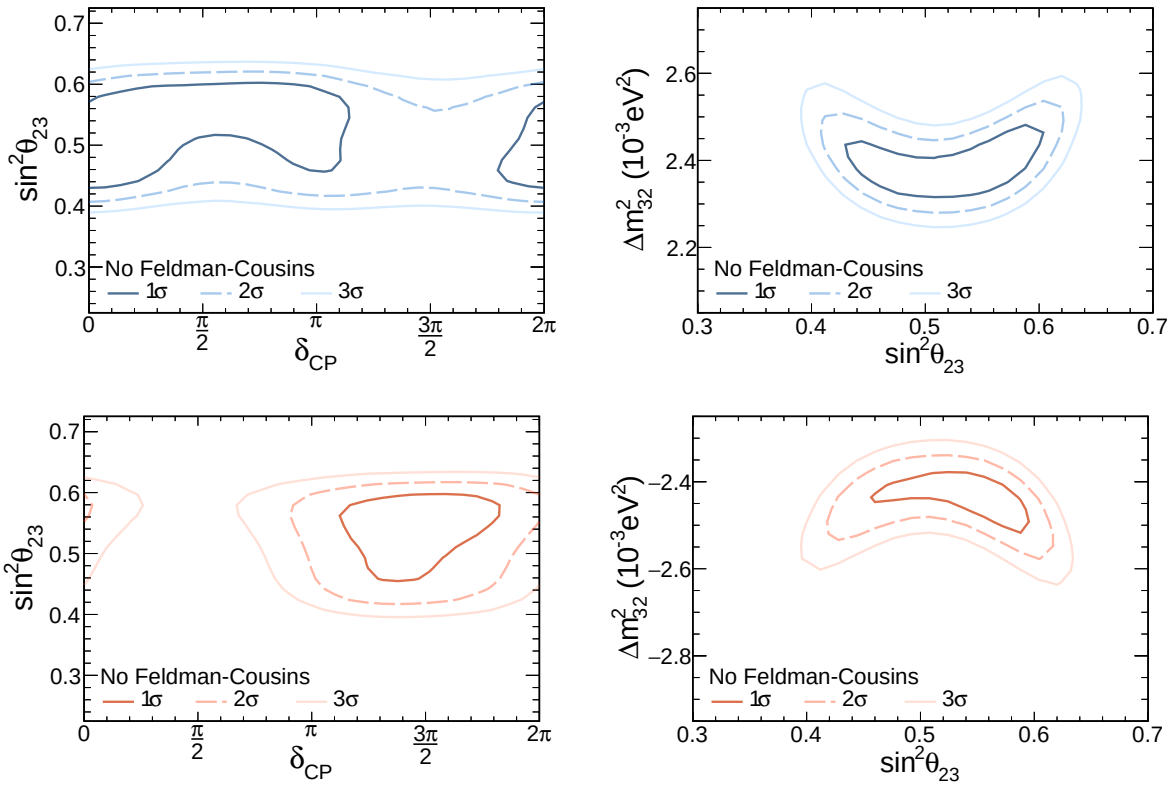

Figure 6.9: Sensitivities assuming the oscillation parameters in table 6.1 for Normal (blue) and Inverted (red) Hierarchy/Ordering. 1, 2, and 3σ allowed regions are profiled over $\sin^2 2\theta_{13}$ and Δm^2_{32} (left) and $\sin^2 2\theta_{13}$ and δ_{CP} (right).

6.3.2 Sensitivities

The potential to determine neutrino mass hierarchy, CP violation, non-maximal mixing and the octant of θ_{23} is calculated in the following way:

- Mass ordering sensitivity: $\chi^2_{\text{wrong ordering}} - \chi^2_{\text{right ordering}}$, profiled over $\sin^2\theta_{23}, \Delta m^2_{32}, \sin^2\theta_{13}$ and δ_{CP}.
- CP violation sensitivity: $\chi^2_{0,\pi} - \chi^2_{\text{all values}}$
- Maximal mixing sensitivity: $\chi^2_{\sin^2\theta_{23}=0.5} - \chi^2_{\text{all values}}$
- θ_{23} octant rejection sensitivity: $\chi^2_{\text{wrong octant}} - \chi^2_{\text{right octant}}$, profiled over Δm^2_{32}, $\sin^2\theta_{13}$, δ_{CP}, and $\sin^2\theta_{23}$.

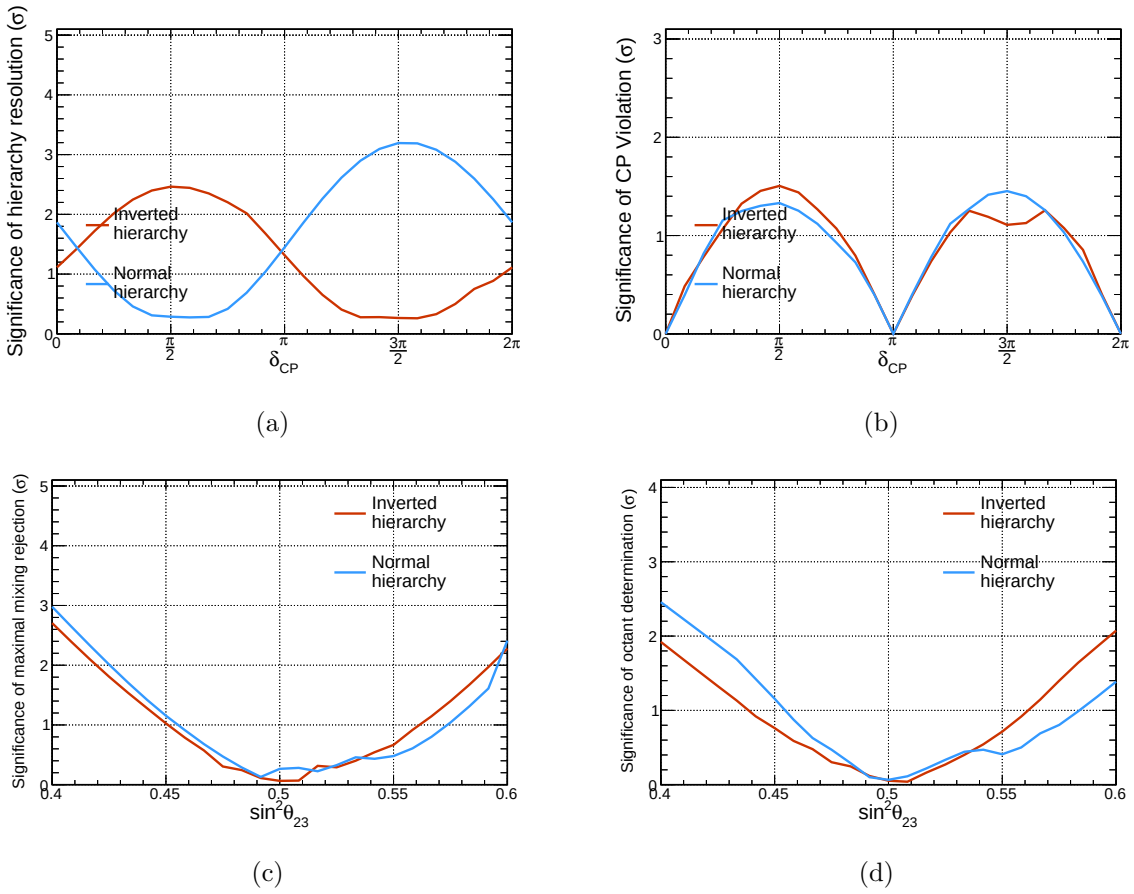

Figure 6.10: Potential rejection of the (a) wrong hierarchy and (b) CP conservation as a function of δ_{CP}; (c) maximal mixing and (d) wrong octant, as functions of $\sin^2\theta_{23}$, assuming true normal (blue) or inverted (red) hierarchy.

6.4 Multiple Universes fit robustness test

Recall from Figure 5.30, that the ND constrain chosen, and that produces the smallest χ^2 in the ND samples, is picked from approximately 1000 different fits. It is a concern that with the 53 parameters parameters to minimize, the seeds used for the fit did not fully explore the parameter space, and therefore a different set of parameter values might better describe the data. This in consequence will produce a different FD prediction, and if the constrain was different it might bias the oscillation result.

A study is designed to test the robustness of the oscillation fit, against variations in the ND constrain selected. The strategy is the following:

- Fake data is the Asimov produced with the NOvA best fit oscillation parameters from table 6.1 and using the constrain from Figure 5.30.
- Select a subset of valid ND constrains to fit oscillation parameters using the Asimov data and these different ND constrains.
- If the variation of these fits is small, then we can be confident that using the best fit (the one that produces the smallest χ^2) from the ND, even if not the optimal, will not make a significant difference in the oscillation measurement.

Figure 5.30 shows multiple allowed values for systematic parameters. These different values produce various post-fit distributions with similar level of agreement. However the range of χ^2 spans from 20517 to > 24000. The distribution of χ^2 values for the valid fits is shown in Figure 6.11. A set of randomly selected fit results, following such distribution, is pictured in Figure 6.12. The systematic parameter values for the 85 constrains with the lowest χ^2 values is shown in Figure 6.13. Notice that the degeneracy in the parameter values found is mostly lifted when the lowest χ^2 fit results are selected. Most parameter values of these constrains match with the best fit, which is highlighted in black. Notice however, that there are parameters still show two values that produce ND distributions with χ^2 between 20517 and 20767, including

ZExpAxialFFSyst2020_EV1,2,3, ZNormCCQE, DISvnCC1pi_2020, and MEC EnhSystSigmaQ3_2_GSFProd5p1.

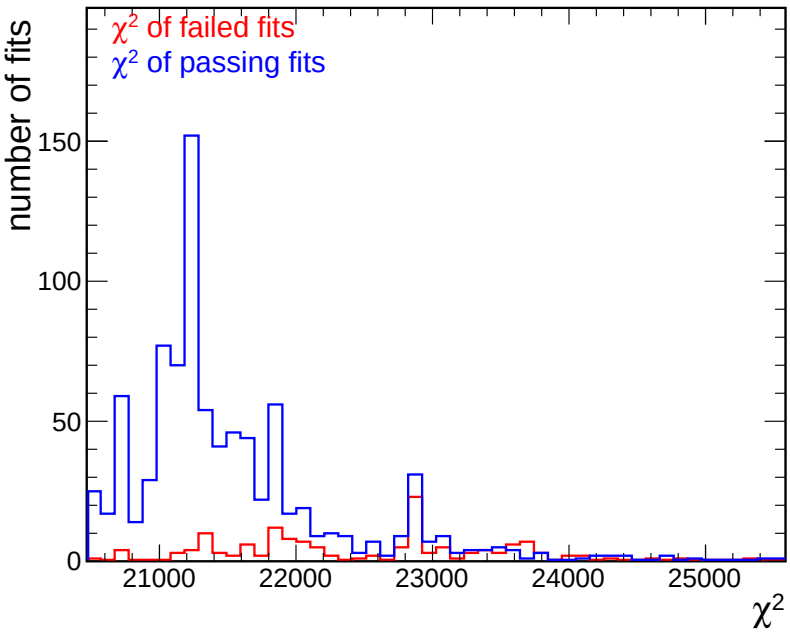

Figure 6.11: χ^2 distribution of 1020 randomly seeded fits to ND data. The blue distribution shows the result of fits that converged, and the red line shows the fits that failed.

For the robustness test, only the top 85 ND constrains (the lowest χ^2 yielding fits, shown in Figure 6.13) and their corresponding covariance are used to fit the Asimov fake data (the same fake data displayed in figures 6.6 and 6.7). Each constrain used is considered a *universe*, and these represent the case where the constrains utilized to fit oscillation parameters are close, but not equal, to the actual parameter values that represent the FD data.

Figure 6.14 displays the overlaid contours of oscillation fits using the Asimov data, as in Figure 6.9, and for each fit with covariance matrices from the 85 ND constrains that correspond to the systematic shifts in Figure 6.13. Notice that the 2 and 3 σ contours are mostly identical to the Asimov contours, displayed in red or blue lines. Only a small dip in the 2σ contour for the Normal Ordering $\delta_{CP} - \sin^2\theta_{23}$ is noticeable. The 1σ contours do show some variation, specially in the Normal Ordering $\delta_{CP} - \sin^2\theta_{23}$ plot. For the same space, a fraction of the fits show a best

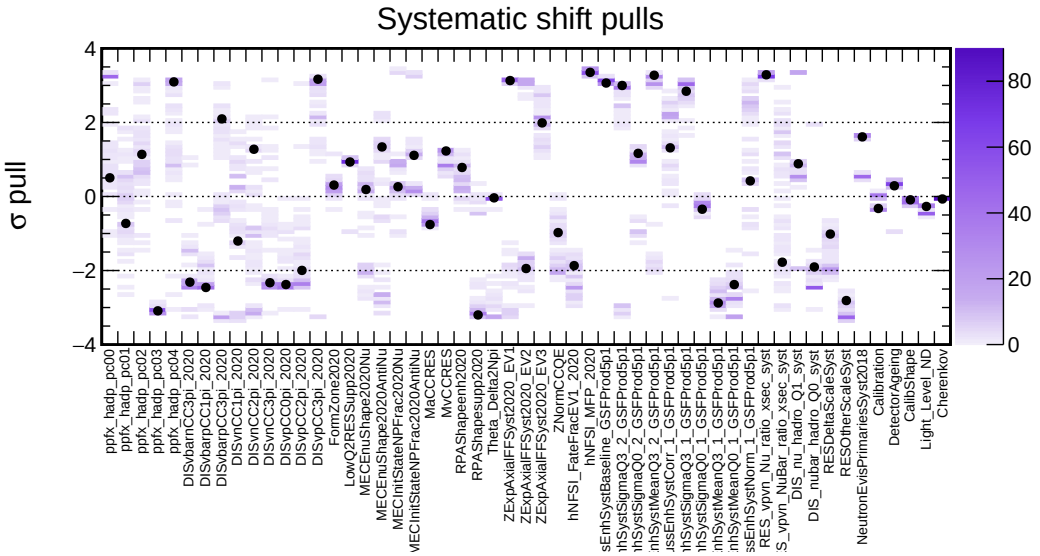

Figure 6.12: ND data for 89 randomly sampled fit results from post-fit χ^2 distribution. The systematic uncertainty shift values highlighted in black markers produce the smallest χ^2.

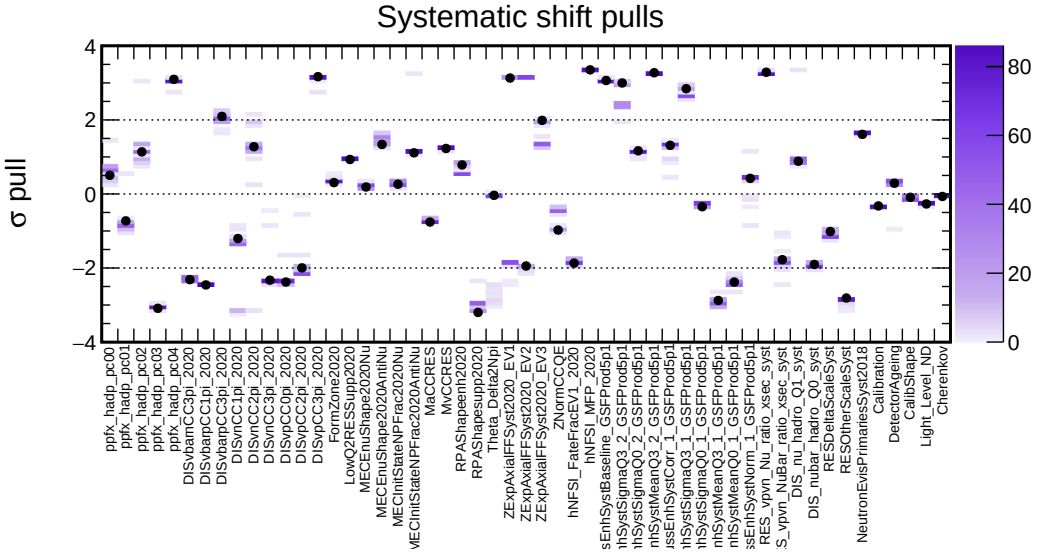

Figure 6.13: ND data fit results for 85 lowest χ^2. The systematic uncertainty shift values highlighted in black markers produce the smallest χ^2.

fit shifted towards $\delta_{CP} = \pi/2$, and no shift in $\sin^2\theta_{23}$. Although this is a non-negligible shift in the δ_{CP} axis, notice that all the best fit points are within the 1σ contour.

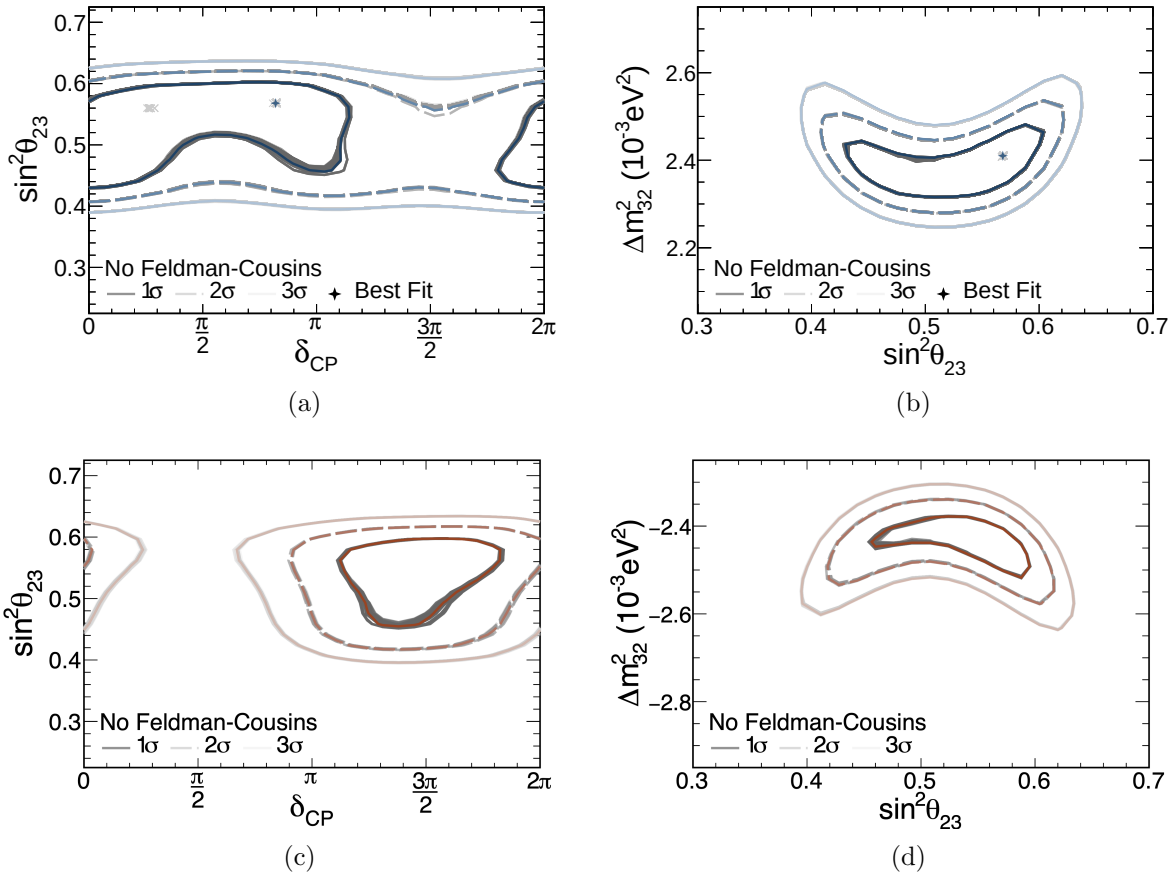

Figure 6.14: Sensitivities for the fit to Asimov data, using different constrains from ND data. The grey lines represent the 1, 2 and 3σ allowed regions for each *universe*(ND constrain) and the red/blue lines represent the result with the correct ND constrain.

6.5 Fake Data fits

The Asimov fit from the previous section demonstrates the technical feasibility of the fitting method . However, it is necessary to study the performance of the fit testing it with different scenarios where the FD data differs from the constrained prediction considered as the Asimov data. The cases of study concern the underlying neutrino interaction model and the quality of the ND constrain. For the first case, the fake data is created with differences in the MEC interaction

model. The second case studies a scenario where the FD prediction contains a constrain that perfectly matches the data, via the introduction of a *residual weight*. In order to compare the results of these different fake data fits in a consistent basis, a set of bias metrics are defined.

6.5.1 Bias Metrics

The mid-point and width of a confidence interval is compared between the Asimov fit and the fit using a different fake data [111]. The 2σ confidence interval is used to asses the fake data studies in this thesis.

There are two sources of uncertainty in the fits: statistical (σ_{stat}) and systematic(σ_{syst}). The systematic uncertainty is calculated subtracting in quadrature the the witdth of the confidence interval from a fit with no systematic parameter (statistical errors only) from the width of the Asimov fit including all systematic parameters:

$$\sigma_{\text{syst}} = \sqrt{\sigma^2_{\text{asimov}} - \sigma^2_{\text{stat}}} \tag{6.6}$$

.

There are two categories of criteria to assess whether the bias from a fake data fit is acceptable. The first is the change in mid-point (Δ_{mid}), compared to the systematic uncertainty σ_{syst}. If the change in the mid-point of the confidence interval is larger than 50% of the systematic uncertainty, the bias would be considered significant. The second criteria is based on the the total width of the interval. If the change of width of the confidence interval, between Asimov and fake data, is larger than 10% of the total width of the Asimov fit interval, this is also considered a significant bias. In summary, a fake data fit is considered to have significant bias if either of the following is true:

- $\Delta_{\text{mid}} > 0.5\sigma_{\text{syst}}$
- $\Delta\sigma > 0.1\sigma_{\text{asimov}}$

These criteria are used to evaluate the constrains on Δm^2_{32} and $\sin^2\theta_{23}$. To compare the fits with respect to δ_{CP}, we only observe qualitative differences in the $\Delta\chi^2$ surfaces. As it is a cyclical

variable, and the 2σ confidence interval can be discontinuous, so σ_{syst} is not as straightforward to compute.

6.5.2 MEC model change fake data studies

Three fake data sets are generated using the same MEC model changes that were used for the ND fits in section 5.4.3. The FD predictions MEC interactions are reweighted as explained in the ND case, and the same oscillation parameters from table 6.1. The oscillation fits are done using the ND constrain and covariance matrix for the corresponding fake data fit to the ND. In other words, the fit is similar to the scheme of Figure 6.3, only substituting the data in ND and Asimov data in FD, for MEC-reweighted predictions. The correlation and covariance matrices are in appendix B.

Minerva weights for 2p2h This fake data fit includes the constrain from 5.21 and the covariance matrix in Figure B.2. The contours that correspond to this fit (grey lines) are compared to the Asimov fit (red/blue lines) in Figure 6.15. The best fit point is practically identical to that of the Asimov fit. The most notorious difference is in the space of δ_{CP} and Δm^2_{32} , where the 1σ contour is larger, allowing a larger set of values for Δm^2_{32} , particularly for the normal ordering (blue). In the case of Δm^2_{32} - $\sin^2\theta_{23}$ space, the contours are only slightly shifted. Note however that the inverted ordering case shows less preferece for the upper octant than the Asimov fit.

QE-like MEC fit This fake data fit includes the constrain from 5.22 and the covariance matrix in Figure B.5. The contours that correspond to this fit (grey lines) are compared to the Asimov fit (red/blue lines) in Figure 6.16. Notice a slight widening of the 1σ contour in the normal ordering δ_{CP} - Δm^2_{32} axes. The inverted ordering Δm^2_{32} - $\sin^2\theta_{23}$ 1σ contour in the inverted ordering case shows slightly less preference for the upper octant, while the normal ordering case is very similar to the Asimov data fit. The best fit point is close to identical to the Asimov fit.

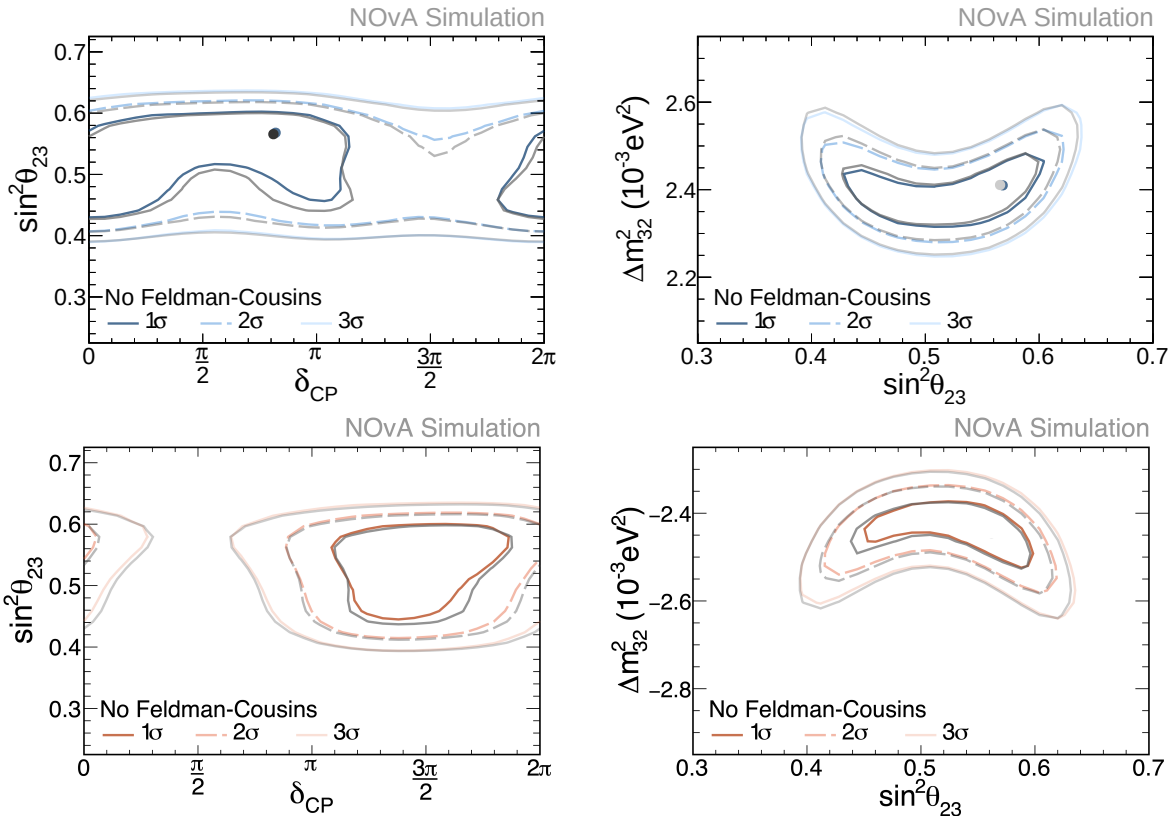

Figure 6.15: Sensitivities assuming the oscillation parameters in table 6.1, comparing MINERvA-weighted MEC fake data (grey) and Asimov data fits, for Normal (blue) and Inverted (red) Hierarchy/Ordering. 1, 2, and 3σ allowed regions are profiled over $\sin^2 2\theta_{13}$ and Δm^2_{32} (left) and $\sin^2 2\theta_{13}$ and δ_{CP} (right).

RES-like MEC fit This fake data fit includes the constrain from 5.23 and the covariance matrix in Figure B.8. The contours that correspond to this fit (grey lines) are compared to the Asimov fit (red/blue lines) in Figure 6.17. Notice a slight contraction of the 1σ contour in the normal ordering δ_{CP} - Δm^2_{32} axes. The Δm^2_{32} - $\sin^2\theta_{23}$ contours are very similar in both normal and inverted mass ordering. The best fit point is close to identical to the Asimov fit.

Aside from the qualitative observations described, the bias of these fits is evaluated using the bias metrics defined previously. It was noticed that the 2σ contours did not shift very much from the Asimov to each of the fake data cases. This is further confirmed by computing the bias metrics for these fits, shown in the table of Figure 6.18, which demonstrates that these fake data

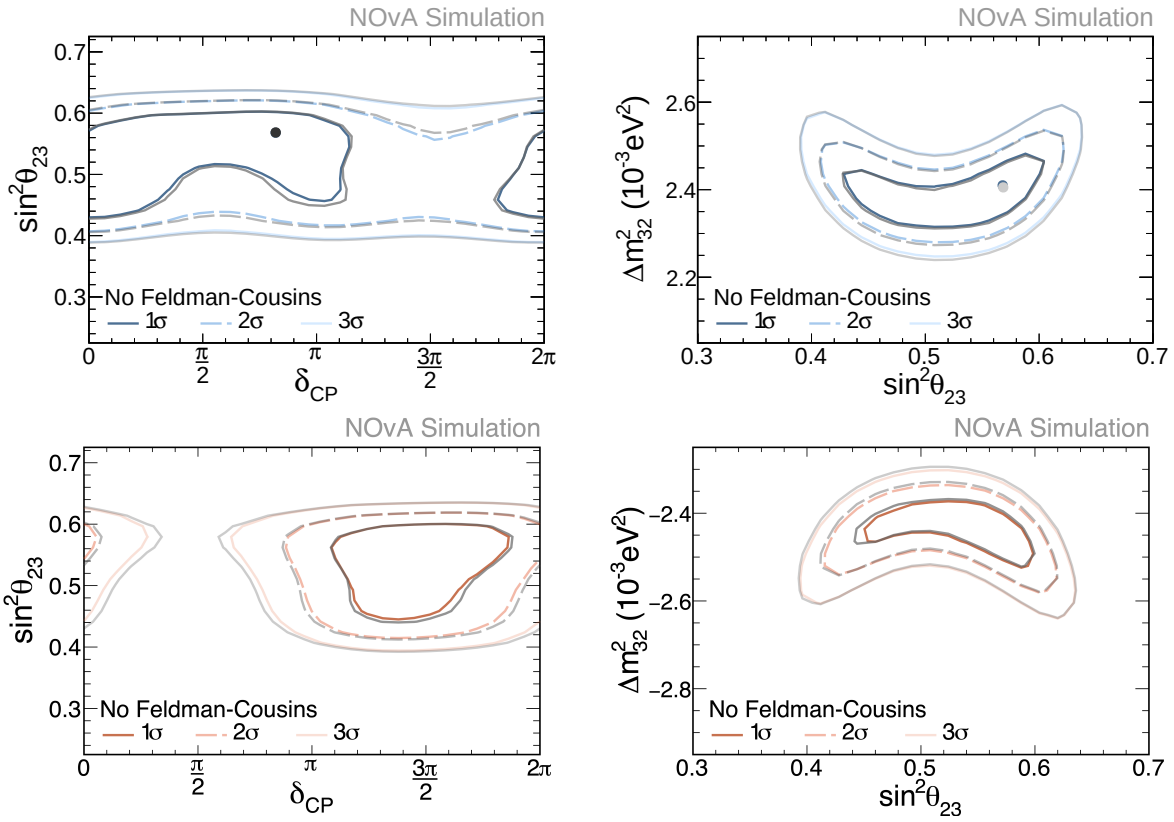

Figure 6.16: Sensitivities assuming the oscillation parameters in table 6.1, comparing QE-like-weighted MEC fake data (grey) and Asimov data fits, for Normal (blue) and Inverted (red) Hierarchy/Ordering. 1, 2, and 3σ allowed regions are profiled over $\sin^2 2\theta_{13}$ and Δm^2_{32} (left) and $\sin^2 2\theta_{13}$ and δ_{CP} (right).

studies show no significant bias. The 2σ confidence intervals are shown in detail in appendix B (figures B.3,B.6 and B.9).

The fact that these fake data studies show no significant bias additionally demonstrates the robustness of this method against variations on the shape of the data which are not explicitly defined by the parameters of table 5.7. In other words, if the data in the ND and FD can be described as close as the constrains of section 5.4.3, the oscillation measurement is unlikely to be significantly biased.

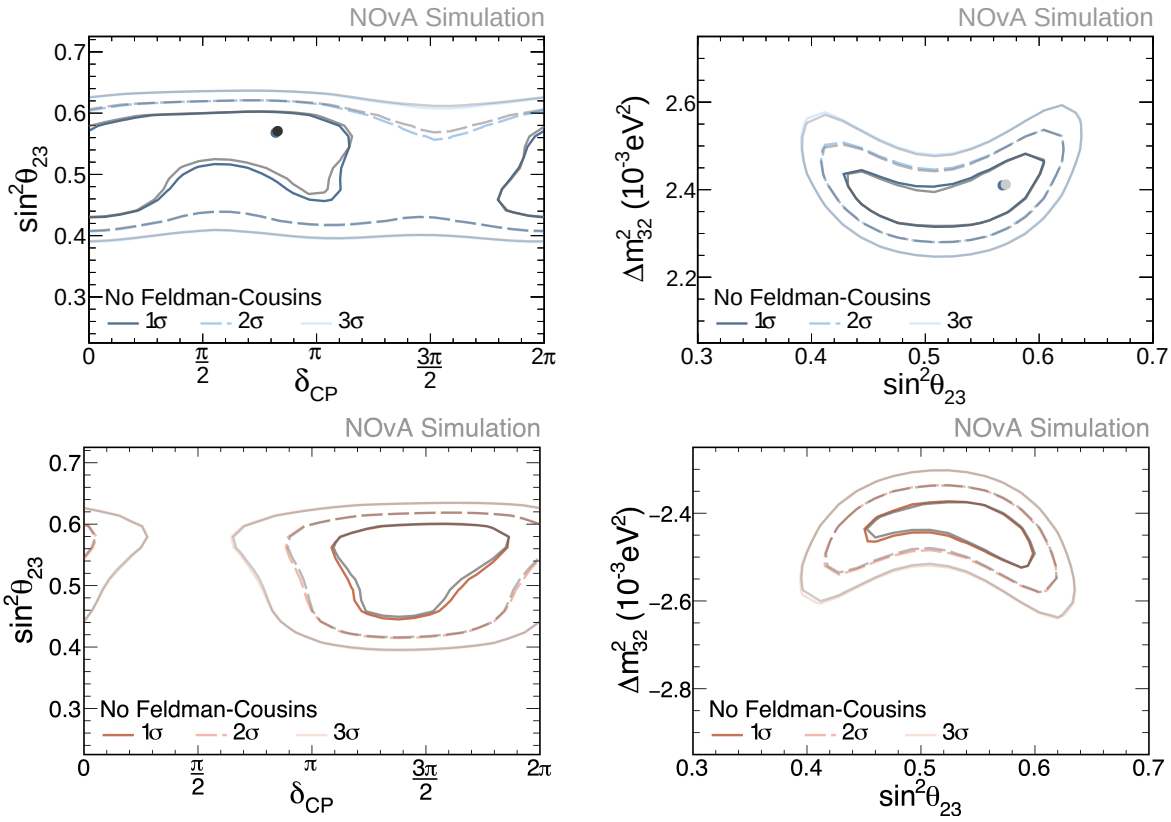

Figure 6.17: Sensitivities assuming the oscillation parameters in table 6.1, comparing RES-like-weighted MEC fake data (grey) and Asimov data fits, for Normal (blue) and Inverted (red) Hierarchy/Ordering. 1, 2, and 3σ allowed regions are profiled over $\sin^2 2\theta_{13}$ and Δm^2_{32} (left) and $\sin^2 2\theta_{13}$ and δ_{CP} (right).

6.5.3 Residual difference fit

Table 5.8 quantifies the agreement of the fitted topology samples based on the χ^2 comparison before and after the fit. The χ^2 per degrees of freedom is significantly reduced, although the simulation does not match the data perfectly. However, the ND data set has very high statistics, and it is a difficult task to determine what is a sufficient level of agreement that does not bias the FD prediction. In order to study the effect of the remaining disagreement between ND data and simulation, and quantify how much this biases the oscillation fit, an alternative FD fake data set that corresponds to perfect ND agreement is implemented. This fake data is created by implementing reweighting bin-by-bin the FD ν_μ topology samples. The weights are obtained by computing the ratio of the ND data and constrained simulation in the same axis (E_ν) that is used

	$\lvert\Delta m^2_{32}\rvert$						$\sin^2\theta_{23}$					
	Best fit point	Mid-point	Width	σ_{syst}			Best fit point	Mid-point	Width	σ_{syst}		
Stats only fit	2.35	2.48187	0.1907	0.1018 Critical: 0.0509			0.493333	0.60106	0.173345	0.0911 Critical: 0.0456		
Asimov fit	2.41	2.51213	0.21618				0.568	0.613086	0.195845			
FDS	BF	Mid-point	Width	Δσ	Δ mid	Sgnf bias	Best fit point	Mid-point	Width	Δσ	Δ mid	Sgnf bias
Minerva	2.41667	2.51203	0.2108	-0.00538	-0.0001	no	0.566667	0.610234	0.194078	-0.001767	-0.002852	no
QE-like	2.4	2.5095	0.21862	0.00244	-0.00263	no	0.566667	0.613536	0.197758	0.001913	0.00045	no
RES-like	2.41667	2.51246	0.21564	-0.00054	0.00033	no	0.573333	0.613611	0.195839	-0.000006	0.000525	no

Figure 6.18: Bias metric table for the MEC model change fake data fits shown in figures 6.16 through B.3. All fake data fits pass the bias metric criteria.

to fit oscillations with the FD samples. Figures 6.19 and 6.20 show the ND topology samples comparing data and simulation, where the ratios correspond to the residual weight that will be applied to the FD samples.

For the FD ν_e predictions, the implementation of the residual weight is slightly different. The ND topology samples can only constrain parameters related to ν_μ interactions. Therefore the residual weight is implemented to the signal component of the ν_e prediction. This means only the fraction of predicted ν_e and $\bar{\nu}_e$ that oscillated from ν_μ /$\bar{\nu}_\mu$ are reweighted. Another difference is that the weight is obtained from the total distribution of ND ν_μ , in the same E_ν bins that are used for the ν_e prediction. Figure 6.21 shows the corresponding distributions to obtain such weights.

Notice that the overall behavior of the ratios corresponds to overprediction at bins in the falling edge (greater than ≈2 GeV), and in some cases, underprediction at the peak of the distributions (bins from 1.5 to 2 GeV).

In order to test the validity of this method, and evaluate the bias, three different Asimov data sets are considered. These are various points-of-interest in the oscillation parameters phase space which are observable by the NOvA experiment. The bi-probability plot shown in Figure 6.22 displays the Asimov points. Table 6.3 specifies the values for each parameter. Asimov point A is what corresponds to the NOvA best fit [10], which was already used in the previous displayed fits.

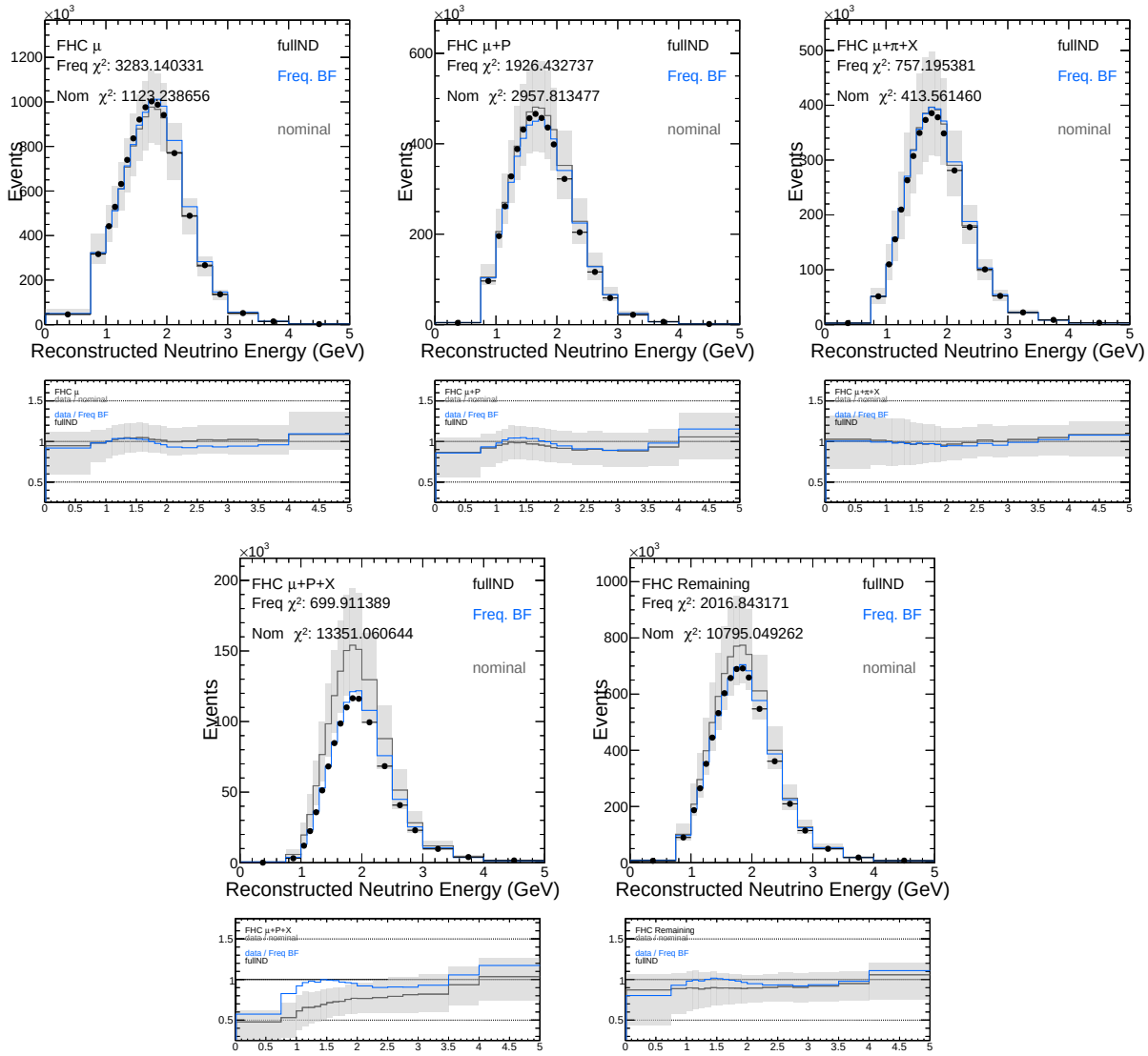

Figure 6.19: ND FHC samples and residual in neutrino energy axis. The grey line represents the nominal simulation, and the blue represents the distribution with residual weights applied. The bottom plots show the ratio of data with respect to each version of the simulation.

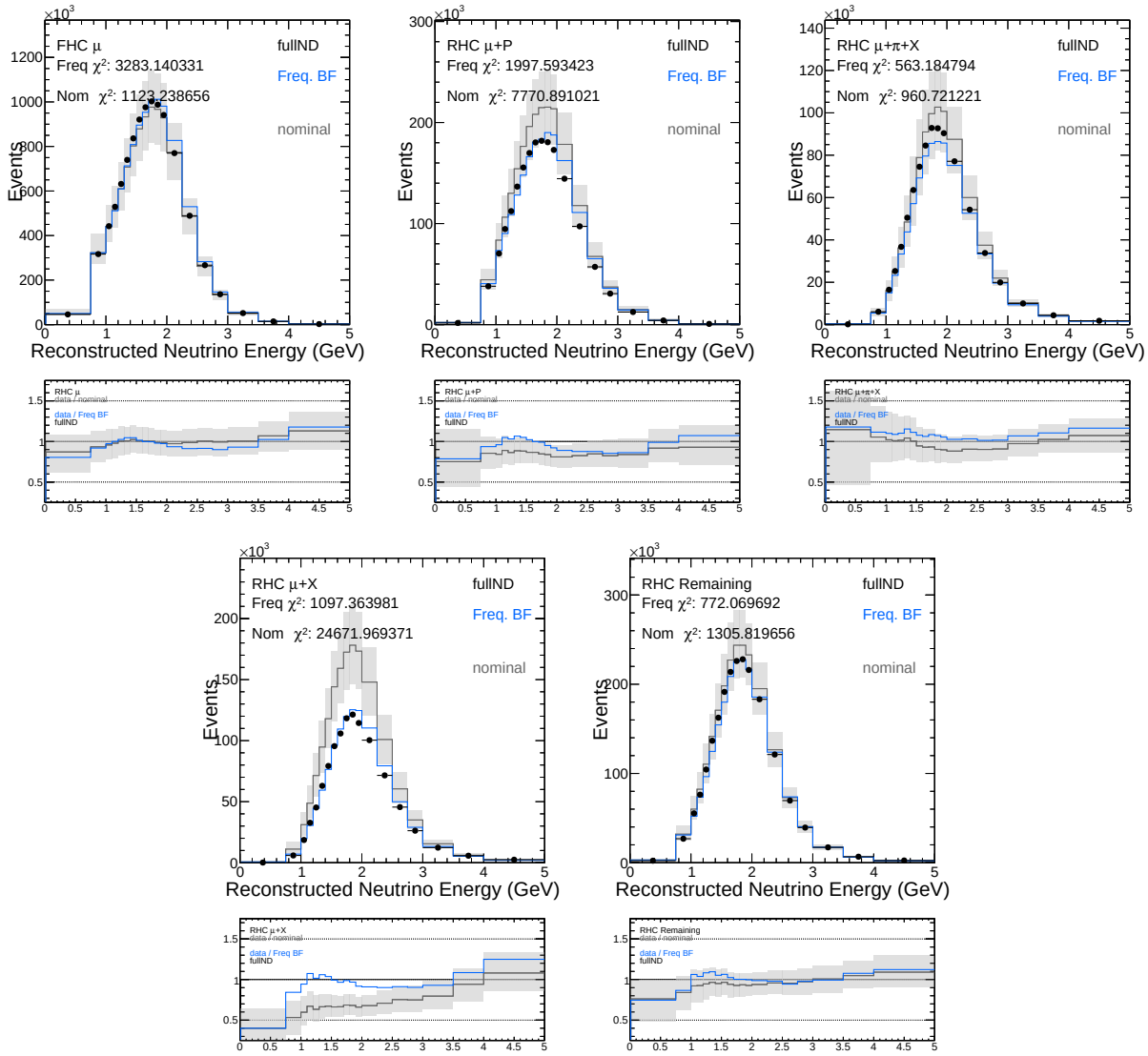

Figure 6.20: The grey line represents the nominal simulation, and the blue represents the distribution with residual weights applied. The bottom plots show the ratio of data with respect to each version of the simulation.

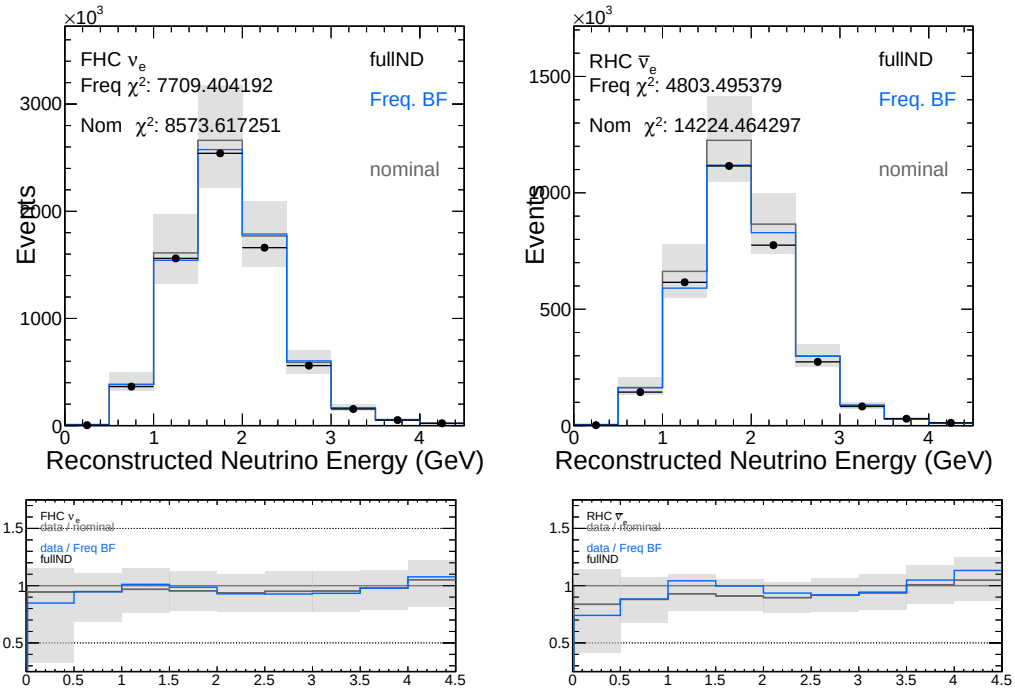

Figure 6.21: ND FHC and RHC total ν_μ samples and residual in neutrino energy axis.

One additional motivation for testing these particular oscillation parameters, is that the expected number of events substantially changes for Asimov B, therefore this tests one of the extreme scenarios that is consistent with the expected observation in the NOvA detectors.

The same reweighting procedure is used for the three Asimov points proposed. The comparison of the Asimov and Residual fake data predictions for each of the cases is in appendix C.

Table 6.3: Specific oscillation parameter values for Asimov points chosen.

Parameter	**Asimov A**	**Asimov B**	**Asimov C**
$\Delta m^2_{32}(\times 10^{-3}\text{eV}^2)$	2.41	2.51	-2.45
$\sin^2\theta_{23}$	0.57	0.53	0.5
δ_{CP}	0.82π	1.5π	1.5π

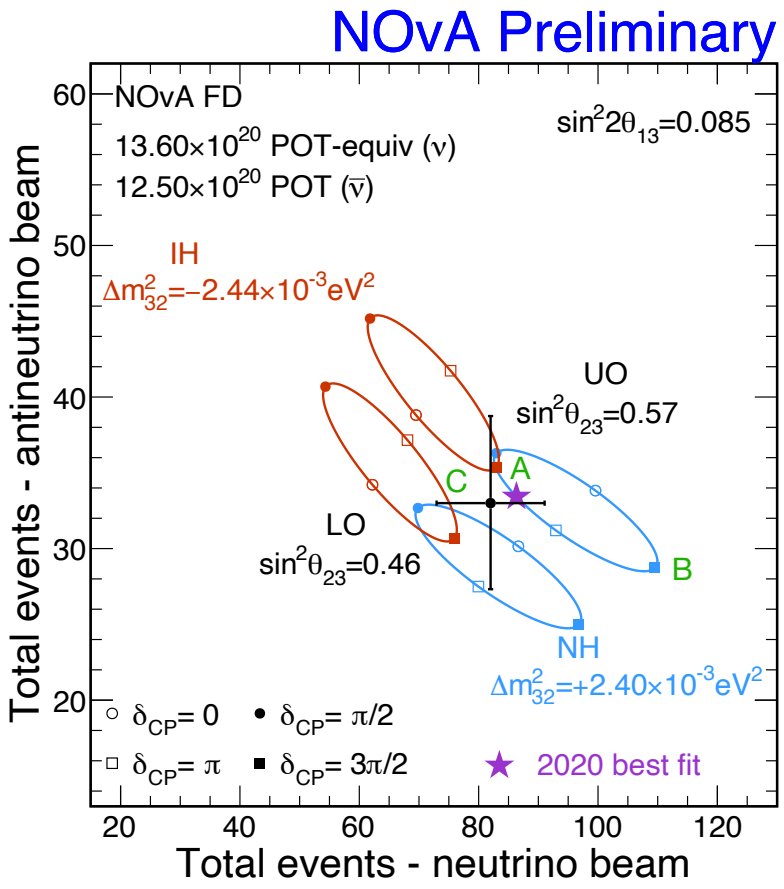

Figure 6.22: Schematic of the bi-event space occupied by chosen Asimov points, overlaid with NOvA data from [10].

Asimov A The Asimov A fake data fit is compared to the residual fake data. Recall from figures 6.19 and 6.20, that overall the residual weights correct for the overprediction at the tail of the E_ν distribution (> 2 GeV). These differences can be described very well by the fit for the FHC distributions (Figure 6.23), and to lesser degree in the RHC distributions (Figure 6.24), particularly for the $\mu + P$ and $\mu + \pi + X$, which remain overpredicted and underpredicted respectively. Figure 6.25 shows the 1D significances overlaid for Asimov and residual fake data fits. The normal ordering, upper octant curves show a shift of the best fit towards lower δ_{CP} and Δm^2_{32} , and an upwards shift of $\sin^2\theta_{23}$, of the residual fits with respect to the Asimov. This is

also osbserved in the contours on Figure 6.26. Notice in this case the residual fit 1σ contours (grey) are wider than the Asimov ones, for all cases. In the Δm^2_{32} - $\sin^2\theta_{23}$ space, the residual fit contours are more symmetrical, thus showing less preference for the upper octant than the Asimov. The bias metrics computed for this fit, using the 2σ confidence interval, are displayed in table 6.4, which concludes no significant bias is found.

Table 6.4: Bias metric table for residual fake data fit with respect to Asimov A, shown in Figure 6.25. All buas metric pass.

Param.	σ_{FDS}		σ_{Asimov}		σ_{stat}	
	Mid	Width	Mid	Width	Mid	Width
$\sin^2\theta_{23}$	0.611895	0.198128	0.613086	0.195845	0.60106	0.173345
Δm^2_{32}	2.52805	0.21674	2.51213	0.21618	2.48187	0.1907

Param	σ_{syst}	Δ_{mid}	$\Delta\sigma$	Critical
$\sin^2\theta_{23}$	0.0911	-0.001191	0.002283	0.0456
Δm^2_{32}	0.1018	0.01592	0.00056	0.0509

Asimov B The Asimov B fake data fit is compared to the residual fake data. Similar to the case of Asimov A, the residual difference weight has the effect or weighting up the tail (after $E_\nu = 2\text{GeV}$). This can be reproduced by the fit for the FHC samples (Figure 6.28), and to lesser degree in the RHC distributions (Figure 6.29), particularly for the $\mu + P$ and $\mu + \pi + X$, which remain overpredicted and underpredicted respectively. Notice however that the ν_e and $\bar{\nu}_e$ samples have very good agreement post-fit. Figure 6.30 shows the 1D significances overlaid for Asimov and residual fake data fits. The normal ordering, upper octant curves show a shift of the best fit towards larger δ_{CP} and $\sin^2\theta_{23}$, of the residual fits with respect to the Asimov. The shift of Δm^2_{32} is from upper octant to close to maximal mixing ($\Delta m^2_{32} \approx 0.5$). This is also observed in the contours on Figure 6.31. Notice in this case the residual fit 1σ contours (grey) are wider than the Asimov ones, for all cases. In the Δm^2_{32} - $\sin^2\theta_{23}$ space, the residual fit contours are more symmetrical, thus showing less preference for the upper octant than the Asimov. Although the shifts in the best fit seem larger than the case of Asimov A, the bias metrics computed for this fit, using the 2σ confidence interval, are displayed in table 6.5, indicate no significant bias.

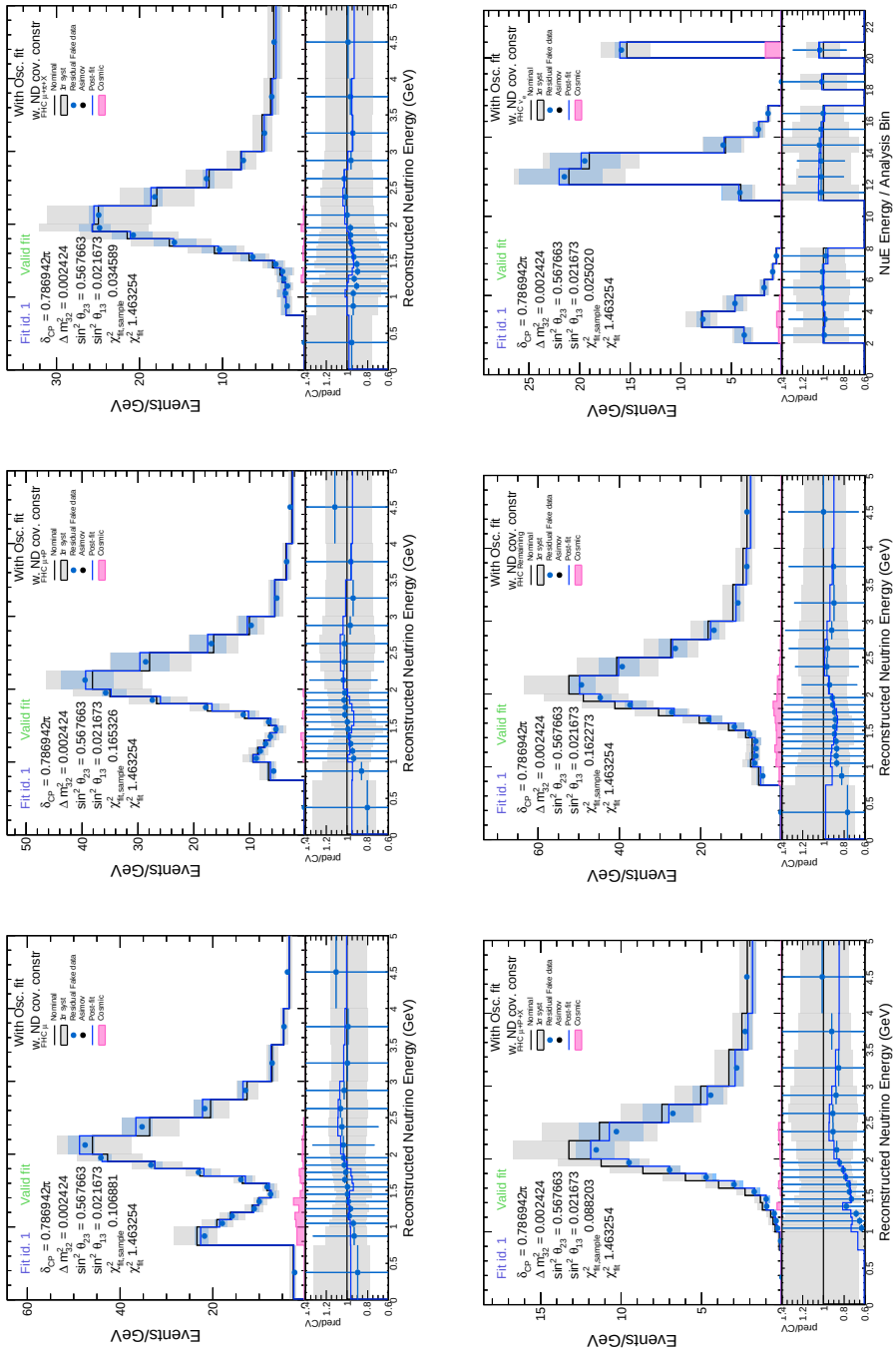

Figure 6.23: FHC predictions fit to residual fake data (blue markers) at Asimov A. The nominal prediction with unconstrained uncertainties is indicated with black and grey error bands. The fitted predictions with reduced uncertainty are indicated in blue. Statistical errors are displayed in the ratio.

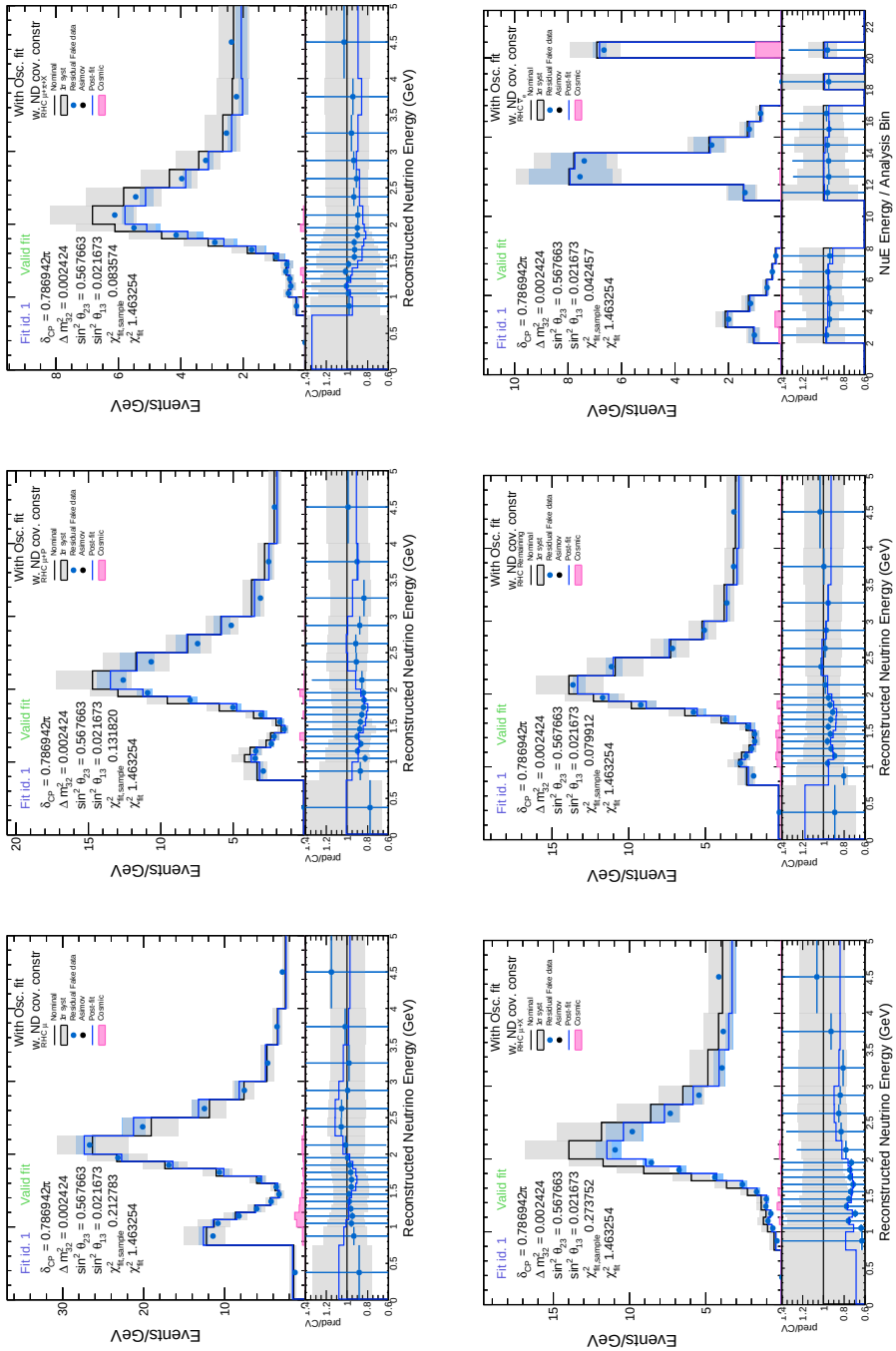

Figure 6.24: RHC predictions fit to residual fake data (blue markers) at Asimov A. The nominal prediction with unconstrained uncertainties is indicated with black and grey error bands. The fitted predictions with reduced uncertainty are indicated in blue. Statistical errors are displayed in the ratio.

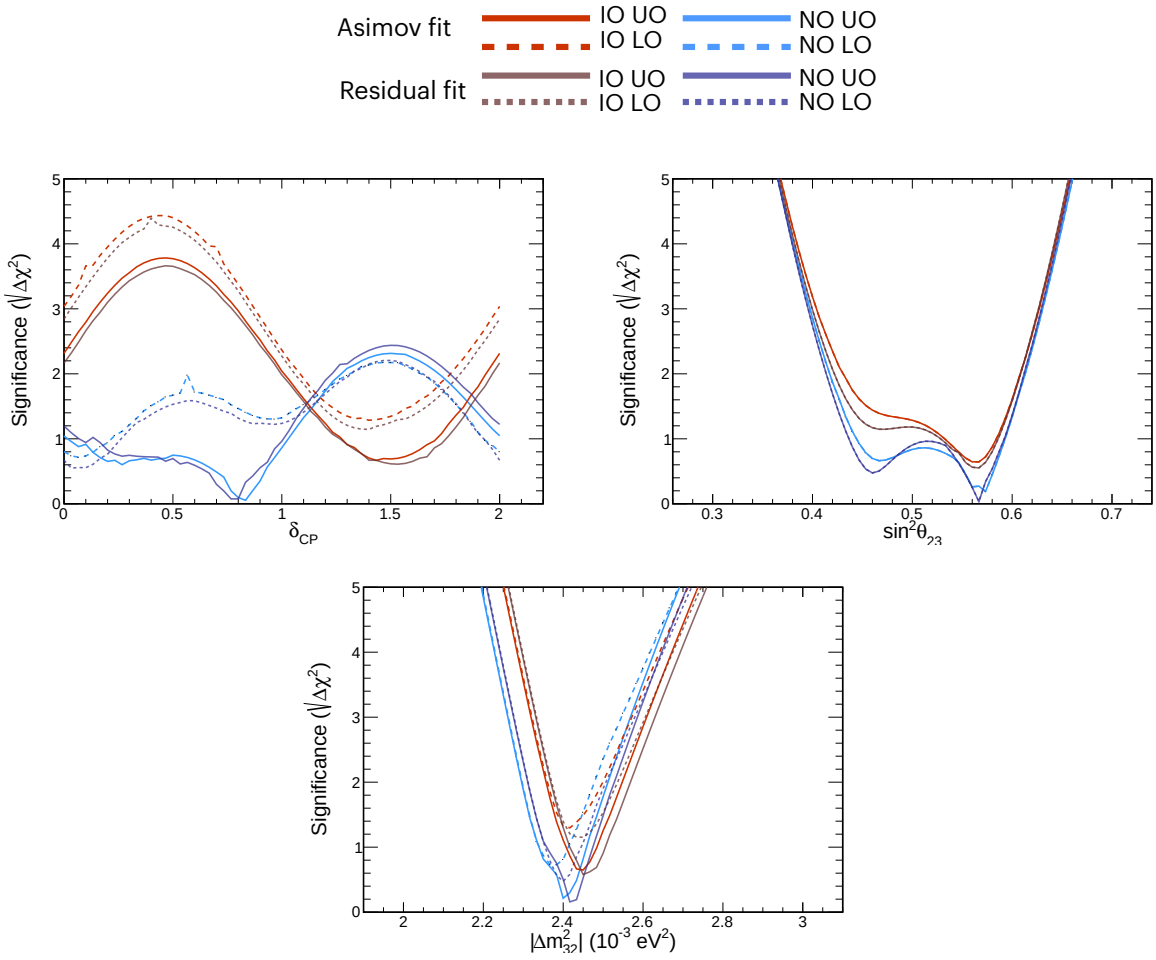

Figure 6.25: One-dimensional significances for δ_{CP} , Δm^2_{32} and $\sin^2\theta_{23}$ in for the Asimov A data and residual fake data (darker shades), shown for Normal (blue) or inverted (red) mass ordering/hierarchy, and for upper (solid line) or lower (dashed line) octants.

Table 6.5: Bias metric table for residual fake data fit with respect to Asimov B, shown in Figure 6.30. All bias metric pass.

Param.	σ_{FDS}		σ_{Asimov}		σ_{stat}	
	Mid	Width	Mid	Width	Mid	Width
$\sin^2\theta_{23}$	0.58635	0.14685	0.588312	0.14578	0.577761	0.12223
Δm^2_{32}	2.63208	0.18328	2.61525	0.18076	2.58256	0.14953

Param.	σ_{syst}	Δ_{mid}	$\Delta\sigma$	Critical
$\sin^2\theta_{23}$	0.0795	-0.001962	0.00107	0.0397
Δm^2_{32}	0.1016	0.01683	0.00252	0.0508

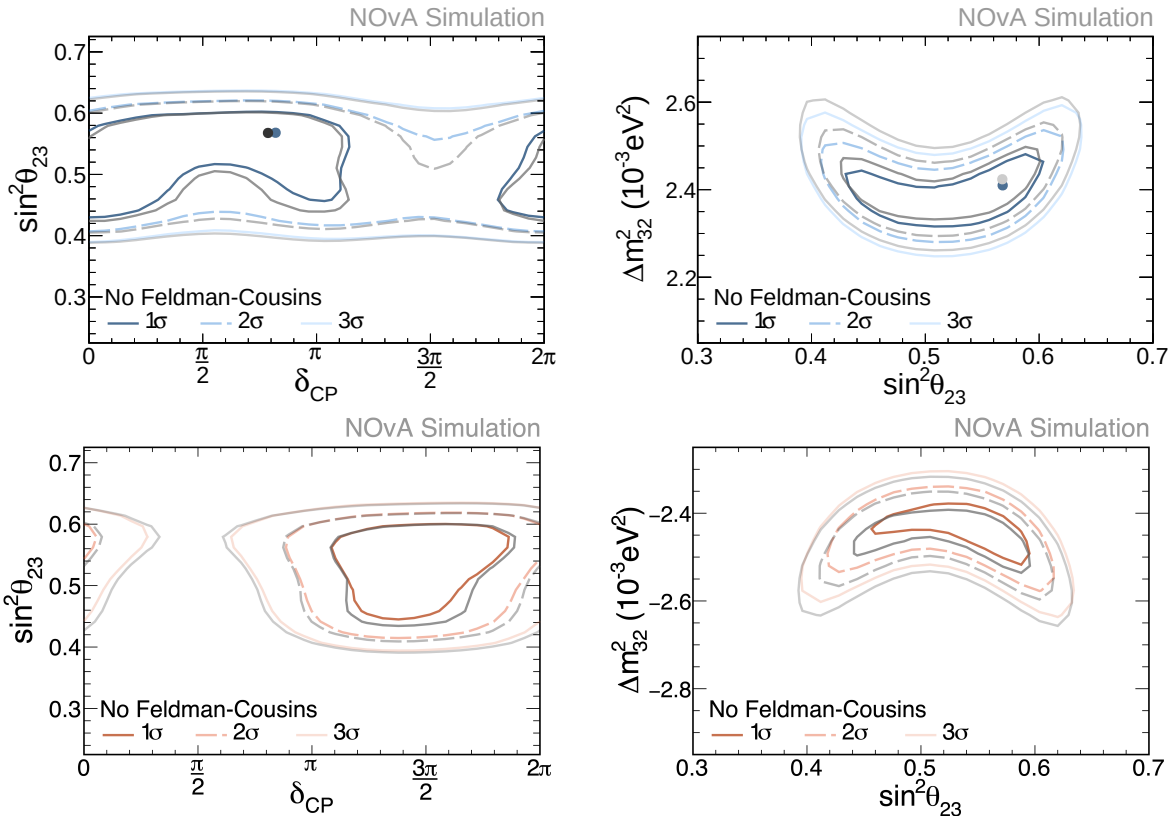

Figure 6.26: Sensitivities assuming the oscillation parameters of Asimov A in table 6.3, comparing residual-weighted fake data (grey) and Asimov data fits, for Normal (blue) and Inverted (red) Hierarchy/Ordering. 1, 2, and 3σ allowed regions are profiled over $\sin^2 2\theta_{13}$ and Δm^2_{32} (left) and $\sin^2 2\theta_{13}$ and δ_{CP} (right).

Asimov C The Asimov C fake data fit is compared to the residual fake data. Similar to the case of Asimov B, the residual difference fit is able to reproduce the shape the FHC samples (Figure 6.33), and to lesser degree in the RHC distributions (Figure 6.34), particularly for the $\mu + P$ and $\mu + \pi + X$, which remain overpredicted and underpredicted respectively. In this case as well, the ν_e and $\bar{\nu}_e$ samples have very good agreement post-fit. Figure 6.35 shows the 1D significances overlaid for Asimov and residual fake data fits. The inverted ordering, lower octant curves show a shift of the best fit towards larger δ_{CP} of the residual fits with respect to the Asimov. The shift of Δm^2_{32} is from maximal mixing towards lower octant, and for $\sin^2\theta_{23}$, the shift is to a higher value. This is also observed in the contours on Figure 6.36. Notice in this case the residual fit 1σ contours (grey) are close to the Asimov ones, with a slight shift towards larger

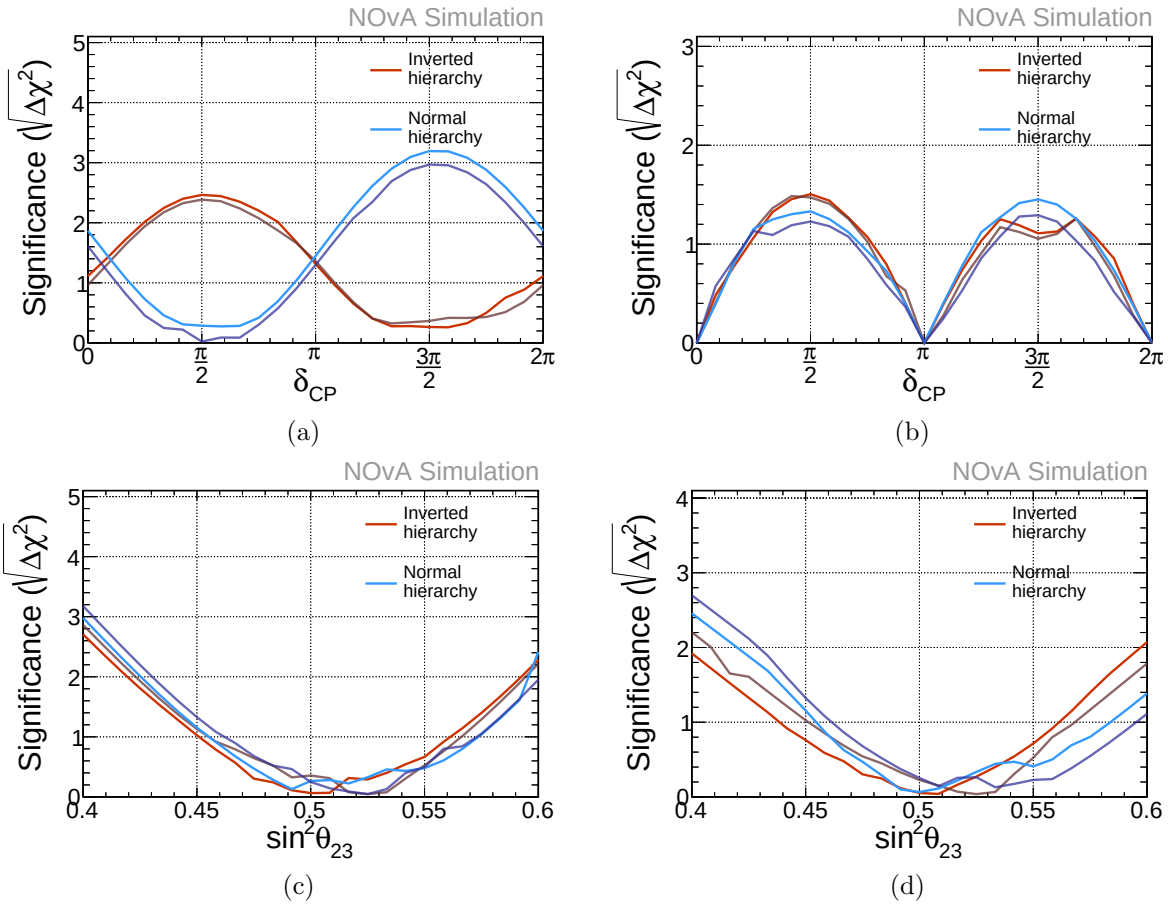

Figure 6.27: Potential rejection of the (a) wrong hierarchy and (b) CP conservation as a function of δ_{CP}; (c) maximal mixing and (d) wrong octant, as functions of $\sin^2\theta_{23}$, assuming true normal (blue) or inverted (red) hierarchy, comparing Asimov A data (lighter shade) and residual fake data fits (darker shade).

δ_{CP} and larger $\sin^2\theta_{23}$. In the Δm^2_{32} - $\sin^2\theta_{23}$ space, the residual fit contours show preference for the lower octant, rather than the more symmetrical shape of the Asimov. Although the shifts in the best fit seem larger than the case of Asimov A, the bias metrics computed for this fit, using the 2σ confidence interval, are displayed in table 6.6, indicate no significant bias.

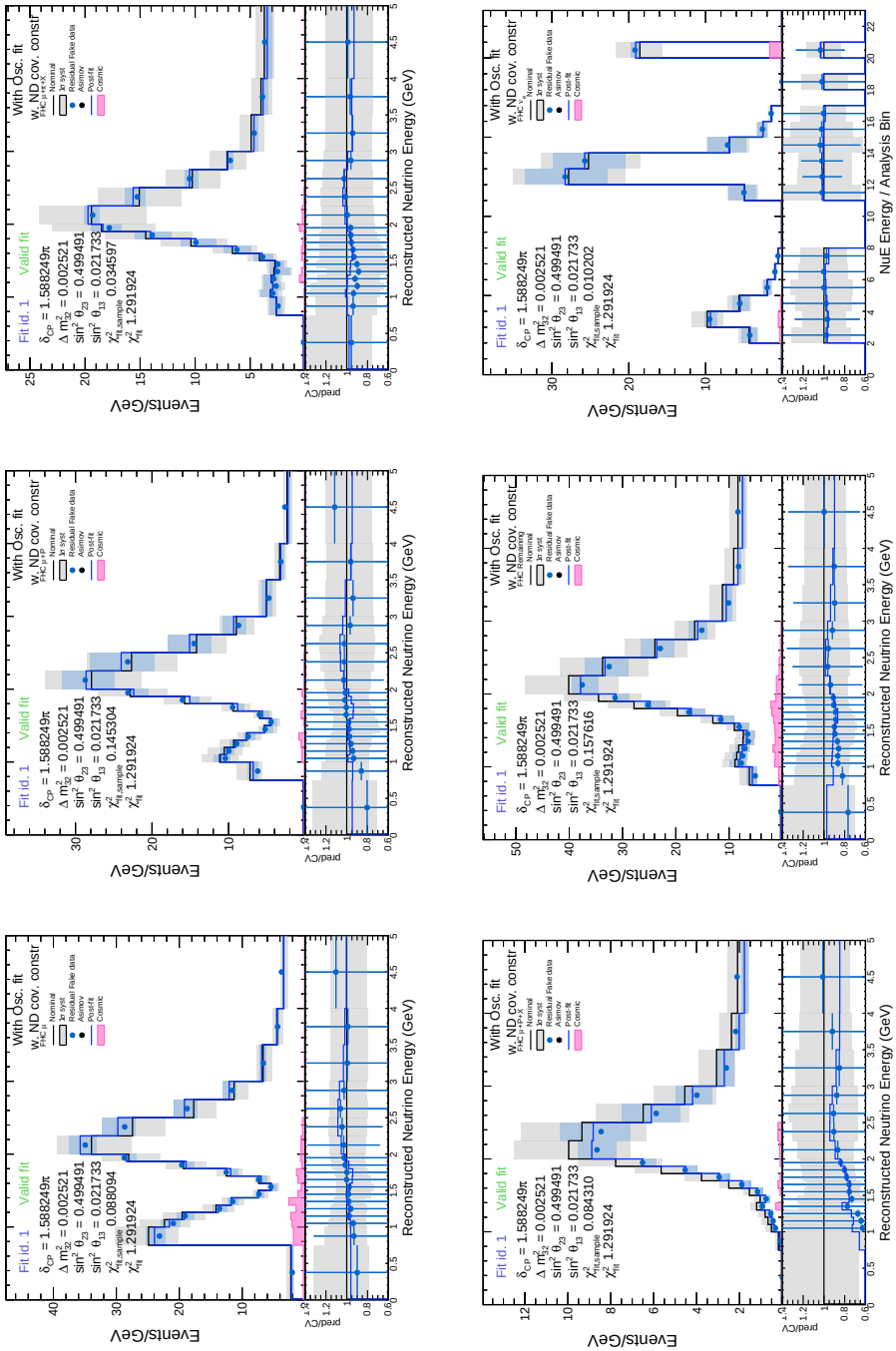

Figure 6.28: FHC predictions fit to residual fake data (blue markers) at Asimov B. The nominal prediction with unconstrained uncertainties is indicated with black and grey error bands. The fitted predictions with reduced uncertainty are indicated in blue. Statistical errors are displayed in the ratio.

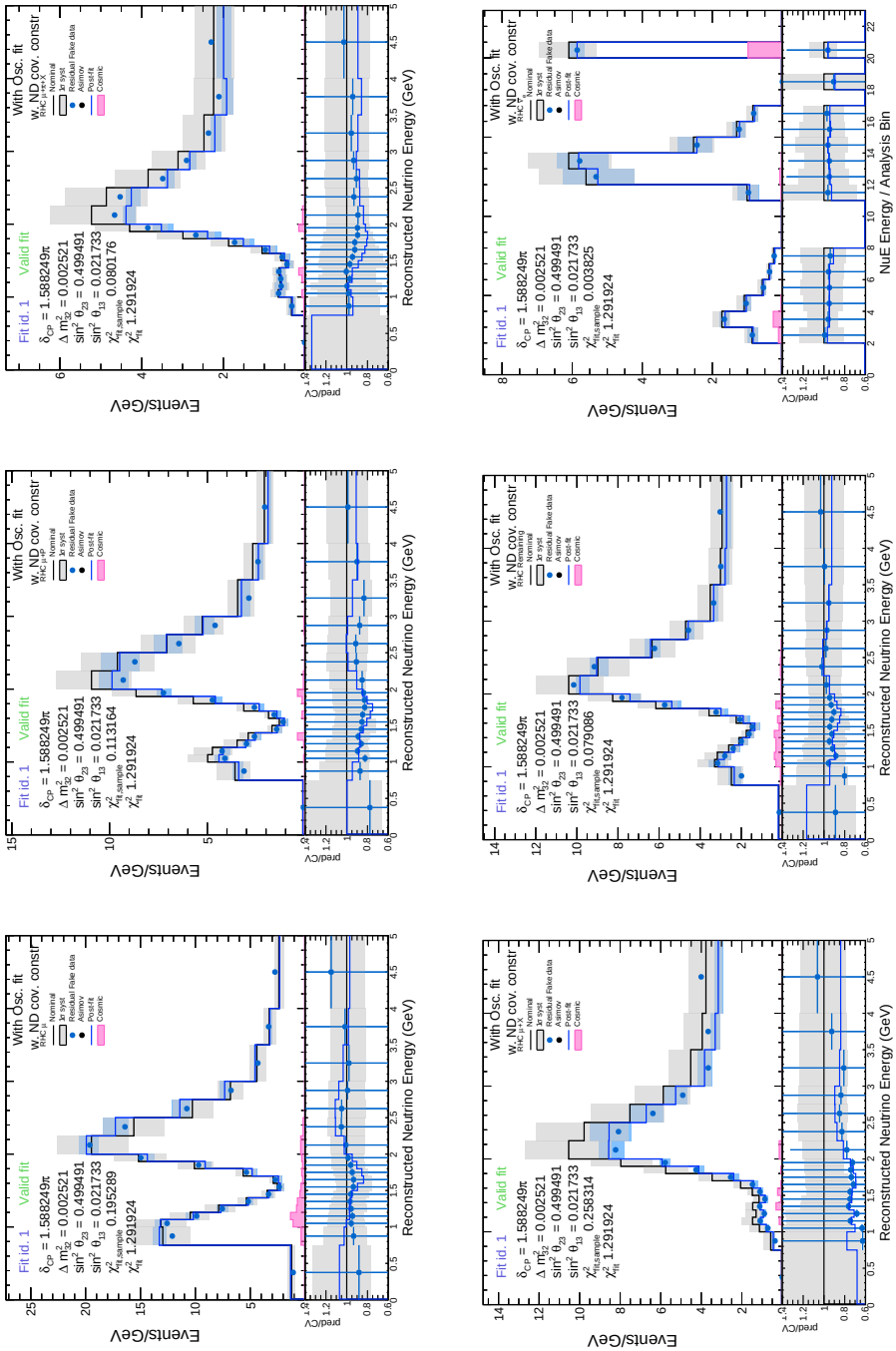

Figure 6.29: RHC predictions fit to residual fake data (blue markers) at Asimov B. The nominal prediction with unconstrained uncertainties is indicated with black and grey error bands. The fitted predictions with reduced uncertainty are indicated in blue. Statistical errors are displayed in the ratio.

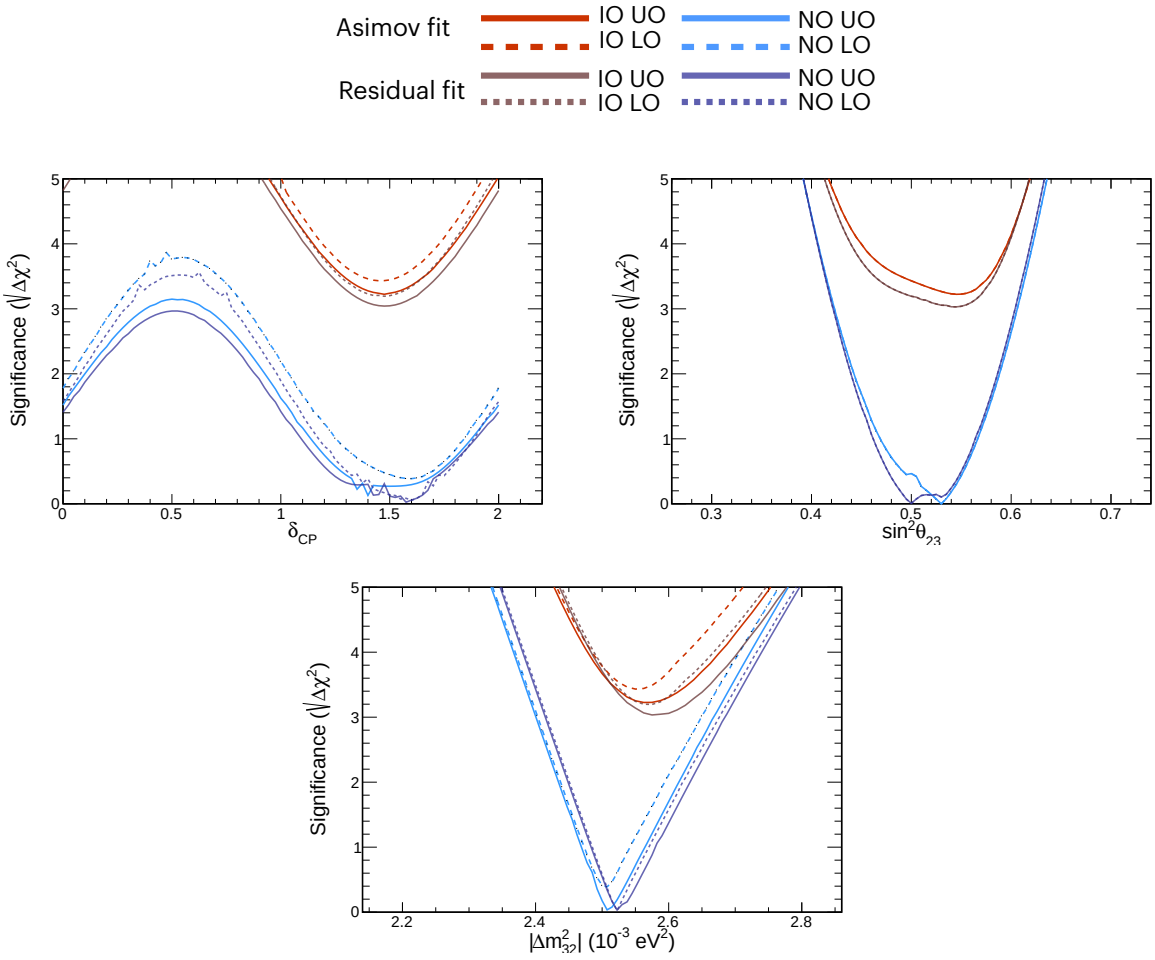

Figure 6.30: One-dimensional significances for δ_{CP} , Δm^2_{32} and $\sin^2\theta_{23}$ in for the Asimov B data and residual fake data (darker shades), shown for Normal (blue) or inverted (red) mass ordering/hierarchy, and for upper (solid line) or lower (dashed line) octants.

Table 6.6: Bias metric table for residual fake data fit with respect to Asimov C, shown in Figure 6.35. All bias metric pass

Param.	σ_{FDS}		σ_{Asimov}		σ_{stat}	
	Mid	Width	Mid	Width	Mid	Width
$\sin^2\theta_{23}$	0.585624	0.15905	0.588229	0.15991	0.577761	0.13374
Δm^2_{32}	-2.52071	0.17838	-2.54915	0.16909	-2.51768	0.13741

Param.	σ_{syst}	Δ_{mid}	$\Delta\sigma$	Critical
$\sin^2\theta_{23}$	0.0877	-0.00268	-0.00857	0.0438
Δm^2_{32}	0.0985	-0.04049	0.00929	0.0493

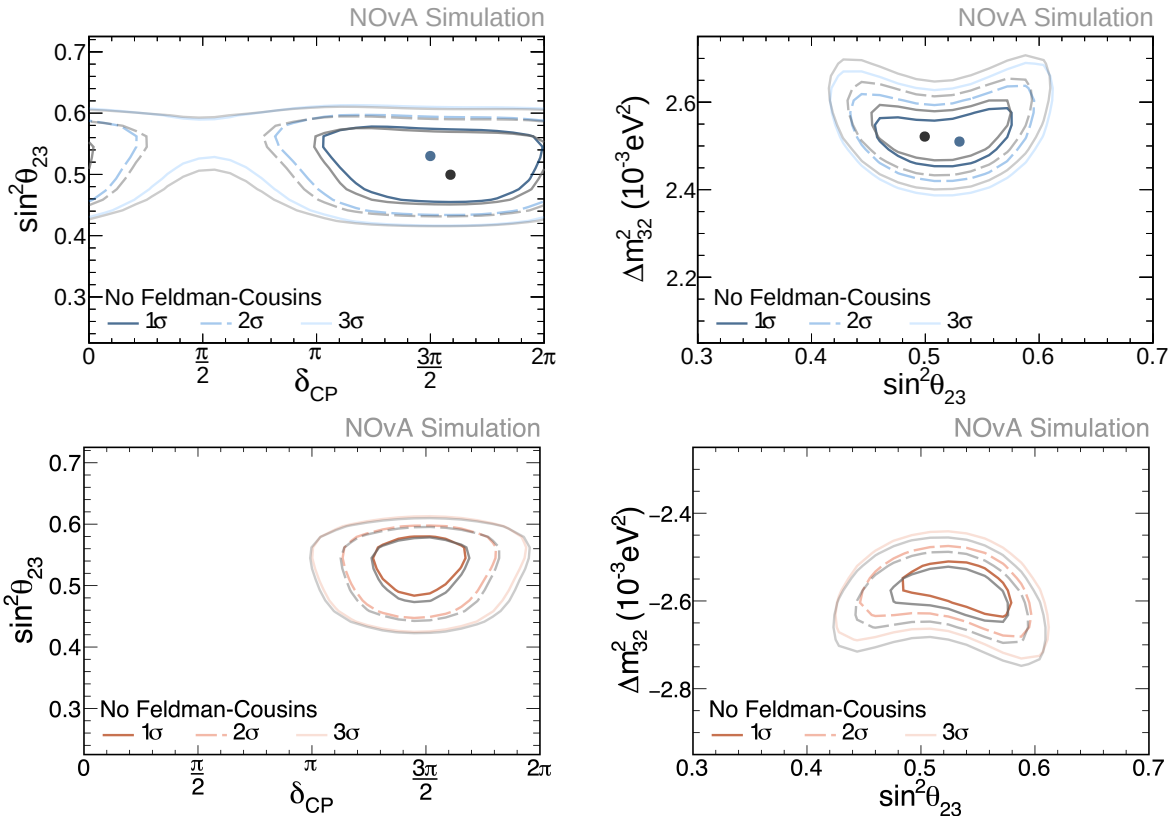

Figure 6.31: Sensitivities assuming the oscillation parameters of Asimov B in table 6.3, comparing residual-weighted fake data (grey) and Asimov data fits, for Normal (blue) and Inverted (red) Hierarchy/Ordering. 1, 2, and 3σ allowed regions are profiled over $\sin^2 2\theta_{13}$ and Δm^2_{32} (left) and $\sin^2 2\theta_{13}$ and δ_{CP} (right).

The three Asimov points tested with the residual fit showed a consistent behavior. The effect of residual difference weight in the fake data suppressed the tail of the E_ν distribution. In addition, it also enhanced the bins between 1-2 GeV, precisely where the oscillation dip lies. The consequence is that the fitted Δm^2_{32} was shifted downwards: for Asimov B, from UO to $\sim$ maximal mixing, and for Asimov C from maximal mixing to LO. The three Asimov points showed a shift towards larger $\sin^2\theta_{23}$. All the fits are dominated by statistical uncertainties, as can be observed by the error bars of figures 6.23 , 6.24, 6.28, 6.29, 6.33 and 6.34. Although all fits showed the same behavior in the shift of best points and the significances, by computing the bias metrics we can conclude that there is no significant bias in the residual fit. This demonstrates that the

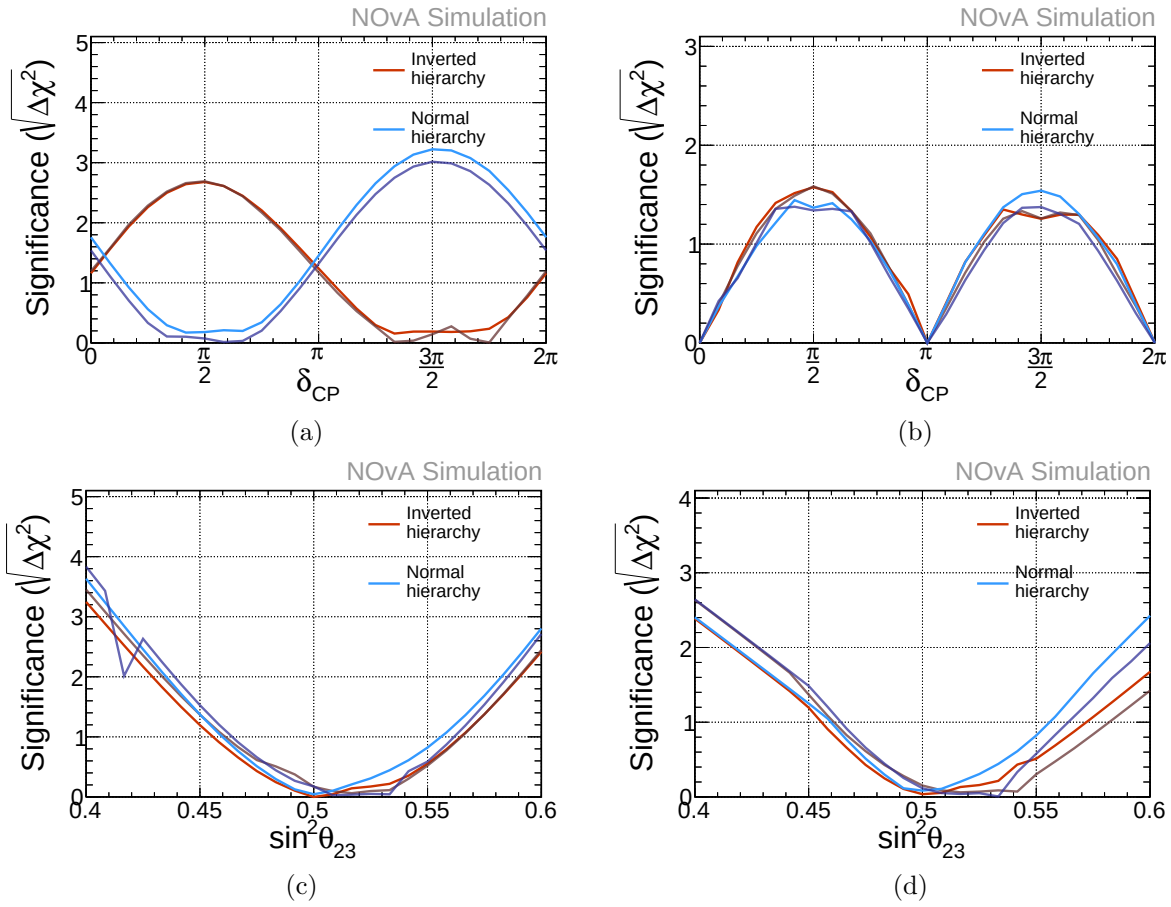

Figure 6.32: Potential rejection of the (a) wrong hierarchy and (b) CP conservation as a function of δ_{CP}; (c) maximal mixing and (d) wrong octant, as functions of $\sin^2\theta_{23}$, assuming true normal (blue) or inverted (red) hierarchy, comparing Asimov B data (lighter shade) and residual fake data fits (darker shade).

current level of agreement in the ND samples, by fitting the 53 parameters listed in table 5.7, is sufficient to produced an unbiased oscillation fit.

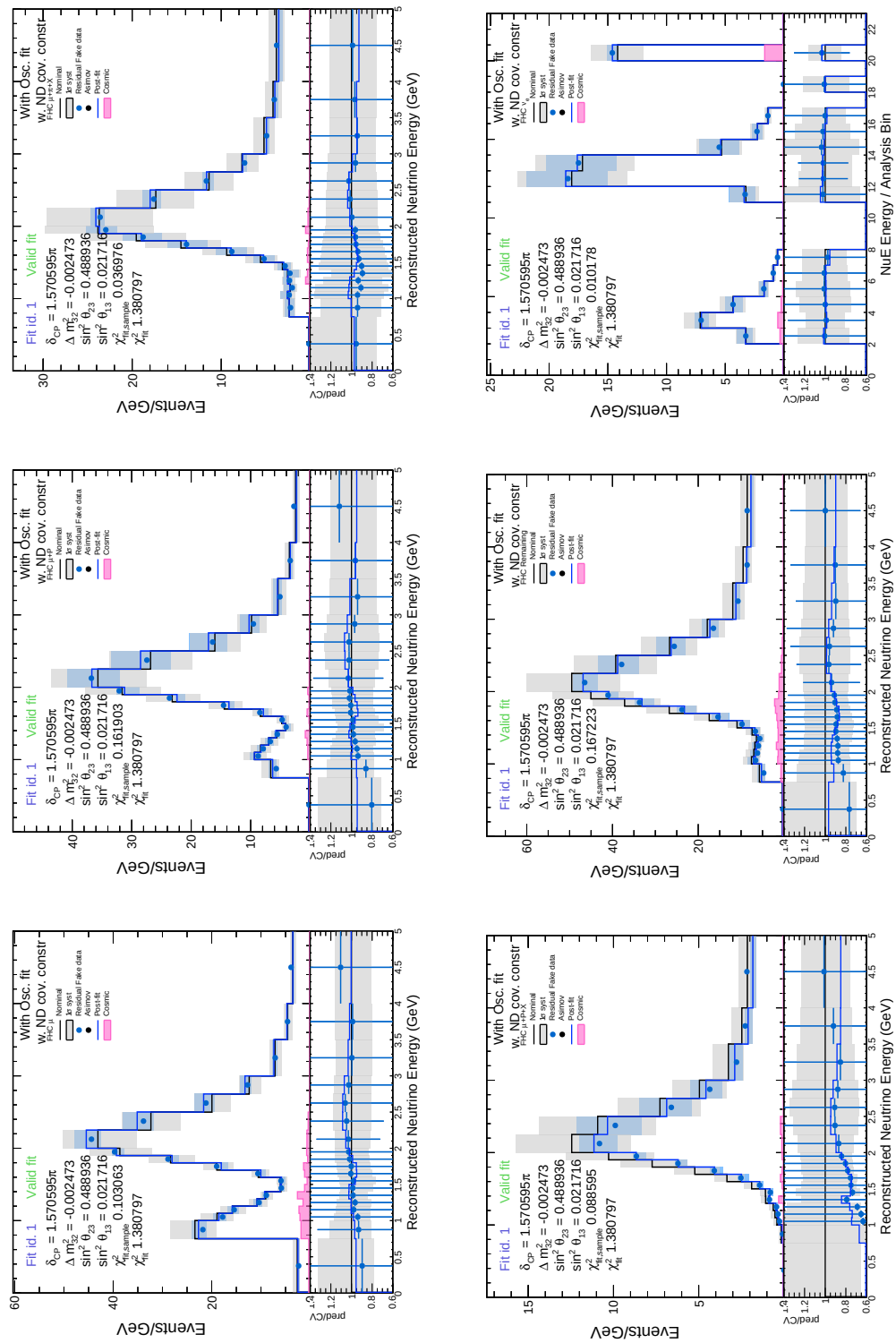

Figure 6.33: FHC predictions fit to residual fake data (blue markers) at Asimov C. The nominal prediction with unconstrained uncertainties is indicated with black and grey error bands. The fitted predictions with reduced uncertainty are indicated in blue. Statistical errors are displayed in the ratio.

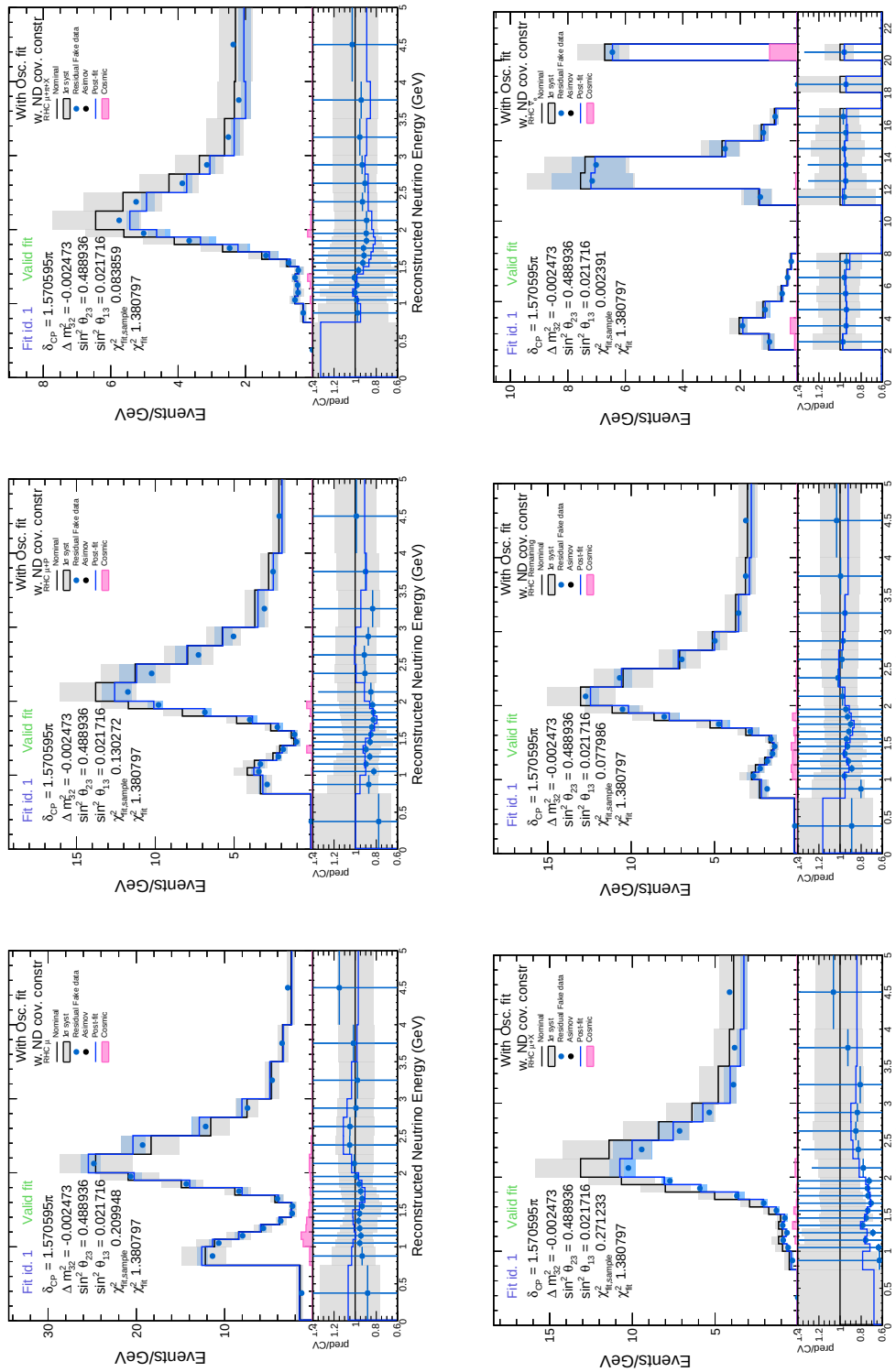

Figure 6.34: RHC predictions fit to residual fake data (blue markers) at Asimov C. The nominal prediction with unconstrained uncertainties is indicated with black and grey error bands. The fitted predictions with reduced uncertainty are indicated in blue. Statistical errors are displayed in the ratio.

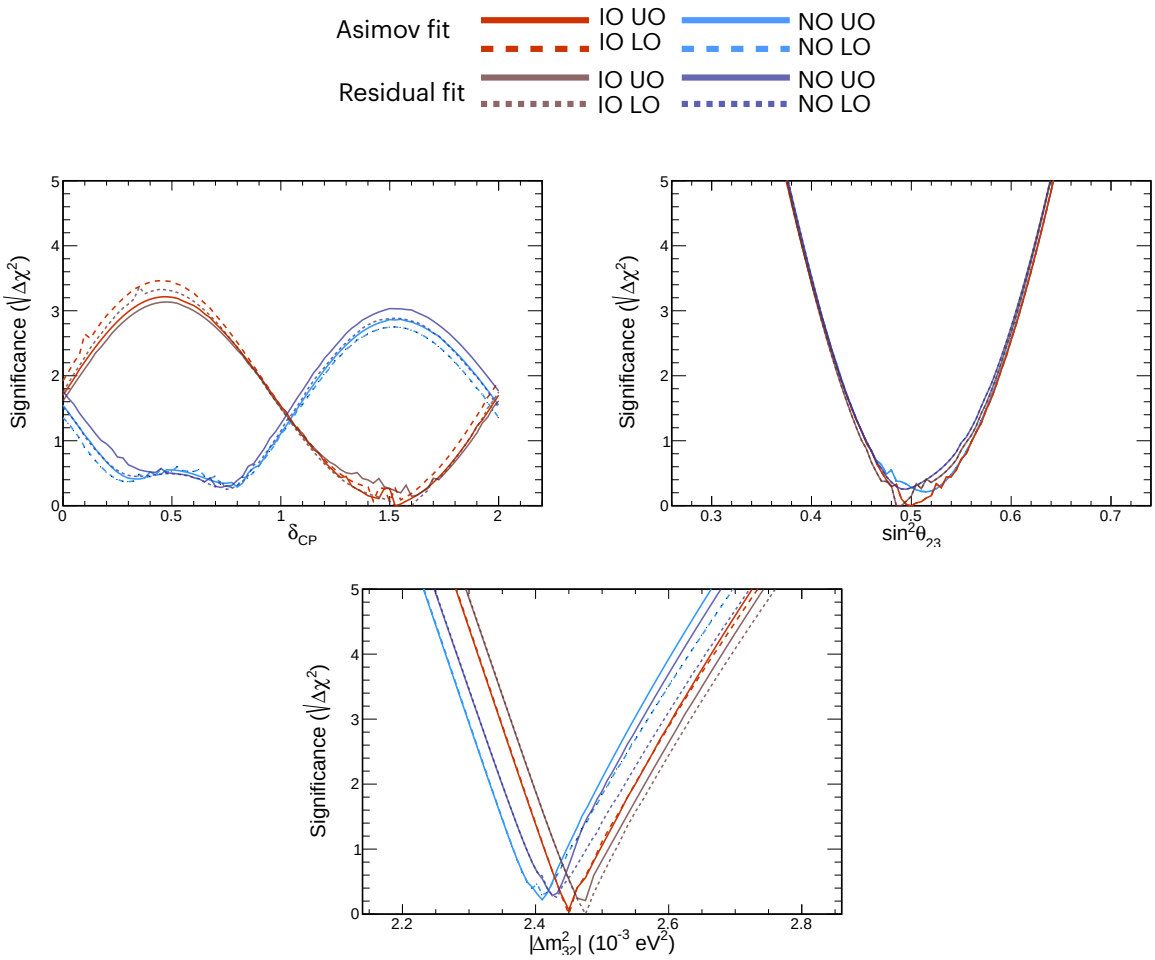

Figure 6.35: One-dimensional significances for δ_{CP} , Δm^2_{32} and $\sin^2\theta_{23}$ in for the Asimov C data and residual fake data (darker shades), shown for Normal (blue) or inverted (red) mass ordering/hierarchy, and for upper (solid line) or lower (dashed line) octants.

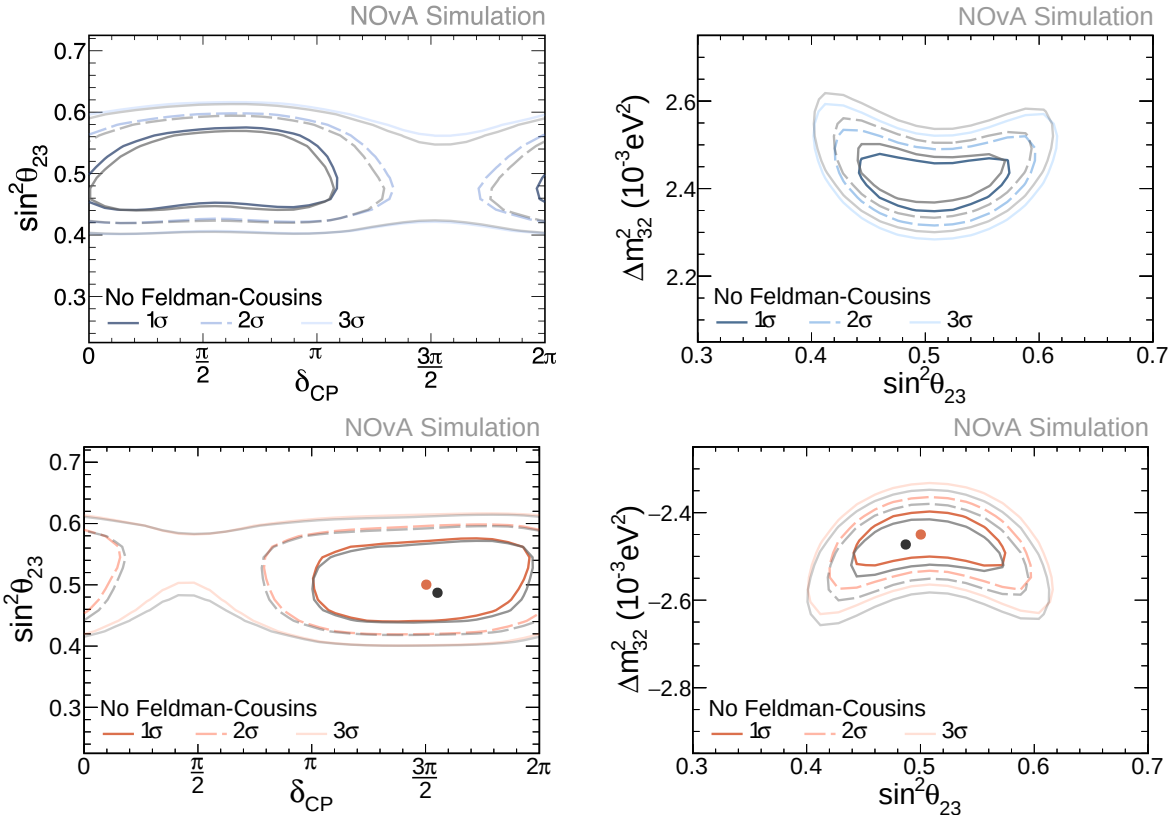

Figure 6.36: Sensitivities assuming the oscillation parameters of Asimov C in table 6.3, comparing residual-weighted fake data (grey) and Asimov data fits, for Normal (blue) and Inverted (red) Hierarchy/Ordering. 1, 2, and 3σ allowed regions are profiled over $\sin^2 2\theta_{13}$ and Δm^2_{32} (left) and $\sin^2 2\theta_{13}$ and δ_{CP} (right).

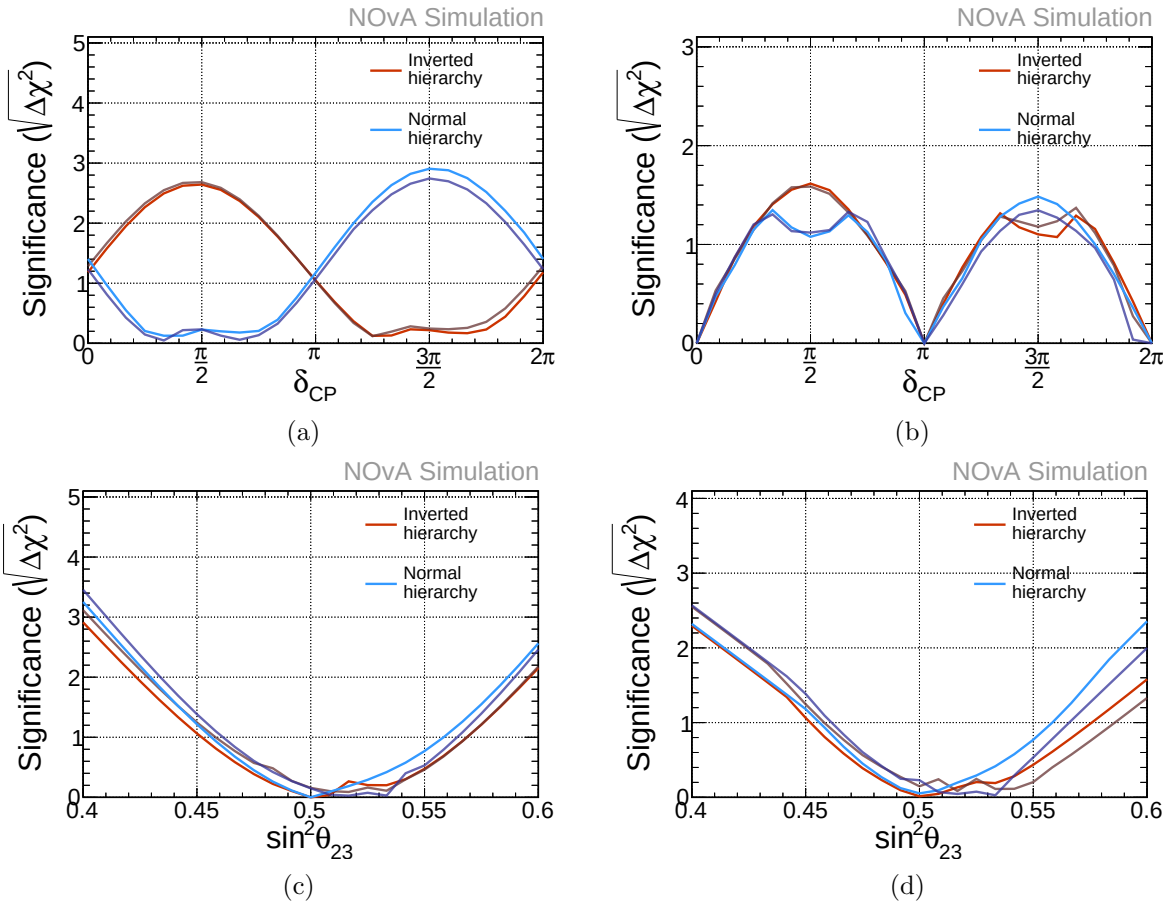

Figure 6.37: Potential rejection of the (a) wrong hierarchy and (b) CP conservation as a function of δ_{CP}; (c) maximal mixing and (d) wrong octant, as functions of $\sin^2\theta_{23}$, assuming true normal (blue) or inverted (red) hierarchy, comparing Asimov C data (lighter shade) and residual fake data fits (darker shade).

CHAPTER 7. CONCLUSION

In NOvA the Near Detector high statistics data set is used to aid to the oscillation fit by constraining model parameters. In recent publications, the main adjustments to the model were related to neutrino interactions, in which the major modification was in the MEC model, leading to the NOvA MEC tune I developed. Although this is a better representation of the ν_μ and $\bar{\nu}_\mu$ data than the standalone simulation based on GENIE, the study of the topology-based samples in chapter 4 demonstrated areas where this tune is deficient. Specifically, the samples with visible pions and multiple hadrons ($\mu + \pi + X, \mu + P + X, \mu + X$) showed over and under prediction. Therefore I developed an expanded fit to constrain most model parameters, including a suite of cross section, flux and detector parameters. This fit required developing additional systematic uncertainties related to these samples via the RES scaling, RES nucleon ratio and DIS hadronization. The set of parameters to which the ND samples are sensitive were constrained with an expanded ND data fit, which showed significant improvement with respect to the NOvA tune, as evaluated by the χ^2 per degrees of freedom.

A significant finding from the study of ND fits is that the current model parameters in the NOvA simulation do not have enough freedom to exactly reproduce the ND data, even with the additional custom systematic uncertainties created for this purpose. The MEC model adjustment has showed to have sufficient freedom to fit the three alternate scenarios reviewed in chapter 5.4.3, and we included additional parameters relevant to the pion / multi-hadron final states.

Chapter 5 explored degeneracies between MEC and QE parameters. Using TKI kinematic variables studied for the $\mu + P$samples (MEC/QE enhanced) showed a potential to separate MEC and QE interactions, but there was no significant effect on the fits. In the future it could be possible consider additional variables optimized for each sample and for other parameters, for example additional muon kinematic variables could better constrain muon energy scale.

The constrain obtained from the ND fit was successfully implemented in the oscillation fit, via a covariance term in the χ^2 minimization. Asimov data was used to demonstrate the feasibility of this fit. Remarkably, a fake data study based on the residual differences of the constrained model to the data showed that, at the current level of statistical power, the ND constrain is sufficient. Namely, no significant bias is observed when implementing the residual weight. The overall effect of the residual weight is to shift $\sin^2\theta_{23}$ towards a larger value and Δm^2_{32} towards a smaller value. With the current level of statistical uncertainties, a perfect representation of the ND data is not needed. The impact of the residual difference remains to be demonstrated at higher statistical power.

In summary, we have developed for the first time in NOvA a method to constrain the neutrino interaction, flux and detector models using the near detector data and transferring this information to the oscillation fit in the far detector. NOvA will continue to take data until 2026, with the projected with the projected 31.5×10^{20} POT for neutrino and antineutrino beam each. With this increase, the statistical uncertainty will be significantly reduced, and therefore the systematic uncertainty constrain developed here could have a significant impact.

BIBLIOGRAPHY

[1] M Sajjad Athar and S. K. Singh. *The physics of neutrino interactions*. Cambridge University Press, Cambridge, England, 2020.

[2] R. L. Workman et al. Review of Particle Physics. *PTEP*, 2022:083C01, 2022. doi: 10.1093/ptep/ptac097.

[3] Charles Drummond Ellis and W. A. Wooster. The average energy of disintegration of radium e. *Proceedings of the Royal Society of London. Series A, Containing Papers of a Mathematical and Physical Character*, 117(776):109–123, 1927. doi: 10.1098/rspa.1927.0168. URL https://royalsocietypublishing.org/doi/abs/10.1098/rspa.1927.0168.

[4] G. Danby, J-M. Gaillard, K. Goulianos, L. M. Lederman, N. Mistry, M. Schwartz, and J. Steinberger. Observation of high-energy neutrino reactions and the existence of two kinds of neutrinos. *Phys. Rev. Lett.*, 9:36–44, Jul 1962. doi: 10.1103/PhysRevLett.9.36. URL https://link.aps.org/doi/10.1103/PhysRevLett.9.36.

[5] J. A. Formaggio and G. P. Zeller. From eV to EeV: Neutrino cross sections across energy scales. *Reviews of Modern Physics*, 84(3):1307–1341, sep 2012. doi: 10.1103/revmodphys.84.1307. URL https://doi.org/10.1103%2Frevmodphys.84.1307.

[6] P. Barreau et al. Deep-inelastic electron scattering from carbon. *Nuclear Physics A*, 402(3): 515–540, 1983. ISSN 0375-9474. doi: https://doi.org/10.1016/0375-9474(83)90217-8. URL https://www.sciencedirect.com/science/article/pii/0375947483902178.

[7] A. Gil, J. Nieves, and E. Oset. Many-body approach to the inclusive (e, e') reaction from the quasielastic to the δ excitation region. *Nuclear Physics A*, 627(4):543–598, dec 1997. doi: 10.1016/s0375-9474(97)00513-7. URL https://doi.org/10.1016%2Fs0375-9474%2897%2900513-7.

[8] Fermilab. Fermilab's accelerator complex. URL https://www.fnal.gov/pub/science/particle-accelerators/accelerator-complex.html. [Online; accessed March 20, 2023].

[9] P. Adamson et al. The NuMI neutrino beam. *Nuclear Instruments and Methods in Physics Research Section A: Accelerators, Spectrometers, Detectors and Associated Equipment*, 806: 279–306, 2016. ISSN 0168-9002. doi: https://doi.org/10.1016/j.nima.2015.08.063. URL https://www.sciencedirect.com/science/article/pii/S016890021501027X.

[10] M. A. Acero et al. Improved measurement of neutrino oscillation parameters by the nova experiment. *Phys. Rev. D*, 106:032004, Aug 2022. doi: 10.1103/PhysRevD.106.032004. URL https://link.aps.org/doi/10.1103/PhysRevD.106.032004.

[11] J. Chadwick. The intensity distribution in the magnetic spectrum of beta particles from radium (B + C). *Verh. Phys. Gesell.*, 16:383–391, 1914.

[12] W. Pauli. Dear radioactive ladies and gentlemen. *Phys. Today*, 31N9:27, 1978. URL https://inspirehep.net/files/8fbe410f873cfd0a088295e3bee4572c.

[13] Fred L. Wilson. Fermi's Theory of Beta Decay. *American Journal of Physics*, 36(12): 1150–1160, 12 1968. ISSN 0002-9505. doi: 10.1119/1.1974382. URL https://doi.org/10.1119/1.1974382.

[14] H. Bethe and R. Peierls. The "neutrino". *Nature*, 133(3362):532–532, 1934. doi: 10.1038/133532a0.

[15] F. Reines and C. L. Cowan. Detection of the free neutrino. *Phys. Rev.*, 92:830–831, Nov 1953. doi: 10.1103/PhysRev.92.830. URL https://link.aps.org/doi/10.1103/PhysRev.92.830.

[16] C. L. Cowan, F. Reines, F. B. Harrison, H. W. Kruse, and A. D. McGuire. Detection of the free neutrino: A Confirmation. *Science*, 124:103–104, 1956. doi: 10.1126/science.124.3212.103.

[17] F. Reines, C. L. Cowan, F. B. Harrison, A. D. McGuire, and H. W. Kruse. Detection of the free antineutrino. *Phys. Rev.*, 117:159–173, Jan 1960. doi: 10.1103/PhysRev.117.159. URL https://link.aps.org/doi/10.1103/PhysRev.117.159.

[18] B. Pontecorvo. Electron and Muon Neutrinos. *Zh. Eksp. Teor. Fiz.*, 37:1751–1757, 1959.

[19] M. Schwartz. Feasibility of using high-energy neutrinos to study the weak interactions. *Phys. Rev. Lett.*, 4:306–307, Mar 1960. doi: 10.1103/PhysRevLett.4.306. URL https://link.aps.org/doi/10.1103/PhysRevLett.4.306.

[20] M. L. Perl and others. Evidence for anomalous lepton production in $e^+ - e^-$ annihilation. *Phys. Rev. Lett.*, 35:1489–1492, Dec 1975. doi: 10.1103/PhysRevLett.35.1489. URL https://link.aps.org/doi/10.1103/PhysRevLett.35.1489.

[21] K. Kodama et al. Observation of tau neutrino interactions. *Physics Letters B*, 504(3): 218–224, apr 2001. doi: 10.1016/s0370-2693(01)00307-0. URL https://doi.org/10.1016%2Fs0370-2693%2801%2900307-0.

[22] M.Z. Akrawy et al. Measurement of the Z^0 mass and width with the opal detector at LEP. *Physics Letters B*, 231(4):530–538, 1989. ISSN 0370-2693. doi: 10.1016/0370-2693(89)90705-3. URL https://www.sciencedirect.com/science/article/pii/0370269389907053.

[23] P. Aarnio et al. Measurement of the mass and width of the Z^0-particle from multihadronic final states produced in e^+e^- annihilations. *Physics Letters B*, 231(4):539–547, 1989. ISSN 0370-2693. doi: https://doi.org/10.1016/0370-2693(89)90706-5. URL https://www.sciencedirect.com/science/article/pii/0370269389907065.

[24] D. DeCamp (ALEPH collaboration) et al. Determination of the number of light neutrino species. *Physics Letters B*, 231(4):519–529, 1989. ISSN 0370-2693. doi: https://doi.org/10.1016/0370-2693(89)90704-1. URL https://www.sciencedirect.com/science/article/pii/0370269389907041.

[25] B. Pontecorvo. Mesonium and anti-mesonium. *Sov. Phys. JETP*, 6:429, 1957.

[26] Ziro Maki, Masami Nakagawa, and Shoichi Sakata. Remarks on the Unified Model of Elementary Particles. *Progress of Theoretical Physics*, 28(5):870–880, 11 1962. ISSN 0033-068X. doi: 10.1143/PTP.28.870. URL https://doi.org/10.1143/PTP.28.870.

[27] V. Gribov and B. Pontecorvo. Neutrino astronomy and lepton charge. *Physics Letters B*, 28 (7):493–496, 1969. ISSN 0370-2693. doi: https://doi.org/10.1016/0370-2693(69)90525-5. URL https://www.sciencedirect.com/science/article/pii/0370269369905255.

[28] B. Pontecorvo. Neutrino Experiments and the Problem of Conservation of Leptonic Charge. *Zh. Eksp. Teor. Fiz.*, 53:1717–1725, 1967.

[29] S M Bilenky. The history of neutrino oscillations. *Physica Scripta*, T121:17–22, jan 2005. doi: 10.1088/0031-8949/2005/t121/001. URL https://doi.org/10.1088%2F0031-8949%2F2005%2Ft121%2F001.

[30] K. S. Hirata et al. Observation of ^{8}B solar neutrinos in the kamiokande-ii detector. *Phys. Rev. Lett.*, 63:16–19, Jul 1989. doi: 10.1103/PhysRevLett.63.16. URL https://link.aps.org/doi/10.1103/PhysRevLett.63.16.

[31] A. I. Abazov et al. Search for neutrinos from the sun using the reaction ^{71}Ga(ν_e,e^-)^{71}ge. *Phys. Rev. Lett.*, 67:3332–3335, Dec 1991. doi: 10.1103/PhysRevLett.67.3332. URL https://link.aps.org/doi/10.1103/PhysRevLett.67.3332.

[32] P. Anselmann et al. Solar neutrinos observed by gallex at gran sasso. *Physics Letters B*, 285 (4):376–389, 1992. ISSN 0370-2693. doi: https://doi.org/10.1016/0370-2693(92)91521-A. URL https://www.sciencedirect.com/science/article/pii/037026939291521A.

[33] Y. Fukuda et al. Evidence for oscillation of atmospheric neutrinos. *Phys. Rev. Lett.*, 81: 1562–1567, Aug 1998. doi: 10.1103/PhysRevLett.81.1562. URL https://link.aps.org/doi/10.1103/PhysRevLett.81.1562.

[34] Y. Fukuda et al. Neutrino induced upward stopping muons in Super-Kamiokande. *Phys. Lett. B*, 467:185–193, 1999. doi: 10.1016/S0370-2693(99)01188-0.

[35] Q. R. Ahmad et al. Direct evidence for neutrino flavor transformation from neutral-current interactions in the sudbury neutrino observatory. *Phys. Rev. Lett.*, 89:011301, Jun 2002. doi: 10.1103/PhysRevLett.89.011301. URL https://link.aps.org/doi/10.1103/PhysRevLett.89.011301.

[36] Carlo Giunti and Chung Wook Kim. *Fundamentals of neutrino physics and astrophysics*. Oxford University Press, London, England, 2007.

[37] M. Sajjad Athar et al. Status and perspectives of neutrino physics. *Progress in Particle and Nuclear Physics*, 124:103947, may 2022. doi: 10.1016/j.ppnp.2022.103947. URL https://doi.org/10.1016%2Fj.ppnp.2022.103947.

[38] S. P. Mikheyev and A. Yu. Smirnov. Resonance Amplification of Oscillations in Matter and Spectroscopy of Solar Neutrinos. *Sov. J. Nucl. Phys.*, 42:913–917, 1985.

[39] L. Wolfenstein. Neutrino oscillations in matter. *Phys. Rev. D*, 17:2369–2374, May 1978. doi: 10.1103/PhysRevD.17.2369. URL https://link.aps.org/doi/10.1103/PhysRevD.17.2369.

[40] V. Barger, K. Whisnant, S. Pakvasa, and R. J. N. Phillips. Matter effects on three-neutrino oscillations. *Phys. Rev. D*, 22:2718–2726, Dec 1980. doi: 10.1103/PhysRevD.22.2718. URL https://link.aps.org/doi/10.1103/PhysRevD.22.2718.

[41] Evgeny K. Akhmedov, Robert Johansson, Manfred Lindner, Tommy Ohlsson, and Thomas Schwetz. Series expansions for three-flavor neutrino oscillation probabilities in matter. *Journal of High Energy Physics*, 2004(04):078, may 2004. doi: 10.1088/1126-6708/2004/04/078. URL https://dx.doi.org/10.1088/1126-6708/2004/04/078.

[42] Richard J. Hill and Gil Paz. Model-independent extraction of the proton charge radius from electron scattering. *Physical Review D*, 82(11), dec 2010. doi: 10.1103/physrevd.82.113005. URL https://doi.org/10.1103%2Fphysrevd.82.113005.

[43] Véronique Bernard, Latifa Elouadrhiri, and Ulf-G Meißner. Axial structure of the nucleon. *Journal of Physics G: Nuclear and Particle Physics*, 28(1):R1–R35, nov 2001. doi: 10.1088/0954-3899/28/1/201. URL https://doi.org/10.1088%2F0954-3899%2F28%2F1%2F201.

[44] Aaron Higuera. FSI models in GENIE, Mar 2018. URL https://indico.fnal.gov/event/16667/contributions/38846/attachments/24070/29782/DUNE_FD_33.pdf.

[45] G. D. Harp. Extension of the isobar model for intranuclear cascades to 1 gev. *Phys. Rev. C*, 10:2387–2396, Dec 1974. doi: 10.1103/PhysRevC.10.2387. URL https://link.aps.org/doi/10.1103/PhysRevC.10.2387.

[46] Concepts rookie book. Web, August 2020. URL https://operations.fnal.gov/rookie_books/concepts.pdf.

[47] D S Ayres et al. The nova technical design report. 10 2007. doi: 10.2172/935497. URL https://www.osti.gov/biblio/935497.

[48] Marco Del Tutto. Blessing Package - Beam Simulation Plots . Internal document. NOvA DocDB 13524, 2016.

[49] Fermilab. Fermilab Creative Services. https://vms.fnal.gov/asset, 2023. Accessed: April 28, 2023.

[50] A. Norman. The nova data acquisition system. *Journal of Physics: Conference Series*, 396 (1):012035, dec 2012. doi: 10.1088/1742-6596/396/1/012035. URL https://dx.doi.org/10.1088/1742-6596/396/1/012035.

[51] Leon M. Mualem. APD Expert Training Documents. Internal document. NOvA DocDB 14143, 2015.

[52] A Norman, R Kwarciany, G Deuerling, and N Wilcer. The nova timing system: A system for synchronizing a long baseline neutrino experiment. *Journal of Physics: Conference Series*, 396(1):012034, dec 2012. doi: 10.1088/1742-6596/396/1/012034. URL https://dx.doi.org/10.1088/1742-6596/396/1/012034.

[53] A. Norman et al. Performance of the NOvA Data Acquisition and Trigger Systems for the full 14 kT Far Detector. *Journal of Physics: Conference Series*, 664(8):082041, dec 2015. doi: 10.1088/1742-6596/664/8/082041. URL https://dx.doi.org/10.1088/1742-6596/664/8/082041.

[54] L. Aliaga et al. Neutrino flux predictions for the numi beam. *Phys. Rev. D*, 94:092005, Nov 2016. doi: 10.1103/PhysRevD.94.092005. URL https://link.aps.org/doi/10.1103/PhysRevD.94.092005.

[55] Fermilab. g4numi. https://cdcvs.fnal.gov/redmine/projects/numi-beam-sim/wiki/G4numi. Accessed: May 26, 2023.

[56] Stefano Agostinelli et al. Geant4-a simulation toolkit. *Nuclear Instruments and Methods in Physics Research Section A Accelerators Spectrometers Detectors and Associated Equipment*, 506:250, 07 2003. doi: 10.1016/S0168-9002(03)01368-8.

[57] Leonidas Aliaga. 2017-2018 beam plots . Internal document. NOvA DocDB 20843, 2018.

[58] Costas Andreopoulos, Christopher Barry, Steve Dytman, Hugh Gallagher, Tomasz Golan, Robert Hatcher, Gabriel Perdue, and Julia Yarba. The genie neutrino monte carlo generator: Physics and user manual, 2015.

[59] J. Nieves, J. E. Amaro, and M. Valverde. Inclusive quasielastic charged-current neutrino-nucleus reactions. *Phys. Rev. C*, 70:055503, Nov 2004. doi: 10.1103/PhysRevC.70.055503. URL https://link.aps.org/doi/10.1103/PhysRevC.70.055503.

[60] R. Gran, J. Nieves, F. Sanchez, and M. J. Vicente Vacas. Neutrino-nucleus quasi-elastic and 2p2h interactions up to 10 gev. *Phys. Rev. D*, 88:113007, Dec 2013. doi: 10.1103/PhysRevD.88.113007. URL https://link.aps.org/doi/10.1103/PhysRevD.88.113007.

[61] Aaron S. Meyer, Minerba Betancourt, Richard Gran, and Richard J. Hill. Deuterium target data for precision neutrino-nucleus cross sections. *Physical Review D*, 93(11), jun 2016. doi: 10.1103/physrevd.93.113015. URL https://doi.org/10.1103%2Fphysrevd.93.113015.

[62] Ch. Berger and L. M. Sehgal. Lepton mass effects in single pion production by neutrinos. *Physical Review D*, 76(11), dec 2007. doi: 10.1103/physrevd.76.113004. URL https://doi.org/10.1103%2Fphysrevd.76.113004.

[63] Ch. Berger and L. M. Sehgal. Partially conserved axial vector current and coherent pion production by low energy neutrinos. *Physical Review D*, 79(5), mar 2009. doi: 10.1103/physrevd.79.053003. URL https://doi.org/10.1103%2Fphysrevd.79.053003.

[64] A Bodek and U K Yang. Higher twist, ξ_w scaling, and effective LOPDFs for lepton scattering in the few GeV region. *Journal of Physics G: Nuclear and Particle Physics*, 29 (8):1899–1905, jul 2003. doi: 10.1088/0954-3899/29/8/369. URL https://doi.org/10.1088%2F0954-3899%2F29%2F8%2F369.

[65] T. Yang, C. Andreopoulos, H. Gallagher, K. Hofmann, and P. Kehayias. A hadronization model for few-GeV neutrino interactions. *The European Physical Journal C*, 63(1):1–10, aug 2009. doi: 10.1140/epjc/s10052-009-1094-z. URL https://doi.org/10.1140%2Fepjc%2Fs10052-009-1094-z.

[66] Michael Dolce, Hugh Gallagher, and Jeremy Wolcott. Central value tuning and uncertainties for hN FSI model in GENIE 3. Internal document. NOvA DocDB 43724, 2020.

[67] Júlia Tena-Vidal et al. Hadronization model tuning in genie v3. *Phys. Rev. D*, 105(1): 012009, 2022. doi: 10.1103/PhysRevD.105.012009.

[68] E. S. Pinzon Guerra et al. Using world charged π^+-nucleus scattering data to constrain an intranuclear cascade model. *Physical Review D*, 99(5), mar 2019. doi: 10.1103/physrevd.99.052007. URL https://doi.org/10.1103%2Fphysrevd.99.052007.

[69] M. A. Acero et al. Adjusting neutrino interaction models and evaluating uncertainties using NOvA near detector data. *The European Physical Journal C*, 80(12), dec 2020. doi: 10.1140/epjc/s10052-020-08577-5. URL https://doi.org/10.1140%2Fepjc%2Fs10052-020-08577-5.

[70] P. A. Rodrigues et al. Identification of nuclear effects in neutrino-carbon interactions at low three-momentum transfer. *Physical Review Letters*, 116(7), feb 2016. doi: 10.1103/physrevlett.116.071802. URL https://doi.org/10.1103%2Fphysrevlett.116.071802.

[71] Alex Rodriguez and Alessandro Laio. Clustering by fast search and find of density peaks. *Science*, 344(6191):1492–1496, 2014. doi: 10.1126/science.1242072. URL https://www.science.org/doi/abs/10.1126/science.1242072.

[72] R. C. Prim. Shortest connection networks and some generalizations. *Bell System Technical Journal*, 36(6):1389–1401, 1957. doi: https://doi.org/10.1002/j.1538-7305.1957.tb01515.x. URL https://onlinelibrary.wiley.com/doi/abs/10.1002/j.1538-7305.1957.tb01515.x.

[73] Leandro A.F. Fernandes and Manuel M. Oliveira. Real-time line detection through an improved hough transform voting scheme. *Pattern Recognition*, 41(1):299–314, 2008. ISSN 0031-3203. doi: https://doi.org/10.1016/j.patcog.2007.04.003. URL https://www.sciencedirect.com/science/article/pii/S0031320307001823.

[74] Mattias Ohlsson, Carsten Peterson, and Alan L. Yuille. Track finding with deformable templates — the elastic arms approach. *Computer Physics Communications*, 71(1):77–98, 1992. ISSN 0010-4655. doi: https://doi.org/10.1016/0010-4655(92)90074-9. URL https://www.sciencedirect.com/science/article/pii/0010465592900749.

[75] M Baird, J Bian, M Messier, E Niner, D Rocco, and K Sachdev. Event reconstruction techniques in nova. *Journal of Physics: Conference Series*, 664(7):072035, dec 2015. doi: 10.1088/1742-6596/664/7/072035. URL https://dx.doi.org/10.1088/1742-6596/664/7/072035.

[76] Raghu Krishnapuram and James M. Keller. A possibilistic approach to clustering. *IEEE Trans. Fuzzy Syst.*, 1:98–110, 1993.

[77] Miin-Shen Yang and Kuo-Lung Wu. Unsupervised possibilistic clustering. *Pattern Recogn.*, 39(1):5–21, jan 2006. ISSN 0031-3203. doi: 10.1016/j.patcog.2005.07.005. URL https://doi.org/10.1016/j.patcog.2005.07.005.

[78] R. Frühwirth. Application of kalman filtering to track and vertex fitting. *Nuclear Instruments and Methods in Physics Research Section A: Accelerators, Spectrometers, Detectors and Associated Equipment*, 262(2):444–450, 1987. ISSN 0168-9002. doi: https://doi.org/10.1016/0168-9002(87)90887-4. URL https://www.sciencedirect.com/science/article/pii/0168900287908874.

[79] Biswaranjan Behera, Gavin Davies, and Fernanda Psihas. Event reconstruction in the nova experiment, 2017.

[80] Brian Rebel. A Window Tracking Algorithm for Cosmic Ray Muons. Internal document. NOvA DocDB 15977, 2016.

[81] A. Aurisano, A. Radovic, D. Rocco, A. Himmel, M.D. Messier, E. Niner, G. Pawloski, F. Psihas, A. Sousa, and P. Vahle. A convolutional neural network neutrino event classifier. *Journal of Instrumentation*, 11(09):P09001, sep 2016. doi: 10.1088/1748-0221/11/09/P09001. URL https://dx.doi.org/10.1088/1748-0221/11/09/P09001.

[82] Christian Szegedy, Wei Liu, Yangqing Jia, Pierre Sermanet, Scott Reed, Dragomir Anguelov, Dumitru Erhan, Vincent Vanhoucke, and Andrew Rabinovich. Going deeper with convolutions, 2014.

[83] Laurens van der Maaten and Geoffrey Hinton. Visualizing data using t-sne. *Journal of Machine Learning Research*, 9(86):2579–2605, 2008. URL http://jmlr.org/papers/v9/vandermaaten08a.html.

[84] Fernanda Psihas. *Modeling nuclear effects in NuWroMonte Carlo neutrino eventgenerator*. Phd thesis, Indiana University, February 2018. Available at https://www.osti.gov/biblio/1437288.

[85] Michael Baird, Erica Smith, Jianming Bian, Louise Suter, Karl Warburton, and Jeremy Wolcott. Reconstruction changes prod5 summary note. February 2020. URL https://nova-docdb.fnal.gov/cgi-bin/private/ShowDocument?docid=43162.

[86] Yann Coadou. Boosted Decision Trees and Applications. *EPJ Web Conf.*, 55:02004, 2013. doi: 10.1051/epjconf/20135502004.

[87] Joshua Porter. Remid retraining 2019 technote. Internal document. NOvA DocDB 42277, December 2019. URL https://nova-docdb.fnal.gov/cgi-bin/private/ShowDocument?docid=42277.

[88] E. Catano-Mur, N. Nayak, A. Sutton, and K. Warburton. Event selection for the 2020 3-flavor analysis. Internal document. NOvA DocDB 44040, March 2020. URL https://nova-docdb.fnal.gov/cgi-bin/private/ShowDocument?docid=44040.

[89] Andrew Sutton. 3flavor 2020 cut flow chart. August 2020. URL https://nova-docdb.fnal.gov/cgi-bin/private/ShowDocument?docid=2678.

[90] Reddy P. Gandrajula and Liudmila Kolupaeva. Cosmic rejection BDT for ν_e appearance analysis. Internal document. NOvA DocDB 42473, December 2019. URL https://nova-docdb.fnal.gov/cgi-bin/private/ShowDocument?docid=42473.

[91] Thomas Karl Warburton. Muon neutrino cosmic rejection technote for the 2020 analysis. Internal document. NOvA DocDB 42358, December 2019. URL https://nova-docdb.fnal.gov/cgi-bin/private/ShowDocument?docid=42358.

[92] X.-G. Lu et al. Measurement of final-state correlations in neutrino muon-proton mesonless production on hydrocarbon at $\langle E_\nu \rangle = 3$. *Physical Review Letters*, 121(2), jul 2018. doi: 10.1103/physrevlett.121.022504. URL https://doi.org/10.1103%2Fphysrevlett.121.022504.

[93] K. Abe et al. Characterization of nuclear effects in muon-neutrino scattering on hydrocarbon with a measurement of final-state kinematics and correlations in charged-current pionless interactions at t2k. *Physical Review D*, 98(3), aug 2018. doi: 10.1103/physrevd.98.032003. URL https://doi.org/10.1103%2Fphysrevd.98.032003.

[94] D. Coplowe et al. Probing nuclear effects with neutrino-induced charged-current neutral pion production. *Physical Review D*, 102(7), oct 2020. doi: 10.1103/physrevd.102.072007. URL https://doi.org/10.1103%2Fphysrevd.102.072007.

[95] F James. Function minimization. 1972. doi: 10.5170/CERN-1972-021.1. URL https://cds.cern.ch/record/883720.

[96] Jeremy Wolcott and Kirk Bays. Cross section central value tune and uncertainties for the 2017 analyses. Internal document. NOvA DocDB 23264, 2017.

[97] P. Adamson et al. Study of quasielastic scattering using charged-current ν_μ-iron interactions in the MINOS near detector. *Physical Review D*, 91(1), jan 2015. doi: 10.1103/physrevd.91.012005. URL https://doi.org/10.1103%2Fphysrevd.91.012005.

[98] Kirk Bays et al. Nova 2020 cross-section tune tech note. Internal document. NOvA DocDB 43962, 2020.

[99] K. Abe et al. Measurement of neutrino and antineutrino oscillations by the t2k experiment including a new additional sample of ν_e interactions at the far detector. *Phys. Rev. D*, 96: 092006, Nov 2017. doi: 10.1103/PhysRevD.96.092006. URL https://link.aps.org/doi/10.1103/PhysRevD.96.092006.

[100] Jeremy Wolcott. Re-diagonalizing beam syst PCA for ND+FD joint fits. Internal document. NOvA DocDB 57721, February 2023.

[101] Nitish Nayak. Flux Systematics for the 2018 NOvA Oscillation Analyses. Internal document. NOvA DocDB 27884, April 2018.

[102] Jonathon Shlens. A tutorial on principal component analysis, 2014.

[103] Erika Catano-Mur, v hewes, and Lisa Koerner. NOvA Production 5.1 Detector Systematics Executive Summary. Internal document. NOvA DocDB 53225, 2023.

[104] Neutron Task Force. Nova neutron systematic for 3-flavor analysis. Internal document. NOvA DocDB 43811, February 2020. URL https://nova-docdb.fnal.gov/cgi-bin/private/ShowDocument?docid=43811.

[105] N. Agafonova et al. Final results of the OPERA experiment on ν_τ appearance in the CNGS neutrino beam. *Physical Review Letters*, 120(21), may 2018. doi: 10.1103/physrevlett.120.211801. URL https://doi.org/10.1103%2Fphysrevlett.120.211801.

[106] Rik Gran. Model uncertainties in light of minerva momentum andenergy transfer data. NuInt 17: 11th International Workshop on Neutrino-Nucleus Scattering in the Few-GeV Region, 2017. URL https://meetings.triumf.ca/event/6/contributions/2324/attachments/1618/1826/NuInt17-20170624-Gran.pdf.

[107] P. A. Zyla et al. Review of Particle Physics. *Progress of Theoretical and Experimental Physics*, 2020(8):083C01, 08 2020. ISSN 2050-3911. doi: 10.1093/ptep/ptaa104. URL https://doi.org/10.1093/ptep/ptaa104.

[108] Michael Dolce. MCMC ND+FD Residual Difference Fit Progress. Internal document. NOvA DocDB 58512, April 2023. URL https://nova-docdb.fnal.gov/cgi-bin/private/ShowDocument?docid=58512.

[109] Glen Cowan, Kyle Cranmer, Eilam Gross, and Ofer Vitells. Asymptotic formulae for likelihood-based tests of new physics. *The European Physical Journal C*, 71(2), feb 2011. doi: 10.1140/epjc/s10052-011-1554-0. URL https://doi.org/10.1140%2Fepjc%2Fs10052-011-1554-0.

[110] M. Tanabashi et al. Review of particle physics. *Phys. Rev. D*, 98:030001, Aug 2018. doi: 10.1103/PhysRevD.98.030001. URL https://link.aps.org/doi/10.1103/PhysRevD.98.030001.

[111] Edward Atkin and others. NOvA-T2K Joint Oscillation Fit: Fake data studies. Internal document. NOvA DocDB 54582, June 2023. URL https://nova-docdb.fnal.gov/cgi-bin/private/ShowDocument?docid=54582.

APPENDIX A. NEAR DETECTOR SAMPLES CONSTRAIN

The fit to data summarized in the last section of chapter 5 constrains various systematic parameters, including those that describe cross section model, beam model and detector response. Each sample has a different composition, which was detailed in chapter 4.6. This appendix displays each sample with the effect of different categories of parameters separately. In other words, the NOvA tune (grey lines) is the pre-fit sample, the color lines are the effect of particular constrains, and the black line is the post-fit sample, or the combination of all of these effects together. These way of displaying the samples highlights the different effects for each topology (i.e. FSI adjustment enchances $\mu + \pi + X$ and suppresess $\mu + P + X$). The categories are defined in the following table:

Table A.1: Categories of systematic parameters

All cross section (xsec)		
QE	MEC	
kZExpEV1Syst2020	kMECEnuShapeSyst2020Nu	
kZExpEV2Syst2020	kMECEnuShapeSyst2020AntiNu	
kZExpEV3Syst2020	kMECInitStateNPFracSyst2020Nu	
ReweightZNormCCQE	kMECInitStateNPFracSyst2020AntiNu	
RPACCQEEnhSyst2020	MEC gauss enhancement parameters (10)	
kRPACCQESuppSyst2020		
RES	DIS	FSI
kRESLowQ2SuppressionSyst2020	DIS$\bar{\nu}$nCC3pi	khNFSISyst2020_EV1
ReweightMaCCRES	DIS$\bar{\nu}$pCC1pi	khNFSISyst2020_MFP
ReweightMvCCRES	DIS$\bar{\nu}$pCC3pi	
ReweightTheta_Delta2Npi	DISνnCC1pi	
kRESDeltaScaleSyst	DISνnCC2pi	
kRESOtherScaleSyst	DISνnCC3pi	
kRESvpvnNuRatioXSecSyst	DISνpCC0pi	
kRESvpvnNuBarRatioXSecSyst	DISνpCC2pi	
	DISνpCC3pi	
	kDISNuHadroQ1Syst	
	kDISNuBarHadroQ0Syst	
Beam/Flux	Detector response	
ppfx_hadp_pc00	Neutron	
ppfx_hadp_pc01	Calibration	
ppfx_hadp_pc02	Calibration Shape	
ppfx_hadp_pc03	Cherenkov	
ppfx_hadp_pc04	Detector Aging	

FHC samples

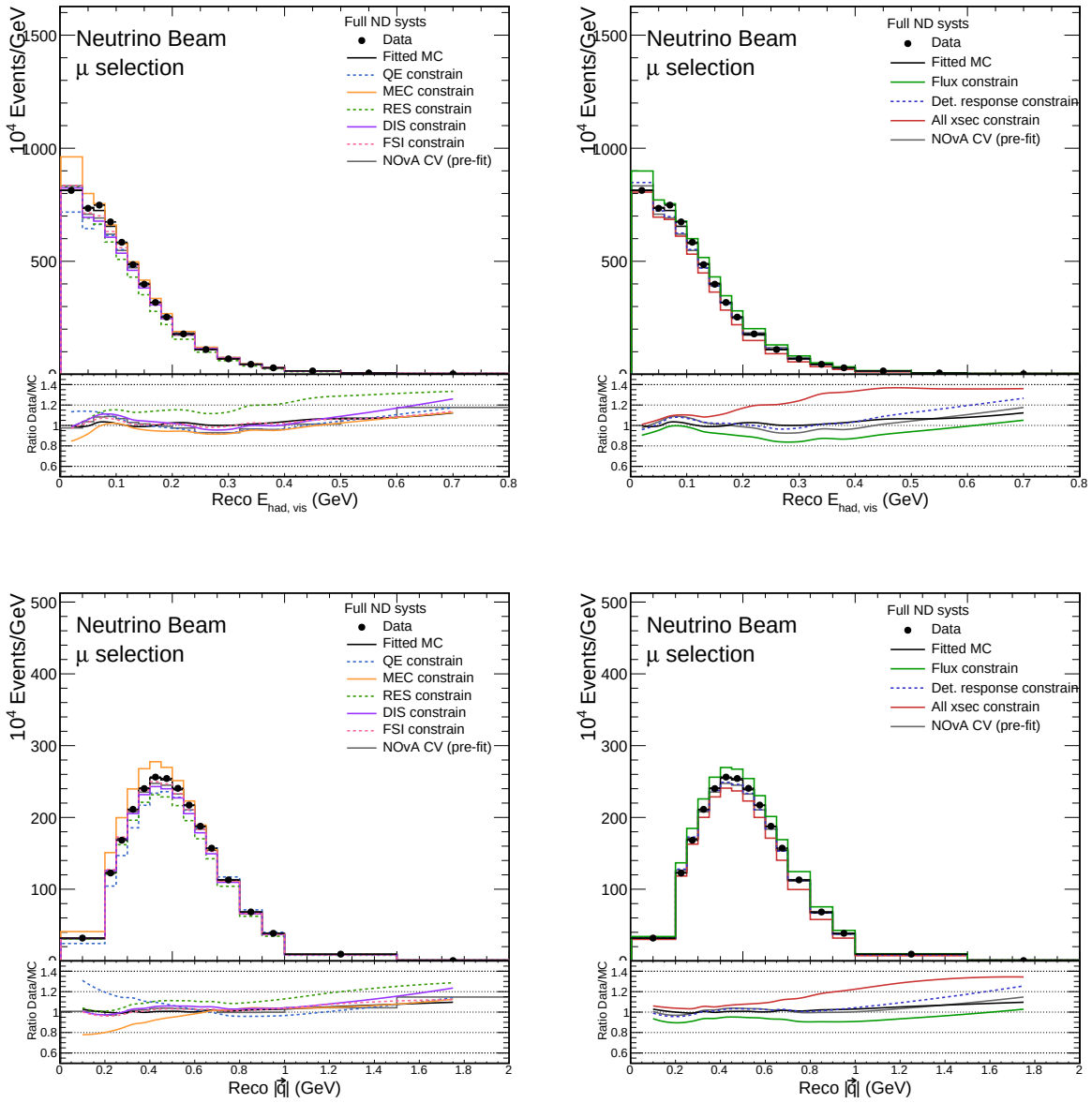

Figure A.1: μ FHC sample

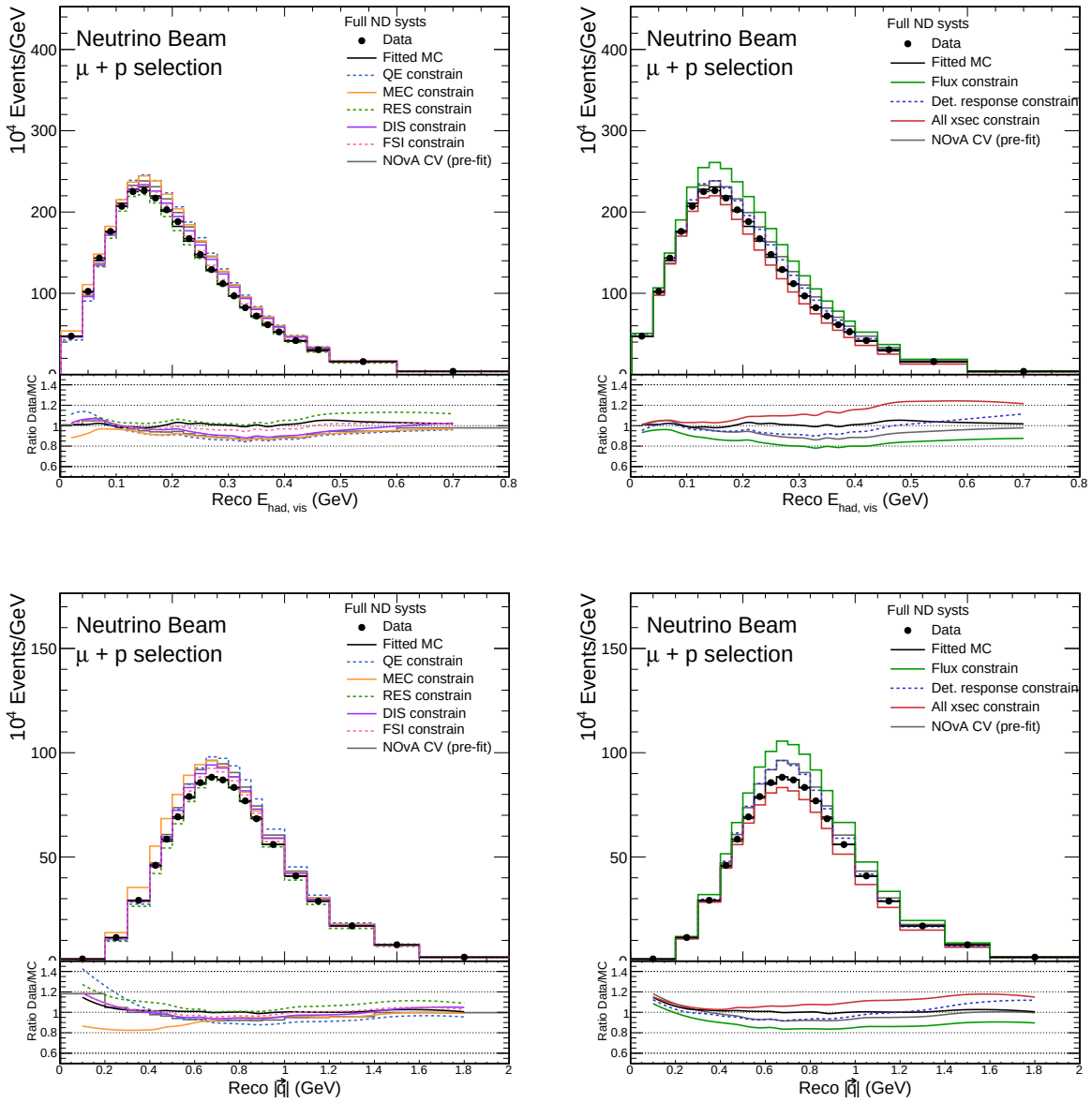

Figure A.2: $\mu + P$ FHC sample

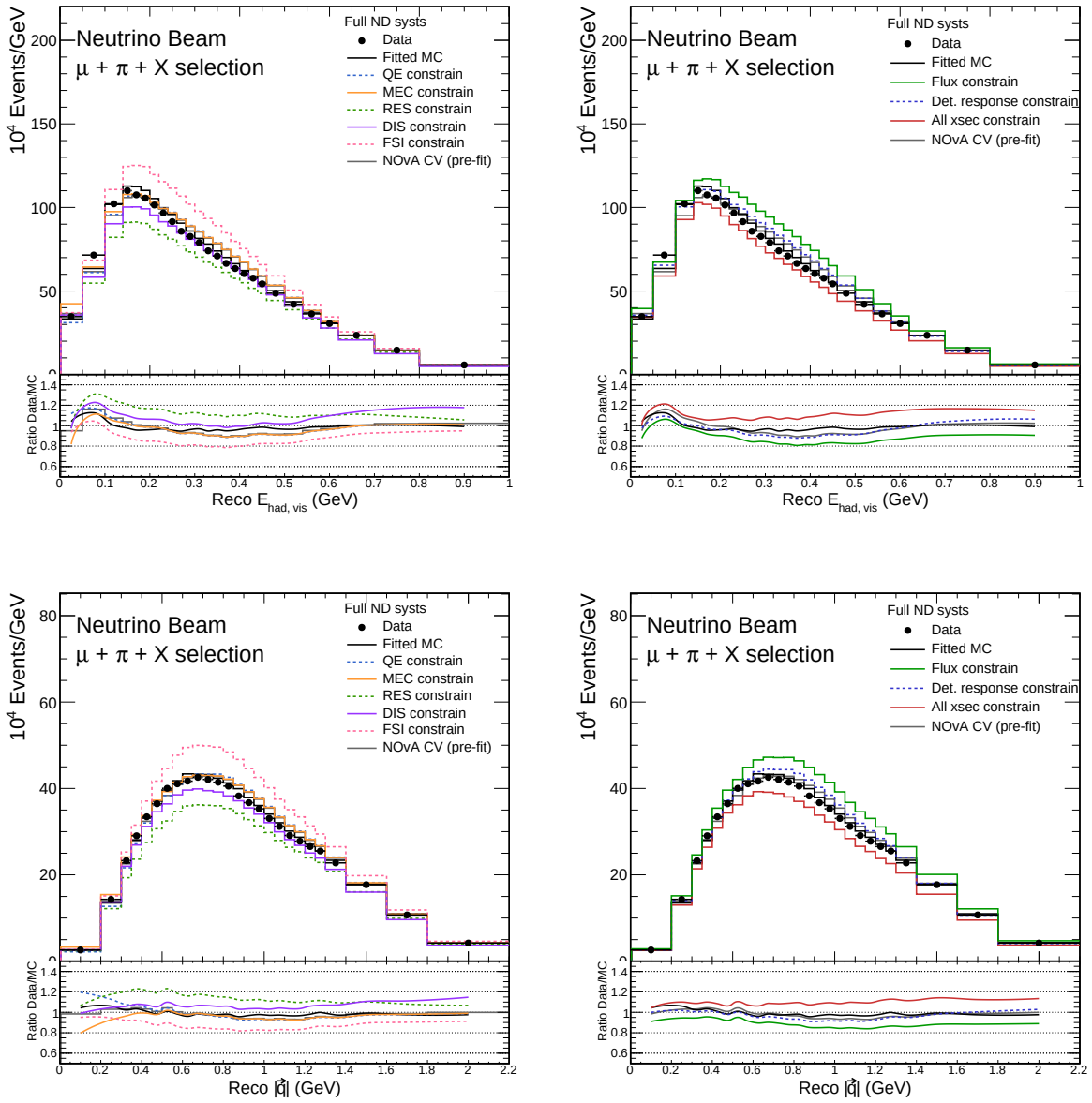

Figure A.3: $\mu + \pi + X$ FHC sample

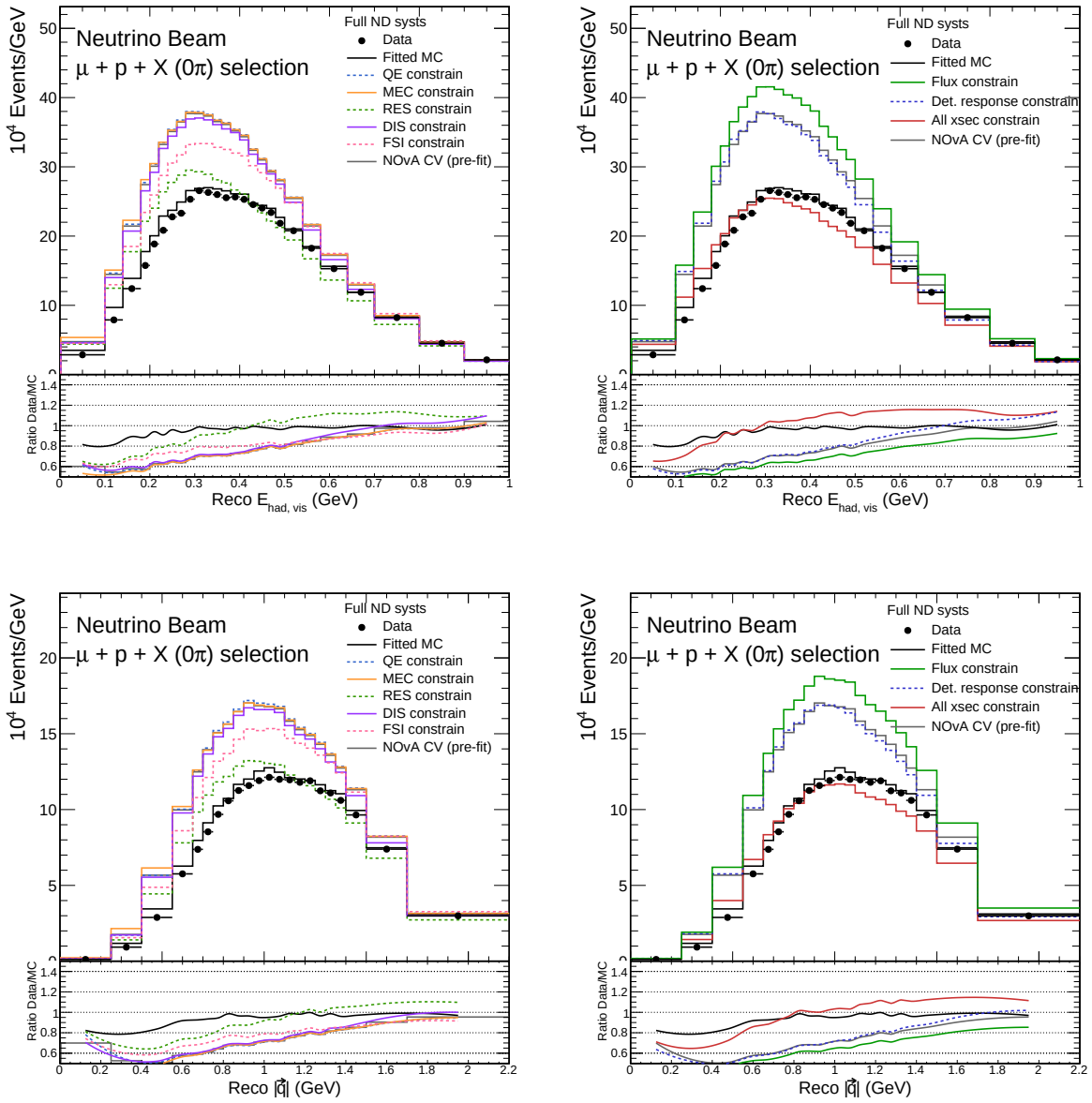

Figure A.4: $\mu + P + X$ FHC sample

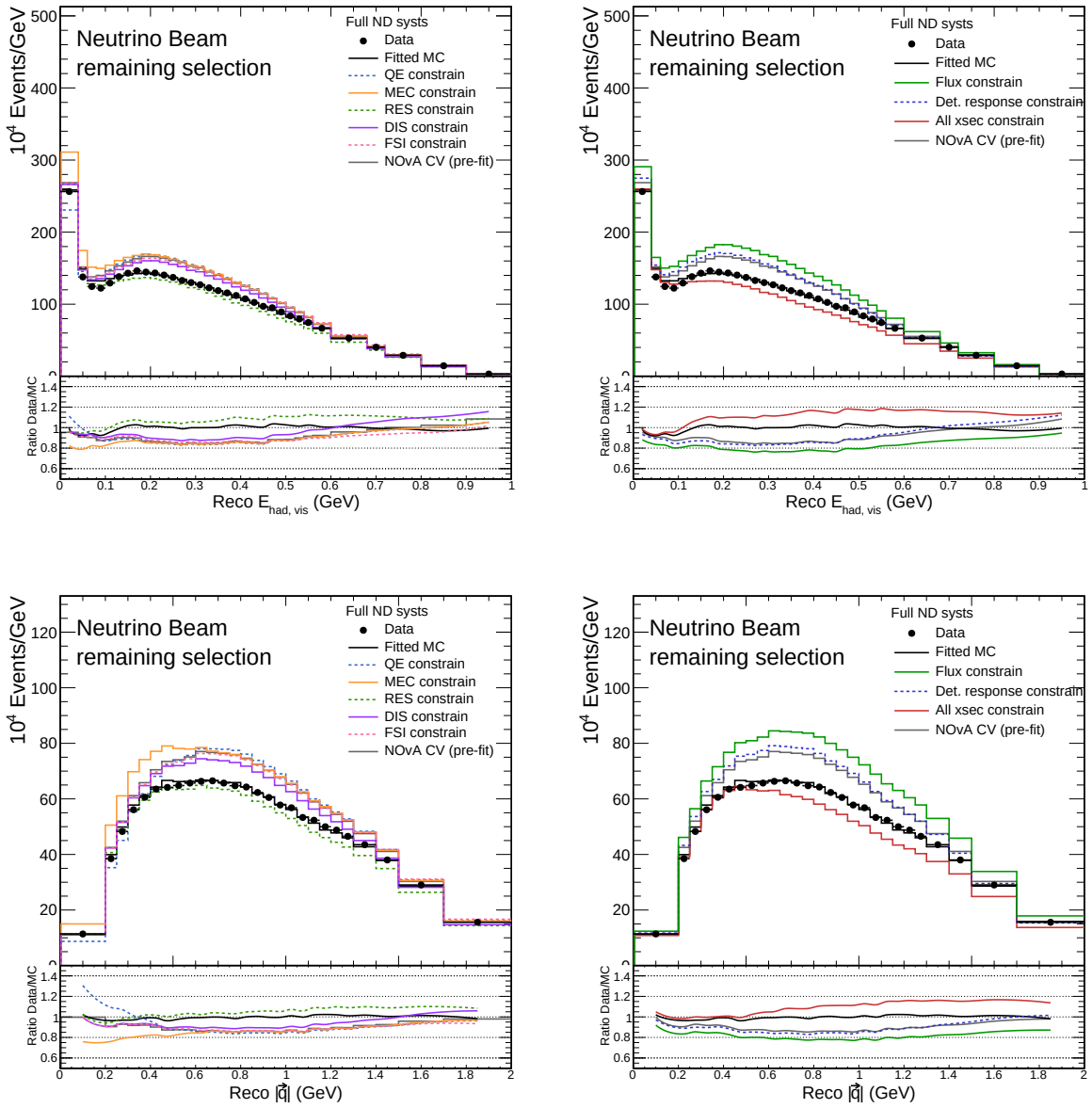

Figure A.5: Remaining FHC sample

RHC samples

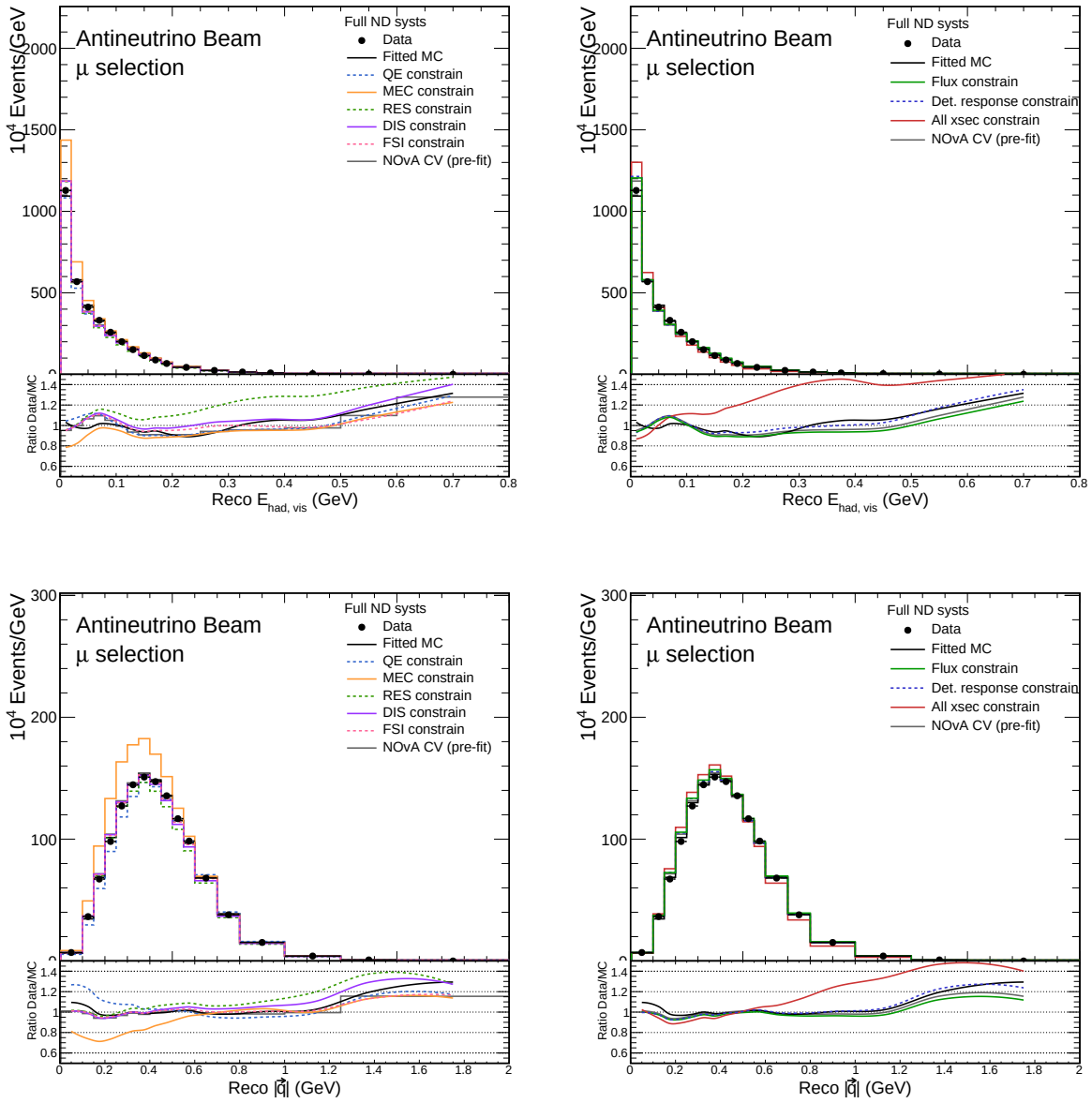

Figure A.6: μ RHC sample

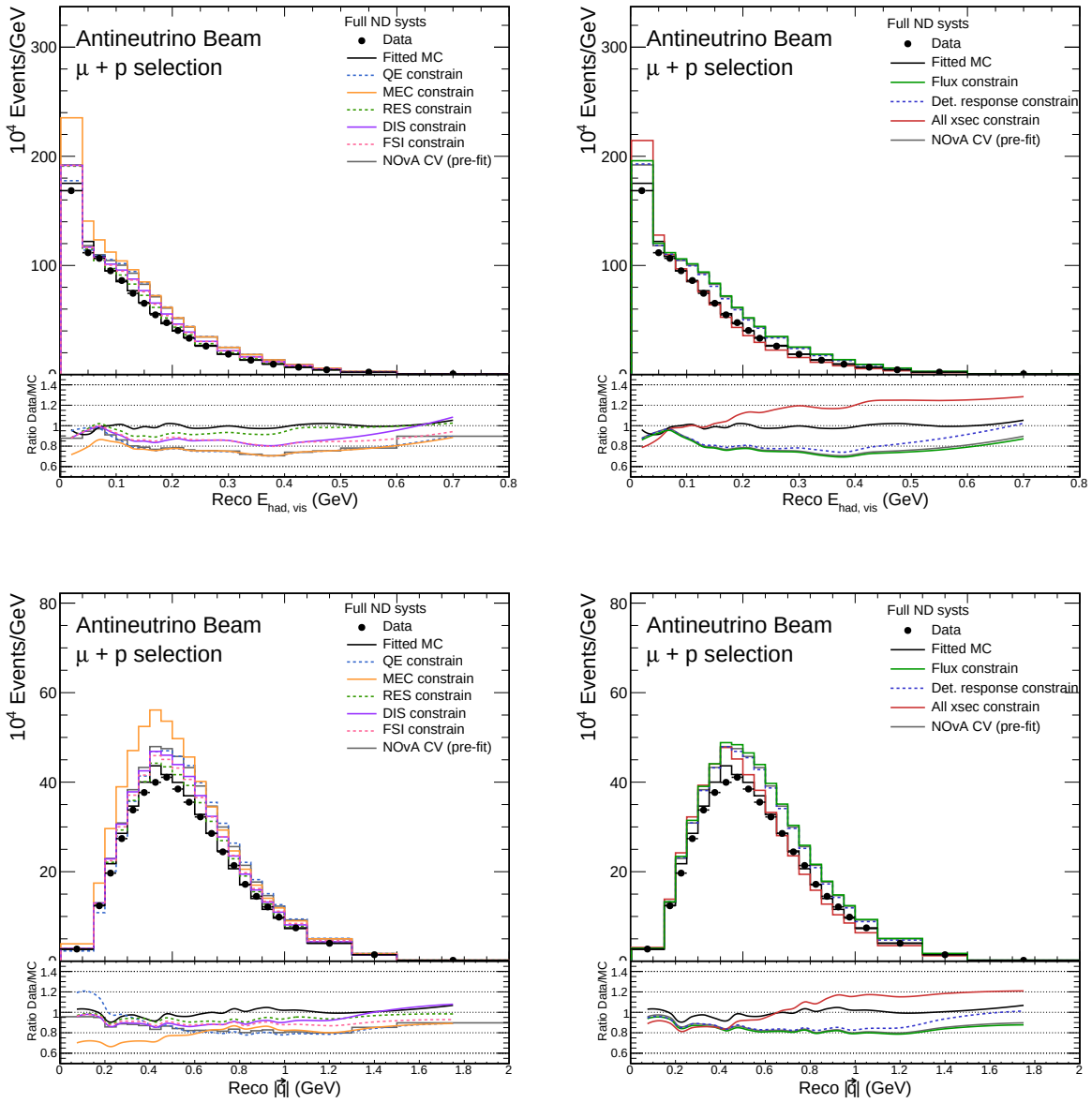

Figure A.7: $\mu + P$ RHC sample

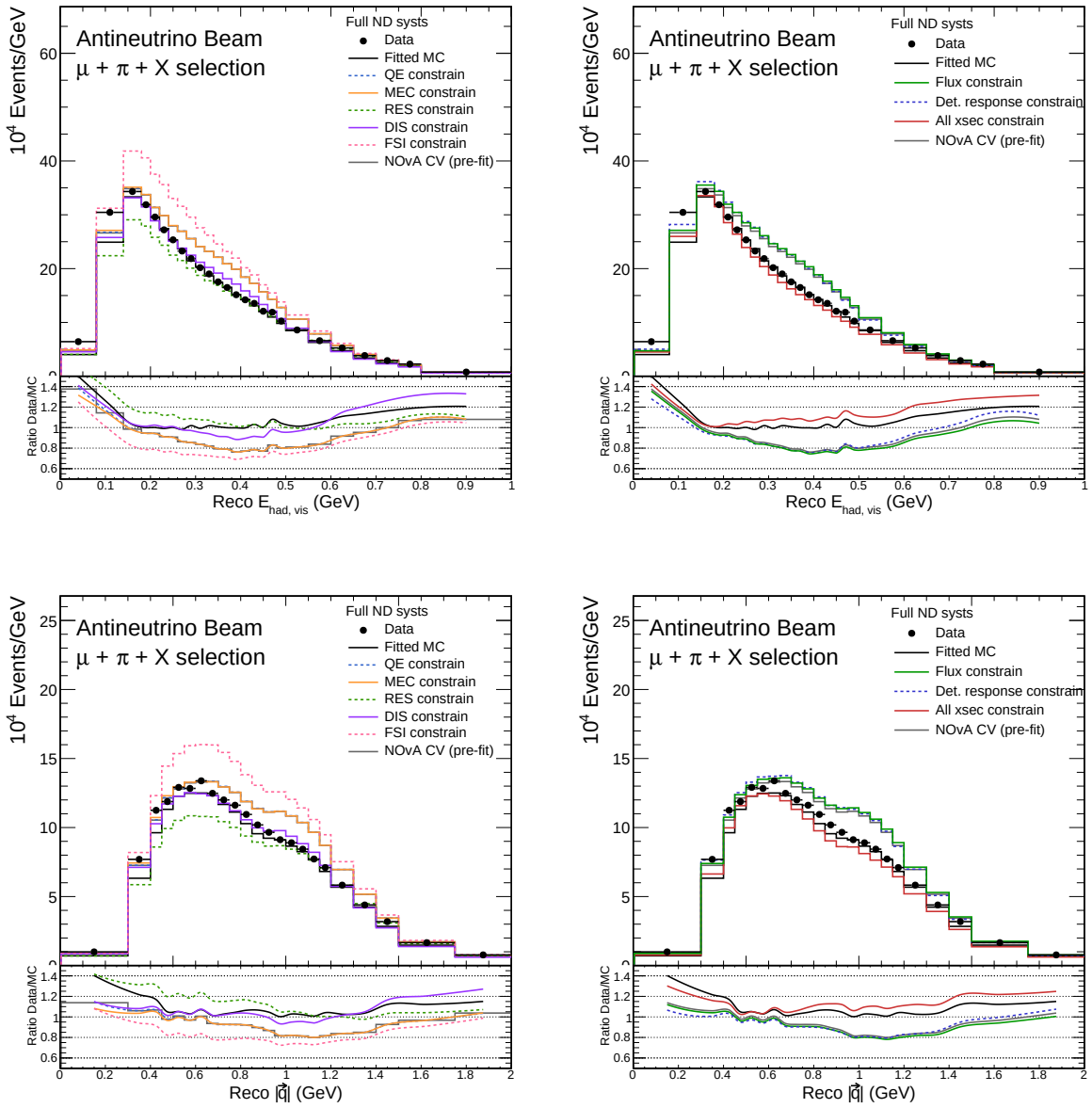

Figure A.8: $\mu + \pi + X$ RHC sample

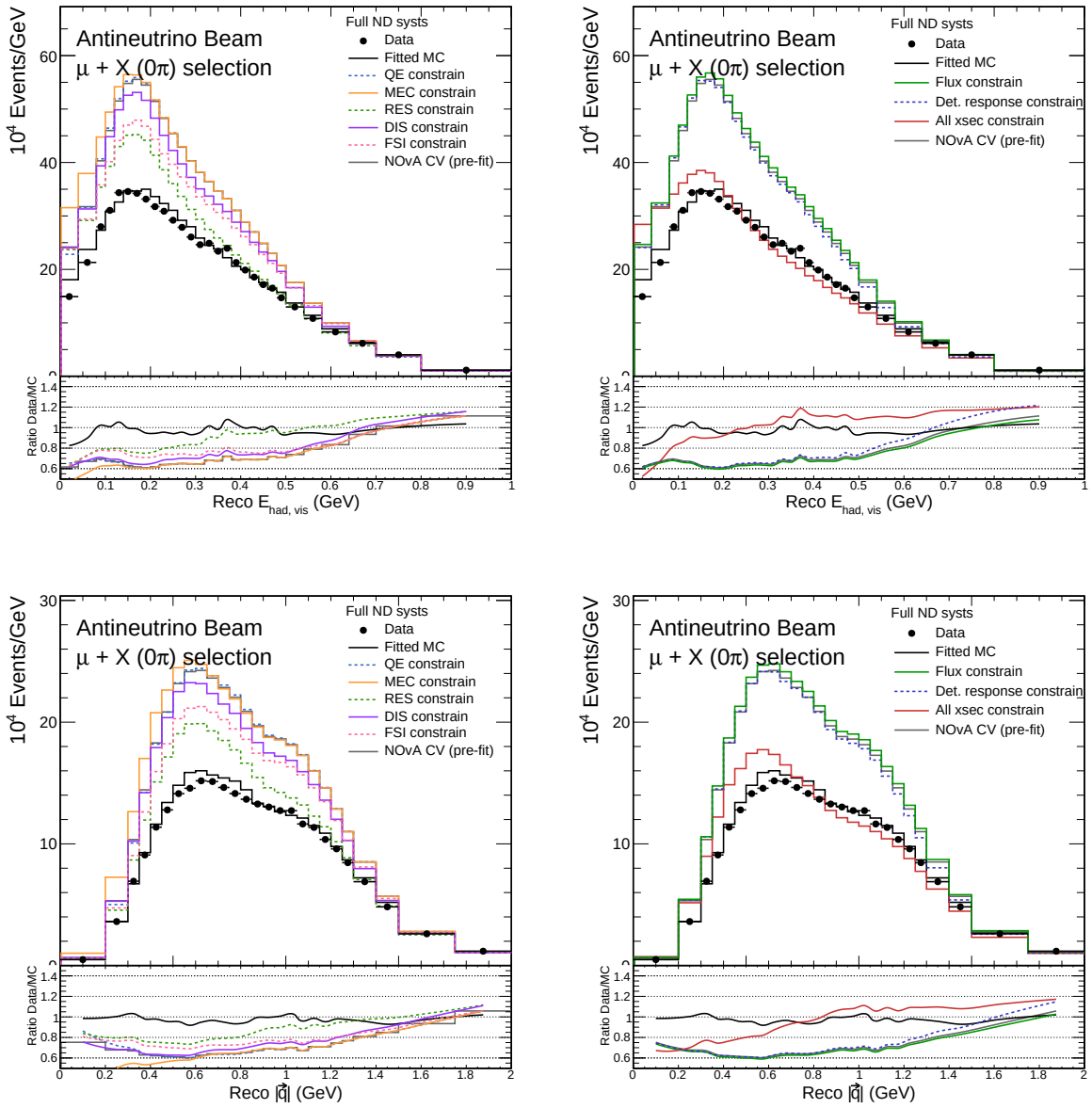

Figure A.9: $\mu + X$ RHC sample

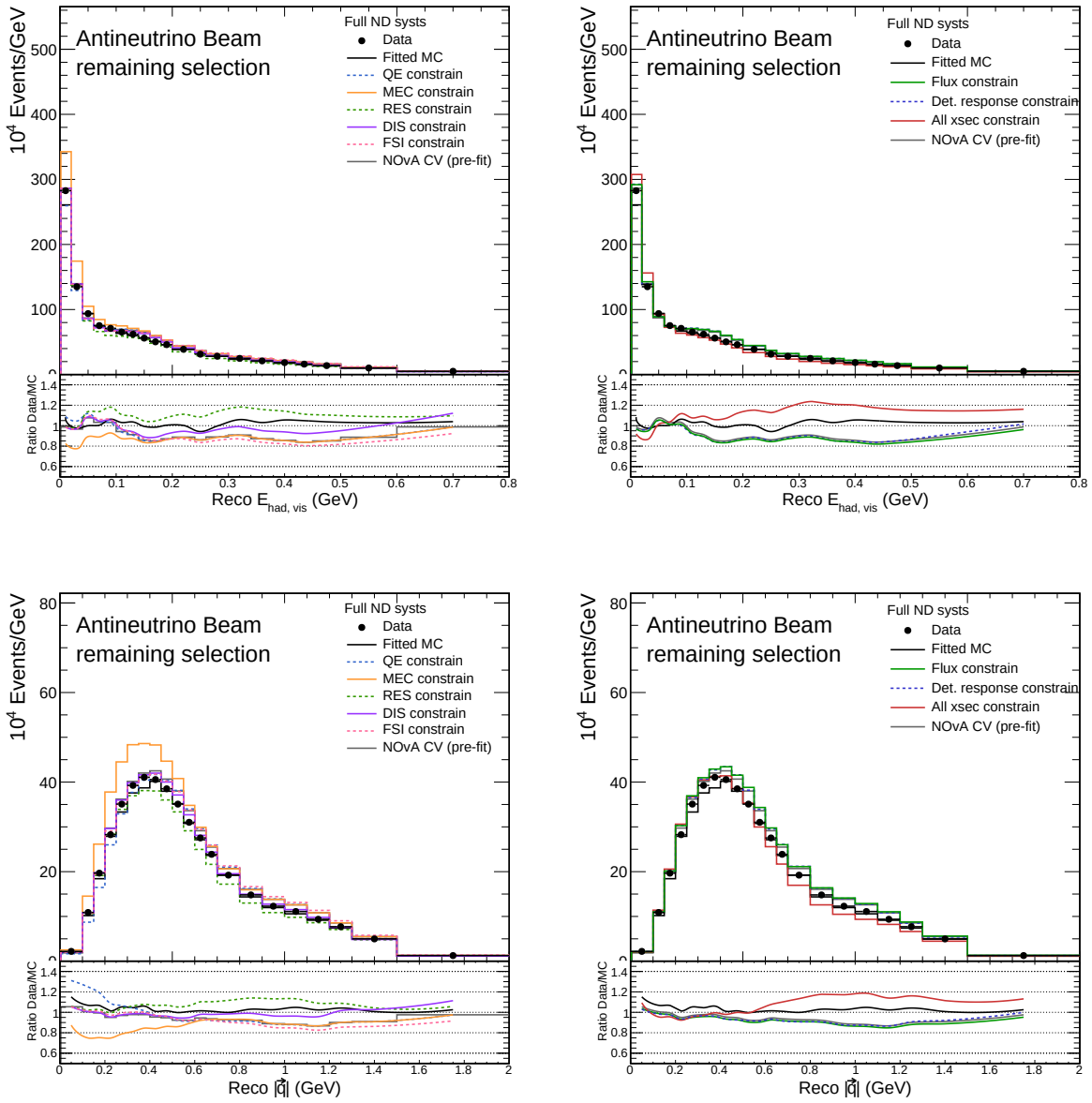

Figure A.10: Remaining RHC sample

APPENDIX B. MEC MODEL CHANGE FAKE DATA FIT ADDITIONAL PLOTS

B.1 MINERvA weights for 2p2h

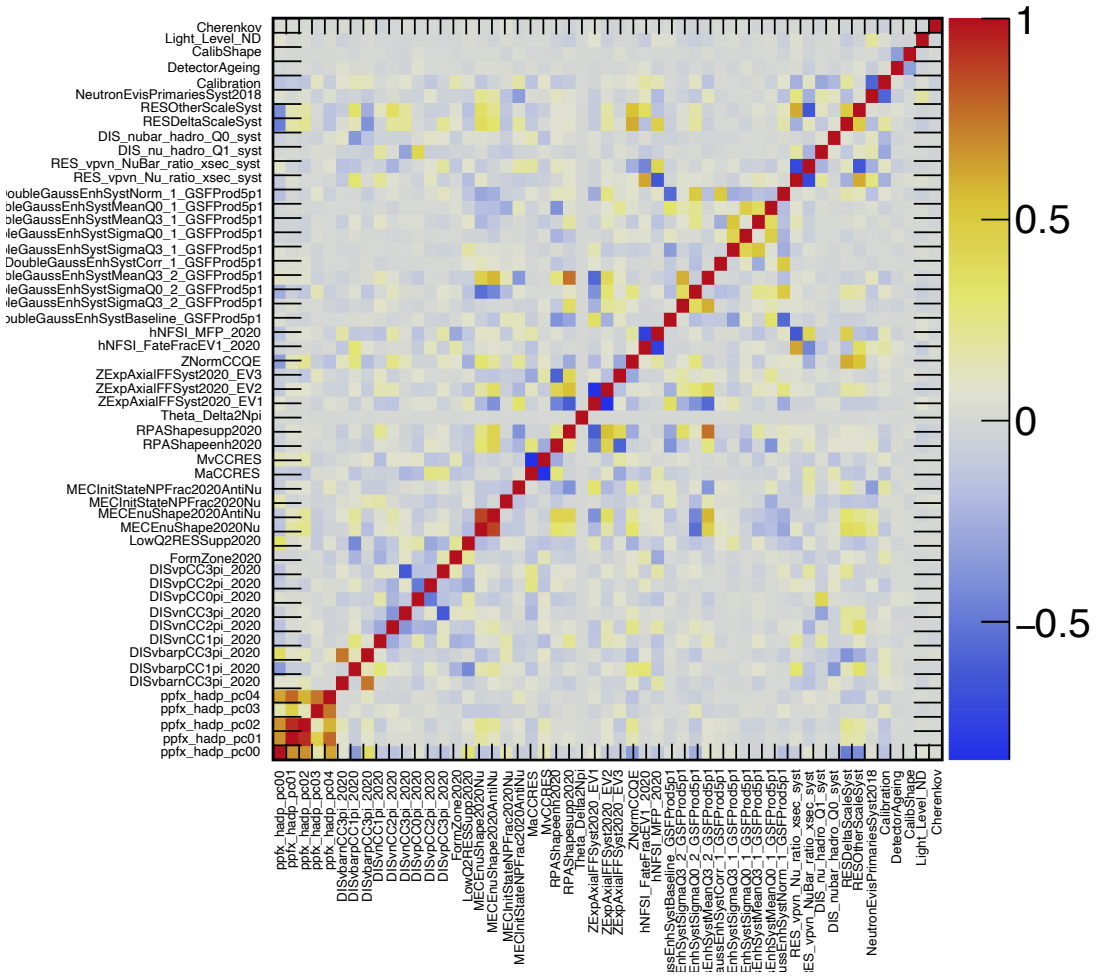

Figure B.1: ND fit correlation matrix of systematic parameters obtained from ND fit.

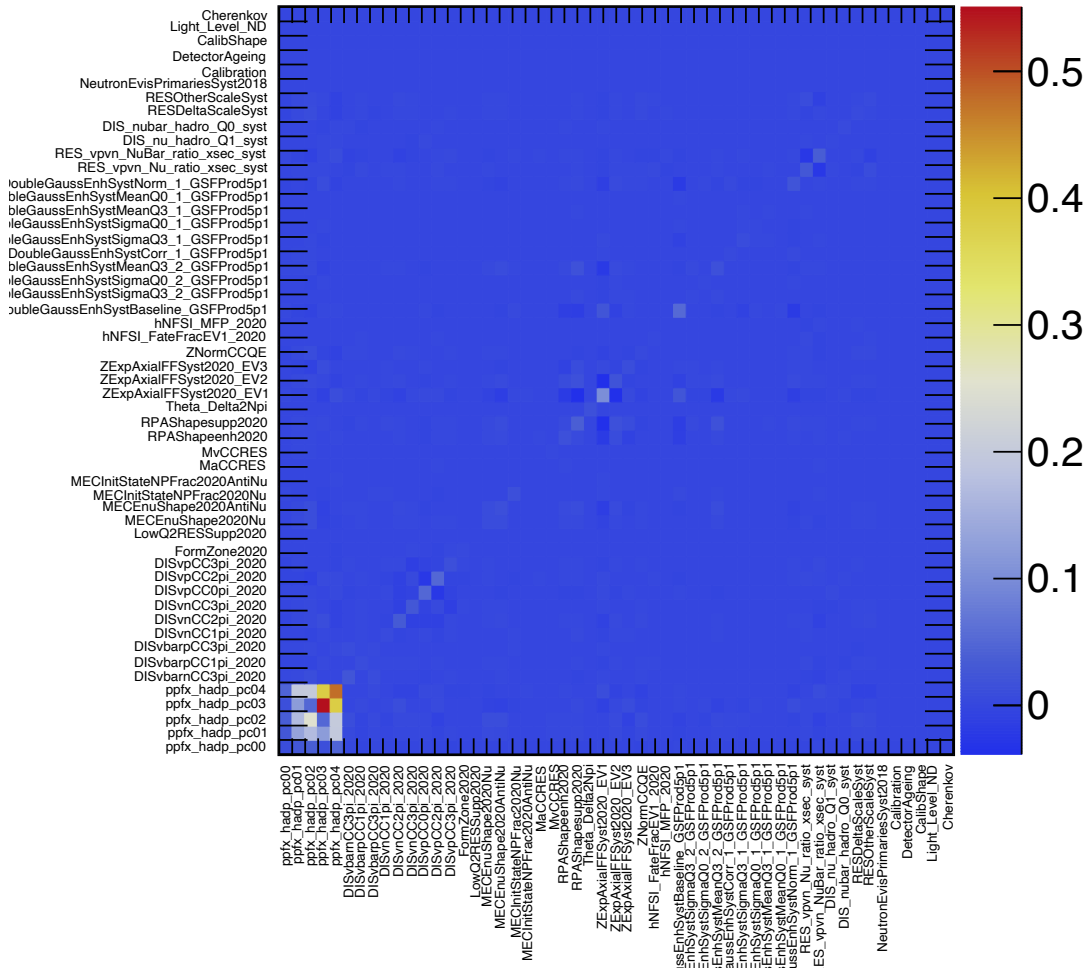

Figure B.2: ND fit covariance matrix of systematic parameters obtained from ND fit.

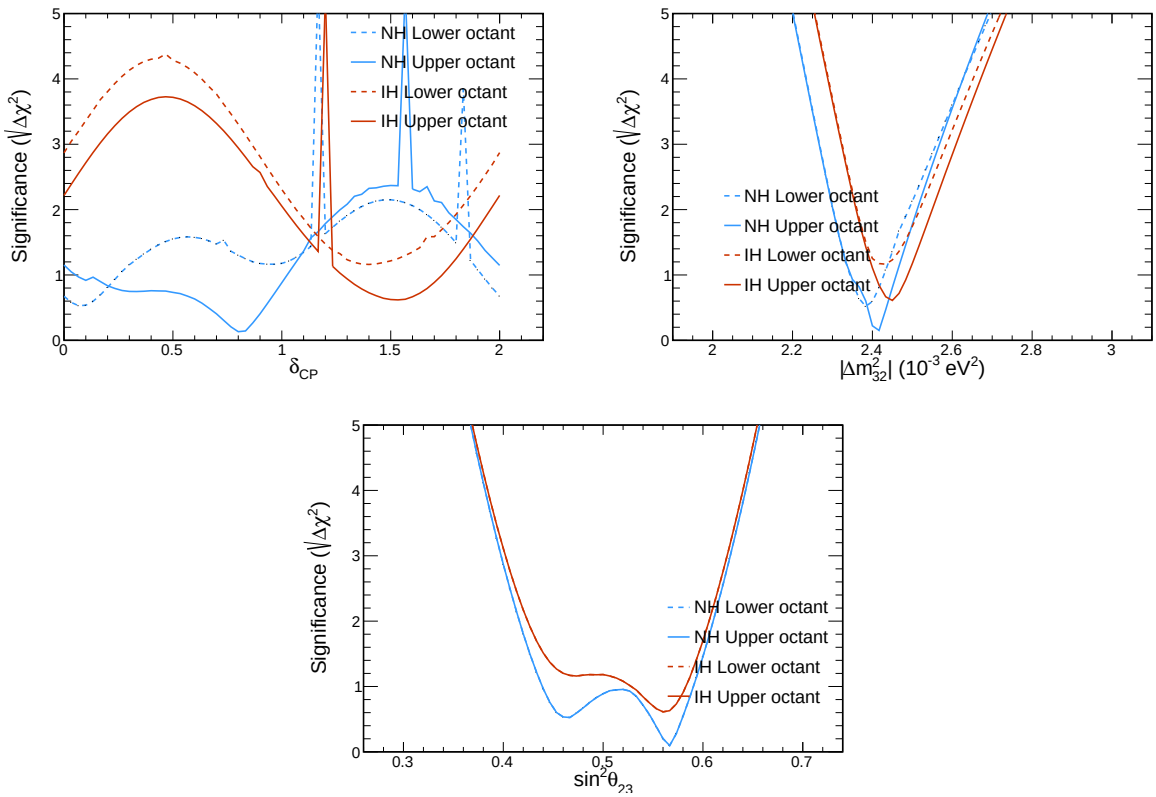

Figure B.3: One-dimensional significances for δ_{CP} , Δm^2_{32} and $\sin^2\theta_{23}$ in the Minerva-reweighted MEC fake data fit, shown for Normal (blue) or inverted (red) mass ordering/hierarchy, and for upper (solid line) or lower (dashed line) octants. The best fit point had $\chi^2_{min} = 1.40$, $\sin^2\theta_{23}$ =2.42×10^{-3}eV^2, $\Delta m^2_{32} = 0.57$, δ_{CP} =0.81π.

B.2 QE-like MEC

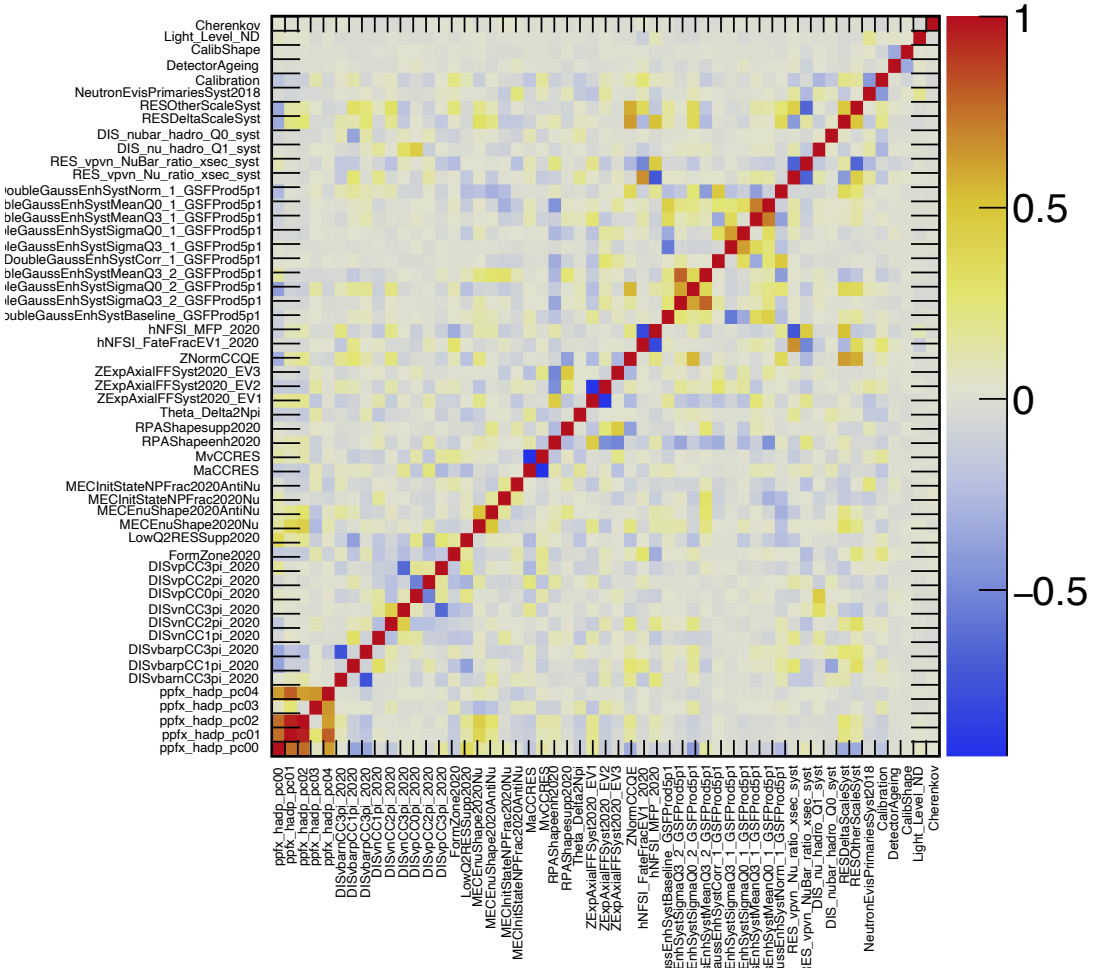

Figure B.4: ND fit correlation matrix of systematic parameters obtained from ND fit.

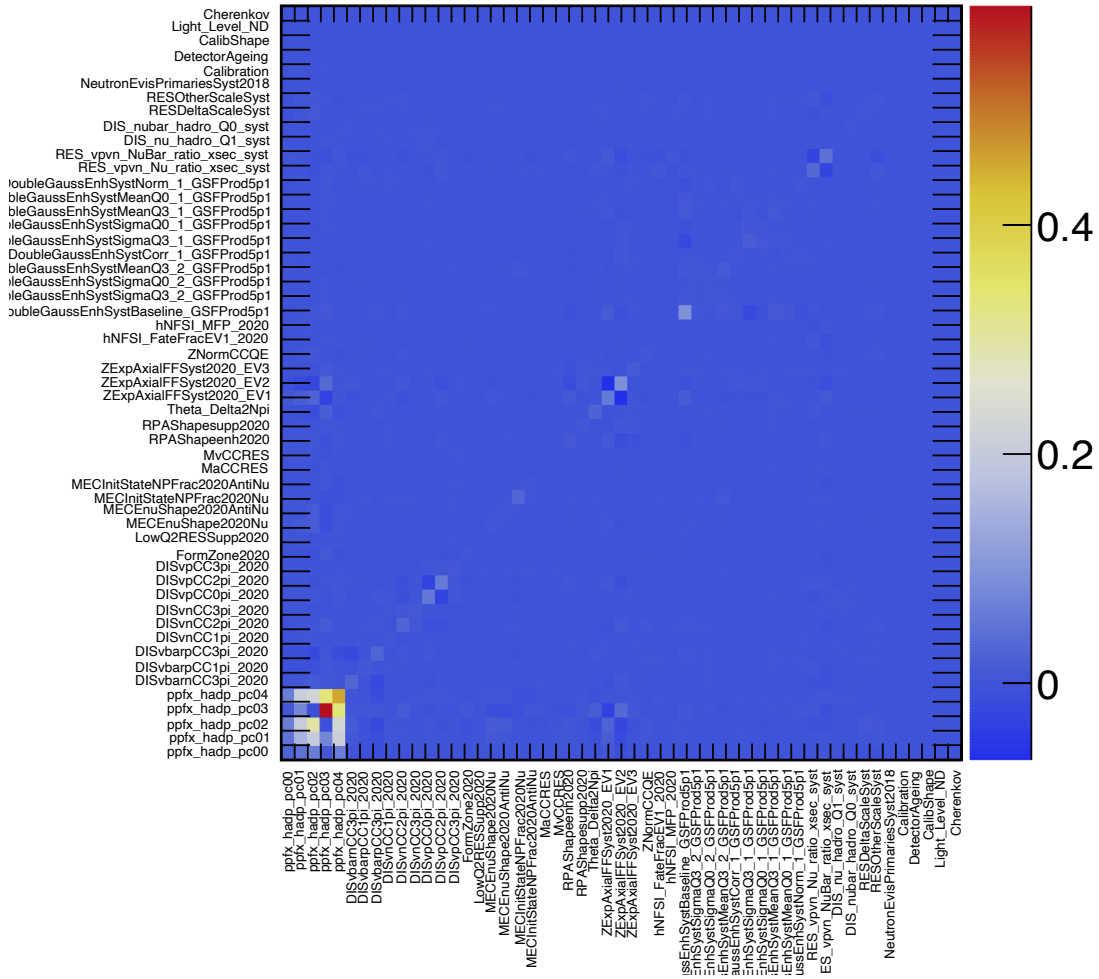

Figure B.5: ND fit covariance matrix of systematic parameters obtained from ND fit.

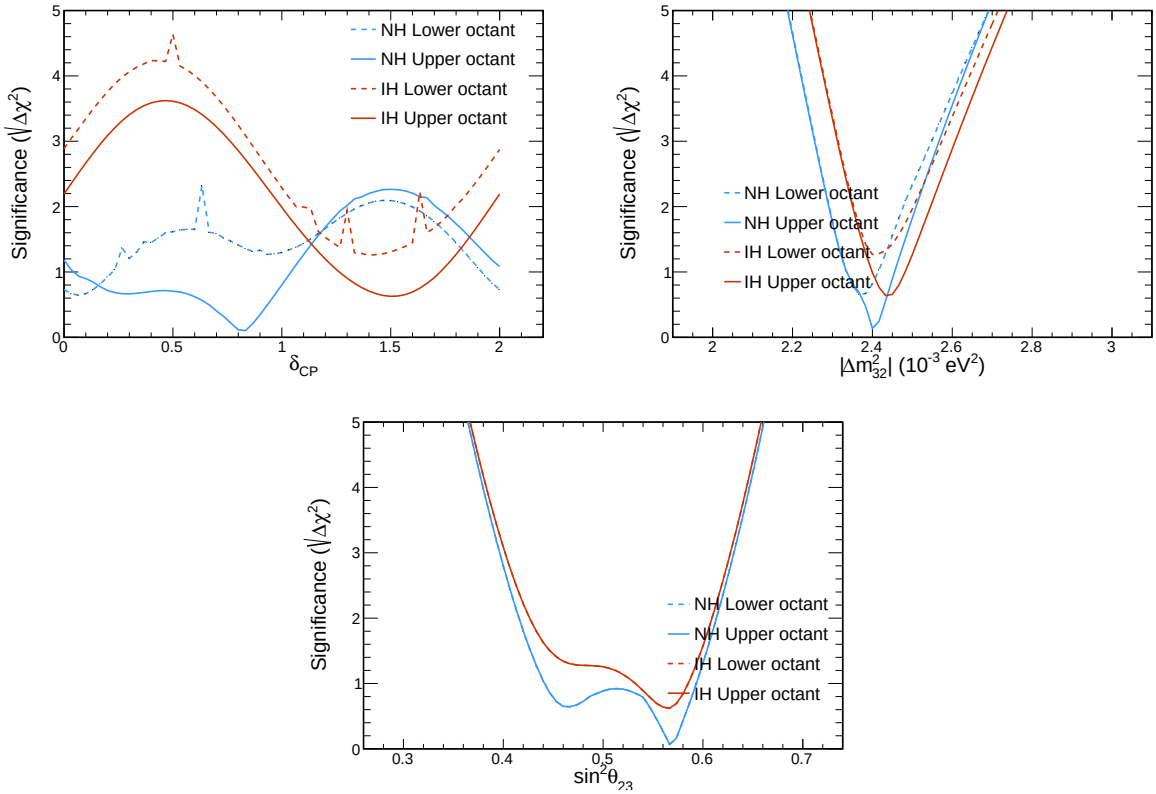

Figure B.6: One-dimensional significances for δ_{CP} , Δm^2_{32} and $\sin^2\theta_{23}$ in the QE-like-reweighted MEC fake data fit, shown for Normal (blue) or inverted (red) mass ordering/hierarchy, and for upper (solid line) or lower (dashed line) octants. The best fit point had $\chi^2_{min} = 0.05$, $\sin^2\theta_{23}$ =2.40×10^{-3}eV^2, $\Delta m^2_{32} = 0.57$, δ_{CP} =0.82π.

B.3 RES-like MEC

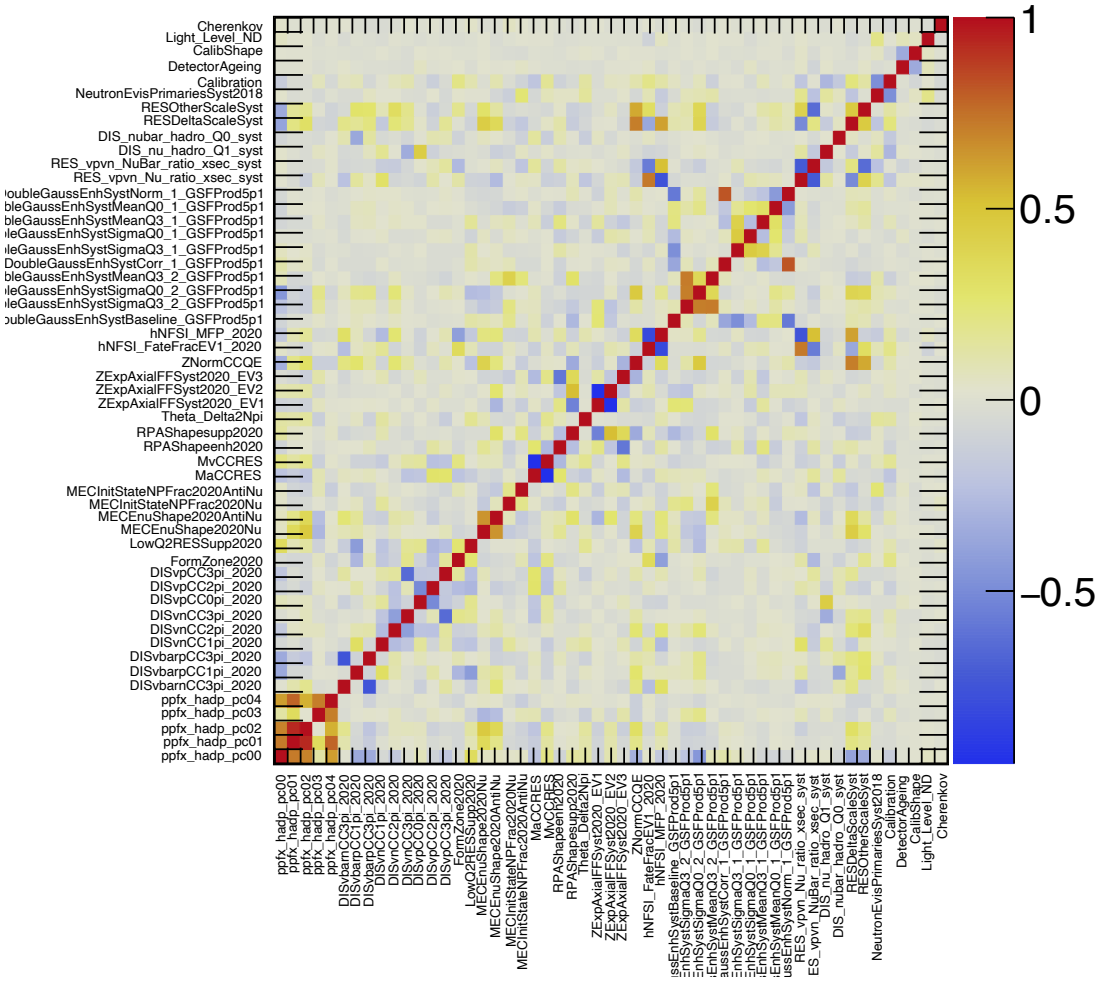

Figure B.7: ND fit correlation matrix of systematic parameters obtained from ND fit.

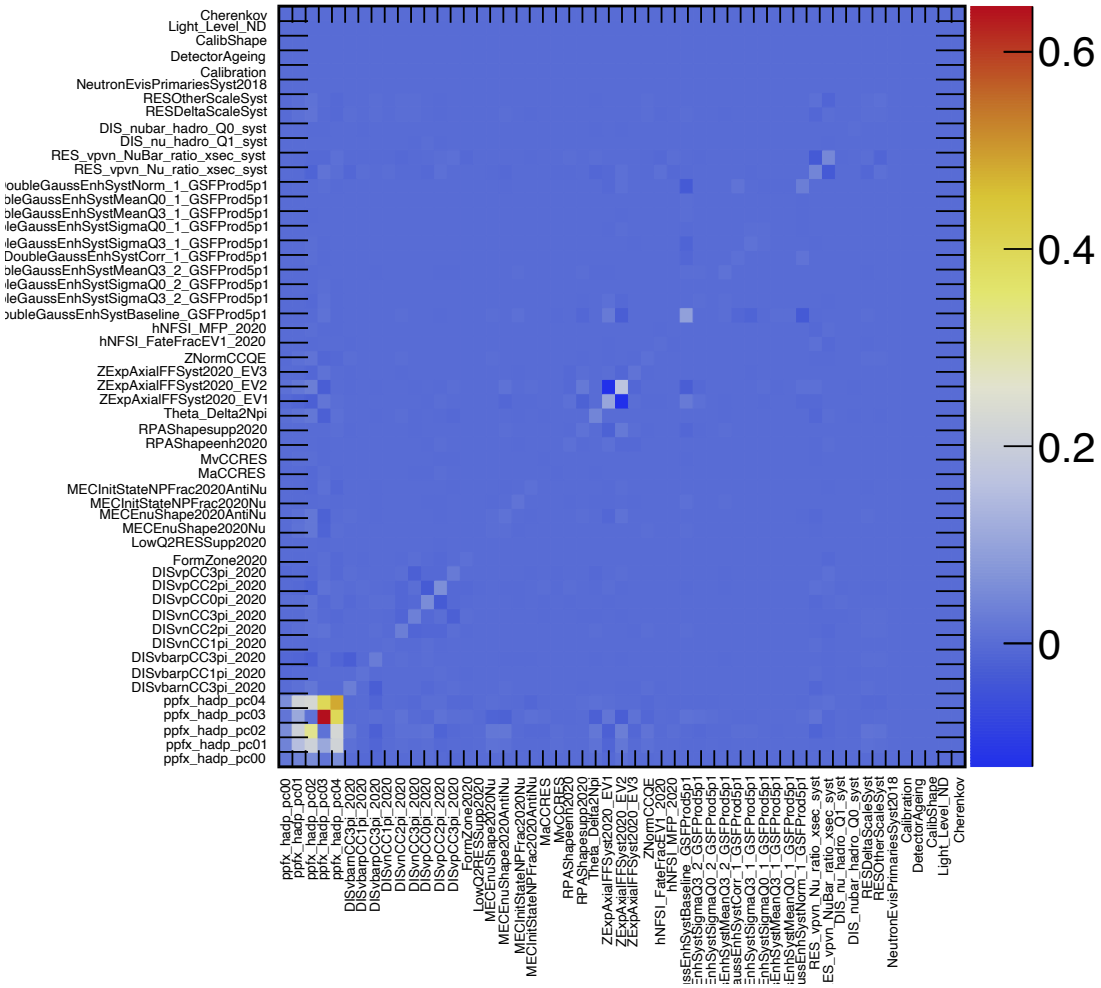

Figure B.8: ND fit covariance matrix of systematic parameters obtained from ND fit.

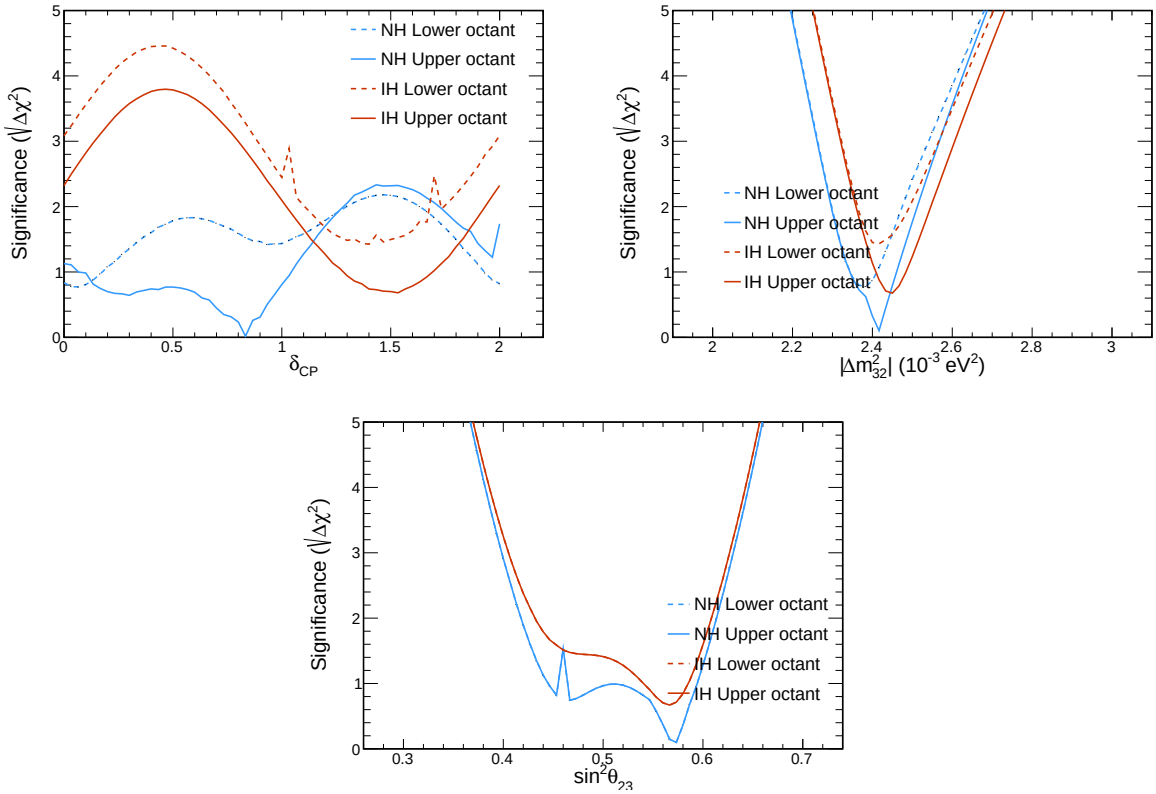

Figure B.9: One-dimensional significances for δ_{CP} , Δm^2_{32} and $\sin^2\theta_{23}$ in the RES-like-reweighted MEC fake data fit, shown for Normal (blue) or inverted (red) mass ordering/hierarchy, and for upper (solid line) or lower (dashed line) octants. The best fit point had $\chi^2_{min} = 0.29$, $\sin^2\theta_{23}$ =2.42×10^{-3}eV^2, $\Delta m^2_{32} = 0.57$, δ_{CP} =0.83π.

APPENDIX C. RESIDUAL FAKE DATA PREDICTIONS

The following sections contain the FD predictions assuming the oscillation parameters in table C.1, compared with the fake data that includes the residual difference weights as explained in section 6.5.3.

Table C.1: Specific oscillation parameter values for Asimov points chosen.

Parameter	**Asimov A**	**Asimov B**	**Asimov C**
$\Delta m^2_{32}(\times 10^{-3}\text{eV}^4)$	2.41	2.51	-2.45
$\sin^2\theta_{23}$	0.57	0.53	0.5
δ_{CP}	0.82π	1.5π	1.5π

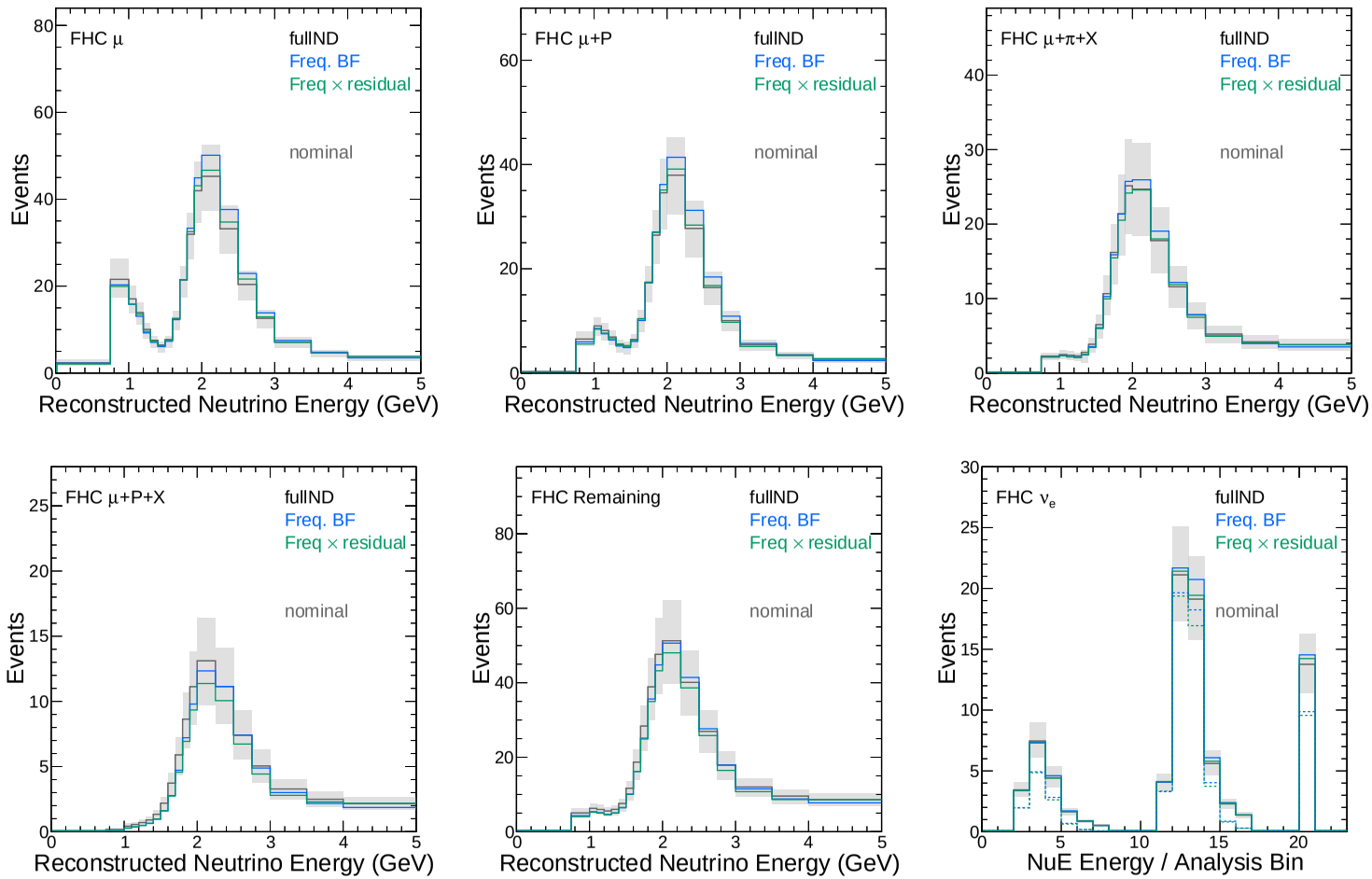

Figure C.1: FD FHC predictions at Asimov A oscillation parameters. The blue line inidcates the constrain from ND applied to FD and the green line has the residual difference weights applied. The grey line and error band indicates the nominal prediction with unconstrained systematic uncertainties. For the ν_e and $\bar{\nu}_e$ cases, the dotted line indicates the ν_μ to ν_e component to which the residual weight was applied.

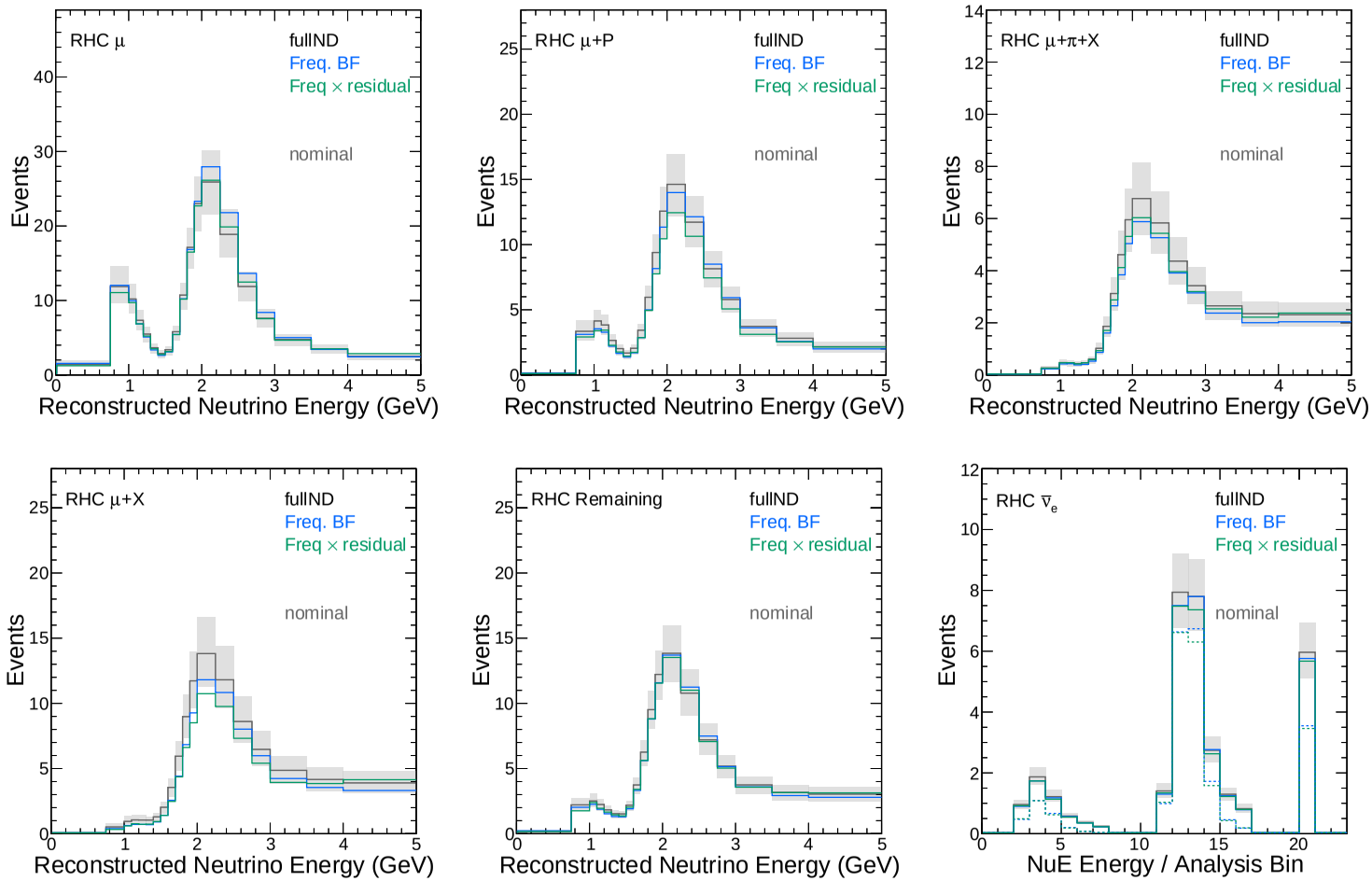

Figure C.2: FD RHC predictions at Asimov A oscillation parameters. The blue line inidcates the constrain from ND applied to FD and the green line has the residual difference weights applied. The grey line and error band indicates the nominal prediction with unconstrained systematic uncertainties. For the ν_e and $\bar{\nu}_e$ cases, the dotted line indicates the ν_μ to ν_e component to which the residual weight was applied.

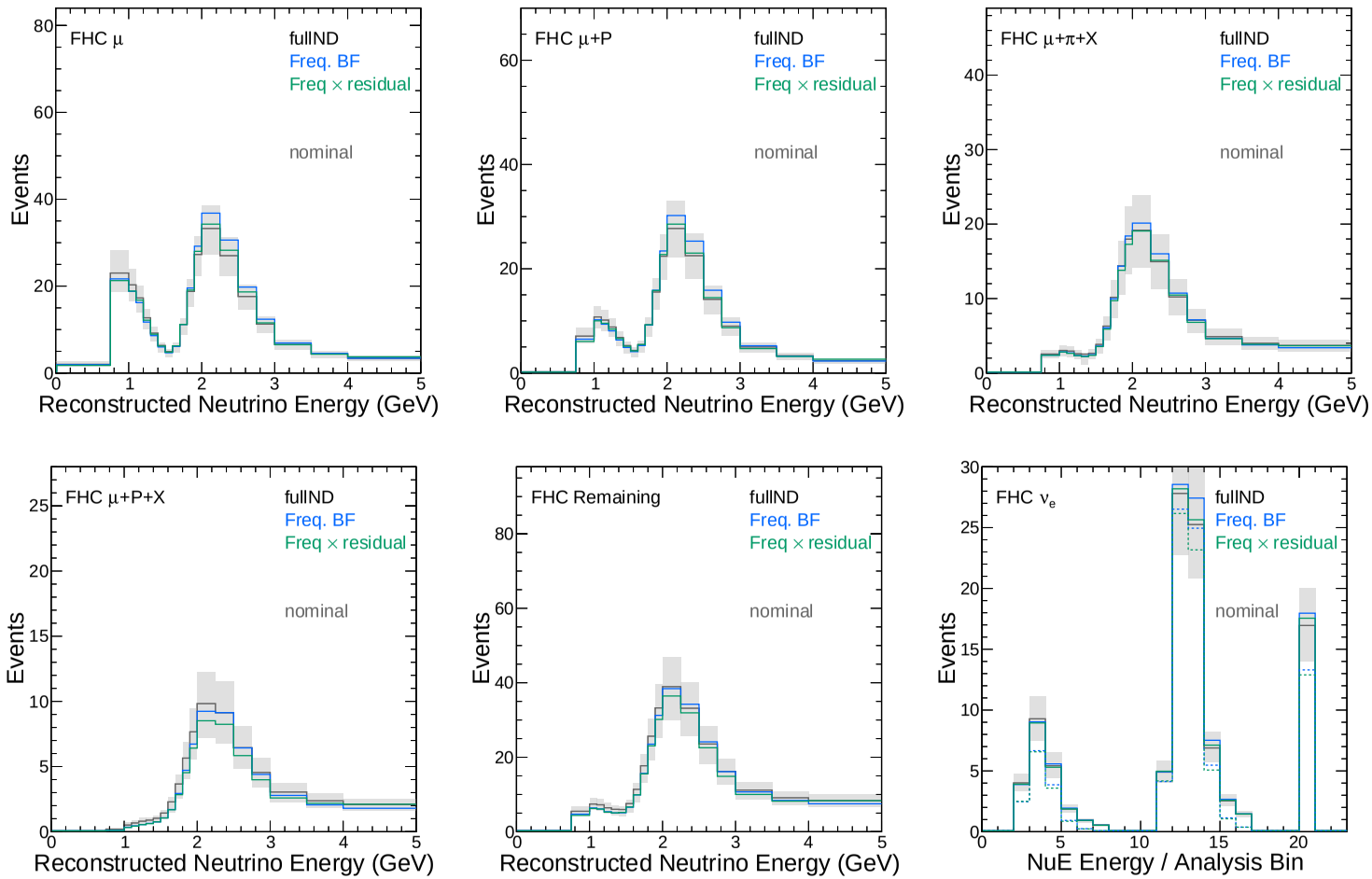

Figure C.3: FD FHC predictions at Asimov B oscillation parameters. The blue line inidcates the constrain from ND applied to FD and the green line has the residual difference weights applied. The grey line and error band indicates the nominal prediction with unconstrained systematic uncertainties. For the ν_e and $\bar{\nu}_e$ cases, the dotted line indicates the ν_μ to ν_e component.

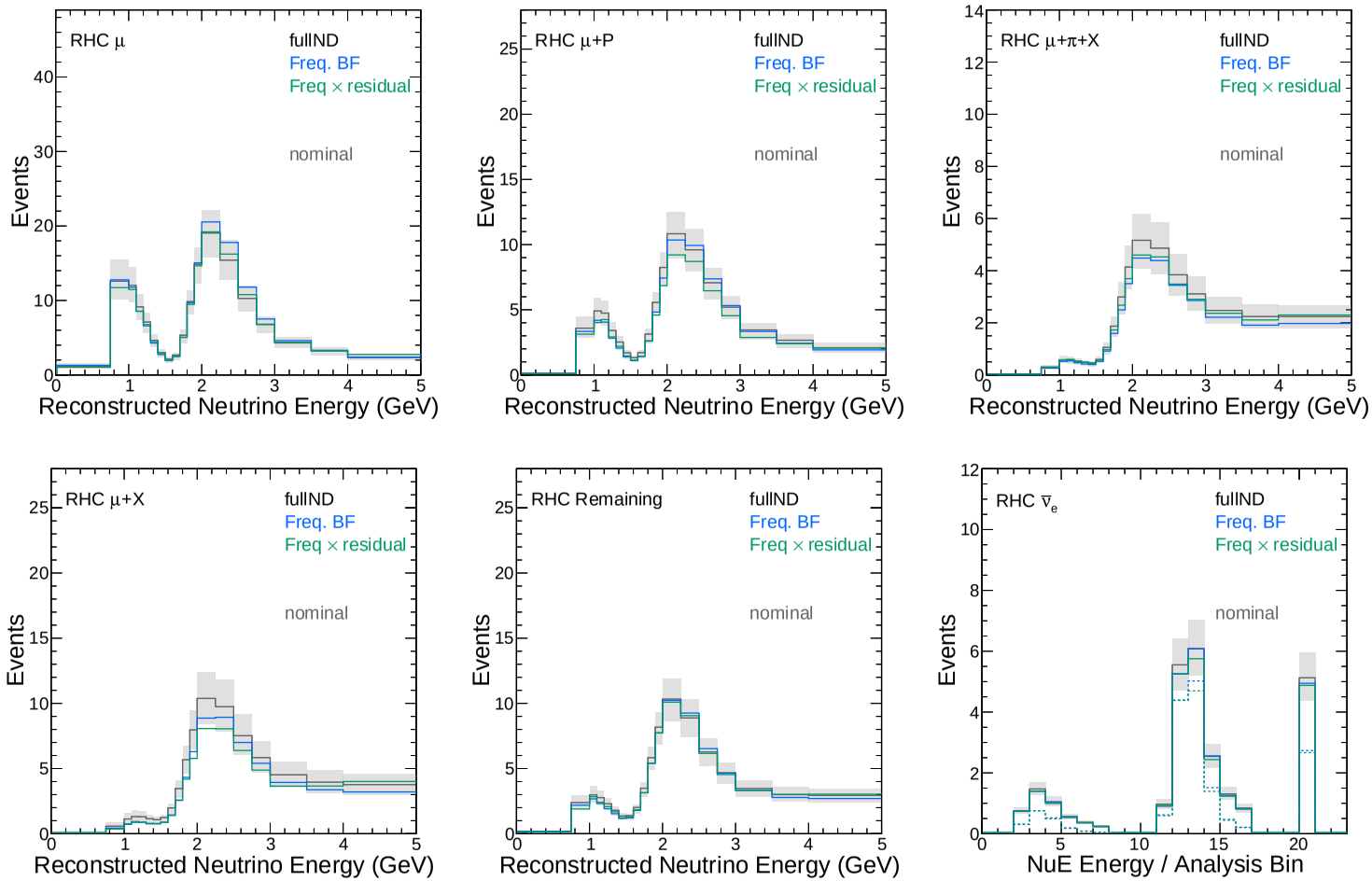

Figure C.4: FD RHC predictions at Asimov B oscillation parameters. The blue line inidcates the constrain from ND applied to FD and the green line has the residual difference weights applied. The grey line and error band indicates the nominal prediction with unconstrained systematic uncertainties. For the ν_e and $\bar{\nu}_e$ cases, the dotted line indicates the ν_μ to ν_e component.

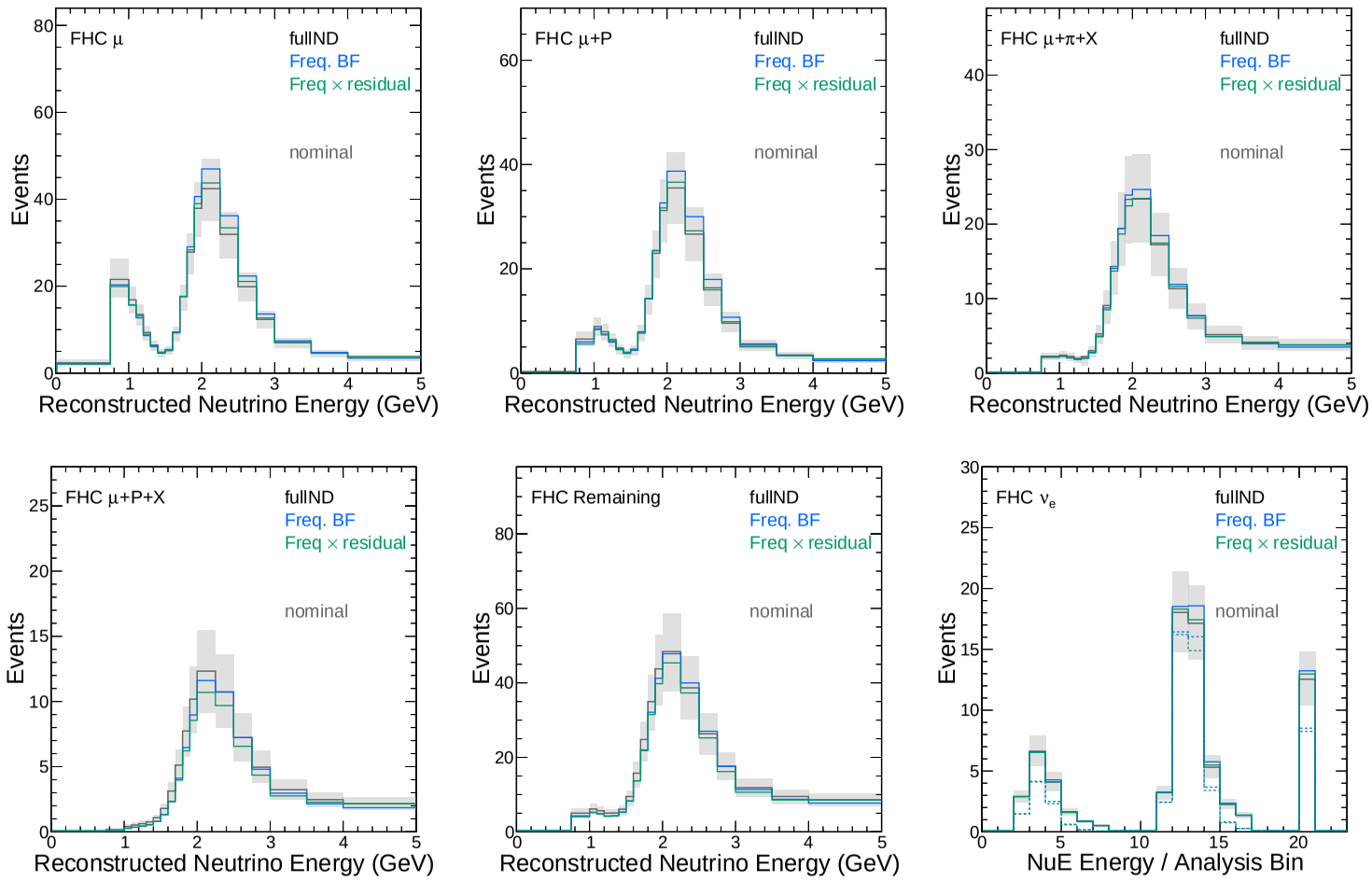

Figure C.5: FD FHC predictions at Asimov C oscillation parameters. The blue line inidcates the constrain from ND applied to FD and the green line has the residual difference weights applied. The grey line and error band indicates the nominal prediction with unconstrained systematic uncertainties. For the ν_e and $\bar{\nu}_e$ cases, the dotted line indicates the ν_μ to ν_e component.

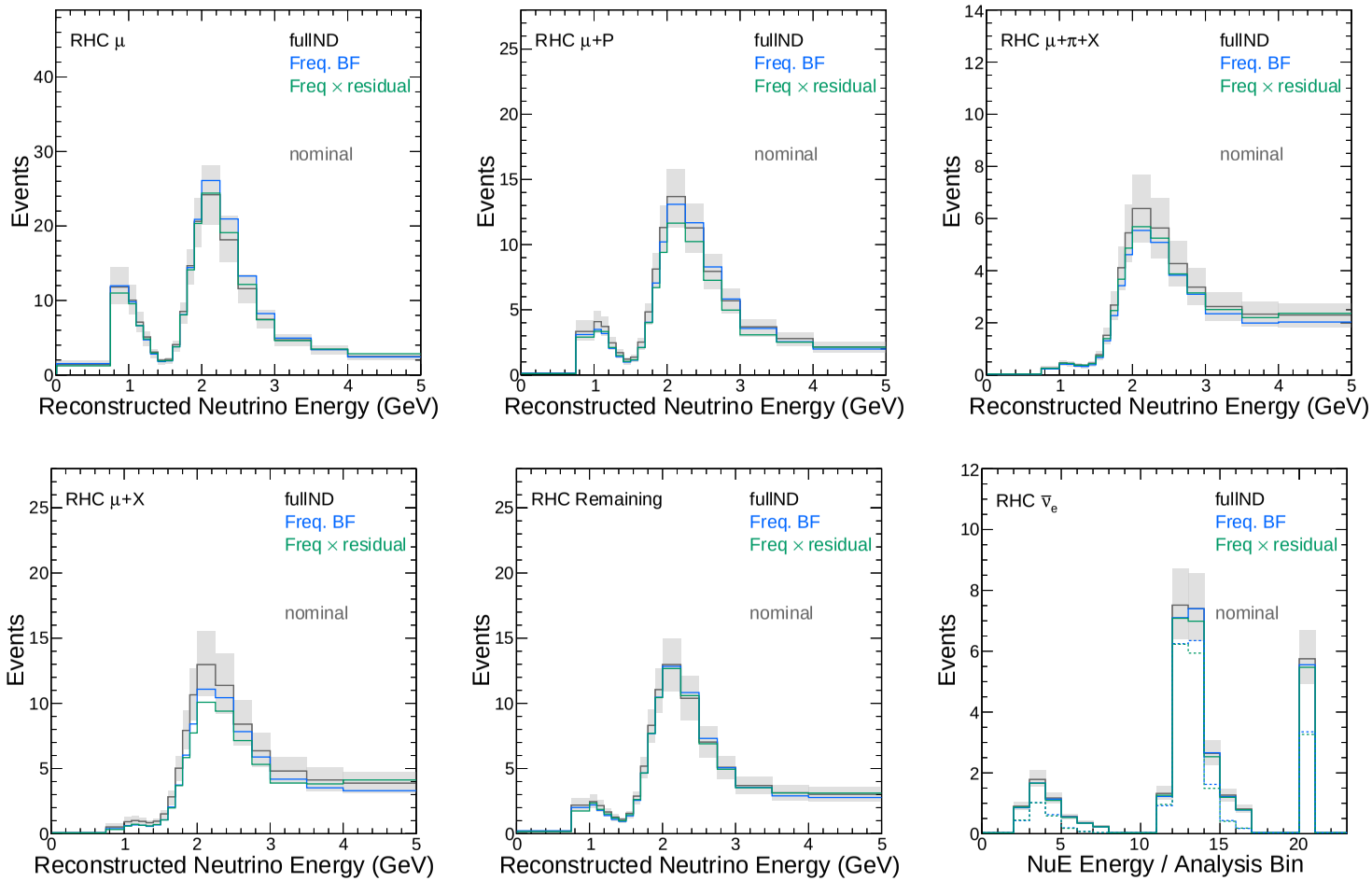

Figure C.6: FD RHC predictions at Asimov C oscillation parameters. The blue line inidcates the constrain from ND applied to FD and the green line has the residual difference weights applied. The grey line and error band indicates the nominal prediction with unconstrained systematic uncertainties. For the ν_e and $\bar{\nu}_e$ cases, the dotted line indicates the ν_μ to ν_e component.